

Electronic Thesis and Dissertation Repository

---

4-17-2023 12:30 PM

## Metal Release of CoCrMo Alloy in Protein-Rich Solutions – Effect of Irradiation, Sliding and Manufacturing Process

Zheng Wei, *The University of Western Ontario*

Supervisor: Hedberg, Yolanda, *The University of Western Ontario*

A thesis submitted in partial fulfillment of the requirements for the Doctor of Philosophy degree in Chemistry

© Zheng Wei 2023

Follow this and additional works at: <https://ir.lib.uwo.ca/etd>

---

### Recommended Citation

Wei, Zheng, "Metal Release of CoCrMo Alloy in Protein-Rich Solutions – Effect of Irradiation, Sliding and Manufacturing Process" (2023). *Electronic Thesis and Dissertation Repository*. 9208.  
<https://ir.lib.uwo.ca/etd/9208>

This Dissertation/Thesis is brought to you for free and open access by Scholarship@Western. It has been accepted for inclusion in Electronic Thesis and Dissertation Repository by an authorized administrator of Scholarship@Western. For more information, please contact [wlsadmin@uwo.ca](mailto:wlsadmin@uwo.ca).

## Abstract

CoCrMo alloys, which have excellent corrosion and wear resistance, are widely used for dental and orthopedic implants in the human body. Because of their wear resistance, they are used in bearing and wearing parts of many artificial implants such as dental crowns and knee and hip joints. Even for the most corrosion-resistant alloys, interfacial reactions occur between the metal surface and the biological environment. The failure of implants or adverse health effects such as brain damage can sometimes be caused by tiny amounts of released metals from the surface of the CoCrMo alloy. Hence, it is very important to investigate the mechanism of corrosion behavior of CoCrMo in protein-rich solutions. This research is mainly focused on the metal release and corrosion behavior of CoCrMo alloy in protein-rich solutions under different simulated conditions and for different manufacturing processes. Implants can sometimes be present in patients who need to undergo cancer radiotherapy, during which the implant or adjacent tissue could be in the irradiation zone. Therefore, the effect of gamma irradiation on the metal release from CoCrMo alloy and 316L stainless steel was investigated. Despite the relatively low total irradiation dose, it was observed that the radiation slightly influenced the extent of metal release from CoCrMo alloy. Based on the excellent wear resistance, CoCrMo alloys usually are used in bearing and wearing parts of implants, where they are exposed to load, friction, and a protein-rich environment. Hence, the effect of sliding, protein aggregation and metal precipitation on metal release from CoCrMo were investigated. In this study, metal release under sliding condition was increased in the presence of bovine serum albumin. However, protein aggregation and metal precipitation can result in underestimation of the extent of metal release from CoCrMo in mixed protein solutions, especially under sliding conditions. Generally, 3D printers are widely used for manufacturing implants of various shapes. However, the print direction may have an influence on the properties of CoCrMo alloys, such as corrosion resistance. The influence of the manufacturing process on protein-induced corrosion for CoCrMo alloy was minor. All these studies give a deep insight in the extent and mechanism of metal release from CoCrMo alloys in protein-rich solutions, which helps to minimize the failure of implants.

## Keywords

CoCrMo, metal release, irradiation, sliding, manufacturing process, protein aggregation, metal precipitation, corrosion, electrochemistry, biocompatibility.

## Summary for Lay Audience

This thesis discusses the use of cobalt-chromium-molybdenum (CoCrMo) alloys in dental and orthopedic implants due to their excellent corrosion and wear resistance. While these metals are ideal for use in the body, the interfacial reactions that occur between the metal surface and the biological environment can lead to the failure of implants or adverse health effects such as brain damage. Thus, it is important to investigate the mechanisms of CoCrMo alloy's corrosion behavior in similar environments as the human body, which means protein-rich solutions.

Another study investigated the effect of gamma irradiation on the metal release from CoCrMo alloy and 316L stainless steel. We found that the relatively low total irradiation doses slightly influenced the extent of metal release from CoCrMo alloy.

It was also discussed how the alloy's excellent wear resistance makes it ideal for use in bearing and wearing parts of implants. However, it was found that the metal release from CoCrMo under sliding conditions increased in the presence of bovine serum albumin, which simulates a common protein in the human body. Further, it was found that protein aggregation and metal precipitation resulted in an underestimation of the extent of metal release from CoCrMo in mixed protein solutions, especially under sliding conditions. This means that the estimated safety of CoCrMo by similar tests can be too high.

Finally, 3D printers are widely used for the manufacturing of implants of various and customized shapes. However, the print direction may have an influence on the properties of CoCrMo alloys, such as corrosion resistance. This thesis found a relatively minor influence, however, it was greater in protein-rich and aggressive environments, such as diluted hydrochloric acid and depended on the surface condition of the alloy.

By investigating the mechanism of corrosion behavior of CoCrMo in protein-rich solutions, it can be better understood how these alloys behave in the body and the safety and effectiveness of the implants can be improved. These studies can help minimize the failure of implants, ultimately leading to better health outcomes for patients who receive these types of implants.

## Co-Authorship Statement

This thesis includes Chapters 3-5, which are reprinted from publications in peer-reviewed scientific journals. They contain published materials in the following journals:

**Chapter 3:** This article was first-authored by the author and co-authored by Jonathan Edin, Anna Emelie Karlsson, Katarina Petrovic, Dr. Inna Soroka, Dr. Inger Odnevall Wallinder and Dr. Yolanda Susanne Hedberg (*Journal of Biomedical Materials Part B*, vol. 106, no. 7, 2018, pp. 2673-2680). All data presented in the article was collected by the author, and the author helped to prepare the first draft of the manuscript. J.E, A.E.K, and K. P assisted with preliminary metal release exposure and measurements (during their B.Sc. thesis work). Dr. Soroka assisted with gamma irradiation exposure and expertise. Dr. Odnevall Wallinder assisted with surface analysis. Dr. Hedberg designed the experiment. The article was edited by Dr. Odnevall Wallinder and Dr. Hedberg.

**Chapter 4:** This article was first-authored by the author and co-authored by Dr. Valentin Romanovski, Dr. Luimar Filho, Dr. Cecilia Persson and Dr. Yolanda Susanne Hedberg (*Journal of Bio-and Tribo-Corrosion*, vol. 8, no. 1, 2022, pp. 1-11). All data presented in the article was collected by the author, and the author prepared the first draft of the manuscript. Dr. Romanovski assisted with digestions and trace metal analysis. Dr. Filho and Dr. Persson assisted with pin-on-disk measurements and expertise. Dr. Hedberg and the author designed the experiment. The article was edited by Dr. Hedberg.

**Chapter 5:** This article was third-authored by the author and co-authored by Dr. Masoud Atapour, Saber Sanaei, Dr. Mohammadali Sheikholeslam, Dr. Jeffrey D. Henderson, Dr. Ubong Eduok, Dr. Yara K. Hosein, Dr. David W. Holdsworth, Dr. Yolanda Susanne Hedberg and Dr. Hamid Reza Ghorbani (*Electrochimica Acta*, 2023, p.142059). The author helped to prepare the first draft of the manuscript, evaluated some experiments (electrochemistry), designed parts of the experiments, and conducted some experiments (confocal laser scanning microscopy).

## Acknowledgments

Without the help and support of many individuals, this doctoral thesis work would not have been possible. I am grateful for the contributions made by everyone I encountered during this challenging period, as each person played a significant role in shaping the outcome of this research project.

First and foremost, I want to express my deepest gratitude to my supervisor, Yolanda Hedberg. Her unwavering support, guidance, and encouragement were critical to the completion of this doctoral thesis. Throughout the entire process, Yolanda's expertise, knowledge, and insightful feedback have been invaluable in shaping the direction of my research and helping me to navigate the challenges I faced. I am grateful for the countless hours she dedicated to reviewing my work, answering my questions, and helping me to push beyond my limits.

I would like to extend my sincere thanks to Dr. Masoud Atapour and his colleagues in Iran for their invaluable cooperation and support throughout my research project. Their willingness to share their expertise and knowledge was crucial to the successful completion of my doctoral thesis.

I would also like to express my gratitude to the entire Shoesmith/Noël research groups for their support. Special thanks go to Dr. Jamie Noël and Dr. Dmitriy Zagidulin for their guidance and mentorship. I would also like to express my sincere appreciation to (soon Dr.) Sina Matin for his help and support in conducting the experimental part of my research.

I am grateful to the individuals in the Hedberg group for their invaluable contributions to my doctoral research. I would like to thank Dr. Ubong Eduok, Dr. Marshall Yang, Saman Nikpour, Seyedeh Marzieh Kalantarian, Zoltan Wolfgang Richter-Bisson, Ekrupe Kaur, Lila Laundry-Mottiar, Waruni Senanayake, Robert Addai, Ola Doktor, and Narges Hajighasemi for their support, encouragement, and camaraderie.

I would like to express my gratitude to the individuals at Surface Science Western, including Dr. Jeffrey D. Henderson, Dr. Sridhar Ramamurthy, Dr. Vahid Dehnavi, and Mr. Ivan Barker for their invaluable contributions to my doctoral research.

Lastly, I would like to acknowledge the unwavering support and encouragement of my family, without whom this accomplishment would not have been possible.

To my parents, Changsheng Wei and Ruimin Xi, I am forever grateful for your unconditional love and support, as well as for instilling in me a strong work ethic and a love of learning.

To my wife, Litao Yin, thank you for your endless patience, love, support, and humour. You were always there for me, providing a listening ear, a shoulder to cry on, and the motivation to keep going, even in the most challenging times.

To my mother-in-law, Yifeng Jiang, thank you for helping to take care of my daughter Elsa during this time. Your support and assistance were greatly appreciated.

Lastly, I would like to thank my dear daughter, Yuxin (Elsa) Wei, for bringing light into my life and providing a constant source of motivation and inspiration. Your presence in my life has been a true blessing.

# Table of Contents

Abstract.....	ii
Summary for Lay Audience.....	iv
Co-Authorship Statement.....	v
Acknowledgments.....	vi
Table of Contents.....	viii
List of Tables.....	xiii
List of Figures.....	xv
List of Symbols and Abbreviations.....	xxi
List of Appendices.....	xxiv
Chapter 1.....	1
1 Introduction of biomedical alloys for implants, CoCrMo Alloy and Metal Release.....	1
1.1 Overview of Artificial Implants.....	1
1.1.1 History of Implants.....	1
1.1.2 Joint replacements in Canada.....	5
1.2 CoCrMo Alloy.....	8
1.3 Manufacturing of relevance for implants.....	10
1.3.1 Warm-worked CoCrMo alloy.....	10
1.3.2 Laser powder bed fusion (LPBF) CoCrMo alloy.....	11
1.4 Metal release.....	14
1.4.1 Metal release and toxicity.....	14
1.4.2 Vroman effect.....	18
1.4.3 Corrosion in Protein Environments, Protein Aggregation, and Precipitation.....	19
1.5 References.....	23



Chapter 2.....	38
2 Justification of experimental choices .....	38
2.1 Synthetic biological fluids .....	38
2.1.1 Phosphate buffered saline .....	39
2.1.2 2-(N-morpholino)ethanesulfonic acid (MES) buffer .....	40
2.2 Justification of protein concentration.....	41
2.2.1 Bovine serum albumin (BSA).....	41
2.2.2 Fibrinogen (Fbn) .....	42
2.3 Metal release estimations .....	42
2.4 References.....	45
Chapter 3.....	50
3 Can Gamma Irradiation during Radiotherapy Influence the Metal Release Process for Biomedical CoCrMo and 316L alloys?.....	50
3.1 Introduction.....	50
3.2 Materials and Methods.....	52
3.2.1 Materials .....	52
3.2.2 Metal Release Exposure and Irradiation.....	52
3.2.3 Trace Metal Analysis .....	53
3.2.4 Analysis of Albumin Size by Dynamic Light Scattering.....	54
3.2.5 Analysis of Surface Composition by Means of X-Ray Photoelectron Spectroscopy .....	55
3.2.6 Statistics .....	56
3.3 Results and Discussion .....	56
3.3.1 Metal release .....	56
3.3.2 Surface Characterization.....	58
3.3.3 Effects of Gamma Irradiation on Size of Albumin.....	60
3.4 Discussion.....	61

3.5	Conclusions.....	63
3.6	References.....	65
Chapter 4.....		71
4	Metal Release from a Biomedical CoCrMo Alloy in Mixed Protein Solutions under Sliding Conditions: Effect of Protein Aggregation and Metal Precipitation .....	71
4.1	Introduction.....	71
4.2	Materials and Methods.....	72
4.2.1	Materials .....	72
4.2.2	Metal Release Investigations in Static Condition (Without Friction).....	72
4.2.3	Metal Release Investigations under Sliding Conditions .....	75
4.2.4	Digestion.....	76
4.2.5	Atomic Absorption Spectroscopy (AAS) .....	77
4.2.6	X-Ray Photoelectron Spectroscopy (XPS).....	78
4.2.7	Statistical Calculations.....	78
4.3	Results and Discussion .....	78
4.3.1	Non-Sequential Release of Metals in Static Conditions.....	78
4.3.2	Sequential Release of Metals in Static Conditions .....	80
4.3.3	Surface Characterization after Sequential Exposure in Static Conditions	83
4.3.4	Sequential Release of Metal under Sliding Conditions .....	86
4.3.5	Influence of Metal Precipitation .....	91
4.3.6	Vroman effect .....	93
4.3.7	Significance, Limitation, and Future directions.....	93
4.4	Conclusions.....	94
4.5	References.....	95
Chapter 5.....		100
5	In vitro corrosion and biocompatibility behavior of CoCrMo alloy manufactured by laser powder bed fusion parallel and perpendicular to the build direction .....	100

5.1	Introduction.....	100
5.2	Materials and methods .....	101
5.2.1	Sample fabrication and characterization.....	101
5.2.2	Microstructure and surface roughness characterization.....	102
5.2.3	X-ray photoelectron spectroscopy (XPS) .....	103
5.2.4	Corrosion studies .....	103
5.2.5	Bioactivity studies.....	104
5.2.6	Cell culture.....	105
5.2.7	Cell adhesion and morphological characterization.....	105
5.2.8	Cell viability.....	106
5.2.9	Statistical analysis.....	107
5.3	Results and discussion .....	107
5.3.1	Microstructure and surface roughness .....	107
5.3.2	Surface characterization.....	110
5.3.3	Corrosion.....	111
5.3.4	Bioactivity and biocompatibility.....	119
5.3.5	Further discussion.....	123
5.4	Conclusions.....	126
5.5	References.....	127
	Chapter 6.....	135
6	The Influence of the Manufacturing Process on the Corrosion of CoCrMo Alloy in Simulated Physiological Environments .....	135
6.1	Introduction.....	135
6.2	Materials and Methods.....	136
6.2.1	Materials and sample preparation .....	136
6.2.2	Metal release test procedure and electrochemistry measurements .....	139

6.2.3	Microwave digestion.....	142
6.2.4	Trace metal analysis in solution.....	142
6.2.5	X-ray diffraction (XRD) analysis .....	143
6.2.6	Scanning electron microscopy (SEM) and confocal microscopy .....	143
6.2.7	X-ray photoelectron spectroscopy (XPS) .....	143
6.2.8	Contact angle analysis.....	144
6.2.9	Statistical analysis.....	144
6.3	Results and Discussion .....	144
6.3.1	Surface characterization.....	144
6.3.2	Metal release .....	148
6.3.3	Electrochemistry .....	150
6.3.4	Contact angle and surface roughness .....	161
6.3.5	XPS .....	163
6.4	Further Discussion .....	164
6.5	Conclusions.....	167
6.6	References.....	168
Chapter 7	.....	176
7	Conclusions and outlook.....	176
7.1	Conclusions.....	176
7.2	Outlook .....	180
Appendices	.....	182
Curriculum Vitae	.....	191

## List of Tables

Table 3-1: Nominal Bulk Alloy Composition of AISI 316L and CoCrMo Alloy (wt. %)	52
Table 3-2: X-Ray Photoelectron Spectroscopy (XPS) Binding Energies and Assignments	56
Table 4-1: Single solution exposures and durations (without friction)	73
Table 4-2: Sequential solution exposures (all sampled after 1, 4, 6, 24 h). The volumes shown are for tests without friction (static conditions). They were 45 mL (first solution) and 20 mL (second solution) in the case of the tests with friction (sliding conditions)	74
Table 4-3: EDS results of CoCrMo disks exposed to PBS with 10 g/L Fbn for 24 h, with a spot focus on the protein aggregates	83
Table 4-4: Observed binding energies and assignments of Co, Cr, Mo, N, C and O of the outermost surface of CoCrMo disks based on X-ray photoelectron spectroscopy (XPS) measurements [34; 35]	85
Table 5-1: As per supplier information, chemical composition of CoCrMo (F75) alloy powder	102
Table 5-2: LPBF setup and parameters	102
Table 5-3: Composition of the simulated body fluid (SBF), with pH 7.4, adjusted with 1 M HCl; adapted from [33]	105
Table 5-4: Cathodic and anodic Tafel constants ( $\beta_a$ and $\beta_c$ ), corrosion current densities ( $i_{corr}$ ), passive current densities ( $i_{pass}$ ) and corrosion potentials ( $E_{corr}$ ) based on potentiodynamic polarization of the LPBF CoCrMo specimens after 1 h immersion in citric acid (CA) (pH=2.4), PBS (pH 7.4), and CA + PBS (pH = 7. 4) solutions at room temperature	114
Table 5-5: EIS fitting parameters (average and standard deviation of two independent specimens). A one-time constant (Randles equivalent electrical circuit) was applied	118
Table 6-1: Chemical composition of the CoCrMo alloy powder. Bal. – balance (remainder to 100 wt.%)	137

Table 6-2: The limits of detection and quantification of Co, Cr and Mo. ....	142
Table 6-3: The percentage of $\gamma$ (FCC) and $\epsilon$ (HCP) phases in the polished LPBF fabricated CoCrMo alloy built in different orientations. ....	147
Table 6-4: The corrosion current densities ( $i_{\text{corr}}$ ), passive current densities ( $i_{\text{pass}}$ , here defined as the current density +120 mV versus $E_{\text{corr}}$ ) and corrosion potentials ( $E_{\text{corr}}$ ) based on potentiodynamic polarization of the CoCrMo specimens immersed in MES+BSA (pH=7.2), and HCl solutions at 37 °C. Mean values and standard deviations of triplicate samples. H - horizontal (XOY); V - vertical (XOZ). ....	155
Table 6-5: EIS parameters and fitting data (average and standard deviation of at least three independent specimens) based on the equivalent circuit models used for MES+BSA and HCl solutions. ....	160
Table 6-6: Mean contact angle values. ....	162
Table 6-7: The surface roughness and surface area of CoCrMo alloy fabricated in horizontal and vertical orientations for the $1.5 \times 1.5$ cm ( $2.25 \text{ cm}^2$ ) coupon.....	162

## List of Figures

Figure 1-1: Schematic illustration of artificial hip joint implants.....	2
Figure 1-2: Top reasons for hip and knee replacement revision in Canada during 2018-2019. [26].....	7
Figure 1-3: Total number of hip and knee replacements including revision in Canada during 2014-2019. [26].....	8
Figure 1-4: The manufacture process of laser powder bed fusion (LPBF).....	12
Figure 1-5: Schematic diagram of different building direction for the hip implant. ....	14
Figure 2-1: A depiction of the chemical structure of MES in 2D and 3D [26]. ....	41
Figure 3-1: Released and nonprecipitated amounts of Co, Cr, and Mo in solution (aq—aqueous) from the CoCrMo alloy (a), and of Fe, Cr, and Ni from the 316L alloy (b) after 0 (few seconds), 0.035 (2 min 13 s), and 1 h of exposure at room temperature with or without irradiation (during the time period 0–0.035 h) in PBS (pH 7.3) or PBS and 10 g/L BSA (pH 7.3). Statistical differences: * $p < 0.05$ , ** $p < 0.01$ , *** $p < 0.001$ . non, nonirradiated; irr, irradiated; <LOD, below limit of detection. ....	58
Figure 3-2: Relative oxidized metal content (wt. %) in the surface oxide of the CoCrMo (a) and 316L (b) alloys, as determined by XPS. Statistically significant differences are indicated (* $p < 0.05$ , ** $p < 0.01$ , *** $p < 0.001$ ). Non-irr., nonirradiated; irr., irradiated.....	60
Figure 3-3: Hydrodynamic size distributions of BSA by intensity (by means of PCCS, a) and by number (by means of NTA, b) of 0.2 $\mu\text{m}$ filtered irradiated and nonirradiated PBS + BSA solutions, and with and without trace amounts of metal ions. non-irr., nonirradiated; irr., irradiated; w ions, with 150 $\mu\text{g/L}$ Co and 5 $\mu\text{g/L}$ Cr. ....	61
Figure 4-1: Illustration of the non-sequential test procedure, and the sequential test procedure, for metal release testing in static conditions (without friction). Conditions: 37 $^{\circ}\text{C}$ , bilinear agitation (22 cycles/minute, 12 $^{\circ}$ ), darkness. ....	74

Figure 4-2: Schematic illustration of the pin movement on the CoCrMo disk set-up for testing under sliding conditions..... 76

Figure 4-3: Released and non-precipitated amounts ( $\mu\text{g}/\text{cm}^2$ ) of Co, Cr and Mo in solution from CoCrMo disks exposed to PBS, PBS+BSA (10g/L), PBS+Fbn (10g/L), PBS+Fbn (10g/L)+BSA(10g/L) or PBS+Fbn (2.67g/L)+BSA (40g/L) at pH 7.2-7.4 after 4 h and 24 h at 37 °C. Significant differences are indicated by asterisks: \*  $p<0.05$ , \*\* $p<0.01$ ; n=3..... 79

Figure 4-4: Released and non-precipitated amounts of Co (a), Cr (b) and Mo (c) in solution from disks of a CoCrMo alloy exposed to four sequential solutions (pH 7.2-7.4); PBS followed by PBS (PBS, PBS), PBS+ 40 g/L BSA followed by PBS+40 g/L BSA (BSA, BSA), PBS+2.67 g/L Fbn followed by PBS+2.67 g/L Fbn (Fbn, Fbn), and PBS+ 40 g/L BSA followed by 2.67 g/L Fbn (BSA, Fbn); exposed at 37 °C and sampled after 1, 4, 6 and 24 h. The second solution was added after 5 h. The error bars show the standard deviation of independent triplicate disks..... 82

Figure 4-5: Representative LOM (left) and SEM (right) micrographs of a CoCrMo disk, which was exposed to PBS with Fbn (10 g/L) for 24 h in static conditions..... 82

Figure 4-6: Relative metal content in the outermost surface oxide of the CoCrMo alloy being abraded (as non-exposed reference) and exposed to four sequential solutions (pH 7.2-7.4); PBS followed by PBS (PBS, PBS), PBS+ 40 g/L BSA followed by PBS+40 g/L BSA (BSA, BSA), PBS+2.67 g/L Fbn followed by PBS+2.67 g/L Fbn (Fbn, Fbn), and PBS+ 40 g/L BSA followed by 2.67 g/L Fbn (BSA, Fbn); exposed at 37 °C for 24 h; studies by means of X-ray photoelectron spectroscopy; statistically significant differences are indicated by asterisks: \*  $p<0.05$ , \*\* $p<0.01$ ; n=2..... 84

Figure 4-7: Released and non-precipitated amounts of Co (a), Cr (b) and Mo (b) in solution from disks of CoCrMo alloy exposed to four solutions under sliding (slide) and non-sliding (non-slide) conditions (pH 7.2-7.4); PBS followed by PBS (PBS, PBS), PBS+40 g/L BSA followed by PBS+40 g/L BSA (BSA, BSA), PBS+2.67 g/L Fbn followed by PBS+2.67 g/L Fbn (Fbn, Fbn), and PBS+ 40 g/L BSA followed by 2.67 g/L Fbn (BSA, Fbn); exposed at 37 °C and sampled after 24 h. The control denotes the background control in the test-setup under sliding conditions (Fig. 4-2). The error bars show the standard deviation of independent



triplicate disks. Significant differences are indicated by asterisks: \*  $p < 0.05$ , \*\* $p < 0.01$ ;  $n = 3$ .  
..... 88

Figure 4-8: Changes in coefficient of friction under sliding conditions. A, B, C denotes different replicate measurements. Only one data set available for “BSA, BSA”. ..... 90

Figure 4-9: The mass ratios of Co (a), Cr (b) and Mo (c) between the bottom and top part of collected solution samples (under sliding conditions) after centrifugation. The Mo values that are equal to zero mean that the bottom fraction was non-detectable. The bottom part of the centrifuge tube contains heavier constituents (wear particles, protein aggregates), if present, compared to the top part of the centrifuge tube. .... 93

Figure 5-1: Optical micrographs of different planes of the CoCrMo specimens: (a,d) top (XY plane), (b,e) mid (XZ plane), (c,f) bottom (XZ plane) areas (inset: merged sides in 3D). SEM micrographs of the printed CoCrMo specimens at (g) low magnification view of as-received XY, (h) low magnification view of as-received XZ, (i) high magnification view of the abraded and etched XY, (j) low magnification view of abraded and etched XZ. (k) XRD patterns of the abraded XY and XZ specimens. (l) Surface texture parameters of the printed CoCrMo in the as-received and abraded conditions. The error bars show the standard deviation of triplicate measurements.  $R_a$  (arithmetical mean deviation of the assessed profile),  $R_p$  (maximum peak height),  $R_q$  (root mean square average of the profile),  $R_v$  (maximum valley depth) and  $R_z$  (maximum height of the profile). .... 109

Figure 5-2: Surface composition estimated from the XPS wide spectra (a) and relative surface composition and speciation of the elements Co, Cr, and Mo (b) of as-received (AR) and abraded (Abr.) CoCrMo surfaces in XY and XZ planes. Corresponding spectra are shown in Figs. S3-S7 (supplementary information). ..... 111

Figure 5-3: Representative cyclic polarization curves (forward and reverse scans) for as-received (AR) and abraded (Abr.) CoCrMo specimens in XY and XZ plane in citric acid (pH=2.4) (a), PBS (pH 7.4) (b), and PBS + citric acid (pH = 7. 4) (c) solutions at room temperature. .... 113

Figure 5-4: Representative Nyquist (a-c), Bode phase angle (d-f), and Bode impedance (insets in d-f) plots of as-received and abraded CoCrMo in planes XY and XZ after 1 h

immersion in citric acid (pH 2.4) (a, d), PBS (pH 7.4) (b, e), and PBS + citric acid (pH 7.4) (c, f) at room temperature. The inset in (a) shows the equivalent electrical circuit for the analysis of the impedance spectra (Table 5-5). Lines – fit; symbols – data points. .... 118

Figure 5-5: SEM images of different specimens after immersion for 7 (D7), 14 (D14), and 28 (D28) days at 37 °C in simulated body fluid. Insets show overview images at lower magnification. .... 120

Figure 5-6: Atomic Ca/P ratio (using EDS) of different specimens after immersion for 7 (D7), 14 (D14), and 28 (D28) days at 37 °C in simulated body fluid. The error bars show the standard deviation among triplicate measurements. The asterisks indicate statistically significant increases compared to the specimens after 7 days (D7): \* -  $p < 0.05$ ; \*\* -  $p < 0.01$ . Examples of corresponding SEM images are shown in Figure S8. .... 121

Figure 5-7: SEM images of the cell-seeded as-received (AR) or abraded (Abr.) XY and XZ CoCrMo surfaces after days 1 and 7. The inset images show images at lower magnification. .... 122

Figure 5-8: Cell viability as compared to control, determined using the MTT assay after 1 (D1), 3 (D3), and 7 (D7) days at 37 °C for triplicate specimens. The asterisks indicate a statistically significant decrease (\* -  $P < 0.05$ ; \*\* -  $P < 0.01$ ) in cell viability. .... 123

Figure 6-1: Building direction and orientation of LPBF printed CoCrMo alloy coupons.... 137

Figure 6-2: The heat treatment process after the additive manufacturing process. .... 138

Figure 6-3: Schematic drawing of exposure and electrochemical measurement..... 141

Figure 6-4: Experimental procedure of exposure and electrochemical measurement. .... 141

Figure 6-5: SEM images of the LPBF fabricated CoCrMo alloy of different surface treatments in different print orientations: a) as-received horizontal (XOY), b) as-received vertical (XOZ), c) polished horizontal, and d) polished vertical. .... 145

Figure 6-6: Confocal microscopy images of as-received CoCrMo alloy fabricated in horizontal (a) and vertical (b) orientations..... 146

Figure 6-7: XRD spectra for the horizontal (XOY) and vertical (XOZ) fabricated CoCrMo alloy after polishing. .... 147

Figure 6-8: Released and non-precipitated amount of Co (a), Cr (b) and Mo (c) per geometric surface area in solution from the LPBF CoCrMo alloy fabricated in horizontal (XOY) and vertical (XOZ) orientations, with and without polishing, after 24 h exposure in MES (5mM) +NaCl (5g/L) +BSA (10g/L) at pH 7.2-7.4 and HCl (0.027M) at 37 °C ..... 150

Figure 6-9: Open circuit potential (representative curves) of CoCrMo alloy fabricated in horizontal (XOY) and vertical (XOZ) orientations, with and without polishing, in MES (5mM) +NaCl (5g/L) +BSA (10g/L) (top) at pH 7.2-7.4 and HCl (0.027M) (bottom) at 37 °C . ..... 152

Figure 6-10: Potentiodynamic polarization curves (starting at the lowest potential and ending at 1.0 V Ag/AgCl) of the as-received (AS) and polished (P) horizontal (H, XOY) and vertical (V, XOZ) CoCrMo samples in 5 mM MES+5 g/L NaCl+10 g/L BSA (top) or 0.027 mM HCl (bottom). Scan rate: 0.167 mV/s. .... 154

Figure 6-11: Experimental impedance plots (Nyquist format) for the as-received and polished CoCrMo alloy fabricated in horizontal (XOY) and vertical (XOZ) orientation after 22 h immersion at 37 °C in the a) MES+BSA, and b) HCl solutions. .... 159

Figure 6-12: Experimental impedance plots (Bode format) for the as-received and polished CoCrMo alloy fabricated in horizontal and vertical orientation after 22 h immersion at 37 °C in the a) MES+BSA, and b) HCl solutions. .... 160

Figure 6-13: The equivalent electric circuits of as-received and polished CoCrMo alloy fabricated in horizontal and vertical orientation immersed at 37 °C in (a) HCl, and (b) MES+BSA, used for the numerical fitting of the impedance data. .... 161

Figure 6-14: Relative surface composition and speciation of the elements Co, Cr, and Mo estimated from the XPS wide spectra of as-received (AS) and polished (P) CoCrMo surfaces fabricated in horizontal (H) and vertical (V) orientation. .... 163

Figure 7-1: Impact of irradiation (Chapter 3), sliding (Chapter 4) and manufacturing process (vertical/horizontal print orientation, Chapter 6) on metal release ratios from CoCrMo alloy exposed to the protein-containing solutions. .... 177

Figure 7-2: The total released amount of metals from forged and LPBF CoCrMo in different solutions, under different conditions (summary of Chapters 3, 4, and 6)..... 178

## List of Symbols and Abbreviations

AAS – atomic absorption spectroscopy

AISI – American iron and steel institute

BE – binding energy

BSA – bovine serum albumin

C – carbon

Co – cobalt

Cl - chlorine

Cr – chromium

Cu - copper

EIS – electrochemical impedance spectroscopy

ELISA - enzyme-linked immunoassay

Fbn – fibrinogen

FCC – face-centered cubic

Fe – iron

GF-AAS – graphite furnace atomic absorption spectroscopy

HCl – hydrochloric acid

HCP - hexagonal close packed

ICP-MS – inductively coupled plasma mass spectroscopy

IRRAS – infrared reflection absorption spectroscopy

LOD - limit of detection

LOM – light optical microscopy

LPBF – laser powder bed fusion

MES - 2-(N-morpholino)ethanesulfonic acid

Mn – manganese

Mo – molybdenum

N – nitrogen

Na - sodium

N/A – no data available

Ni – nickel

NTA – nanoparticle tracking analysis

OCP – open-circuit potential

P – phosphate

p - probability

PBS – phosphate buffered saline

PCCS – photon cross-correlation spectroscopy

S – sulfur

SEM – scanning electron microscopy

Si – silicon

Ti – titanium

XPS – x-ray photoelectron spectroscopy

## List of Appendices

Appendix A: Chapter 5 Supplementary .....	182
Appendix B: Copyright and Permission .....	190



## Chapter 1

### 1 Introduction of biomedical alloys for implants, CoCrMo Alloy and Metal Release

#### 1.1 Overview of Artificial Implants

##### 1.1.1 History of Implants

Implants generally refer to devices that are implanted into the human body for a long time or a period of time. Commonly used metallic implant materials in clinic include stainless steel, titanium alloy and cobalt-chromium alloy, which are mainly used to replace the damaged or diseased hard tissue of patients, such as hip, knee, dental, and vascular stent implants.

Artificial hip replacement is one of the most important and effective procedures for the treatment of the end-stage of diseases such as necrosis of the femoral head, hip dysplasia, degenerative hip arthritis, and rheumatoid arthritis [1]. It refers to the replacement of the diseased or damaged joints with biocompatible materials, which can relieve joint pain, improve the mobility of joints, or correct deformities. Nowadays, the artificial hip joint implants usually include four parts which are the acetabular component, plastic liner, femoral head and stem, as shown in Figure 1-1.

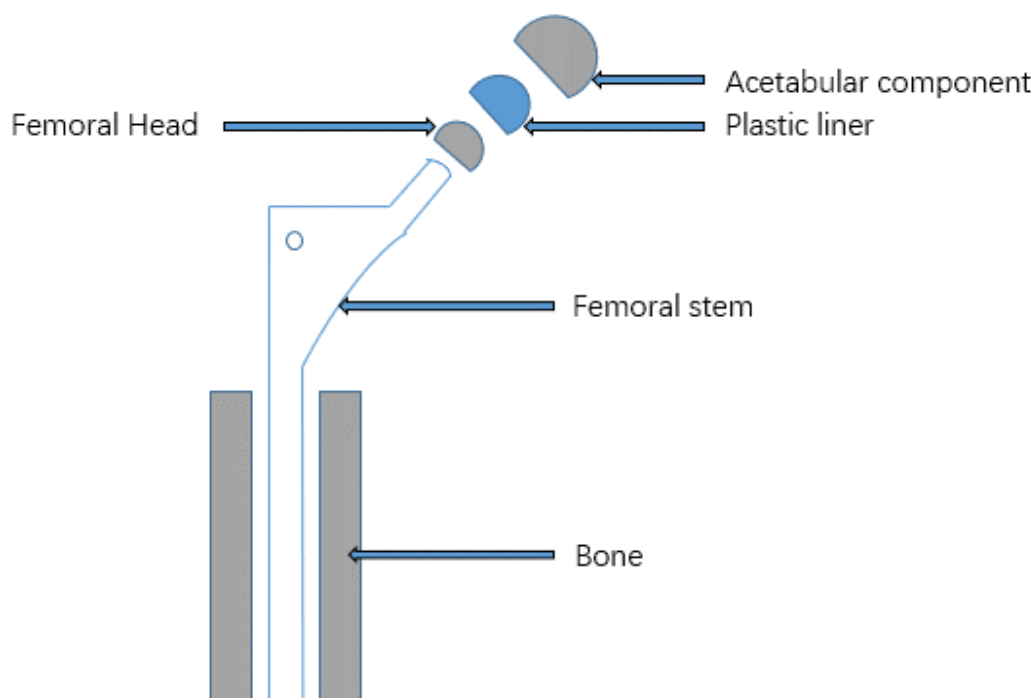


**Figure 1-1: Schematic illustration of artificial hip joint implants.**

Artificial hip replacement has a history of more than 100 years, from the early stage of exploration to today's more mature development stage. At present, artificial hip replacement is widely used. In 1923, American surgeon Marius Smith-Petersen first performed glass arthroplasty on the surface of the femoral head, which is considered the originator of hip replacement [2]. Afterwards Smith-Petersen changed the glassy hemisphere mold to metallic vitallium mold [2]. Phillip Wiles at the Middlesex Hospital, London, Canada performed a total hip replacement for 6 patients with stainless steel prosthesis in 1938 [3]. Phillip secured the acetabular prosthesis with screws and bolted the femoral head prosthesis to the femoral neck and is considered the first orthopedic surgeon to implement a true total hip replacement. In 1939, Austin Moore and F.R Thompson of America designed the long straight-handle artificial femoral head and the long-curved handle femoral head prosthesis, respectively [4]. This later became the prototype for the Muller and Harris total hip femoral head prosthesis [5]. In 1946, Judet performed a half-joint prosthesis in France using a femoral head prosthesis with an acrylate-hot formed straight handle that was emanated from under the large rotor [6]. In

1950, Moore and Thompson respectively designed artificial femoral head prostheses of self-locking CoCrMo alloy and put them into clinical use [4]. In 1953, George McKee used a modified Thompson stem and a new one-piece cobalt-chromium alloy sleeve as the new acetabulum [7]. The prosthesis model has been borrowed by many people, such as Charnley, who used it as a model for the cementitious prosthesis in 1965 [8]. McKee is considered one of the scholars who has made significant contributions to modern total artificial hip replacement. This is the initial stage of the formation of the artificial hip joint. In 1962, Dr. Charnley of the United Kingdom designed a 22.225 mm metal femoral head and ultra-polymer polyethylene acetabulum combination prosthesis and fixed it with bone cement [9]. Come to this day, Charnley's artificial hip joint has become the "gold standard" for measuring other artificial hip joints, and he is also known as the "father of modern total hip replacement". Muller was a Swiss orthopedic surgeon of the same period as Charnley, who improved the total hip prosthesis on Charnley's basis, using a 32 mm femoral head instead of a 22.225 mm femoral head [10]. This large ball head increases hip mobility and prevents dislocation even better. After this, the artificial hip joint has entered a stage of rapid development, which is also the joint development stage of bone cement fixation and non-bone cement fixation prosthesis. At the beginning of the 21st century, trabecular fixation technology based on additive manufacturing also began to appear.

In the history of the development of artificial hip joints, bone cement occupies an important position. In the late 1950s, Charnley popularized the technique with dentist cement. Subsequently, the theoretical technology of bone cement fixation was gradually accepted by the majority of orthopedic doctors [11]. Bone cement fixation can achieve good early fixation, but there are still problems of peripheral bone lysis caused by debris particles and fragmentation caused by fatigue effects [12]. In theory, the roughness of the reinforced prosthesis can enhance its binding strength to bone cement, but it is still controversial. It is believed that with the continuous improvement of bone cement technology and the emergence of new bone cement materials, bone cement fixed joint replacement will continue to exist for a long time.

In the early 1970s, researchers began to explore the development of non-cementitious fixation prostheses, to further improve the long-term effect after joint replacement. The fixation principle is bone ingrowth or bone on growth to fix the prosthesis. In the initial stage of non-bone cement fixation, screws or tight pressing fits are mostly used, and the bone and the surface of the prosthesis are closely bio-fixed through bone growth, to achieve a firm bond between the bone and the prosthesis interface [13; 14]. Hybrid fixation for total hip arthroplasty was proposed in 1989, which combines the above two fixation methods, that is, the femoral stalk prosthesis is fixed by bone cement and the acetabular prosthesis is fixed by non-bone cement [15].

Currently, for initial hip replacement the lateral fixation of the acetabulum tends to be non-cementitious fixation, and is used only when there is significant bone loss in the acetabulum during resurfacing surgery. Mixed fixation is also common for total hip replacement, i.e., cemented with bone cement on the stalk side of the femur and biofixation is used on the acetabular side.

At present, the materials commonly used in artificial joints mainly include metal materials, polyethylene materials, ceramic materials, and some materials with less clinical application or are in the experimental stage, including carbon fiber, glass fiber and PEEK [16-18]. Metal materials for the artificial joints mainly include metals and alloys. The advantages of metal materials are reflected in good biocompatibility, good comprehensive mechanical properties, excellent biocorrosion resistance and physical properties. The medical metal materials commonly used in clinical practice mainly include stainless steel, cobalt-based alloys, titanium (Ti) and titanium alloys.

Polyethylene materials include ultra-high molecular weight polyethylene and high cross-linked ultra-high molecular weight polyethylene materials. Because of its excellent wear resistance, impact resistance, self-lubrication and other properties, it has been widely promoted and applied in the clinic. In addition, ceramic materials are also used in artificial joints. Ceramic materials mainly include aluminum oxide, zirconium oxide and hydroxyapatite bioactive ceramics. It not only has good biocompatibility, but also has ultra-high hardness, wear resistance and corrosion resistance, which can effectively solve

the problem of ion/metal release of metal prosthesis materials and bone dissolution caused by wear particles of polymer prosthesis materials [19-21].

As a new digital forming technology that gradually emerged in the late 1980s, the development of 3D printing technology in the medical field has increasingly received attention. In 2007, Italian surgeon Dr. Guido Grappiolo implanted the world's first 3D printed acetabular Delta-TT cup in collaboration with Lima and metal 3D printing equipment manufacturer Arcam [22].

### 1.1.2 Joint replacements in Canada

In recent centuries, with the rapid development of medical technology and the continuous improvement of people's health needs, artificial hip joint and knee technology has been more widely used than ever. Unfortunately, more problems have gradually surfaced. Limited by technical conditions, the experience of the surgeon, artificial joint indications and material selection errors, some patients have after artificial joint replacement surgery suffered from pain, limb shortening, severe joint function and other problems and their hip replacement had to be revised [23]. Artificial hip or knee revision (the replacement of a failed artificial joint) is a rather complex and high-tech procedure in which a loose or worn broken artificial prosthesis is removed and reinserted a new artificial joint into the body. It can solve the problem of serious decline in the quality of life of patients due to prosthesis loosening, fractures, infections and other complications after artificial hip replacement, and achieve the effect of relieving pain and restoring joint function [24]. It is achieved by reconstructing the anatomical structure of the hip joint and replacing the prosthesis, but it is by no means a simple "old for new", it needs to consider a series of problems such as anatomical and histological changes caused by the previous surgery, the difficulty of removing the old prosthesis, bone defects, etc. [25]. The impact on the implantation stability of the new prosthesis is a series of problems, and the problems it faces are far greater than the initial artificial joint replacement, which is a thorny problem in clinical orthopedics.

In figure 1-2, the top three reasons for hip and knee revisions in Canada are shown during 2018-2019, which are infection, aseptic loosening and instability [26]. Indications for

artificial joint revision are: joint infection, joint dislocation, periprosthetic fracture, polyethylene liner wear, periprosthetic osteolysis, prosthesis loosening, nerve damage and prosthesis rupture [27]. Therefore, the problems faced by artificial joint revision surgery are many and complex, due to the different surgical approaches used by doctors at the time of the initial surgery. The degree of damage to soft tissues and the degree of repair varies, the fixation method of artificial joint prosthesis in the initial surgery is different, and the difficulty of prosthesis removal is also very different. In addition, most patients have different degrees of bone defects, and the choice of methods for treating bone defects is also different. As a result, artificial joint revision surgery is much more complex and difficult than initial replacement surgery, and the results may not be as satisfactory as initial replacement surgery. In addition, the incidence of revision surgery, bleeding, infection, dislocation, thromboembolism, nerve damage and fracture is also relatively high [27]. Infection is the main reason that cause the hip and knee replacement revision in Canada [26]. The complexity of the retouch procedure makes the importance of the delicate operation of the initial surgery even more prominent. These are all things to be understood and faced by artificial joint revision surgery, and only with sufficient theory, thought, special instruments and physical preparation before surgery can the operation be completed perfectly. In addition, it is also key to the success of the operation to let the patient understand the relevant situation and difficulty of the revision surgery and to obtain the patient's cooperation.

The first artificial hip replacement is very important to the patients. However, the implant can be failure, because of femoral neck fracture, femoral head necrosis, and acetabular fractures. Therefore, the second or third surgeries may happen to the patients. Not only the trauma may be increased, but also the cost of treatment. If the joint infection is caused by other issues, the consequences (pus, sinus tract, pain, joint stiffness, etc.) for the patients are greater, which imposes a heavy financial and psychological burden on patients and their families [28-31]. Therefore, it is very important to investigate the cause of failure of the artificial hip implants.

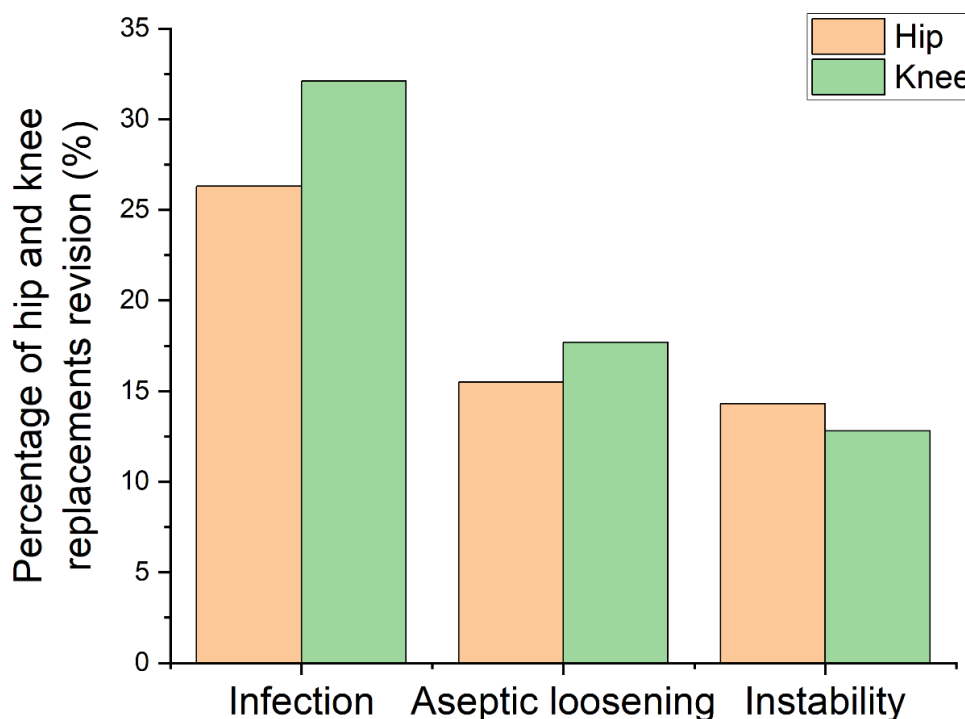


**Figure 1-2: Top reasons for hip and knee replacement revision in Canada during 2018-2019. [26]**

The number of hip and knee replacements performed in Canada were 62,016 and 75,345 in 2018-2019. The total number of hip and knee replacements in Canada during 2014 to 2019 are shown in the Figure 1-3 [26]. Over those 5 years, this number was increased every year. In 2020-2021, COVID-19 was raging around the world. Due to the COVID-19 pandemic, many joint replacement surgeries were cancelled in order to free up the hospital capacity. Therefore, the number of hip and knee replacement surgeries declined by 20 percent. However, this does not mean that the number of hip and knee replacement surgeries will be lower than before the pandemic. Between 2014 and 2019, the replacements of knees were higher than the hip replacements. The reason that caused this phenomenon is possibly that the knee is much easier injured. However, knee replacement surgery is more complex than hip replacement surgery. Therefore, there are more knee replacement revision surgeries than hip replacement revisions.

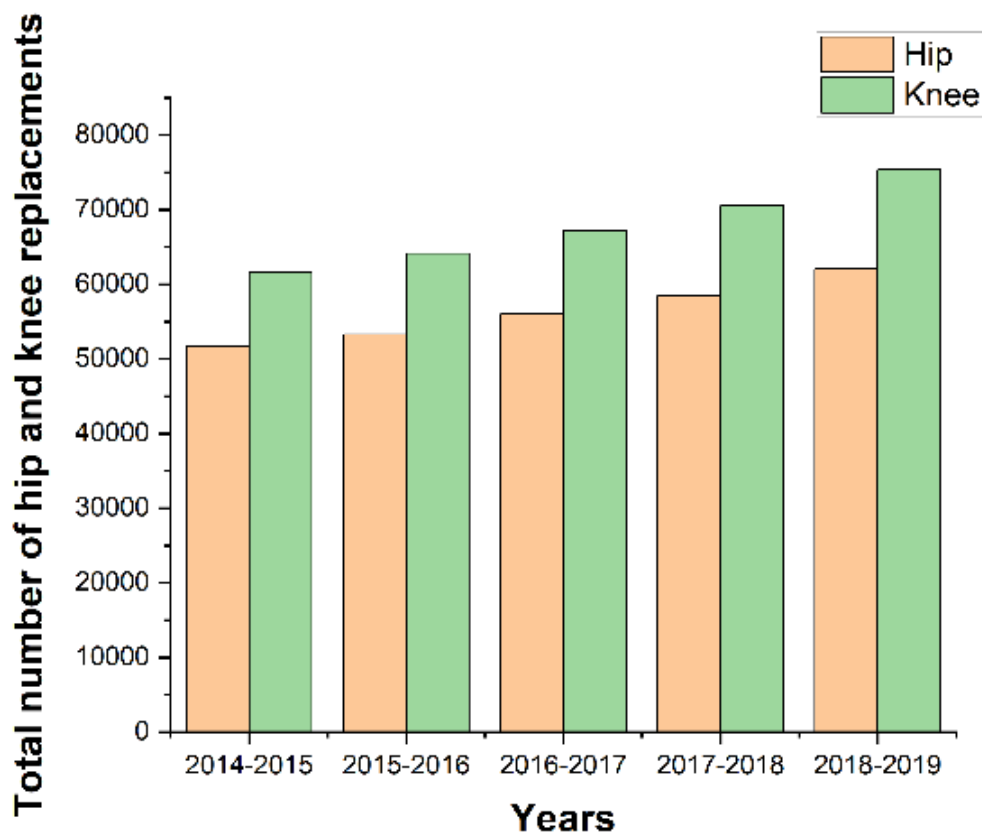


**Figure 1-3: Total number of hip and knee replacements including revision in Canada during 2014-2019. [26]**

## 1.2 CoCrMo Alloy

Cobalt-Chromium-Molybdenum alloy is a cobalt-based alloy. It was originally developed by Elwood Haynes, because of its good wear resistance, corrosion resistance and high temperature resistance and many other excellent properties, initially mainly used in aerospace, deep-sea diving equipment and other severe environment working machine parts [32; 33]. Since 1937, CoCrMo alloys have been initially used as implants in the medical field, and in the late 1970s, they have been widely used as bone replacement materials in clinical practice [34-36]. Nowadays, artificial femoral heads prepared from CoCrMo alloy still occupy a large part of the global market. Compared with other implant materials such as pure titanium and nickel-titanium, CoCrMo alloy is still very competitive because of its low cost and relatively simple manufacturing process



requirements, and its safety and mechanical properties which have withstood the test of clinical research for many years [37].

CoCrMo alloy is also a relatively biocompatible material commonly used in medicine. Medical cobalt-chromium alloy (CoCrMo F75) has good biocompatibility, good fatigue resistance, strong corrosion resistance and high comprehensive mechanical properties, and has always occupied an important position in the field of oral restoration and artificial joint manufacturing [38]. For oral restorations and medical implants, wear resistance is regarded as one of the main factors affecting the success of surgery and implant life, so the study of the tribological properties of CoCrMo alloy is the key to the successful application of personalized implants. Chiba et al. [39] studied the wear properties of medical CoCrMo alloys from the microstructure and found that the CoCrMo alloys with fine grains are more likely to induce martensitic phase transitions and show better wear resistance, which indirectly explains the good wear resistance of additive manufacturing formed cobalt-chromium alloys. Henriques et al. [40] studied the microstructure, corrosion resistance, hardness and wear resistance of casting and hot-pressed CoCrMo alloys. The harder the CoCrMo alloys, the greater the wear resistance would be.

CoCrMo alloy can be passivated in the human environment containing about 0.9% NaCl (mass fraction), which is an important basis for ensuring its biocompatibility [41; 42]. Tribocorrosion is the main corrosion mechanism of CoCrMo alloys, when exposed to friction. When it is used as an artificial joint, it will bear the alternating load and contact surface wear generated during the walking process of the human body, resulting in damage to the surface passivation film [43; 44]. Wear and corrosion play a mutually reinforcing role. If there are problems such as unreasonable design or assembly, mechanical scratches during the manufacturing process, and irregular surfaces, there will be crevices between the head and neck joints of the hip joint [45; 46]. The oxygen content in the crevices is low and continuously consumed, thus hindering the repassivation of the alloy surface. This also makes it easy to form a local crevice corrosion environment. Factors such as the reduction of the pH value of the solution caused by the hydrolysis of metal ions, the entry of Cl<sup>-</sup> into the crevice, and the increase

in temperature caused by the wear process will further lead to the unstable electrochemical state of the fresh metal surface, thereby affecting the passivation and accelerating corrosion [41; 47; 48]. J. Gilbert et al. [49] analyzed the actual corrosion of 148 hip implants taken from patients, found that the tapered joint between the head and neck was the most prone to corrosion, proposed the mechanism of mechanical action to promote the occurrence of crevice corrosion, and pointed out that in the case of infection and inflammation, the corrosion rate will further increase. The study of R.H. Oskouei et al. [50] also pointed out that the position of the hip joint with threads is more prone to crevice corrosion. Researchers have systematically studied the wear and corrosion behavior of CoCrMo alloys in a simulated human environment and also pointed out that about 22-50% of the metal loss is related to corrosion reactions when CoCrMo alloys undergo corrosion in joint synovial fluid [51; 52].

## 1.3 Manufacturing of relevance for implants

### 1.3.1 Warm-worked CoCrMo alloy

The CoCrMo alloy is a commonly used material in biomedical applications, and it can be produced through various manufacturing methods such as casting, warm working, and additive manufacturing [53]. Lost-wax casting is a popular method for producing CoCrMo components, as it allows for precise shaping and dimensions to be achieved through machining [54]. This process is often used in the manufacture of implantable metal devices. However, casting can sometimes result in defects such as coarse grains and porosity due to the limited cooling rate [55]. Porosity in castings can weaken their mechanical strength, rendering them useless [56]. Large pores can also create stress concentrations that may lead to cracks and early failure during use. To address this issue, vacuum casting and hot isostatic pressing techniques are often used to eliminate porosity caused by gas and internal voids caused by solid phase shrinkage, respectively [57]. The lost-wax casting process typically involves the following steps: designing a wax mold, manufacturing a shell, dewaxing, melting the shell, pouring the molten metal, separating the casting from the mold, and cleaning the casting [58].

Due to the relatively low mechanical properties of the castings, important engineering structures that are subject to heavy loads are usually made of wrought alloys [59]. The process of manufacturing wrought alloys is the mechanical deformation of castings. The purpose of mechanical deformation includes improving the grain structure; crushing secondary phase regions; eliminating the voids inside the casting; and introducing strain energy internally to achieve homogeneous composition [60]. In order to improve the performance of the alloy, the cobalt-based alloy implant also adopts mechanical deformation processing technology. The mechanical deformation process can break the cast structure of the alloy and obtain a fine fibrous structure of the grain. The mechanical processes commonly used are hot forging, rolling, extrusion and stamping. Compared with cast CoCrMo alloy, wrought cobalt-based alloy has excellent mechanical properties [61].

### 1.3.2 Laser powder bed fusion (LPBF) CoCrMo alloy

After traditional casting and forging, CoCrMo alloy can be improved in terms of microstructure through heat treatment and hot isostatic pressing, and in terms of corrosion and wear resistance through the application of surface deposition layers. These techniques are often used to optimize the performance of the alloy. In recent years, additive manufacturing processes have also gradually developed into another effective way to produce CoCrMo alloys. Additive manufacturing is a near-net shaping technology that has developed rapidly in recent years and has significant advantages in manufacturing artificial joint grafts with complex shapes. Several studies have indicated that the corrosion resistance of CoCrMo alloys produced via additive manufacturing is comparable to or superior to that of traditionally cast and wrought alloys. In addition, these additively manufactured alloys tend to have a lower coefficient of friction and wear rate compared to cast alloys [39; 62; 63]. Additionally, compared to traditional manufacturing techniques, additive manufacturing is particularly well-suited for producing special structural materials with component and structural gradients that can meet specific functional requirements in various environments, such as the human body. In the process of printing CoCrMo alloy, W. Harun et al. [64] reserved holes of 25-95%

volume fraction to resemble the alloy stiffness to that of the bone, which can effectively avoid the stress shielding effect.

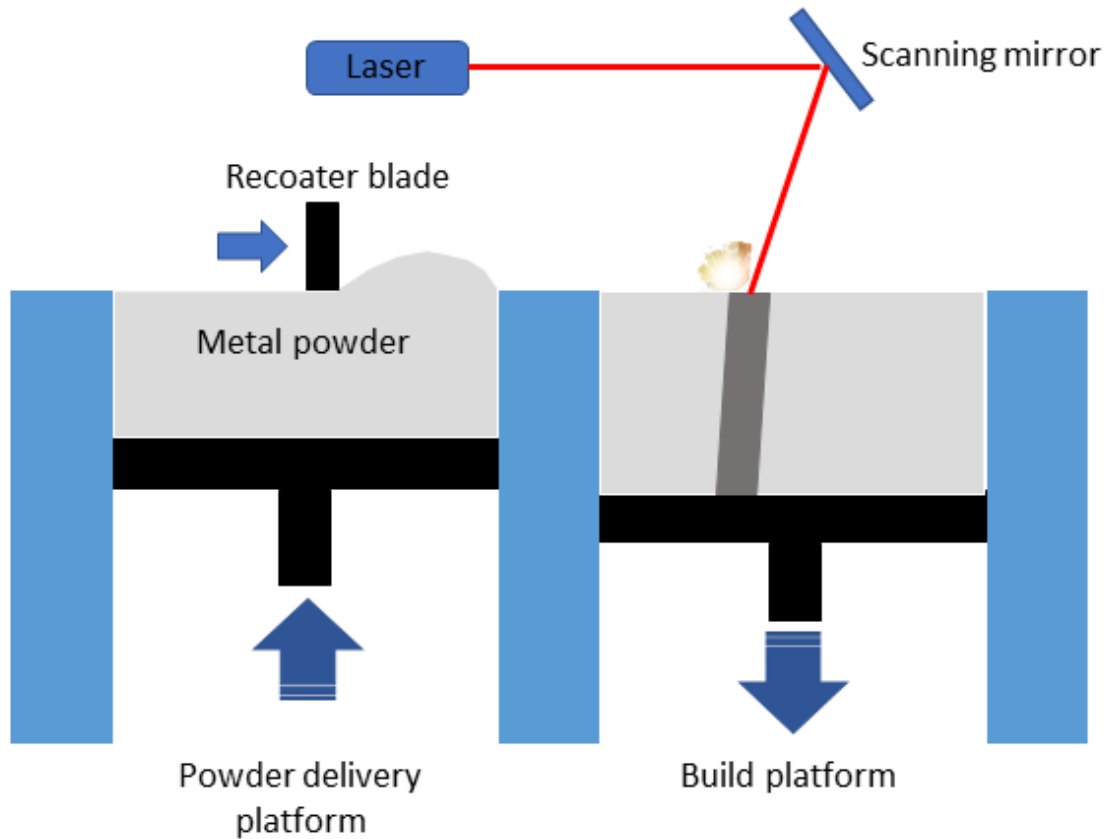


**Figure 1-4: The manufacture process of laser powder bed fusion (LPBF).**

The additive manufacturing of CoCrMo alloy is mainly produced by laser powder bed fusion (LPBF) technology, and the typical layer-by-layer printing process is shown in Figure 1-4. The properties of CoCrMo alloy produced using the laser powder bed fusion (LPBF) process can be influenced by various factors, including manufacturing defects, microstructure, crystal texture, and residual stress. These characteristics are specific to the LPBF process and may affect the performance of the resulting alloy. During the layer-by-layer printing process of additive manufacturing, materials undergo a complex heat treatment process, resulting in the microstructure of additive manufacturing alloys being significantly different from those made by traditional processes. On the one hand, the cooling rate of the traditional casting process is 273-373 K/s, and the cooling rate of the LPBF process is greater than 105 K/s, which easier forms a metastable microstructure

[65]. On the other hand, the heating of the post-printing layer is equivalent to the aging treatment of the solidified layer, which will also change the composition of the matrix phase and the number of second phases. Microstructure characteristics such as molten pool boundary, cytometric structure, and nano-sized precipitate will affect the corrosion resistance of additive alloys. The Mo-rich cell structure of the CoCrMo alloy manufactured by LBPF is conducive to improving the corrosion resistance, but the molten pool boundary will reduce the corrosion resistance [66]. Research on whether  $\alpha$  phase (body center cubic) is precipitated during additive manufacturing is controversial. Y. Lu et al. [67] observed the formation of  $\alpha$  phase after solution treatment at 1150 °C following the furnace cooling in the CoCrW alloy made by LPBF. However, other research pointed that there is no formation of  $\alpha$  phase in the CoCrMo alloy made by LPBF [68]. As with traditional casting and wrought alloys, heat treatment after 3D printing can be used to improve the microstructure and material properties of the resulting alloy. This technique is similar to those used in traditional manufacturing methods. M. Zhang et al. pointed out that the proportion of  $\epsilon$ -Co phase and precipitated carbide increased in the CoCrMo alloy manufactured by LPBF, with the prolongation of the aging time at 900 °C. The  $\epsilon$ -Co phase preferentially nucleates on the grain boundaries of the  $\gamma$ -Co phase, resulting in increased hardness and wear resistance [69].

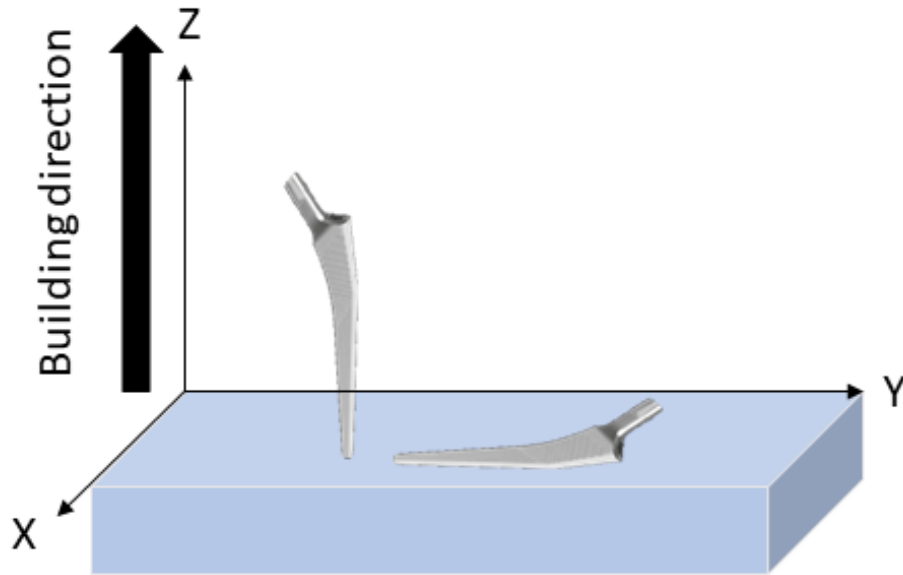


**Figure 1-5: Schematic diagram of different building direction for the hip implant.**

Due to the layer-by-layer printing process, the post-layer plays the role of aging heat treatment for the previous printing layer. Therefore, the content of the  $\epsilon$ -Co phase inside the component, the content of  $\gamma$ -Co phase in the surface microstructure is higher. A. Takaichi et al. [39] pointed out that the columnar crystals at the XZ interface (shown in Figure 1-5) of CoCrMo alloys produced by LBPF exhibited a preferred orientation in the  $\langle 001 \rangle$  direction and gradually disappeared with the increase of input energy. After the manufactured CoCrMo alloy was solution treated at 1150 °C for 1 hour, the fusion line and grain structure disappeared, but the anisotropy was not completely eliminated. The fatigue strength of the XY interface is higher than the XZ interface. This has been explained by that the XZ cross-section sample included more print layers and possibly more print defects, which could affect the properties of the CoCrMo alloy [70].

## 1.4 Metal release

### 1.4.1 Metal release and toxicity

Metal release can be defined as the release of all metal species, such as ions, complexes, and colloids, from the metallic materials into solution due to chemical or physical processes [71]. As mentioned before, CoCrMo alloy is widely used in metal-on-metal

total hip and knee arthroplasty. After the arthroplasty, Cobalt (Co), Chrome (Cr) and Molybdenum (Mo) ions or particles will be released from the alloy. A large number of released metal wear debris, such as nanometer particles and oxides, can be found in iliac joints and surrounding body fluids and tissues, enter the systemic circulation through the endothelial reticulum system, and deposit in the liver, spleen, lymph nodes and bone marrow tissues [72-79]. At the same time, metal ions such as Co and Cr originating from chemical degradation of metal particles by body fluids can cause the increase of metal ions in peripheral blood. According to one study on 84 patients, two years after arthroplasty surgery, the serum content of Co and Cr ions in patients increased by 15.3 times and 5.2 times, respectively, compared to that before surgery [80]. A high dose of metal degradation products released after total hip and knee arthroplasty surgery can cause many local and systemic adverse reactions, clinically called metal debris adverse reactions, including inflammation around the prosthesis, aseptic necrosis of soft tissues, formation of inflammatory pseudotumor, abnormal functions of major organs such as liver and kidney, and abnormal functions of the immune system [81]. These adverse reactions are related to cytotoxicity, sensitization, deformity of metal ions and nanotoxicity of metal particles. Therefore, the biosafety of CoCrMo alloys is receiving extensive attention from, among others, surgeons, engineers, and manufacturers.

The metallic material does not cause allergic reactions and carcinogenicity in the human body, but metal ions and their formation of organometallic compounds, and inorganic metal salts may cause biological toxicity to the human body, in which the release of metal ions is mainly caused by corrosion [82; 83]. The harmful reactions of metal ions to the human body are mainly toxic, carcinogenic, genotoxic and sensitizing [84; 85]. Usually, body fluids are corrosive to implants that replace hard tissue. Ions, especially chlorides and peroxide, and proteins can promote corrosion by dissolving oxides, by directly promoting metal oxidation, or by causing certain localized corrosion types. When medical metal materials are placed for a long time in aqueous medium containing electrolytes such as alkali metals ions, organic acids, and chloride ions, corrosion will occur, and active chloride ions promote the dissolution of metal ions [86; 87]. When the surface of the implant has defects such as inclusions, cavities, precipitations, segregation of elements in the grains and grain boundaries, and cracks in the passivation film,

localized electrochemical corrosion is easily induced [88-90]. As is well known, human body fluids are a complex environment. There are several amino acids, proteins, vitamins, polysaccharides, cells and other organic ingredients, that can influence the corrosion rate of metallic biomaterials [91-96]. Thus, they could induce the metal release of implants. Under normal conditions, the value of pH in human body is neutral, but it can be increased or decreased when there is an infection [97; 98]. Drastic changes in the pH of body fluids may accelerate the release of harmful ions from the metal [99; 100].

Biomedical metal materials undergo many types of corrosion in body fluids, such as crevice corrosion, fatigue corrosion, fretting corrosion, uniform corrosion, pitting corrosion, galvanic corrosion, intergranular corrosion and stress corrosion cracking. When different metal elements are present in the implanted metal material at the same time, the element with the most negative galvanic potential will be corroded preferentially. For most load-bearing implants used in the human body, stress corrosion cracking and fretting corrosion are the main causes of inducing metal release. For example, in one study, the concentration of cobalt in the serum was increased 40 times after 144 h fretting corrosion for uncoated CoCrMo alloy, while the concentration of cobalt increased less for a coated specimen [101]. Therefore, based on the surface electrochemical characteristics of metal materials and the force or wear conditions in the application environment, the selection of suitable coatings to improve the corrosion resistance of the matrix has been proposed to effectively inhibit the release of harmful ions and improve the biocompatibility of the biomedical metal materials [102-104].

Generally, the toxicity mechanism or pathogenesis of metals is one of the following: cutting of the functional groups necessary for the performance activity of biological macromolecules; replacement of metal ions required for the function of the biomacromolecules; altering the biomolecular composition of structure in the human body [105]. Metal ions often cause damage by altering the composition or structure of some biological macromolecules such as proteins, nucleic acids and biofilms. Most of the metal ions produced by medical metal materials are positively charged, and easily combine with organic or inorganic substances in human body fluids to form complex organic or inorganic compounds. Some of these compounds are highly toxic, and the



threshold concentration of some metal ions in the human body is very low. When certain metal ions, such as cobalt and chromium ions, enter body fluids, they trigger many biological reactions, such as blood reactions and tissue reactions [106-108]. Due to the negative charge of platelets, blood cells and proteins in human blood [109; 110], a high dose of positive charged metal ions can cause thrombosis symptoms [111]. The concentration of Cr and Co were found to increase in the urine, blood, synovial fluid and joint capsules in a study on 22 patients in Canada [101]. Co and Cr can be disseminated from the orthopedic implant to other sites, accumulating in the kidneys, heart, liver and spleen [112; 113]. The cytotoxicity of metal salts in the human body is greater for Co than for Cr. In in-vitro tests, it has been shown that Co and Cr also have sensitization and carcinogenic tendencies [114].

Co ions entering the cell can induce the overproduction of oxygen radicals, catalyze the overproduction of free radicals through Fenton reactions, and catalyze the formation of highly toxic hydroxyl radicals by hydrogen peroxide [115-117]. They can also inhibit the antioxidant capacity of cells. For example, lipoic acid which is an antioxidant in cells can be consumed by Co ions in large quantities during Co poisoning, thereby enhancing free radicals while weakening the antioxidant capacity of cells. The result is an oxidation/antioxidation imbalance in the cells [118]. Cobalt-induced cytotoxic damage seems to be the first round of attack on tissue cells from the two aspects of enhancing free radical damage to tissue and weakening the antioxidant system. The resulting intracellular oxidative/antioxidative imbalance further results in significantly increased intracellular concentrations of malondialdehyde and lipid peroxide and peroxynitrate [118]. The cells are finally stimulated to release a variety of apoptotic signals in the harsh environment of excess free radicals, eventually leading to cell apoptosis [119]. Kairovic et al. [118] found in in-vitro experiments that cobalt ion caused a significant difference in mitochondrial membranes potential. Furthermore, there was a concentration-dependent decrease in the content of adenosine triphosphate (ATP) induced by cobalt ions. This confirmed that the main reason why cobalt ions specifically affect mitochondrial function is because cobalt ions specially coordinate and bind to sulfhydryl-containing molecular structure in the tricarboxylic acid cycle [118]. Thus, consuming lipoic acid stored in mitochondria and causing the oxidative decarboxylation reaction of pyruvate with lipoic

acid as a cofactor of acetyl coenzyme A (acetyl-CoA), inhibited or destroyed in tricarboxylic acid recovery [118]. Eventually, it leads to impaired oxygen uptake by mitochondria. The fundamental reason why mitochondria have become the main target of cobalt ion attack is because cobalt ions have a natural high affinity for sulfur atoms, which is an important reason for cobalt ions to specifically attack mitochondria. Since mitochondria are the respiratory organs of cells [120], once mitochondria are attacked, a series of hypoxic lesions will inevitably occur. The site where mitochondria receive oxygen is at the end of the electron transport chain, so hypoxia can interrupt the flow of electrons within the mitochondria, causing oxidative phosphorylation disorders and leading to intracellular ATP deficiency. As a result, various energy demand functions in the cell will be impaired [121].

Chromium is an essential nutrient required in the small amounts for the proper functioning of the human body [122]. Chromium ions, such as trivalent chromium (Cr(III)) and hexavalent chromium (Cr(VI)) and their intermediates, cause cytotoxicity, genotoxicity and carcinogenicity in the context of oxidative stress and oxidative tissue damage [123]. Trivalent chromium is generally considered to be less toxic than the hexavalent chromium, but high levels of it can still cause adverse health effects, such as allergic reactions. Hedberg et al.'s research found that the release of Cr(III) from construction workers' shoes was significantly higher than the amount of Cr(VI) that causes Cr allergies [124]. Hexavalent chromium is the most toxic form of chromium and can cause adverse health effects [125]. When hexavalent chromium reach a certain dose, they will interfere with the normal redox reaction in-vivo, which in turn will disrupt cell transmission signals and gene expression [126].

Mo exists in the form of molybdenum cofactor in the active site of enzymes. Although there is literature on the fatal consequences of Mo deficiency, there are relatively few cases of Mo toxicity [97].

#### 1.4.2 Vroman effect

Since there are hundreds of different proteins in the blood, only the most important ones, such as albumin and fibrinogen, can be studied. Albumin is a protein that is found in high

concentrations in the blood plasma (35-50 mg/mL), making up about 50% of the total protein in the plasma. Albumin plays an important role in maintaining the proper balance of fluids in the body, as well as transporting various substances throughout the bloodstream. It is produced in the liver and released into the circulation, where it performs these functions [127]. Fibrinogen is a protein (2-4 mg/mL) that is abundant in plasma and plays a central role in blood clotting, by binding to glycoprotein receptors on platelet membranes to bind and aggregate platelets [128]. In 1969, Leo Vroman and his colleagues observed fibrinogen adsorbing from plasma to the surface of glass, anodized tantalum, and silicon oxide, and found that fibrinogen underwent a change that was difficult to detect immunologically within seconds or minutes of contact with the surface [129]. Vroman and his colleagues were limited by detection methods and could not distinguish between possible causes of conversion. The loss of immunoreactivity might have been due to the structure and orientation of fibrinogen fixed on the solid surface, or adsorbed fibrinogen replaced by other plasma proteins, or adsorbed fibrinogen decomposed by enzymes such as hemoplasmin, or other proteins that are adsorbed, so that the structure and orientation of fibrinogen are changed, so that the reactivity of its antigen determinant changes. The reasons for this phenomenon were suggested to be: (1) the structure of adsorbed fibrinogen changes and causes a decrease in antiserum reactivity; (2) Fibrinogen is replaced by one or more different plasma proteins. Later, when many researchers studied fibrinogen adsorption with labeled fibrinogen and enzyme-linked immunoassay (ELISA), they observed that the fibrinogen that began to adsorb was replaced by proteins with high affinity to the surface in the plasma [130-133]. In summary, the Vroman effect is defined as the initial adsorption of a small protein on the surface of the material, followed by its replacement with a macromolecular protein with higher binding affinity [71].

### 1.4.3 Corrosion in Protein Environments, Protein Aggregation, and Precipitation

When biomedical metal materials are implanted in the human body, the surface quickly reacts with body fluids, inducing corrosion [134]. The metal ions released during the corrosion process and the corrosion products formed interfere with the behavior of

surrounding cells, which in turn affects the microenvironment of the tissues surrounding the implant. Corrosion can also affect the safe service life of materials in the body. Uniform corrosion will continuously reduce the cross-section of the material, but it can still maintain certain mechanical properties and maintain its supporting effect before reaching the breaking strength of the material [135]. Localized corrosion can lead to stress concentration and cause fatigue fracture, which is sudden and will greatly shorten the service life of the material [136]. Generally, there are two main factors affecting the degradation of metal implants: first, material characteristics, such as composition, processing process, surface properties and shape design; The second is the physiological environment, such as a large number of ions, organic molecules and cells and other substances, as well as the pH, temperature and oxygen content of the local environment [91]. The complexity of the biological environment makes it difficult to predict or determine the corrosion behavior of metallic materials, and the corrosion rate of the same metallic materials can vary greatly from body fluid to body fluid. In in-vitro testing, the inorganic components of commonly used simulated body fluids are close to their true content in the organism, while organic components such as amino acids, proteins, vitamins, polysaccharides, and cells are often overlooked. Proteins, polysaccharides and cells can influence the corrosion behavior of metallic materials [93; 137].

In living organisms, proteins are relatively large biomolecules and have a tendency to aggregate at the liquid/solid interface. The adsorption of proteins on the surface of the implant is not only related to physiological activities such as cell adhesion and rejection, but also changes the corrosion behavior of the material - the acceleration or decrease of the corrosion rate, the change of the corrosion mode [138].

In 1982, Clark and Williams [139] studied the effect of protein in normal saline on the corrosion of metal elemental powder (size 10~100  $\mu\text{m}$ ). Bovine serum albumin and fibrin accelerated the dissolution of Cr powder, nickel (Ni) powder, copper (Cu) powder and Co powder, and had almost no effect on the dissolution of Ti powder and Al powder but slowed down the dissolution of Mo powder. This work provides guidance on how to select the appropriate solution components for in-vitro testing of medical metal materials, and specifically states that proteins should be an important part of in-vitro test solutions.

Therefore, clarifying the adsorption of proteins on the surface of metal materials and the influence of proteins on material corrosion will help reduce the difference in in-vivo and in-vitro test results, to find a more suitable in-vitro test environment for medical metal materials and make reasonable predictions on the in-vivo degradation behavior of metal implants.

Protein aggregation is usually achieved through a series of processes, starting with changes in the internal structure of the protein leading to the formation of dimers or oligomers, followed by aggregate growth, and finally the formation of subvisible or visible particles [140]. After the protein is massively aggregated, the large aggregate particles eventually precipitate. The released metal ions from the implants can promote protein aggregation and precipitation [141]. Metal ions in proteins promote stable or partial folding of peptide chains. High-valent metal ions promote the stable structure of peptide chains by collecting charged residues on the protein surface. Therefore, metal ions can induce protein aggregation and precipitation.

The aim of this thesis is to evaluate the metal release of CoCrMo alloys in different protein-containing solutions under different testing conditions of relevance for the human body. This is achieved by several complementing techniques probing the metal, its surface, and the solution. Furthermore, experimental conditions and their influence on possible underestimations of released metals to the solution are also discussed and evolved throughout the thesis. Also, the influence of the manufacturing and surface treatment methods, also of relevance for biomedical implant materials, is also investigated.

The study of metal release from CoCrMo alloy and its effects on irradiation, sliding, and manufacturing processes holds significant importance for several reasons. Firstly, understanding the behavior of CoCrMo alloy under various conditions, such as irradiation and sliding wear, enables researchers to optimize the material properties for enhanced performance and longevity in implants. Secondly, investigating the impact of manufacturing processes on metal release from CoCrMo alloy helps identify potential improvements in production techniques to minimize material degradation and ensure

better patient outcomes. Lastly, this research contributes to the development of more effective industry guidelines and regulatory standards, ultimately promoting safer and more reliable implant technologies for patients worldwide.

## 1.5 References

- [1] Polkowski, G. G., et al. "Total Hip Arthroplasty in the Very Young Patient." *JAAOS-Journal of the American Academy of Orthopaedic Surgeons*, vol. 20, no. 8, 2012, pp. 487-497.
- [2] Smith, P. M. N. "Evolution of Mould Arthroplasty of the Hip Joint." *The Journal of bone and joint surgery. British volume*, vol. 30, no. 1, 1948, pp. 59-75.
- [3] Wiles, P. "The Surgery of the Osteo-Arthritic Hip." *Clinical orthopaedics and related research*, no. 417, 2003, pp. 3-16.
- [4] Hernigou, P., et al. "Hip Hemiarthroplasty: From Venable and Bohlman to Moore and Thompson." *International orthopaedics*, vol. 38, 2014, pp. 655-661.
- [5] Markatos, K., et al. "Hallmarks in the History and Development of Total Hip Arthroplasty." *Surgical Innovation*, vol. 27, no. 6, 2020, pp. 691-694.
- [6] Schreurs, B. W., et al. "Histology of the Bone-Implant Interface 45 Years after Bilateral Implantation of a Judet Acrylic Hip Prosthesis: A Case Report." *Acta orthopaedica belgica*, vol. 67, no. 4, 2001, pp. 403-406.
- [7] Mostofi, S. B. "George Kenneth Mckee 1906–1991." *Who's Who in Orthopedics*, 2005, pp. 226-228.
- [8] Charnley, J. "A Biomechanical Analysis of the Use of Cement to Anchor the Femoral Head Prosthesis." *The Journal of bone and joint surgery. British volume*, vol. 47, no. 2, 1965, pp. 354-363.
- [9] "Arthroplasty of the Hip: A New Operation\*." *Clinical Orthopaedics and Related Research (1976-2007)*, vol. 95, 1973, pp. 4-8.
- [10] Egli, S., et al. "Comparison of Polyethylene Wear with Femoral Heads of 22 Mm and 32 Mm: A Prospective, Randomised Study." *The Journal of bone and joint surgery. British volume*, vol. 84, no. 3, 2002, pp. 447-451.

- [11] Fregert, S. "Occupational Hazards of Acrylate Bone Cement in Orthopaedic Surgery." vol. 54, Taylor & Francis, 1983, pp. 787-789.
- [12] Hernigou, P., et al. "Fixation of the Cemented Stem: Clinical Relevance of the Porosity and Thickness of the Cement Mantle." *The Open Orthopaedics Journal*, vol. 3, 2009, p. 8.
- [13] Ereth, M. H., et al. "Cemented Versus Noncemented Total Hip Arthroplasty—Embolism, Hemodynamics, and Intrapulmonary Shunting." *Mayo Clinic Proceedings*, vol. 67, Elsevier, 1992, pp. 1066-1074.
- [14] Maggs, J., et al. "The Relative Merits of Cemented and Uncemented Prostheses in Total Hip Arthroplasty." *Indian journal of orthopaedics*, vol. 51, 2017, pp. 377-385.
- [15] Harris, W. H., et al. "Hybrid Total Hip Arthroplasty." *Clinical Orthopaedics and Related Research (1976-2007)*, vol. 249, 1989, pp. 21-29.
- [16] Semlitsch, M., et al. "Properties of Implant Alloys for Artificial Hip Joints." *Medical and Biological Engineering and Computing*, vol. 18, 1980, pp. 511-520.
- [17] Wang, A., et al. "Carbon Fiber Reinforced Polyether Ether Ketone Composite as a Bearing Surface for Total Hip Replacement." *Tribology International*, vol. 31, no. 11, 1998, pp. 661-667.
- [18] Song, J., et al. "Study on the Wettability and Tribological Behaviors of Glass Fiber Reinforced Poly (Ether-Ether-Ketone) against Different Polymers as Bearing Materials for Artificial Cervical Disc." *Biotribology*, vol. 4, 2015, pp. 18-29.
- [19] Kurtz, S. M., et al. "Do Ceramic Femoral Heads Reduce Taper Fretting Corrosion in Hip Arthroplasty? A Retrieval Study." *Clinical Orthopaedics and Related Research®*, vol. 471, 2013, pp. 3270-3282.
- [20] Gallo, J., et al. "Advantages and Disadvantages of Ceramic on Ceramic Total Hip Arthroplasty: A Review." *Biomedical papers*, vol. 156, no. 3, 2012, pp. 204-212.



- [21] Affatato, S., et al. "Mixed Oxides Prosthetic Ceramic Ball Heads. Part 3: Effect of the ZrO<sub>2</sub> Fraction on the Wear of Ceramic on Ceramic Hip Joint Prostheses. A Long-Term in Vitro Wear Study." *Biomaterials*, vol. 22, no. 7, 2001, pp. 717-723.
- [22] Nancharaiah, T. "A Review Paper on Metal 3d Printing Technology." *Advances in Materials Processing and Manufacturing Applications: Proceedings of iCADMA 2020, 2021*, pp. 251-259.
- [23] Gonzalez, M. H., et al. "The Failed Total Knee Arthroplasty: Evaluation and Etiology." *JAAOS-Journal of the American Academy of Orthopaedic Surgeons*, vol. 12, no. 6, 2004, pp. 436-446.
- [24] Marks, R. "Body Mass Characteristics of Hip Osteoarthritis Patients Experiencing Aseptic Loosening, Periprosthetic Fractures, Dislocation, and Infections after Total Hip Replacement." *ClinicoEconomics and Outcomes Research*, 2009, pp. 7-16.
- [25] Li, X., et al. "Hemiarthroplasty Compared to Total Hip Arthroplasty for the Treatment of Femoral Neck Fractures: A Systematic Review and Meta-Analysis." *Journal of Orthopaedic Surgery and Research*, vol. 16, no. 1, 2021, pp. 1-9.
- [26] Information, Canadian Institute for Health. "Hip and Knee Replacements in Canada: Cjrr Annual Statistics Summary." 2020.
- [27] Khodarahmi, I., et al. "Advanced Mr Imaging after Total Hip Arthroplasty: The Clinical Impact." *Seminars in Musculoskeletal Radiology*, vol. 21, Thieme Medical Publishers, 2017, pp. 616-629.
- [28] Wang, G. J., et al. "Fibrin Sealant Reduces Perioperative Blood Loss in Total Hip Replacement." *Journal of long-term effects of medical implants*, vol. 13, no. 5, 2003.
- [29] Repantis, T., et al. "Comparison of Minimally Invasive Approach Versus Conventional Anterolateral Approach for Total Hip Arthroplasty: A Randomized Controlled Trial." *European Journal of Orthopaedic Surgery & Traumatology*, vol. 25, 2015, pp. 111-116.

- [30] Korovessis, P., et al. "Metallosis after Contemporary Metal-on-Metal Total Hip Arthroplasty: Five to Nine-Year Follow-Up." *JBJS*, vol. 88, no. 6, 2006, pp. 1183-1191.
- [31] Dobzyniak, M., et al. "Early Failure in Total Hip Arthroplasty." *Clinical Orthopaedics and Related Research®*, vol. 447, 2006, pp. 76-78.
- [32] Bortun, C. M., et al. "Surface Characterization of Some CoCrMo Alloys Used in RPD Technology." *Revista de Chimie*, vol. 63, no. 9, 2012, pp. 906-910.
- [33] Fleming, T. J., et al. "The Effect of Induction Heating Power on the Microstructural and Physical Properties of Investment Cast Astm-F75 CoCrMo Alloy." *Journal of Materials Research and Technology*, vol. 8, no. 5, 2019, pp. 4417-4424.
- [34] Sullivan, R. M. "Implant Dentistry and the Concept of Osseointegration: A Historical Perspective." *J Calif Dent Assoc*, vol. 29, no. 11, 2001, pp. 737-745.
- [35] Ivanoff, C. J., et al. "Influence of Bicortical or Monocortical Anchorage on Maxillary Implant Stability: A 15-Year Retrospective Study of Brånemark System Implants." *International Journal of Oral & Maxillofacial Implants*, vol. 15, no. 1, 2000.
- [36] Rajput, R., et al. "A Brief Chronological Review of Dental Implant History." *International Dental Journal of Students Research*, vol. 4, no. 3, 2016, pp. 105-107.
- [37] Chan, C. W., et al. "A Preliminary Study to Enhance the Tribological Performance of CoCrMo Alloy by Fibre Laser Remelting for Articular Joint Implant Applications." *Lubricants*, vol. 6, no. 1, 2018, p. 24.
- [38] Aherwar, A., et al. "Cobalt Based Alloy: A Better Choice Biomaterial for Hip Implants." *Trends in Biomaterials & Artificial Organs*, vol. 30, no. 1, 2016.
- [39] Takaichi, A., et al. "Microstructures and Mechanical Properties of Co-29cr-6mo Alloy Fabricated by Selective Laser Melting Process for Dental Applications." *journal of the mechanical behavior of biomedical materials*, vol. 21, 2013, pp. 67-76.

- [40] Henriques, B., et al. "Microstructure, Hardness, Corrosion Resistance and Porcelain Shear Bond Strength Comparison between Cast and Hot Pressed CoCrMo Alloy for Metal–Ceramic Dental Restorations." *journal of the mechanical behavior of biomedical materials*, vol. 12, 2012, pp. 83-92.
- [41] Huang, X., et al. "Crevice Corrosion Behaviors of CoCrMo Alloy and Stainless Steel 316L Artificial Joint Materials in Physiological Saline." *Corrosion Science*, vol. 197, 2022, p. 110075.
- [42] Rylska, D., et al. "Chemical Passivation as a Method of Improving the Electrochemical Corrosion Resistance of Co-Cr-Based Dental Alloy." *Acta of Bioengineering and Biomechanics*, vol. 19, no. 2, 2017, pp. 73-78.
- [43] Zhang, H., et al. "Tribological Performance of Artificial CoCrMo Prosthesis by Elid Grinding Process." *Integrated Ferroelectrics*, vol. 217, no. 1, 2021, pp. 225-232.
- [44] Jiang, H. "Static and Dynamic Mechanics Analysis on Artificial Hip Joints with Different Interface Designs by the Finite Element Method." *Journal of Bionic Engineering*, vol. 4, no. 2, 2007, pp. 123-131.
- [45] Oskouei, R. H., et al. "A New Finding on the in-Vivo Crevice Corrosion Damage in a CoCrMo Hip Implant." *Materials Science and Engineering: C*, vol. 79, 2017, pp. 390-398.
- [46] Zhu, D., et al. "In Vitro Fretting Crevice Corrosion Damage of Cocrmo Alloys in Phosphate Buffered Saline: Debris Generation, Chemistry and Distribution." *Acta biomaterialia*, vol. 114, 2020, pp. 449-459.
- [47] Radice, S., et al. "Effects of Bovine Serum Albumin and Hyaluronic Acid on the Electrochemical Response of a CoCrMo Alloy to Cathodic and Anodic Excursions." *Journal of Bio-and Tribo-Corrosion*, vol. 5, 2019, pp. 1-12.
- [48] Bettini, E., et al. "Influence of Metal Carbides on Dissolution Behavior of Biomedical CoCrMo Alloy: SEM, TEM and AFM Studies." *Electrochimica Acta*, vol. 56, no. 25, 2011, pp. 9413-9419.

- [49] Gilbert, J. L., et al. "Medical Implant Corrosion: Electrochemistry at Metallic Biomaterial Surfaces." *Degradation of Implant Materials*, edited by Noam Eliaz, Springer New York, 2012, pp. 1-28.
- [50] Milimonfared, R., et al. "The Distribution and Severity of Corrosion Damage at Eight Distinct Zones of Metallic Femoral Stem Implants." *Metals*, vol. 8, no. 10, 2018, p. 840.
- [51] Royhman, D., et al. "Fretting-Corrosion in Hip Taper Modular Junctions: The Influence of Topography and Ph Levels—an in-Vitro Study." *journal of the mechanical behavior of biomedical materials*, vol. 118, 2021, p. 104443.
- [52] Liao, Y., et al. "CoCrMo Metal-on-Metal Hip Replacements." *Physical Chemistry Chemical Physics*, vol. 15, no. 3, 2013, pp. 746-756.
- [53] Amanov, A. "Effect of Post-Additive Manufacturing Surface Modification Temperature on the Tribological and Tribocorrosion Properties of Co-Cr-Mo Alloy for Biomedical Applications." *Surface and Coatings Technology*, vol. 421, 2021, p. 127378.
- [54] Augustyn, N. J., et al. "The Influence of Prosthetic Elements Manufacturing Technology on Properties and Microstructure Shaping Co-Cr-Mo Alloys." *Engineering of Biomaterials*, vol. 23, no. 156, 2020, pp. 24-31.
- [55] Dharmar, S., et al. "Radiographic and Metallographic Evaluation of Porosity Defects and Grain Structure of Cast Chromium Cobalt Removable Partial Dentures." *The Journal of Prosthetic dentistry*, vol. 69, no. 4, 1993, pp. 369-373.
- [56] Henriques, B., et al. "Mechanical Properties of Hot Pressed CoCrMo Alloy Compacts for Biomedical Applications." *Materials & Design*, vol. 83, 2015, pp. 829-834.
- [57] Cornacchia, G., et al. "Microstructural, Mechanical, and Tribological Characterization of Selective Laser Melted CoCrMo Alloy under Different Heat Treatment Conditions and Hot Isostatic Pressing." *Advanced Engineering Materials*, vol. 24, no. 4, 2022, p. 2100928.

- [58] Pattnaik, S., et al. "Developments in Investment Casting Process—a Review." *Journal of Materials Processing Technology*, vol. 212, no. 11, 2012, pp. 2332-2348.
- [59] Hermawan, H., et al. "Metals for Biomedical Applications." *Biomedical engineering—from theory to applications*, vol. 1, 2011, pp. 411-430.
- [60] Handbook, ASM. "Metallography and Microstructures." Edited by GF Vander Voort, ASM International, vol. 9, 2004.
- [61] Tipper, J. L., et al. "Quantitative Analysis of the Wear and Wear Debris from Low and High Carbon Content Cobalt Chrome Alloys Used in Metal on Metal Total Hip Replacements." *Journal of Materials Science: Materials in Medicine*, vol. 10, 1999, pp. 353-362.
- [62] Puskar, T., et al. "A Comparative Analysis of the Corrosive Effect of Artificial Saliva of Variable pH on DMLS and Cast Co-Cr-Mo Dental Alloy." *Materials*, vol. 7, no. 9, 2014, pp. 6486-6501.
- [63] De Castro Girão, D., et al. "An Assessment of Biomedical CoCrMo Alloy Fabricated by Direct Metal Laser Sintering Technique for Implant Applications." *Materials Science and Engineering: C*, vol. 107, 2020, p. 110305.
- [64] Harun, W.S.W., et al. "A Review of Powder Additive Manufacturing Processes for Metallic Biomaterials." *Powder Technology*, vol. 327, 2018, pp. 128-151.
- [65] Kong, D., et al. "Corrosion of Metallic Materials Fabricated by Selective Laser Melting." *npj Materials Degradation*, vol. 3, no. 1, 2019, p. 24.
- [66] Qian, B., et al. "Defects-Tolerant Co-Cr-Mo Dental Alloys Prepared by Selective Laser Melting." *Dental materials*, vol. 31, no. 12, 2015, pp. 1435-1444.
- [67] Lu, Y., et al. "Microstructure, Mechanical Property and Metal Release of as-SLM CoCrW Alloy under Different Solution Treatment Conditions." *journal of the mechanical behavior of biomedical materials*, vol. 55, 2016, pp. 179-190.

- [68] Li, H., et al. "Microstructural Features of Biomedical Cobalt–Chromium–Molybdenum (CoCrMo) Alloy from Powder Bed Fusion to Aging Heat Treatment." *Journal of Materials Science & Technology*, vol. 45, 2020, pp. 146-156.
- [69] Zhang, M., et al. "An Investigation into the Aging Behavior of CoCrMo Alloys Fabricated by Selective Laser Melting." *Journal of Alloys and Compounds*, vol. 750, 2018, pp. 878-886.
- [70] Seki, E., et al. "Effect of Heat Treatment on the Microstructure and Fatigue Strength of CoCrMo Alloys Fabricated by Selective Laser Melting." *Materials Letters*, vol. 245, 2019, pp. 53-56.
- [71] Hedberg, Y. S., et al. "Metal Release from Stainless Steel in Biological Environments: A Review." *Biointerphases*, vol. 11, no. 1, 2016, pp. 901-917.
- [72] Park, Y. S., et al. "Early Osteolysis Following Second-Generation Metal-on-Metal Hip Replacement." *JBJS*, vol. 87, no. 7, 2005, pp. 1515-1521.
- [73] Traisnel, M., et al. "Corrosion of Surgical Implants." *Clinical Materials*, vol. 5, no. 2-4, 1990, pp. 309-318.
- [74] McKellop, H. A., et al. "The Origin of Submicron Polyethylene Wear Debris in Total Hip Arthroplasty." *Clinical Orthopaedics and Related Research®*, vol. 311, 1995, pp. 3-20.
- [75] Huber, M., et al. "Postmortem Study of Femoral Osteolysis Associated with Metal-on-Metal Articulation in Total Hip Replacement: An Analysis of Nine Cases." *JBJS*, vol. 92, no. 8, 2010, pp. 1720-1731.
- [76] Lopez, G. D. "Biodeterioration and Corrosion of Metallic Implants and Prostheses." *Medicina*, vol. 53, no. 3, 1993, pp. 260-274.
- [77] Schmalzried, T. P., et al. "Polyethylene Wear Debris and Tissue Reactions in Knee as Compared to Hip Replacement Prostheses." *Journal of Applied Biomaterials*, vol. 5, no. 3, 1994, pp. 185-190.

- [78] Koerten, H. K., et al. "Observations at the Articular Surface of Hip Prostheses: An Analytical Electron Microscopy Study on Wear and Corrosion." *Journal of Biomedical Materials Research: An Official Journal of The Society for Biomaterials, The Japanese Society for Biomaterials, and The Australian Society for Biomaterials and the Korean Society for Biomaterials*, vol. 54, no. 4, 2001, pp. 591-596.
- [79] Sieber, H. P., et al. "Analysis of 118 Second-Generation Metal-on-Metal Retrieved Hip Implants." *The Journal of bone and joint surgery. British volume*, vol. 81, no. 1, 1999, pp. 46-50.
- [80] Lazennec, J. Y., et al. "Outcome and Serum Ion Determination up to 11 Years after Implantation of a Cemented Metal-on-Metal Hip Prosthesis." *Acta orthopaedica*, vol. 80, no. 2, 2009, pp. 168-173.
- [81] Liu, Y., et al. "In Vivo Corrosion of CoCrMo Alloy and Biological Responses: A Review." *Materials technology*, vol. 33, no. 2, 2018, pp. 127-134.
- [82] Schalock, P. C., et al. "Metal Hypersensitivity Reactions to Implants: Opinions and Practices of Patch Testing Dermatologists." *Dermatitis*, vol. 24, no. 6, 2013, pp. 313-320.
- [83] Egorova, K. S., et al. "Toxicity of Metal Compounds: Knowledge and Myths." *Organometallics*, vol. 36, no. 21, 2017, pp. 4071-4090.
- [84] Dayan, A. D., et al. "Mechanisms of Chromium Toxicity, Carcinogenicity and Allergenicity: Review of the Literature from 1985 to 2000." *Human & experimental toxicology*, vol. 20, no. 9, 2001, pp. 439-451.
- [85] Martin, C. A., et al. "In Vitro and in Vivo Evidence of the Cytotoxic and Genotoxic Effects of Metal Ions Released by Orthodontic Appliances: A Review." *Environmental toxicology and pharmacology*, vol. 40, no. 1, 2015, pp. 86-113.
- [86] Cieslak, W. R., et al. "Properties of the Passive Films Formed on Ferritic Stainless Steels in Cl<sup>-</sup> Solutions." *Corrosion*, vol. 40, no. 10, 1984, pp. 545-550.

- [87] Bozzini, B., et al. "An Electrochemical Impedance Investigation of the Behavior of Anodically Oxidized Titanium in Human Plasma and Cognate Fluids, Relevant to Dental Applications." *Journal of Materials Science: Materials in Medicine*, vol. 19, 2008, pp. 3443-3453.
- [88] Wang, Q., et al. "Failure Mechanisms in CoCrMo Modular Femoral Stems for Revision Total Hip Arthroplasty." *Journal of Biomedical Materials Research Part B: Applied Biomaterials*, vol. 105, no. 6, 2017, pp. 1525-1535.
- [89] Dikici, B., et al. "Corrosion of Metallic Biomaterials." *Advances in Metallic Biomaterials: Tissues, Materials and Biological Reactions*, 2015, pp. 275-303.
- [90] Hall, D. J., et al. "Mechanical, Chemical and Biological Damage Modes within Head-Neck Tapers of CoCrMo and Ti6Al4V Contemporary Hip Replacements." *Journal of Biomedical Materials Research Part B: Applied Biomaterials*, vol. 106, no. 5, 2018, pp. 1672-1685.
- [91] Marco, I., et al. "In Vivo and in Vitro Degradation Comparison of Pure Mg, Mg-10Gd and Mg-2Ag: A Short Term Study." *European Cells & Materials*, vol. 33, 2017, pp. 90-104.
- [92] Wang, Y., et al. "In Vitro Degradation Behavior of M1a Magnesium Alloy in Protein-Containing Simulated Body Fluid." *Materials Science and Engineering: C*, vol. 31, no. 3, 2011, pp. 579-587.
- [93] Heikal, F. E. T., et al. "Serum Albumin Can Influence Magnesium Alloy Degradation in Simulated Blood Plasma for Cardiovascular Stenting." *Materials Chemistry and Physics*, vol. 220, 2018, pp. 35-49.
- [94] Burstein, G. T., et al. "Nucleation of Corrosion Pits in Ringer's Solution Containing Bovine Serum." *Corrosion Science*, vol. 49, no. 11, 2007, pp. 4296-4306.
- [95] Yamamoto, A., et al. "Effect of Inorganic Salts, Amino Acids and Proteins on the Degradation of Pure Magnesium in Vitro." *Materials Science and Engineering C*, vol. 29, 2009, pp. 1559-1568.



- [96] Gu, X. N., et al. "Influence of Artificial Biological Fluid Composition on the Biorrosion of Potential Orthopedic Mg–Ca, Az31, Az91 Alloys." *Biomedical Materials*, vol. 4, no. 6, 2009, p. 065011.
- [97] Berkmann, J. C., et al. "Early Ph Changes in Musculoskeletal Tissues Upon Injury—Aerobic Catabolic Pathway Activity Linked to Inter-Individual Differences in Local Ph." *International Journal of Molecular Sciences*, vol. 21, no. 7, 2020, p. 2513.
- [98] Ono, S., et al. "Increased Wound Ph as an Indicator of Local Wound Infection in Second Degree Burns." *Burns*, vol. 41, no. 4, 2015, pp. 820-824.
- [99] Hanawa, T. "Metal Ion Release from Metal Implants." *Materials Science and Engineering: C*, vol. 24, no. 6, 2004, pp. 745-752.
- [100] Virtanen, S., et al. "Special Modes of Corrosion under Physiological and Simulated Physiological Conditions." *Acta biomaterialia*, vol. 4, 2008, pp. 468-476.
- [101] Sargeant, A., et al. "Hip Implants—Paper Vi—Ion Concentrations." *Materials & Design*, vol. 28, no. 1, 2007, pp. 155-171.
- [102] Poinern, G. E. J., et al. "Biomedical Magnesium Alloys: A Review of Material Properties, Surface Modifications and Potential as a Biodegradable Orthopaedic Implant." *American Journal of Biomedical Engineering*, vol. 2, no. 6, 2012, pp. 218-240.
- [103] Huynh, V., et al. "Surface Activation and Pretreatments for Biocompatible Metals and Alloys Used in Biomedical Applications." *International Journal of Biomaterials*, vol. 2019, 2019.
- [104] Agarwal, S., et al. "Biodegradable Magnesium Alloys for Orthopaedic Applications: A Review on Corrosion, Biocompatibility and Surface Modifications." *Materials Science and Engineering: C*, vol. 68, 2016, pp. 948-963.
- [105] Stohs, S. J., et al. "Oxidative Mechanisms in the Toxicity of Metal Ions." *Free radical biology and medicine*, vol. 18, no. 2, 1995, pp. 321-336.

- [106] Pereira, M. L., et al. "Chromium Accumulation and Ultrastructural Changes in the Mouse Liver Caused by Stainless Steel Corrosion Products." *Journal of Materials Science: Materials in Medicine*, vol. 6, 1995, pp. 523-527.
- [107] Black, J. "Does Corrosion Matter?" *The Journal of bone and joint surgery. British volume*, vol. 70, no. 4, 1988, pp. 517-520.
- [108] Tracana, R. B., et al. "Mouse Inflammatory Response to Stainless Steel Corrosion Products." *Journal of Materials Science: Materials in Medicine*, vol. 5, no. 9-10, 1994, pp. 596-600.
- [109] O'brien, J. R. "The Adhesiveness of Native Platelets and Its Prevention." *Journal of clinical pathology*, vol. 14, no. 2, 1961, pp. 140-149.
- [110] Fonseca, L. C., et al. "Nanocomposites Based on Graphene Oxide and Mesoporous Silica Nanoparticles: Preparation, Characterization and Nanobiointeractions with Red Blood Cells and Human Plasma Proteins." *Applied Surface Science*, vol. 437, 2018, pp. 110-121.
- [111] Bock, P. E., et al. "Activation of Intrinsic Blood Coagulation by Ellagic Acid: Insoluble Ellagic Acid-Metal Ion Complexes Are the Activating Species." *Biochemistry*, vol. 20, no. 25, 1981, pp. 7258-7266.
- [112] Czarnek, K., et al. "Selected Aspects of the Action of Cobalt Ions in the Human Body." *Central European Journal of Immunology*, vol. 40, no. 2, 2015, pp. 236-242.
- [113] Keegan, G. M., et al. "A Systematic Comparison of the Actual, Potential, and Theoretical Health Effects of Cobalt and Chromium Exposures from Industry and Surgical Implants." *Critical reviews in toxicology*, vol. 38, no. 8, 2008, pp. 645-674.
- [114] Bal, W., et al. "Induction of Oxidative DNA Damage by Carcinogenic Metals." *Toxicology letters*, vol. 127, no. 1-3, 2002, pp. 55-62.

- [115] Gilbert, J. L., et al. "Direct in Vivo Inflammatory Cell-Induced Corrosion of CoCrMo Alloy Orthopedic Implant Surfaces." *Journal of biomedical materials research Part A*, vol. 103, no. 1, 2015, pp. 211-223.
- [116] Liu, Y., et al. "The Effect of Simulated Inflammatory Conditions and Fenton Chemistry on the Electrochemistry of CoCrMo Alloy." *Journal of Biomedical Materials Research Part B: Applied Biomaterials*, vol. 106, no. 1, 2018, pp. 209-220.
- [117] Liu, Y., et al. "The Effect of Simulated Inflammatory Conditions and Ph on Fretting Corrosion of CoCrMo Alloy Surfaces." *Wear*, vol. 390, 2017, pp. 302-311.
- [118] Karovic, O., et al. "Toxic Effects of Cobalt in Primary Cultures of Mouse Astrocytes: Similarities with Hypoxia and Role of Hif-1 $\alpha$ ." *Biochemical pharmacology*, vol. 73, no. 5, 2007, pp. 694-708.
- [119] Sinha, K., et al. "Oxidative Stress: The Mitochondria-Dependent and Mitochondria-Independent Pathways of Apoptosis." *Archives of toxicology*, vol. 87, 2013, pp. 1157-1180.
- [120] Weibel, E. R. *The Pathway for Oxygen: Structure and Function in the Mammalian Respiratory System*. Harvard University Press, 1984.
- [121] Peng, J., et al. "Hyperglycemia, P53, and Mitochondrial Pathway of Apoptosis Are Involved in the Susceptibility of Diabetic Models to Ischemic Acute Kidney Injury." *Kidney international*, vol. 87, no. 1, 2015, pp. 137-150.
- [122] Anderson, R. A. "Chromium as an Essential Nutrient for Humans." *Regulatory toxicology and pharmacology*, vol. 26, no. 1, 1997, pp. S35-S41.
- [123] Singh, J., et al. "Chromium-Induced Genotoxicity and Apoptosis: Relationship to Chromium Carcinogenesis." *Oncology Reports*, vol. 5, no. 6, 1998, pp. 1307-1325.
- [124] Hedberg, Y. S., et al. "Chromium(III), Chromium(VI), and Cobalt Release from Leathers Produced in Nicaragua." *Contact Dermatitis*, vol. 80, no. 3, 2019, pp. 149-155.

- [125] Pellerin, C., et al. "Reflections on Hexavalent Chromium: Health Hazards of an Industrial Heavyweight." *Environmental health perspectives*, vol. 108, no. 9, 2000, pp. A402-A407.
- [126] Saha, R., et al. "Sources and Toxicity of Hexavalent Chromium." *Journal of Coordination Chemistry*, vol. 64, no. 10, 2011, pp. 1782-1806.
- [127] Bernardi, M., et al. "Role of Human Albumin in the Management of Complications of Liver Cirrhosis." *Journal of clinical and experimental hepatology*, vol. 4, no. 4, 2014, pp. 302-311.
- [128] Savage, B., et al. "Selective Recognition of Adhesive Sites in Surface-Bound Fibrinogen by Glycoprotein IIb-IIIa on Nonactivated Platelets." *Journal of Biological Chemistry*, vol. 266, no. 17, 1991, pp. 11227-11233.
- [129] Vroman, L., et al. "Identification of Rapid Changes at Plasma–Solid Interfaces." *Journal of biomedical materials research*, vol. 3, no. 1, 1969, pp. 43-67.
- [130] Slack, S. M., et al. "The Effects of Temperature and Buffer on Fibrinogen Adsorption from Blood Plasma to Glass." *Journal of Biomaterials Science, Polymer Edition*, vol. 2, no. 3, 1991, pp. 227-237.
- [131] Wojciechowski, P., et al. "Phenomenology and Mechanism of the Transient Adsorption of Fibrinogen from Plasma (Vroman Effect)." *Journal of colloid and interface science*, vol. 111, no. 2, 1986, pp. 455-465.
- [132] Turbill, P., et al. "Proteins Involved in the Vroman Effect During Exposure of Human Blood Plasma to Glass and Polyethylene." *Biomaterials*, vol. 17, no. 13, 1996, pp. 1279-1287.
- [133] Adams, A. L., et al. "Convex-Lens-on-Slide: A Simple System for the Study of Human Plasma and Blood in Narrow Spaces." *Journal of biomedical materials research*, vol. 18, no. 6, 1984, pp. 643-654.

- [134] Talha, M., et al. "Role of Protein Adsorption in the Bio Corrosion of Metallic Implants—a Review." *Colloids and Surfaces B: Biointerfaces*, vol. 176, 2019, pp. 494-506.
- [135] Minciuna, M. G., et al. "Electrochemical Behavior of CoCrMo and Cocrmosi5 Alloys at Different Simulated Physiological Medium." *Revista de Chimie (Bucharest)*, vol. 65, 2014, pp. 1138-1141.
- [136] Lanzutti, A., et al. "Corrosion Fatigue Failure of a High Carbon CoCrMo Modular Hip Prosthesis: Failure Analysis and Electrochemical Study." *Engineering Failure Analysis*, vol. 105, 2019, pp. 856-868.
- [137] Vidal, C. V., et al. "Influence of Protein Adsorption on Corrosion of Biomedical Alloys." *Bio-Tribocorrosion in Biomaterials and Medical Implants*, Elsevier, 2013, pp. 187-219.
- [138] Manivasagam, G., et al. "Biomedical Implants: Corrosion and Its Prevention-a Review." *Recent Patents on Corrosion Science*, vol. 2, no. 1, 2010, pp. 40-54.
- [139] Clark, G. C. F., et al. "The Effects of Proteins on Metallic Corrosion." *Journal of biomedical materials research*, vol. 16, no. 2, 1982, pp. 125-134.
- [140] Wang, W., et al. "Protein Aggregation—Mechanisms, Detection, and Control." *International journal of pharmaceutics*, vol. 550, no. 1-2, 2018, pp. 251-268.
- [141] Hedberg, Y. S., et al. "Synergistic Effects of Metal-Induced Aggregation of Human Serum Albumin." *Colloids and Surfaces B: Biointerfaces*, vol. 173, 2019, pp. 751-758.

## Chapter 2

### 2 Justification of experimental choices

#### 2.1 Synthetic biological fluids

Synthetic biological fluids are a crucial aspect in the assessment of biomedical materials such as 316L stainless steel, CoCrMo alloy, and titanium alloys [1-3]. By utilizing these synthetic fluids, researchers are able to recreate the environment within the human body to test the performance and safety of the materials. This enables improvement in the materials' biocompatibility and reduces the potential for failure or adverse reactions [4].

Furthermore, it offers a standard and controlled testing environment, resulting in consistent and dependable results. This is very important in the creation of new biomedical materials and devices, as a comprehensive understanding of how the material behaves in a biological setting is imperative for its effective utilization. A range of synthetic biological fluids exist, each with its own distinct properties that make it suitable for evaluating various aspects of biomedical materials. Some of the more prevalent types of synthetic biological fluids include:

1) Simulated body fluid (SBF): is a synthetic solution that has been designed to closely mimic the ion concentration of human blood plasma. It is kept under conditions of mild pH and physiological temperature, which accurately recreate the environment within the human body [5]. Examples of the use of SBF in analyzing the corrosion resistance of biomaterials can be found in the study of synthetic body fluids such as artificial blood plasma, artificial urine, Hank's solution, Ringer's solution, and artificial saliva [6-8]. There is a wide range of compositions used for these. However, all of these solutions maintain physiological pH and ionic strength. The simpler versions of these solutions do not contain any proteins, organic molecules, or divalent cations (magnesium or calcium), whereas these can be present in the more complex versions that have been used. These solutions are typically buffered with phosphate or carbonate buffer systems.

2) Simulated synovial fluid (SSF): is a synthetic solution designed to imitate the chemical composition of the fluid found in joints [4]. It is utilized to assess the wear and friction properties of implant materials, providing valuable information in the design and development of joint replacements and other implant materials [9]. In general, SSF is comprised of a combination of salts, lubricants, and other relevant substances aimed at replicating the environment present in the joints [10]. In SSF, hyaluronic acid is a common ingredient. Hyaluronic acid is a naturally occurring polysaccharide that can be found in synovial fluid and serves as an important factor for joint lubrication and shock absorption [11-13]. In some cases, proteins such as albumin may be added to SSF in order to replicate the protein content found in synovial fluid [13].

### 2.1.1 Phosphate buffered saline

Phosphate buffered saline (PBS) is a synthetic biological fluid, which is widely used in the biomedical and life science fields. PBS has a stable and neutral pH around 7.4, which is similar to the pH of human body [14]. PBS is designed to maintain the ionic strength and pH of human plasma by using the sodium chloride (NaCl) to regulate the osmotic pressure and a phosphate-based buffer ( $\text{Na}_2\text{HPO}_4$  and  $\text{KH}_2\text{PO}_4$ ) system to regular the pH [15]. NaCl helps to regulate the osmotic pressure of the solution, making it suitable for a variety of biological experiments [16].  $\text{Na}_2\text{HPO}_4$  and  $\text{KH}_2\text{PO}_4$  help to regulate the pH of the solution by providing a source of phosphate ions [17].

PBS is a frequently used solution for metal release experiments. Its stable and neutral pH of 7.4 allows it to accurately mimic biological conditions, while its isotonic nature helps preserve cell viability and prevent osmotic stress [18]. Additionally, its compatibility with many biological materials and its widespread availability at an affordable cost make it a practical choice for this type of analysis. Overall, PBS's unique features make it a highly suitable solution for evaluating metal release from biomedical materials.

The formation of complexes or nanoparticles between phosphate in the PBS and metal ions, such as cobalt(II) ions, can result in aggregation and metal precipitation [19-22]. The metal precipitation can lead to an underestimation of metal release from the biomaterials. In this thesis, PBS was used as primary simulated biological buffer to

investigate the metal release of CoCrMo, while it later was substituted with MES-buffered saline (see next section).

### 2.1.2 2-(N-morpholino)ethanesulfonic acid (MES) buffer

MES buffer is frequently used in synthetic biological fluids. It has a pH range of 6.1-6.5 but can be adjusted to pH 7.4 by sodium hydroxide [23]. The chemical structure is depicted in Figure 2-1. Because of the absence of phosphate, it can help to prevent the formation of complexes or nanoparticles between metal ions and phosphate, such as cobalt phosphate [20]. A study on many different buffers showed that MES buffer was least likely to bind to copper ions [24]. Therefore, it is speculated that it can reduce the effect on the metal precipitation, and hence the underestimation of the metal release results of biomaterials. Compared to the PBS buffer, MES buffer may be the better choice. The concentration of MES was 5 mM in this thesis (Chapter 6), which was suitable for many biological experiments. Additionally, 5 mM is a relatively low concentration and minimizes the potential interference of the buffer with the reaction or process being studied. In order to increase the ionic strength of the solution and keep the solution relevant for human body conditions, NaCl was added into the MES buffer. NaCl can also help to stabilize the pH of the buffer and to improve the solubility of the proteins.

Initially, PBS buffer was selected as the primary buffer for the research. However, further investigation revealed that metal precipitation was affecting the metal release interpretation. After discovering the influence of metal precipitation on the metal release analysis with PBS buffer (primarily in Chapters 3-4 and [19; 25]), it was decided to switch to using MES buffer in Chapter 6 of this thesis.



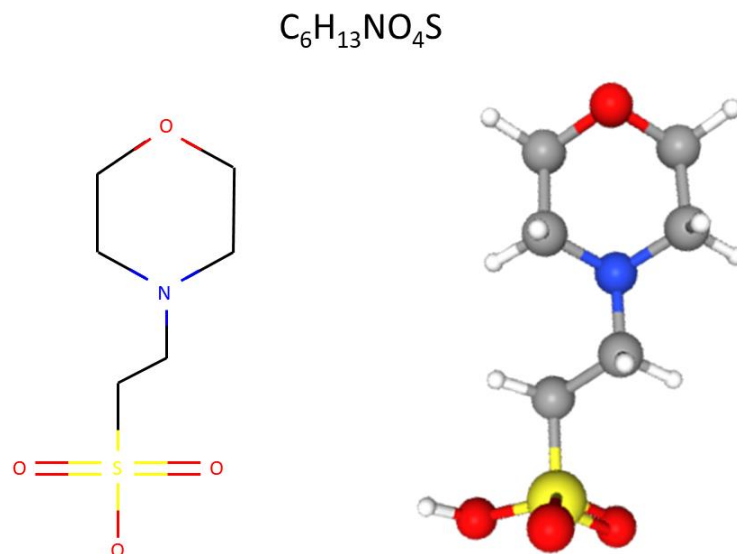


**Figure 2-1: A depiction of the chemical structure of MES in 2D and 3D [26].**

## 2.2 Justification of protein concentration

### 2.2.1 Bovine serum albumin (BSA)

Albumin as a protein can be found in humans and animals [27]. It is a globular protein that can be soluble in water and plays a critical role in many physiological processes [28]. BSA is a type of albumin that is composed of 583 amino acids, and its molecular weight is approximately 66,000 g/mol. BSA is stabilized by 18 cross-linked cystine residues [29]. BSA is a highly soluble and stable protein that is derived from the blood plasma of cows [30]. It is widely used in biological research. In order to simulate composition of blood plasma in the human body, the concentration of BSA is typically in the range of 40-60 g/L [31; 32]. In synovial fluid, it is about 12 g/L [33].

In this thesis, BSA was utilized to imitate blood plasma and examine the metal release of CoCrMo alloy under various circumstances, especially in Chapters 3 and 4. By using BSA, the study aimed to replicate the biological environment in order to evaluate the metal release from the CoCrMo alloy. During the course of the Ph.D. studies, it was noted that the proteins aggregated and the released metals precipitated, which had an impact on the estimate of the metal release and risked to underestimate the extent of

corrosion. In Chapter 4, these issues were thoroughly discussed and demonstrated. By reducing the concentration of BSA, we aimed to minimize the effect of protein aggregation on the metal release data and to obtain more accurate results. The final choice of the BSA concentration was 10 g/L in Chapter 6.

### 2.2.2 Fibrinogen (Fbn)

Fbn is a crucial component in blood plasma that is responsible for enabling blood clotting. The normal range of Fbn levels in human blood plasma is typically 2-4 g/L [34]. The molecular weight of Fbn is approximately 340,000 g/mol, and it is composed of around 2,964 amino acids in the human blood plasma [35; 36]. In Chapter 4, a mixture of 40 g/L BSA and 2.7 g/L Fbn was used to simulate the composition of human blood plasma to some extent.

The definition of the Vroman effect was introduced in Chapter 1. In order to simulate the Vroman effect in the experiments of Chapter 4, a mixture of BSA and Fbn was used to represent the proteins in the human blood plasma. In this study, BSA was used to represent the initial protein adsorption onto the CoCrMo alloy surface. As Fbn is a larger protein compared to BSA, its larger size makes it more likely to replace BSA that has adsorbed onto the surface of the CoCrMo alloy. Therefore, Fbn was then added to replace the BSA after a certain amount of time had elapsed.

## 2.3 Metal release estimations

In this study, a primary focus was placed on precisely quantifying the amount of metal released from the CoCrMo alloys and 316L stainless steel (Chapter 3 only) under different conditions when in contact with the biological fluids using trace metal analytical techniques, such as atomic absorption spectroscopy (AAS) and inductively coupled plasma mass spectrometry (ICP-MS). The testing conditions were carefully controlled to simulate the in-vitro environment to ensure the relevance and applicability of the metal release data.

A surface area-to-volume ratio (loading) of 1 cm<sup>2</sup>/mL was used in this thesis (as close as experimentally possible), justified as follows. A higher loading results in higher

concentrations of aqueous species, which facilitates their detection for highly corrosion-resistant materials (as in this thesis), however, a too high loading would result in a solution saturation effect. A loading of 1 cm<sup>2</sup>/mL (or lower) has previously been found to not risk any solution saturation effects for stainless steels [37-39]. By adopting this approach, it is aimed to minimize experimental variability and achieve more accurate, relevant, and comparable measurements of metal release.

For all metal release experiments in this thesis, one blank sample (solution without any metal specimen) was exposed in parallel with three replicates. The blank sample acts as a negative control to quantify and identify any background concentration or contamination that may interfere with the results. In trace metal analyses, a certain background concentration is expected (even ultrapure chemicals contain trace metal levels) and it needs therefore to be determined and subtracted. Also, it can be determined whether the sample concentrations are higher than the background concentrations. The three sample replicates aim to minimize experimental error and to evaluate the reproducibility of the experiments while also assessing the standard deviation. This is in particular important for alloy specimens that could undergo localized corrosion, as this is a stochastic process and can result in high variability among replicate samples under certain experimental conditions. The metal release from the CoCrMo alloys and 316L stainless steel is the sum of the background-corrected measured metal in solution (aqueous metal) and the released metal that has precipitated out from solution, as follows [40]:

$$\begin{aligned} \text{Metal release} &= \text{total measured aqueous metal} \\ &+ \text{precipitated and adsorbed metal} - \text{blank concentration} \end{aligned}$$

Several factors have a notable impact on the amount of metal species released that subsequently precipitate from solution or are incorporated in surface-adsorbed protein layers; solution pH, solution composition, protein concentration, ionic strength, and other factors such as friction and wear (presence of nanoparticles). Therefore, it is impossible to accurately estimate the amount of all metal release experimentally, especially in complex solutions of neutral pH, where metals such as cobalt would precipitate.

The released amount of non-precipitated metals from one metal specimen is calculated by following equation:

$$\text{Aqueous/released amount } (\mu\text{g}/\text{cm}^2) = \frac{(c_{\text{Sample}} (\mu\text{g}/\text{L}) - c_{\text{Blank}} (\mu\text{g}/\text{L})) \times \text{DF} \times V}{A_{\text{Sample}} (\text{cm}^2)}$$

Where:  $c_{\text{Sample}}$  is the concentration of a replicate solution sample,  $c_{\text{Blank}}$  is the concentration of the corresponding blank sample measured by AAS and ICP-MS, DF is the dilution factor (or the product of individual dilution factors, if several), V is the volume of the exposure solution, and A is the coupon or disk surface area. This is calculated for each of the three independent samples. Typically, the average and standard deviation of these triplicate samples is then shown in the result section.

## 2.4 References

- [1] Manam, N. S., et al. "Study of Corrosion in Biocompatible Metals for Implants: A Review." *Journal of Alloys and Compounds*, vol. 701, 2017, pp. 698-715.
- [2] Hedberg, Y. S., et al. "Metal Release from Stainless Steel in Biological Environments: A Review." *Biointerphases*, vol. 11, no. 1, 2016, pp. 901-917.
- [3] Geetha, M., et al. "Ti Based Biomaterials, the Ultimate Choice for Orthopaedic Implants—a Review." *Progress in materials science*, vol. 54, no. 3, 2009, pp. 397-425.
- [4] Merola, M., et al. "Materials for Hip Prostheses: A Review of Wear and Loading Considerations." *Materials*, vol. 12, no. 3, 2019, p. 495.
- [5] Kokubo, T. "Bioactive Glass Ceramics: Properties and Applications." *Biomaterials*, vol. 12, no. 2, 1991, pp. 155-163.
- [6] Nagalakshmi, R., et al. "Corrosion Behavior of Biomaterials in Synthetic Biological Solutions—an Overview." *Eur. Chem. Bull*, vol. 2, 2013, pp. 171-179.
- [7] Yilmaz, B., et al. "Historical Development of Simulated Body Fluids Used in Biomedical Applications: A Review." *Microchemical Journal*, vol. 155, 2020, p. 104713.
- [8] Marino, C. E. B., et al. "EIS Characterization of a Ti-Dental Implant in Artificial Saliva Media: Dissolution Process of the Oxide Barrier." *Journal of Electroanalytical Chemistry*, vol. 568, 2004, pp. 115-120.
- [9] Takadama, H. et al. "A Simulated Synovial Fluid for Wear Characterization of Artificial Hip Joints by a Hip Joint Simulator." *Key Engineering Materials*, vol. 309, Trans Tech Publ, 2006, pp. 1273-1276.
- [10] Ghosh, S., et al. "Tribological Role of Synovial Fluid Compositions on Artificial Joints—a Systematic Review of the Last 10 Years." *Lubrication Science*, vol. 26, no. 6, 2014, pp. 387-410.
- [11] Goa, K., et al. "Hyaluronic Acid." *Drugs*, vol. 47, no. 3, 1994, pp. 536-566.

- [12] Swann, D. A., et al. "Role of Hyaluronic Acid in Joint Lubrication." *Annals of the rheumatic diseases*, vol. 33, no. 4, 1974, p. 318.
- [13] Ward, P. D., et al. "Hyaluronic Acid: Its Role in Voice." *Journal of Voice*, vol. 16, no. 3, 2002, pp. 303-309.
- [14] Tang, Q., et al. "A Ph-Responsive Self-Healing Hydrogel Based on Multivalent Coordination of Ni<sup>2+</sup> with Polyhistidine-Terminated Peg and Ida-Modified Oligochitosan." *Journal of Materials Chemistry B*, vol. 7, no. 1, 2019, pp. 30-42.
- [15] Hedberg, Y. S., et al. "Surface-Protein Interactions on Different Stainless Steel Grades: Effects of Protein Adsorption, Surface Changes and Metal Release." *Journal of Materials Science: Materials in Medicine*, vol. 24, 2013, pp. 1015-1033.
- [16] Clegg, J. S. "The Control of Emergence and Metabolism by External Osmotic Pressure and the Role of Free Glycerol in Developing Cysts of *Artemia Salina*." *Journal of Experimental Biology*, vol. 41, no. 4, 1964, pp. 879-892.
- [17] Hendry, E. B. "The Preparation of Iso-Osmotic Phosphate Buffer Solutions." *Edinburgh Medical Journal*, vol. 55, no. 3, 1948, p. 142.
- [18] Rossi, F., et al. "Biological Buffered Saline Solution as Solvent in Agar-Carbomer Hydrogel Synthesis." *Chemical Papers*, vol. 64, no. 5, 2010, pp. 573-578.
- [19] Hedberg, Y. S., et al. "Synergistic Effects of Metal-Induced Aggregation of Human Serum Albumin." *Colloids and Surfaces B: Biointerfaces*, vol. 173, 2019, pp. 751-758.
- [20] Mei, N., et al. "Influence of Biocorona Formation on the Transformation and Dissolution of Cobalt Nanoparticles under Physiological Conditions." *ACS omega*, vol. 4, no. 26, 2019, pp. 21778-21791.
- [21] Hedberg, Y. S., et al. "Metal Release and Speciation of Released Chromium from a Biomedical CoCrMo Alloy into Simulated Physiologically Relevant Solutions." *Journal*

of Biomedical Materials Research Part B: Applied Biomaterials, vol. 102, no. 4, 2014, pp. 693-699.

[22] Hedberg, Y. S., et al. "Interaction of Albumin and Fibrinogen with Stainless Steel: Influence of Sequential Exposure and Protein Aggregation on Metal Release and Corrosion Resistance." *Corrosion*, vol. 73, no. 12, 2017, pp. 1423-1436.

[23] Bugbee, B. G., et al. "An Evaluation of MES (2 (N-Morpholino) Ethanesulfonic Acid) and Amberlite Irc-50 as Ph Buffers for Nutrient Solution Studies." *Journal of plant nutrition*, vol. 8, no. 7, 1985, pp. 567-583.

[24] Mash, H. E., et al. "Complexation of Copper by Zwitterionic Aminosulfonic (Good) Buffers." *Analytical chemistry*, vol. 75, no. 3, 2003, pp. 671-677.

[25] Cappellini, F., et al. "Mechanistic Insight into Reactivity and (Geno)Toxicity of Well-Characterized Nanoparticles of Cobalt Metal and Oxides." *Nanotoxicology*, vol. 12, no. 6, 2018, pp. 602-620.

[26] Kim, S., et al. "Pubchem 2023 Update." *Nucleic Acids Research*, vol. 51, no. D1, 2022, pp. 1373-1380.

[27] Kianfar, E. "Protein Nanoparticles in Drug Delivery: Animal Protein, Plant Proteins and Protein Cages, Albumin Nanoparticles." *Journal of Nanobiotechnology*, vol. 19, no. 1, 2021, p. 159.

[28] Sharma, V., et al. "Rheology of Globular Proteins: Apparent Yield Stress, High Shear Rate Viscosity and Interfacial Viscoelasticity of Bovine Serum Albumin Solutions." *Soft matter*, vol. 7, no. 11, 2011, pp. 5150-5160.

[29] Lin, V. J. C., et al. "Raman Studies of Bovine Serum Albumin." *Biopolymers: Original Research on Biomolecules*, vol. 15, no. 1, 1976, pp. 203-218.

[30] Jahanban, E. A., et al. "Recent Developments in the Detection of Bovine Serum Albumin." *International journal of biological macromolecules*, vol. 138, 2019, pp. 602-617.

- [31] Heakal, F. E. T., et al. "Serum Albumin Can Influence Magnesium Alloy Degradation in Simulated Blood Plasma for Cardiovascular Stenting." *Materials Chemistry and Physics*, vol. 220, 2018, pp. 35-49.
- [32] Liu, L., et al. "Influence of Bovine Serum Albumin on Corrosion Behaviour of Pure Zn in Phosphate Buffered Saline." *Journal of Materials Science: Materials in Medicine*, vol. 32, 2021, pp. 1-16.
- [33] Bennike, T., et al. "A Normative Study of the Synovial Fluid Proteome from Healthy Porcine Knee Joints." *Journal of proteome research*, vol. 13, no. 10, 2014, pp. 4377-4387.
- [34] Qiu, J., et al. "Preoperative Plasma Fibrinogen, Platelet Count and Prognosis in Epithelial Ovarian Cancer." *Journal of Obstetrics and Gynaecology Research*, vol. 38, no. 4, 2012, pp. 651-657.
- [35] Sovova, Z., et al. "Extension of the Human Fibrinogen Database with Detailed Clinical Information—the Ac-Connector Segment." *International Journal of Molecular Sciences*, vol. 23, no. 1, 2022, p. 132.
- [36] Herrick, S., et al. "Fibrinogen." *The international journal of biochemistry & cell biology*, vol. 31, no. 7, 1999, pp. 741-746.
- [37] Hedberg, Y. S., et al. "In-Vitro Biocompatibility of CoCrMo Dental Alloys Fabricated by Selective Laser Melting." *Dental materials*, vol. 30, no. 5, 2014, pp. 525-534.
- [38] Mazinianian, N., et al. "Comparison of the Influence of Citric Acid and Acetic Acid as Simulant for Acidic Food on the Release of Alloy Constituents from Stainless Steel Aisi 201." *Journal of Food Engineering*, vol. 145, no. C, 2015, pp. 51-63.
- [39] Wang, X., et al. "Bioaccessibility of Nickel and Cobalt in Powders and Massive Forms of Stainless Steel, Nickel-or Cobalt-Based Alloys, and Nickel and Cobalt Metals in Artificial Sweat." *Regulatory toxicology and pharmacology*, vol. 106, 2019, pp. 15-26.



[40] Hedberg, Y. S. "Stainless Steel in Biological Environments–Relation between Material Characteristics, Surface Chemistry and Toxicity." KTH Royal Institute of Technology, 2012.

## Chapter 3

### 3 Can Gamma Irradiation during Radiotherapy Influence the Metal Release Process for Biomedical CoCrMo and 316L alloys?

#### 3.1 Introduction

CoCrMo alloys and stainless steel grade AISI 316L are biomedical alloys widely used for different dental implants, orthodontic appliances and devices, artificial joint prostheses or orthopedic temporary devices [1-4]. They are therefore often present in patients that undergo a radiation cancer treatment (radiotherapy), and might be in the irradiated zone. A common example is radiotherapy of prostate cancer in the presence of artificial hip joints, which make radiotherapy and imaging by computed tomography more complicated due to shielding and perturbation effects [5; 6]. Reports and reviews on failed implants or insufficient osseointegration after/during radiotherapy for both hip joints [7-9] and dental implants [10-17] indicate risks of implant failure or loss of the implant upon irradiation, most probably due to tissue damage. These risks increase with increasing irradiation dose [10; 11; 15; 18] This has been questioned in some recent reviews and studies [19; 20], and patients that undergo radiotherapy have been recommended dental implant therapy if following some guidelines (e.g., strict monitoring) [16; 20-23]. Pelvic irradiation of patients with gynecological cancer without implants did not result in a higher risk of hip replacement afterward [24]. The reviews and studies that suggest an increased risk for failed implants or osseointegration caused by irradiation explained this risk to be related to damage of the bone or soft tissue, altered mechanical properties of the bone, and increased risks of infections. The metallic implant itself may also be affected by gamma irradiation radiotherapy. During radiotherapy, ionizing radiation, in particular gamma-radiation, will be absorbed and result in excitation and ionization of water and aqueous organic systems. These processes cause formation of oxidative and reductive radicals and species [25; 26], for example,  $\text{OH}^\cdot$ ,  $\text{O}_2^\cdot$ ,  $\text{H}_2\text{O}_2$ ,  $\text{HO}_2^\cdot$ ,  $\text{HO}_2$ ,  $\text{H}^\cdot$ ,  $\text{H}^\cdot$ ,  $\text{H}_2$ ,  $\text{O}_3^\cdot$ ,  $\text{O}^\cdot$ , and  $\text{H}_2\text{O}^\cdot$ . These species may affect the metal release process, the surface oxide characteristics, and/or the corrosion behavior of the

implant material. The amount of produced radicals depends on solution pH and is proportional to the total irradiation dose [26]. Most studies that investigate metal release and corrosion of stainless steels or other metals and alloys have been performed at higher temperatures and irradiation doses as compared to what would be relevant for the human body and radiotherapy (37°C and 10–145 Gy [14] total irradiation dose). An early study on stainless steel AISI 304 in the temperature range from 65 to 250°C in water of different pH and dissolved oxygen content observed a thicker surface oxide and transformation of released metals to insoluble corrosion products, but not an increased total amount of released metals upon exposure to gamma irradiation with a total dose of 120,000–225,000 Gy [27]. An evident surface oxidation effect was also observed for a Ni-Cr-Fe Inconel 600 alloy in water (pH 6–10.6) at 150°C, exposed to gamma-irradiation with a total dose of 295,200 Gy [28]. The study reported increased release of metals upon irradiation for solutions of the lower pH levels [28]. A study on stainless steel AISI 316L at relatively harsh conditions (320°C, 3 weight parts per million H<sub>2</sub>, neutral pH, a total proton irradiation dose up to 1.04×10<sup>9</sup> Gy) revealed accelerated corrosion and depletion of chromium from the surface oxide upon irradiation [29].

To the best of our knowledge, no studies exist that investigate metal release from biomedical materials at conditions of relevance for radiotherapy. This is of interest, since elevated levels, possibly toxic, of released metals upon radiotherapy could detrimentally affect the clinical outcome of the cancer treatment and/or the implant biocompatibility. This might furthermore be of particular interest in high risk groups for implant complications [30-34] and/or for the rare cases of metal-induced sarcoma [35-37].

The aim of this study was to investigate the extent of metal release from the biomedical materials stainless steel AISI 316L and cobalt-chromium-molybdenum alloy at simulated physiological conditions induced by gamma irradiation with a total dose of relevance for radiotherapy.

## 3.2 Materials and Methods

### 3.2.1 Materials

Samples of a medical grade cobalt-chromium- molybdenum (CoCrMo) alloy with nitrogen addition in disk shape of 22 mm in diameter and 2 mm in thickness (a total surface area of 9.0 cm<sup>2</sup>) were supplied by Ionbond, Switzerland, and produced by Aubert & Duval, France, by means of vacuum induction melting followed by electroslag remelting and warm working. The material conforms to the ASTM F1537 Alloy 1 standard. Coupons from sheets of AISI 316L stainless steel (cold-rolled), sized approximately 1.5×1.5 cm<sup>2</sup> (with a total surface area of 4.6–4.8 cm<sup>2</sup>), were supplied by Thyssen Krupp, Germany. Nominal bulk compositions are given in Table 3-1.

**Table 3-1: Nominal Bulk Alloy Composition of AISI 316L and CoCrMo Alloy (wt. %)**

	Co	Cr	Fe	Mn	Ni	Mo	C	P	Si	S	N	W
CoCrMo	Bal <sup>a</sup> .	27.9	0.22	0.59	0.11	5.9	0.074	<0.005	0.57	0.00018	0.18	<0.5
AISI316L	N/A	16.6	Bal.	1.0	10.6	2.1	0.03	0.02	0.4	0.001	N/A	N/A

### 3.2.2 Metal Release Exposure and Irradiation

All samples were ground by 1200 grit SiC, ultrasonically cleaned in acetone and isopropyl alcohol for 5 min, dried with cold nitrogen gas, and aged (desiccator, room temperature) for 24 h to enable a defined surface oxide. The samples were then entirely immersed into the solution in acid-cleaned glass vessels. The solution volume was 20 or 30 mL to completely immerse the coupons or disks and enable solution sampling after different exposure times (in the case of CoCrMo disks). The sample area to solution volume ratio was approximately 0.3 cm<sup>2</sup>/mL and accounted for in the metal release results presented in the unit of µg/cm<sup>2</sup>. In all cases, triplicate samples and one blank sample (without metal samples) were exposed in parallel into phosphate buffered saline (PBS), pH 7.3 ± 0.1, and also in PBS with bovine serum albumin (BSA), 10 g/L (A7906, Sigma Aldrich), denoted PBS 1 BSA, pH 7.3 ± 0.1. PBS was composed of 8.77 g/L NaCl, 1.28 g/L Na<sub>2</sub>HPO<sub>4</sub>, 1.36 g/L KH<sub>2</sub>PO<sub>4</sub>, adjusted with 50% NaOH, pH 7.2–7.4 (all at analytical grade, from VWR or Sigma Aldrich, Sweden), and ultrapure water (18.2 MΩ

cm, Millipore, Solna, Sweden). The albumin concentration was lower than present in human blood (about 40 g/L) [38], though higher than approximately 0.5–1 g/L that is necessary to adsorb a monolayer of BSA on stainless steel and to significantly enhance the metal release from 316L [39]. The 10 g/L BSA concentration was hence chosen as it requires less sample preparation prior to trace metal analysis, as compared with higher concentrations. All samples were irradiated (a Gammacell 1000 Elite, MDS Nordion) for 2 min and 13 s at a gamma irradiation rate of 0.124 Gy/s, resulting in a total irradiation dose of 16.49 Gy. Four milliliter of the 20 mL (316L) or 30 mL (CoCrMo) solution was directly sampled at 0 min (a few seconds) prior to irradiation and another 4 mL directly after irradiation (denoted 2 min and 13 s, or 0.035 h). The exposure was thereafter continued without irradiation for another 58 min (total exposure time of 1 h), after which the metal coupon/disk was separated from the solution. Since no agitation or temperature control was possible inside the gamma cell, all exposures were performed at room temperature and without agitation. Parallel nonirradiated reference samples were treated in the same way outside of the irradiation cell. This resulted in 12 independent CoCrMo samples, 12 independent 316L samples and eight blank solution samples, all sampled at three time points (resulting in 96 solution samples). After the 60 min exposure time, the coupons/disks were rinsed with ultrapure water, dried with nitrogen gas, and stored in a desiccator for post surface analysis. The solution was acidified to a pH < 2, and analyzed with graphite furnace atomic absorption spectroscopy (GF- AAS) on iron (Fe), chromium (Cr), and nickel (Ni) for the 316L samples, and on cobalt (Co), Cr, and molybdenum (Mo) for the CoCrMo samples. All chemicals were of at least analytical grade, and all equipment and vessels were acid- cleaned by 10% nitric acid for 24 h, and rinsed four times with ultrapure water.

### 3.2.3 Trace Metal Analysis

Solution metal analysis was performed using AAS (AAnalyst 800 instrument, Perkin Elmer), with graphite furnace mode. Calibration curves were based on at least four calibration standards and quality control samples of known concentration were analyzed regularly. The limits of detection, as determined by three times the highest standard deviation of the blank samples, were approximately 1 µg/L for all elements. Some sample

concentrations were lower than the corresponding blank concentrations, or lower than the limit of detection denoted “<LOD.” In all cases, the released and non-precipitated amount of measured metals in solution in the unit  $\mu\text{g}/\text{cm}^2$  is based on the average concentration of three independent replicate samples with the corresponding blank concentration subtracted, multiplied by the initial exposure volume (e.g., 0.03, 0.026, and 0.022 L for CoCrMo disks after 0 min, 2 min and 13 s, and 1 h), and divided by the exposed coupon/disk surface area. The error bars in the figures show the standard deviation of three independent samples.

### 3.2.4 Analysis of Albumin Size by Dynamic Light Scattering

In order to investigate whether albumin aggregates or changes its size upon irradiation or due to released metal ions, independent duplicate solution samples of PBS + BSA were prepared with or without the addition of 150  $\mu\text{g}/\text{L}$  Co (from  $\text{CoCl}_2$ ) and 5  $\mu\text{g}/\text{L}$  Cr (from chromium(III) oxalate trihydrate), concentrations that approximately correspond to observed metal concentrations released during 60 min from the CoCrMo disks. The solutions were filtered by 0.2  $\mu\text{m}$  polytetrafluoroethylene Acrodisc CR 25 mm syringe filters prior to irradiation. Some filtered solution samples were irradiated (as described previously), while others remained as references, that is, eight independent solution samples in total. After treatment, all solution samples were investigated within 1–6 h by means of two different dynamic light scattering techniques: Photon-cross-correlation-spectroscopy (PCCS; Nanophox, Sympatec GmbH, Germany) with a 632.8 nm laser, and nanoparticle tracking analysis (NTA) using a Nanosight NS300 instrument (Malvern, Uppsala, Sweden) with a 405 nm laser. Both measurements were conducted at 25°C, with the viscosity of water as input value. For PCCS, a control measurement of 23-nm latex nanoparticles gave reliable results and measurement of ultrapure water revealed only minor particle contamination.

For each sample in Eppendorf cuvettes (Eppendorf AG, Germany, UVette Routine pack, LOT No. C153896Q), duplicate sequential readings were performed for 120 s each. A nonnegative least squares algorithm was used by the instrument to determine the intensity size distribution. All 16 correlation functions were found acceptable, except one (that measurement was excluded), and all count rates were significantly (5–46 kcps) exceeding

background values (ultrapure water, 0.5 kcps). For NTA, triplicate measurements with 60 s captures were performed. The intensity and particle concentration of all samples ( $6.9 \pm 2.1$  particles/frame) were significantly exceeding the background value (ultrapure water), for which 0.25 particles per frame were observed. The NTA 3.2 software was employed to analyze the data.

### 3.2.5 Analysis of Surface Composition by Means of X-Ray Photoelectron Spectroscopy

X-ray photoelectron spectroscopy (XPS) was used for surface compositional analysis of the CoCrMo disks and 316L coupons, and a nonexposed (ground, cleaned, and aged) disk/coupon for comparison. Two different locations were analyzed on two independent disks/coupons for each condition. Wide spectra and detailed spectra (20 eV pass energy) on Co 2p, Cr 2p, Mo 3d, for CoCrMo disks, and on Fe 2p, Ni 2p, Mn 2p, and Cr 2p for 316L coupons, as well as O 1s of each test item including carbon (C 1s) and N 1s were run using a Kratos AXIS UltraDLD X-ray photoelectron spectrometer (Kratos Analytical) with a monochromatic Al X-ray source (150 W) on areas approximately sized  $700 \times 300 \mu\text{m}^2$ . The information depth is about 5–10 nm. Compositional findings of the outermost surface oxide are in the following presented as the relative mass ratio of oxidized metals only. For 2p metals (Co, Fe, Ni, Mn, and Cr), the 2p  $3/2$  peaks were resolved into their metallic and oxidic peaks (Table 3-2). For Mo 3d, the distinct metallic 3d  $5/2$  peak ( $228.2 \pm 0.2$  eV) as well as the metallic 3d  $3/2$  ( $231.3 \pm 0.2$  eV) peak were subtracted from the 3d peaks in order to obtain the oxidic fraction. C1s at 285.0 eV (denoted C1) was used as internal standard. For the disks/coupons exposed in PBS 1 BSA, also the atomic fraction of the nitrogen peak ( $399.5 \pm 0.9$  eV) to the sum of the oxidized carbon peaks (denoted C2, at  $286.7 \pm 0.2$  eV, and C3, at  $288.5 \pm 0.3$  eV) was calculated.

**Table 3-2: X-Ray Photoelectron Spectroscopy (XPS) Binding Energies and Assignments**

Sample	Binding Energy <i>a</i> (eV)	Assignment	References
Co 2p <sub>3/2</sub>	778.8 ± 0.16	Co metal	51
	782.3 ± 2.3	Oxidized Co	
Fe 2p <sub>3/2</sub>	707.1 ± 0.13	Fe metal	51
	712.3 ± 1.2	Oxidized Fe	
Cr 2p <sub>3/2</sub>	574.6 ± 0.16	Cr metal	51
	577.7 ± 0.8	Cr(III)	
Mo 3d	228.2 ± 0.2, 231.3 ± 0.2	Mo metal	52
	232.6 ± 0.3, 235.8 ± 0.1	MoO <sub>3</sub>	
Ni 2p <sub>3/2</sub>	853.0 ± 0.14	Ni metal	51
Mn 2p <sub>3/2</sub>	641.3	Oxidized Mn	51
N 1s	394.4 ± 0.07 (if no BSA)	metal nitride	53
	399.5 ± 0.9	Amine/amide species	54
C 1s	285.0	C–C, C–H bonds	54
	286.7 ± 0.2	C–N, C–O bonds	
	288.5 ± 0.3	C=C–O, O=C– bonds	
O 1s	530.7 ± 0.3	Lattice oxide	51
	531.8 ± 0.3	Hydroxide, hydrated, or defective oxide	
	533.2 ± 0.3	Water, organic oxide	

### 3.2.6 Statistics

To identify the significance of differences, a Student's *t* test of unpaired data with unequal variance (KaleidaGraph v. 4.0) was employed between two different data sets of independent samples. In the case of different time points for the same disks/coupons, a test of paired data was used. Differences are counted as significant when  $p < 0.05$ , with higher significance for a smaller *p* values.

## 3.3 Results and Discussion

### 3.3.1 Metal release

For CoCrMo, the released and non-precipitated amount of Co and Cr in solution increased 1.6–3-fold with exposure time ( $p < 0.05$  for most cases comparing 0 and 1 h), Figure 3-1(a). Statistical differences in solution concentrations of Co and Cr were observed between nonirradiated and irradiated disks after the irradiation period (2 min and 13 s), Figure 3-1(a), but not after 1 h of exposure. No significant difference was observed between PBS without and with BSA.



Differences could not be calculated for Mo, since the concentrations were below the limits of detection after 0 and 0.03 h, however, the trends were similar as for Co and Cr. In the case of 316L, one of the three coupons showed in several cases higher release compared to the other two coupons. This resulted in large error bars and disabled any statistical comparison. However, the time dependence (increased release with time) was stronger as compared to CoCrMo, due to a very low release during the first seconds of immersion (0 h), Figure 3-1(a, b). For Ni, significantly lower amounts of Ni in solution were observed after 1 h of exposure for the irradiated coupons in PBS as compared to the nonirradiated coupons, despite similar amounts after 2 min and 13 s for the same coupons, Figure 3-1(b). After 1 h of exposure, released amounts in PBS 1 BSA were 3–32-fold larger as compared to PBS, however, these differences were not statistically significant. Co was the main released element quantified in solution for the CoCrMo disks and Fe the dominant element released from 316L, even when normalized to their corresponding bulk content in Table 3-1. Cr was the least released element quantified in solution for 316L, and Mo the least released element for CoCrMo, Figure 3-1. Cr was detected to a smaller extent for AISI 316L as compared to CoCrMo, Figure 3-1.

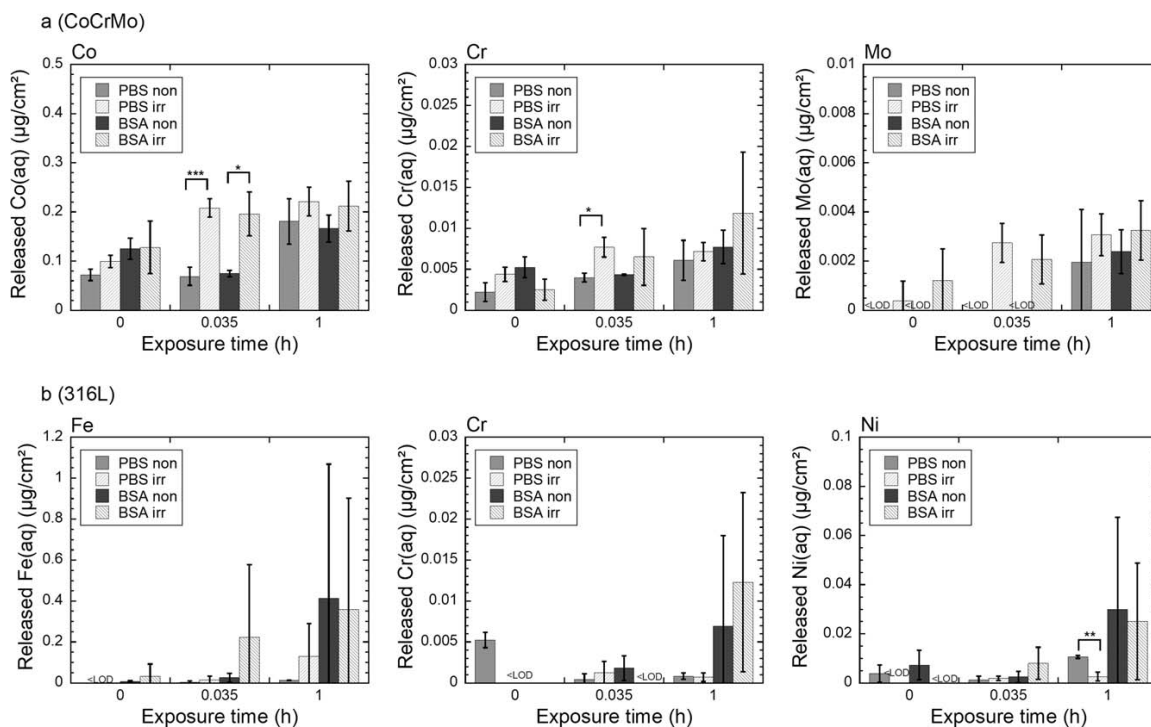


**Figure 3-1: Released and nonprecipitated amounts of Co, Cr, and Mo in solution (aq—aqueous) from the CoCrMo alloy (a), and of Fe, Cr, and Ni from the 316L alloy (b) after 0 (few seconds), 0.035 (2 min 13 s), and 1 h of exposure at room temperature with or without irradiation (during the time period 0–0.035 h) in PBS (pH 7.3) or PBS and 10 g/L BSA (pH 7.3). Statistical differences: \*  $p < 0.05$ , \*\*  $p < 0.01$ , \*\*\*  $p < 0.001$ . non, nonirradiated; irr, irradiated; <LOD, below limit of detection.**

### 3.3.2 Surface Characterization

XPS revealed a surface oxide composition of oxidized cobalt (Co 2p<sub>3/2</sub> line at  $782.3 \pm 2.3$  eV), chromium (at  $577.7 \pm 0.8$  eV, corresponding to trivalent chromium), and molybdenum (with two main peaks at  $232.6 \pm 0.3$  and  $235.8 \pm 0.1$  eV corresponding to MoO<sub>3</sub>) for CoCrMo, and of oxidized iron ( $712.3 \pm 1.2$  eV), chromium (at  $577.3 \pm 0.8$  eV, corresponding to trivalent chromium), and manganese (641.3 eV, only for the abraded reference coupon) for 316L, Table 3-2. The binding energy positions were independent of irradiation or exposure to PBS. The ratio of Co, Cr, and Mo in the surface oxide of the abraded reference disk corresponded nearly to the bulk composition, Figure 3-2(a). Upon

immersion in all solutions for one hour, the surface oxide became enriched in Cr. This enrichment (coupled with a Co depletion) is expected from earlier studies [40]. A small, but statistically significant Cr enrichment and Co depletion was also observed for disks exposed to PBS + BSA (nonirradiated) as compared to PBS (both nonirradiated and irradiated), Figure 3-2(a). This is also in agreement with previous observations [40]. Mo was statistically significant enriched in PBS 1 BSA as compared to PBS (for irradiated disks), Figure 3-2(a). No difference in the ratio of metal peaks to oxidized metal peaks (0.4 by mass) was observed between the differently exposed CoCrMo disks. The ratio was though higher as compared to the abraded reference disks (0.3 by mass), which indicates a thinner oxide after exposure. Due to individual differences among the coupons, no statistical differences between the reference coupon and the exposed coupons, the irradiation conditions, or the solutions, were observed for 316L, Figure 3-2(a). However, calculated ratios of metal peaks to oxidized peaks indicated a statistically significant ( $p < 0.05$ ) thicker oxide for 316L coupons exposed to PBS as compared to the abraded reference coupons (0.24 and 0.29 by mass as compared to 0.35 of the reference), while the oxide of coupons exposed to PBS 1 BSA seemed to be thinner (though not statistically different, 0.43 and 0.47 by mass). Small, but statistically significant ( $p < 0.05$ ), differences were also observed for the irradiated coupons as compared to nonirradiated 316L coupons in both PBS and PBS + BSA. This indicates in both cases a thinner oxide in the case of irradiation.

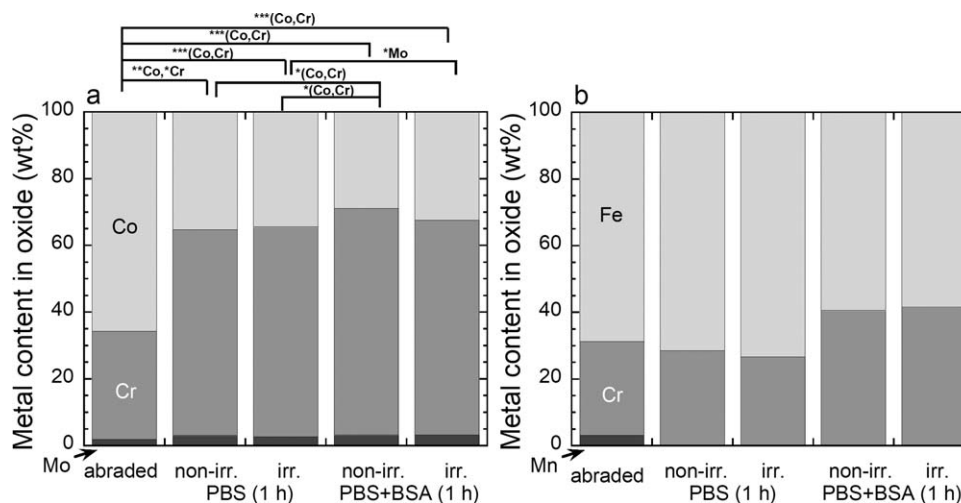


**Figure 3-2: Relative oxidized metal content (wt. %) in the surface oxide of the CoCrMo (a) and 316L (b) alloys, as determined by XPS. Statistically significant differences are indicated (\*  $p < 0.05$ , \*\*  $p < 0.01$ , \*\*\*  $p < 0.001$ ). Non-irr., nonirradiated; irr., irradiated.**

The measured atomic ratio of  $N/(C2 \pm C3)$  was slightly lower compared with the theoretical ratio of 0.48 of BSA [41] ( $0.41 \pm 0.1$  in nonirradiated and in irradiated PBS + BSA for rinsed CoCrMo disks, and  $0.35 \pm 0.04$  in nonirradiated and in irradiated PBS + BSA for rinsed 316L coupons).

### 3.3.3 Effects of Gamma Irradiation on Size of Albumin

PCCS and NTA measurements were conducted of filtered ( $0.2 \mu\text{m}$ ) irradiated and nonirradiated PBS + BSA solutions in order to investigate whether the applied gamma irradiation induced albumin aggregation, which could influence the measured amount of released metals in solution or the metal release process. Since previous studies [40; 42] showed the ability of released metal ions in solution to cause albumin aggregation, the same conditions were investigated for albumin solutions containing  $150 \mu\text{g/L}$  Co and  $5 \mu\text{g/L}$  Cr. These concentrations are similar to their corresponding released levels in solution after 1 h for the CoCrMo alloy. Figure 3-3 shows the hydrodynamic size distribution of albumin, measured by PCCS (a) and NTA (b). As seen in the figure, no significant difference in albumin size was observed either upon irradiation or in the absence or presence of these trace metal concentrations. A slight change in size, visible

by an additional peak at 13 nm, was detected by both PCCS and NTA measurements for irradiated samples as compared to nonirradiated solution samples. However, this difference was not statistically significant. Albumin self-aggregates at all sizes below the cut-off value of the membrane filter (200 nm), Figure 3-3(b), but is mostly present as a monomer (theoretical triangular structure of  $8 \times 8 \times 3 \text{ nm}^3$ ) [43] Figure 3-3(a).

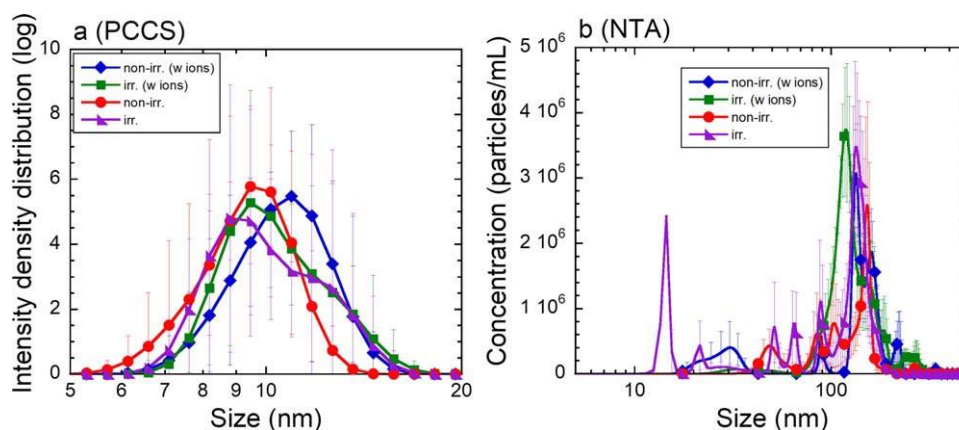


**Figure 3-3: Hydrodynamic size distributions of BSA by intensity (by means of PCCS, a) and by number (by means of NTA, b) of 0.2  $\mu\text{m}$  filtered irradiated and nonirradiated PBS + BSA solutions, and with and without trace amounts of metal ions. non-irr., nonirradiated; irr., irradiated; w ions, with 150  $\mu\text{g/L}$  Co and 5  $\mu\text{g/L}$  Cr.**

### 3.4 Discussion

Radiotherapy for cancer treatments is usually given at daily fractions up to 2 Gy, 3–5 times per week, with a total irradiation dose of 10–145 Gy [14]. For high-risk patients, radiotherapy at a total dose of 10–20 Gy may also be given to prevent heterotopic bone formation, a complication for hip arthroplasty [44], which treats the condition equally effective pre- and postoperatively [45]. The total irradiation dose used in this study is hence highly relevant for such treatments, however, the dose rate is higher as compared to what is used in radiotherapy.

Irradiation-induced radicals can be both reductive and oxidative [25; 26], and can therefore theoretically both result in reductive or oxidative dissolution of the surface

oxides and oxidative dissolution (corrosion) of the metal beneath the (damaged) surface oxide [46]. Despite the relatively low total irradiation dose, we observed that the radiation slightly influenced the extent of metal release from CoCrMo (increased directly after irradiation) and in the case of AISI 316L, both the extent of metal release (decreased Ni after 1 h) and oxide thickness (reduced upon irradiation). This can be interpreted as an effect of oxidation of the alloy surface caused by the gamma irradiation that may result in surface passivation (stabilization of surface oxide). Passivation means in this context a further stabilization of the barrier properties of the surface oxide even though the surface oxides of CoCrMo and 316L also were passive prior to irradiation, as indicated by generally very low amounts of released metals. This passivation effect is in agreement with an early study on AISI 304 where significantly higher irradiation doses and temperatures were investigated [27]. Passivation is known to initially cause a higher release of the least stable elements of the surface oxide, Fe in the case of AISI 316L and Co in the case of CoCrMo [40], while it decreases the overall amount of metal release after improved passivation [46-48]. Both joint prostheses and dental prostheses are partially exposed to friction, which may result in a partial or complete destruction of the surface oxide, similarly to the abrasion procedure in this study applied 24 h prior to the irradiation exposure. It can hence be assumed that the surface of implant parts exposed to friction would face a new passivation each time when irradiated, with an initially increased amount of metal release, while surfaces of implant parts that are not exposed to friction and therefore maintain their passive surface oxides would not experience any increased metal release upon irradiation treatments. Irradiation-induced metal release and passivation of implant parts that are exposed to friction requires further investigations both directly after abrasion/friction and after long-term immersion, or their combination. Furthermore, implants that have a damaged surface oxide or on-going corrosion [1; 2]. for example, due to misalignment, galvanic corrosion (due to different metallic implant materials in contact), or an on-going infection or inflammation, might be at risk to release elevated amounts of metals upon irradiation treatments. This might be particularly important for patients with on-going or known hypersensitivity reactions to metals, and requires further investigations.

That albumin was able to increase the extent of metal release from AISI 316L and change the surface oxide composition (however, not statistically significant in this study), while no such effect was observed for CoCrMo, is in agreement with previous studies [39; 40; 46; 49]. It has been speculated whether the lack of increased metal release from CoCrMo in the presence of albumin is related to a different protein-surface interaction, as compared to AISI 316L, or due to an increased metal-induced protein aggregation that may result in an underestimation of the amount of released metals in solution from CoCrMo [40; 42]. However, for the low concentrations of released metals in this study and the short time period of exposure to gamma irradiation, no protein aggregation effect was discerned. This observation further suggests that the lower effect of irradiation on the metal release in albumin-containing solution as compared to PBS without albumin for AISI 316L most probably was not due to albumin aggregation.

The metal release rate from CoCrMo was highest during the first few seconds of immersion. A similar trend has for instance been shown for AISI 316L powder in physiological solutions [50]. However, released amounts of metals after a few seconds from the 316L coupons of this study were not measurable. Decreased metal release rates with time furthermore show the importance of a rapidly passivating surface oxide that adjusts to the new environment and results in lower extent of released metals. However, it could also mean that repeated destruction of the surface oxide (e.g., by friction due to joint movements or chewing) would result in relatively high amounts of released metals during the first seconds following the friction event.

Further studies should therefore investigate repeated friction in combination with fractionated irradiation treatments at conditions of relevance for radiotherapy ( $\leq 2$  Gy per occasion).

### 3.5 Conclusions

The amount of released metals from biomedical stainless steel AISI 316L and CoCrMo in physiologically relevant fluids (PBS with and without 10 g/L BSA at pH 7.3) was investigated as a function of gamma irradiation with a total dose of relevance for radiotherapy. The following main conclusions were drawn:

1. Generally, the effect of irradiation (total dose of 16.5 Gy) was small, but detectable in some cases. It is therefore expected to be only clinically relevant in cases where other factors such as friction and corrosion, possibly synergistically, exist.
2. Irradiated CoCrMo disks released higher amounts of metals directly after irradiation (during the first 2 min and 13 s) as compared to nonirradiated CoCrMo disks. No differences in released metals were observed during the concomitant nonirradiated exposure up to 60 min for the same disks. This was most probably related to an irradiation-accelerated surface passivation effect.
3. No significant differences in metal release among the different investigated conditions were observed for 316L due to individual differences among replicate coupons, except that nickel release was lower after 1 h of exposure in irradiated coupons in PBS as compared to nonirradiated coupons (despite similar or higher levels directly after irradiation, 2 min and 13 s, of the same coupons). This indicates an irradiation-accelerated surface passivation effect.
4. The presence of albumin in solution resulted in a reduced surface oxide thickness for 316L, coupled to nonsignificant increased amounts of released metals and a nonsignificant enrichment of chromium in the surface oxide. No such effects were observed for CoCrMo except for a slight enrichment of chromium in the surface oxide in the presence of albumin.
5. Most metals were released into solution from CoCrMo during the first seconds of immersion, independent of whether they were exposed to radiation or not.
6. No albumin aggregation in solution was observed at the conditions of this study either in the presence or absence of metal ions or irradiation.



### 3.6 References

- [1] Virtanen, S. "Corrosion of Biomedical Implant Materials." *Corrosion Reviews*, vol. 26, no. 2-3, 2008, pp. 147-171.
- [2] Virtanen, S., et al. "Special Modes of Corrosion under Physiological and Simulated Physiological Conditions." *Acta biomaterialia*, vol. 4, 2008, pp. 468-476.
- [3] Milošev, I. "Metallic Materials for Biomedical Applications: Laboratory and Clinical Studies." *Pure and Applied Chemistry*, vol. 83, no. 2, 2011, pp. 309-324.
- [4] Chen, Q., et al. Thouas. "Metallic Implant Biomaterials." *Materials Science and Engineering: R: Reports*, vol. 87, 2015, pp. 1-57.
- [5] Aubin, M., et al. "The Use of Megavoltage Cone-Beam Ct to Complement Ct for Target Definition in Pelvic Radiotherapy in the Presence of Hip Replacement." *The British Journal of Radiology*, vol. 79, no. 947, 2006, pp. 918-921.
- [6] Reft, C., et al. "Dosimetric Considerations for Patients with Hip Prostheses Undergoing Pelvic Irradiation. Report of the AAPM Radiation Therapy Committee Task Group 63." *Medical Physics*, vol. 30, no. 6, 2003, pp. 1162-1182.
- [7] Donati, D., et al. "Modular Prosthetic Replacement of the Proximal Femur after Resection of a Bone Tumour." *Bone & Joint Journal*, vol. 83, no. 8, 2001, pp. 1156-1160.
- [8] Jacobs, J. J., et al. "Early Failure of Acetabular Components Inserted without Cement after Previous Pelvic Irradiation." *The Journal of Bone and Joint Surgery. American Volume*, vol. 77, no. 12, 1995, pp. 1829-1835.
- [9] Massin, P., et al. "Total Hip Replacement in Irradiated Hips. A Retrospective Study of 71 Cases." *Bone & Joint Journal*, vol. 77, no. 6, 1995, pp. 847-852.
- [10] Esser, E., et al. "Dental Implants Following Radical Oral Cancer Surgery and Adjuvant Radiotherapy." *International Journal of Oral & Maxillofacial Implants*, vol. 12, no. 4, 1997, pp. 552-557.

- [11] Granström, G. "Osseointegration in Irradiated Cancer Patients: An Analysis with Respect to Implant Failures." *Journal of Oral and Maxillofacial Surgery*, vol. 63, no. 5, 2005, pp. 579-585.
- [12] Ihde, S., et al. "Effects of Radiation Therapy on Craniofacial and Dental Implants: A Review of the Literature." *Oral Surgery, Oral Medicine, Oral Pathology, Oral Radiology, and Endodontology*, vol. 107, no. 1, 2009, pp. 56-65.
- [13] Sugerman, P. B., et al. "Patient Selection for Endosseous Dental Implants: Oral and Systemic Considerations." *International Journal of Oral and Maxillofacial Implants*, vol. 17, no. 2, 2002, pp. 191-201.
- [14] Smith, N., A., et al. "Irradiated Patients and Survival Rate of Dental Implants: A Systematic Review and Meta-Analysis." *The Journal of Prosthetic dentistry*, vol. 116, no. 6, 2016, pp. 858-866.
- [15] Chrcanovic, B. R., et al. "Dental Implants in Irradiated Versus Nonirradiated Patients: A Meta-Analysis." *Head & Neck*, vol. 38, no. 3, 2016, pp. 448-481.
- [16] Mancha de la Plata, M., et al. "Osseointegrated Implant Rehabilitation of Irradiated Oral Cancer Patients." *Journal of Oral and Maxillofacial Surgery*, vol. 70, no. 5, 2012, pp. 1052-1063.
- [17] Chen, H., et al. "Smoking, Radiotherapy, Diabetes and Osteoporosis as Risk Factors for Dental Implant Failure: A Meta-Analysis." *PloS one*, vol. 8, no. 8, 2013, p. 71955.
- [18] Nooh, N. "Dental Implant Survival in Irradiated Oral Cancer Patients: A Systematic Review of the Literature." *International Journal of Oral & Maxillofacial Implants*, vol. 28, no. 5, 2013, pp. 1233-1242.
- [19] Zen, F. E. V., et al. "Viability of Dental Implants in Head and Neck Irradiated Patients: A Systematic Review." *Head & Neck*, vol. 38, no. S1, 2016, pp. E2229-E2240.

- [20] Schiegnitz, E., et al. "Oral Rehabilitation with Dental Implants in Irradiated Patients: A Meta-Analysis on Implant Survival." *Clinical oral investigations*, vol. 18, no. 3, 2014, pp. 687-698.
- [21] Anderson, L., et al. "The Influence of Radiation Therapy on Dental Implantology." *Implant dentistry*, vol. 22, no. 1, 2013, pp. 31-38.
- [22] Harrison, J. S., et al. "Dental Implants for Patients Who Have Had Radiation Treatment for Head and Neck Cancer." *Special Care in Dentistry*, vol. 23, no. 6, 2003, pp. 223-229.
- [23] Wagner, W., et al. "Osseointegration of Dental Implants in Patients with and without Radiotherapy." *Acta Oncologica*, vol. 37, no. 7-8, 1998, pp. 693-696.
- [24] Dybvik, E., et al. "Pelvic Irradiation Does Not Increase the Risk of Hip Replacement in Patients with Gynecological Cancer: A Cohort Study Based on 8,507 Patients." *Acta orthopaedica*, vol. 85, no. 6, 2014, pp. 652-656.
- [25] Ershov, B. G., et al. "A Model for Radiolysis of Water and Aqueous Solutions of H<sub>2</sub>, H<sub>2</sub>O<sub>2</sub> and O<sub>2</sub>." *Radiation Physics and Chemistry*, vol. 77, no. 8, 2008, pp. 928-935.
- [26] Dispenza, C., et al. "Radiation-Engineered Functional Nanoparticles in Aqueous Systems." *Journal of Nanoscience and Nanotechnology*, vol. 15, no. 5, 2015, pp. 3445-3467.
- [27] Ishigure, K., et al. "Effect of Gamma Radiation on the Release of Corrosion Products from Carbon Steel and Stainless Steel in High Temperature Water." *Nuclear Technology*, vol. 50, no. 2, 1980, pp. 169-177.
- [28] Musa, A. Y., et al. "Combined Effect of Gamma-Radiation and Ph on Corrosion of Ni-Cr-Fe Alloy Inconel 600." *Corrosion Science*, vol. 109, 2016, pp. 1-12.
- [29] Raiman, S. S., et al. "Accelerated Corrosion and Oxide Dissolution in 316L Stainless Steel Irradiated in Situ in High Temperature Water." *Journal of Nuclear Materials*, vol. 493, 2017, pp. 207-218.

- [30] Mabileau, G., et al. "Metal-on-Metal Hip Resurfacing Arthroplasty: A Review of Periprosthetic Biological Reactions." *Acta orthopaedica*, vol. 79, no. 6, 2008, pp. 734-747.
- [31] Beaulé, P. E., et al. "Risk Factors Affecting Outcome of Metal-on-Metal Surface Arthroplasty of the Hip." *Clinical orthopaedics and related research*, vol. 418, 2004, pp. 87-93.
- [32] Park, H. S., et al. "Factors Affecting the Clinical Success of Screw Implants Used as Orthodontic Anchorage." *American Journal of Orthodontics and Dentofacial Orthopedics*, vol. 130, no. 1, 2006, pp. 18-25.
- [33] Moy, P. K., et al. "Dental Implant Failure Rates and Associated Risk Factors." *International Journal of Oral & Maxillofacial Implants*, vol. 20, no. 4, 2005, pp. 569-577.
- [34] Delaunay, C., et al. "Metal-on-Metal Bearings Total Hip Arthroplasty: The Cobalt and Chromium Ions Release Concern." *Orthopaedics & Traumatology: Surgery & Research*, vol. 96, no. 8, 2010, pp. 894-904.
- [35] Ward, J., et al. "Metal-Induced Sarcoma: A Case Report and Literature Review." *Clinical orthopaedics and related research*, vol. 252, 1990, pp. 299-306.
- [36] Keegan, G. M., et al. "A Systematic Comparison of the Actual, Potential, and Theoretical Health Effects of Cobalt and Chromium Exposures from Industry and Surgical Implants." *Critical reviews in toxicology*, vol. 38, no. 8, 2008, pp. 645-674.
- [37] Wagner, P., et al. "Increased Cancer Risks among Arthroplasty Patients: 30 Year Follow-up of the Swedish Knee Arthroplasty Register." *European Journal of Cancer*, vol. 47, no. 7, 2011, pp. 1061-1071.
- [38] Peters, T. J. "Serum Albumin." *Advances in protein chemistry*, vol. 37, 1985, pp. 161-245.

- [39] Hedberg, Y. S., et al. "Surface-Protein Interactions on Different Stainless Steel Grades – Effects of Protein Adsorption, Surface Changes and Metal Release." *Journal of Materials Science - Materials in Medicine*, vol. 24, no. 4, 2013, pp. 1015-1033.
- [40] Hedberg, Y. S., et al. "Metal Release and Speciation of Released Chromium from a Biomedical CoCrMo Alloy into Simulated Physiologically Relevant Solutions." *Journal of Biomedical Materials Research Part B: Applied Biomaterials*, vol. 102, no. 4, 2014, pp. 693-699.
- [41] Hirayama, K., et al. "Rapid Confirmation and Revision of the Primary Structure of Bovine Serum Albumin by Esims and Frit-Fab Lc/Ms." *Biochemical and Biophysical Research Communications*, vol. 173, no. 2, 1990, pp. 639-646.
- [42] Hedberg, Y. S., et al. "Can Cobalt(II) and Chromium(III) Ions Released from Joint Prostheses Influence the Friction Coefficient?" *ACS Biomaterials Science & Engineering*, vol. 1, no. 8, 2015, pp. 617-620.
- [43] He, X. M., et al. "Atomic Structure and Chemistry of Human Serum Albumin." *Nature*, vol. 358, no. 6383, 1992, pp. 209-215.
- [44] Anthony, P., et al. "Prevention of Heterotopic Bone Formation with Early Post Operative Irradiation in High Risk Patients Undergoing Total Hip Arthroplasty: Comparison of 10.00 Gy Vs 20.00 Gy Schedules." *International Journal of Radiation Oncology Biology Physics*, vol. 13, no. 3, 1987, pp. 365-369.
- [45] Seegenschmiedt, M. H., et al. "Prevention of Heterotopic Ossification About the Hip: Final Results of Two Randomized Trials in 410 Patients Using Either Preoperative or Postoperative Radiation Therapy." *International Journal of Radiation Oncology Biology Physics*, vol. 39, no. 1, 1997, pp. 161-171.
- [46] Hedberg, Y. S., et al. "Metal Release from Stainless Steel in Biological Environments: A Review." *Biointerphases*, vol. 11, no. 1, 2016, pp. 901-917.

- [47] Mazinianian, N., et al. "Metal Release Mechanisms for Passive Stainless Steel in Citric Acid at Weakly Acidic Ph." *Journal of the Electrochemical Society*, vol. 163, no. 10, 2016, pp. C686-C693.
- [48] Mazinianian, N., et al. "Metal Release and Corrosion Resistance of Different Stainless Steel Grades in Simulated Food Contact." *Corrosion* vol. 72, no. 6, 2016, pp. 775-790.
- [49] Hedberg, Y. S., et al. "In-Vitro Biocompatibility of CoCrMo Dental Alloys Fabricated by Selective Laser Melting." *Dental materials*, vol. 30, no. 5, 2014, pp. 525-534.
- [50] Hedberg, Y. S., et al. "Size Matters: Mechanism of Metal Release from 316l Stainless Steel Particles Is Governed by Size-Dependent Properties of the Surface Oxide." *Materials Letters*, vol. 122, 2014, pp. 223-226.
- [51] Biesinger, M. C., et al. "Resolving surface chemical states in XPS analysis of first row transition metals, oxides and hydroxides: Cr, Mn, Fe, Co and Ni." *Applied Surface Science*, vol. 257, no.7, 2011, pp. 2717-2730.
- [52] Lu, Y. C., et al. "An XPS study of the passive and transpassive behavior of molybdenum in deaerated 0.1 M HCl." *Corrosion science*, vol. 29, no. 8, 1989, pp. 927-937.
- [53] Cao, B., et al. "Mixed close-packed cobalt molybdenum nitrides as non-noble metal electrocatalysts for the hydrogen evolution reaction." *Journal of the American Chemical Society*, vol. 135, no. 51, 2013, pp. 19186-19192.
- [54] Ithurbide, A., et al. "XPS and flow-cell EQCM study of albumin adsorption on passivated chromium surfaces: Influence of potential and pH." *Electrochimica Acta*, vol. 53, no. 3, 2007, pp. 1336-1345.

## Chapter 4

# 4 Metal Release from a Biomedical CoCrMo Alloy in Mixed Protein Solutions under Sliding Conditions: Effect of Protein Aggregation and Metal Precipitation

## 4.1 Introduction

Biomedical materials made of cobalt-chromium (28 wt.%)–molybdenum (6 wt.%) (CoCrMo) alloys are commonly used in artificial prostheses and dental implants for surfaces that are exposed to friction and load [1; 2]. CoCrMo alloys possess both a high corrosion resistance and excellent wear resistance [2] making them relatively high-resistant to tribocorrosion processes, which involve both mechanical, electrochemical, and in some cases other chemical processes, often in a synergistic way [2-5].

The release of  $\text{Co}^{\text{II}}$  and  $\text{Cr}^{\text{III}}$  ions and complexes, or wear nanoparticles, from CoCrMo surfaces into protein-rich physiological environments can result in protein binding [6-9], protein aggregation [10; 11], and adverse health effects [12] such as allergic reactions [13] and neurodegenerative diseases [14-16].

The interface between CoCrMo and softer materials such as ultra-high molecular-weight polyethylene (UHMWPE), the common interface in so-called metal-on-polymer (MOP) hip joint prostheses, is challenging to understand in the presence of proteins, as these can induce lubricating effects [17; 18], aggregate due to metal release [10], and induce dominating chemical release mechanisms that are difficult to investigate [4; 19].

A physiological environment consists not only of one type of protein. The presence of several types of proteins can influence the adsorption, surface protein exchange rate, and hence lubricating properties and chemically induced release mechanisms. The Vroman effect describes the substitution of surface-adsorbed proteins by proteins with a higher surface affinity, which are often larger in size [20]. This exchange can be very rapid (seconds to minutes) [21]. The metal released from stainless steels of grades AISI 316L and 303 was found to be influenced by the Vroman effect [22]. A corresponding study on CoCrMo alloy has not been published yet.

Under shear conditions, protein aggregates can also be formed mechanically [23; 24]. Further, it has been shown that released molybdate ions from CoCrMo alloys can change the structure of the adsorbed protein film by cross-linking proteins, forming a gel-like structure [25; 26].

This study aimed at investigating the effect of different proteins (albumin and fibrinogen) on metal release from CoCrMo in static and sliding conditions.

## 4.2 Materials and Methods

### 4.2.1 Materials

Specimens used in metal release studies were biomedical grade cobalt-chromium (28 wt.%) -molybdenum (6 wt.%) (CoCrMo) alloy disks of 22 mm in diameter and 2 mm in thickness (a total surface area of 9.0 cm<sup>2</sup>), supplied by Ionbond, Switzerland, and certified by Aubert & Duval, France. They were produced by means of vacuum induction melting followed by electroslag remelting and warm working. The materials conformed to ASTM F1537 Alloy 1. For specimens used in the wear test, the CoCrMo disks were 21.9 mm in diameter and 5 mm in thickness (ASTM F1537-11), supplied by the same supplier and of similar manufacturing and composition.

### 4.2.2 Metal Release Investigations in Static Condition (Without Friction)

Prior to metal release tests, all disks were grinded by 1200 grit SiC paper with water, and ultrasonically cleaned in acetone and isopropyl alcohol for 7 min, subsequently. After that, the cleaned disks were dried with nitrogen gas at room temperature and stored in a desiccator at room temperature for 24 hours to form a well-defined passive film on the surface prior to exposure. During exposure, the ratio of the specimen surface area to solution volume was approximately 1 cm<sup>2</sup>/mL (0.9 cm<sup>2</sup> surface area in 9 mL solution) and exactly measured for each specimen. Exposure was conducted in closed and acid-cleaned polyethylene vessels and the specimens were completely immersed in the solution. For all tested conditions (solutions and time points), one blank sample without any specimen and triplicate samples (with individual specimens exposed in similar



conditions) were exposed. Phosphate buffered saline (PBS), adjusted with 50% ultrapure NaOH to pH 7.3±0.1, containing 8.77 g/L NaCl, 1.28 g/L Na<sub>2</sub>HPO<sub>4</sub>, and 1.36 g/L KH<sub>2</sub>PO<sub>4</sub> (all analytical grade), PBS with 2.67 or 10 g/L fibrinogen from bovine plasma (Fbn, Sigma Aldrich F8630, Sweden) and/or 40 g/L bovine serum albumin (BSA, Sigma Aldrich A7906, Sweden) were prepared in ultrapure water (resistivity of 18.2 MΩcm, Millipore, Sweden). All exposures were conducted in a Stuart platform-rocker incubator at 37±0.5 °C in dark conditions and agitated bi-linearly at 12° inclination and 22 cycles/min. Independent CoCrMo disks were exposed in five different single solutions for 4 and 24 h, compiled in Table 4-1. Sequential tests, in which half of the solution was exchanged after 5 h, are further schematically illustrated in Fig. 4-1. The two subsequent solutions are specified in Table 4-2 and the solution sampling was conducted after 1, 4, 6, and 24 h for each exposure vessel. After exposure, CoCrMo disks were separated from solutions, rinsed by ultrapure water, and dried by nitrogen gas. They were then stored in a desiccator (<10% relative humidity) before examination by means of light optical microscopy (LOM), scanning electron microscopy (SEM), energy dispersive X-ray spectroscopy (EDS) and X-ray photoelectron spectroscopy (XPS).

**Table 4-1: Single solution exposures and durations (without friction).**

Media	Duration
PBS, pH 7.2-7.4	4 h, 24 h
PBS+Fbn (10g/L), pH 7.2-7.4	4 h, 24 h
PBS+BSA (10g/L), pH 7.2-7.4	4 h, 24 h
PBS+Fbn (10g/L)+BSA (10g/L), pH 7.2-7.4	4 h, 24 h
PBS+Fbn (2.67g/L)+BSA (40g/L), pH 7.2-7.4	4 h, 24 h

The solution samples were acidified to a pH<2 with 65% ultrapure HNO<sub>3</sub> and stored frozen at -25 °C. All vessels were acid-cleaned in 10 % HNO<sub>3</sub> for at least 24 h, washed 4 times by ultrapure water, and dried in ambient conditions.

**Table 4-2: Sequential solution exposures (all sampled after 1, 4, 6, 24 h). The volumes shown are for tests without friction (static conditions). They were 45 mL (first solution) and 20 mL (second solution) in the case of the tests with friction (sliding conditions).**

First solution (10 mL)	Second solution (5 mL)
PBS, pH 7.2-7.4	PBS, pH 7.2-7.4
PBS+BSA (40 g/L), pH 7.2-7.4	PBS+BSA (40 g/L), pH 7.2-7.4
PBS+Fibrinogen (2.67 g/L), pH 7.2-7.4	PBS+Fibrinogen (2.67 g/L), pH 7.2-7.4
PBS+BSA (40 g/L), pH 7.2-7.4	PBS+Fibrinogen (5.34 g/L), pH 7.2-7.4

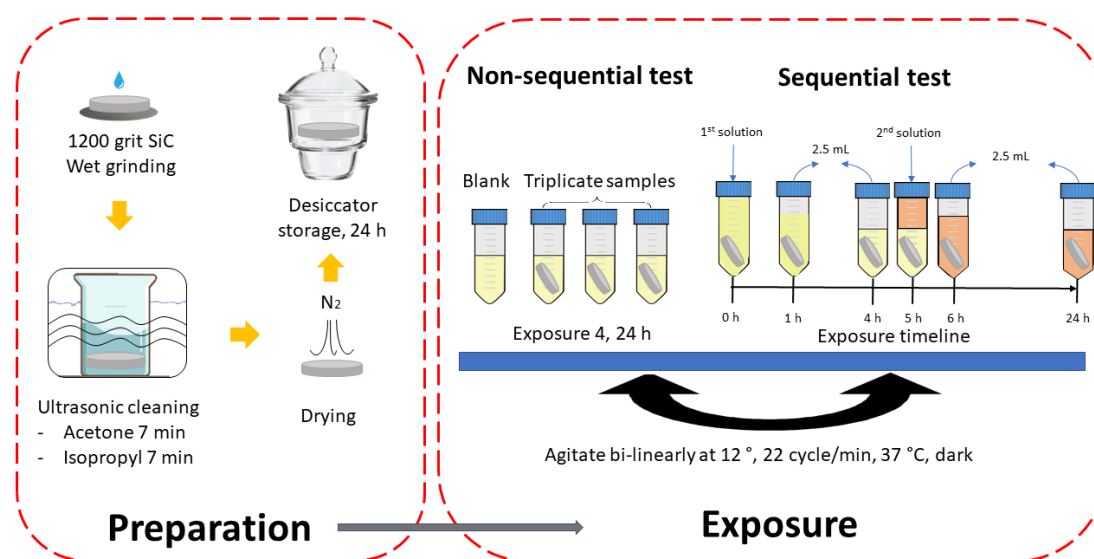


**Figure 4-1: Illustration of the non-sequential test procedure, and the sequential test procedure, for metal release testing in static conditions (without friction).**

**Conditions: 37 °C, bilinear agitation (22 cycles/minute, 12°), darkness.**

### 4.2.3 Metal Release Investigations under Sliding Conditions

Tests of CoCrMo disks under friction (sliding conditions) were performed in the form of a multidirectional test against a flat ultra-high molecular weight polyethylene (UHMWPE) pin (GUR® 1020) of 1.905 cm length and  $0.9525 \pm 0.005$  cm diameter, illustrated in Fig. 4-2. The applied load was set to 150 N, the frequency to 2 Hz and the stroke length to 7 mm on each sample. The contact pressure was 2.1 MPa, which is comparable to the 9 MPa in a CoCrMo-UHMWPE hip joint [27] and 150-fold higher than the contact pressure, for which an increase in friction coefficient was detected in the presence of metal-induced protein aggregates [28]. The test was run for 172,800 cycles (24 h). The CoCrMo disks were exposed to the sequential solutions specified in Table 4-2, with a total volume of 45 mL (first solution) and 20 mL (second solution). The specimens were completely immersed throughout the test. Four parallel measurements were conducted on a blank sample (without CoCrMo disk) and triplicate samples in a heated stainless steel holder and plastic container (PMMA) at  $37 \pm 3$  °C. This procedure was conducted four times for all four sequential solution in the same order as in Table 4-2 (starting with PBS). Prior to the first measurement and in between each measurement, the sample holders were cleaned with a liquid ultrasonic cleaning detergent for 10 minutes in an ultrasonic bath, then rinsed in deionized water three times for 3 minutes in an ultrasonic bath, then soaked in 95% methyl alcohol for 5 minutes and finally dried with nitrogen gas. The friction coefficient was monitored throughout the exposure, and solution samples were taken after 1, 4, 6, and 24 h (10 mL). The solution samples were further centrifuged using an Eppendorf centrifuge 5702 (3,000 relative centrifugal force for 10 min) and separated into supernatant (5 mL, denoted “top” in the following) and the remaining solution (5 mL, denoted “bottom” in the following). All solution samples were acidified to a  $\text{pH} < 2$  with 65% ultrapure  $\text{HNO}_3$  and stored frozen at  $-25$  °C.

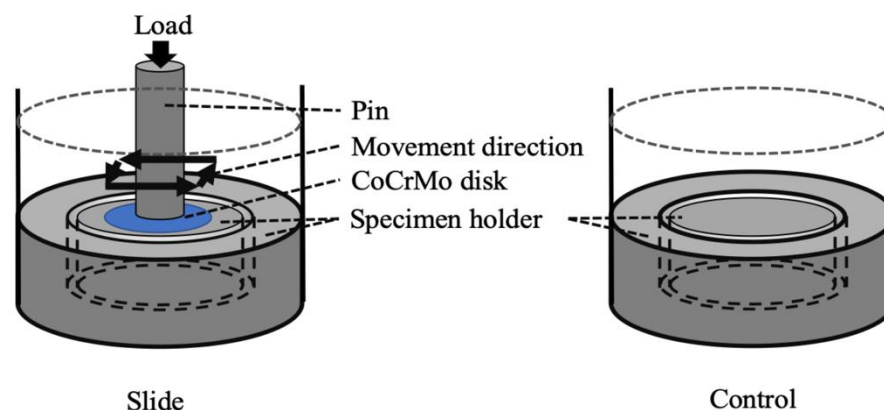


**Figure 4-2: Schematic illustration of the pin movement on the CoCrMo disk set-up for testing under sliding conditions.**

#### 4.2.4 Digestion

Prior to trace metal analysis, the solution samples were digested to avoid the formation of hydrogels in the protein-rich solution samples and a potential loss of analyte. After unfreezing, 2 mL of single solution samples (Table 4-1) or 2.5 mL of sequential solution samples (Table 4-2) and the top or bottom solution samples of the tests in sliding conditions were diluted with ultrapure water and at least 0.5 mL 30% ultrapure hydrogen peroxide to a total volume of approximately 10 mL. The samples were then digested using an UV digester (Metrohm 705 UV digester) at a temperature between 90 and 95 °C for several hours until the solutions were transparent and odorless. The final volume was recorded, and the dilution factor (DF) for each solution sample was calculated based on the recorded volume divided by the initial volume of the added sample solution. The measured concentration of each solution sample was then multiplied by the individual sample DF and further treated as described in the next section.

#### 4.2.5 Atomic Absorption Spectroscopy (AAS)

The amounts of Co, Cr and Mo in the solution samples were analyzed by means of graphite furnace atomic absorption spectroscopy, GF-AAS (Perkin Elmer AA800 analyst). Quality control samples of known concentrations were analyzed every fifth sample (after four regular solution samples). The calibration was based on one blank sample (1% ultrapure HNO<sub>3</sub>) and at least three Co, Cr, or Mo containing standards covering the sample concentration range. If the sample concentrations were higher than the calibration range, the samples were diluted and reanalyzed. Triplicate readings were performed for each solution sample. The limits of detection (based on three times the highest standard deviation of the blank values) were 1.7 µg/L Co, 1.2 µg/L Cr, and 0.9 µg/L Mo. The blank values were negligible (close to or below limits of detection) in the case of the tests in static conditions.

For metal release estimations from the tests in static conditions, the released metal amount per exposed specimen surface area (µg/cm<sup>2</sup>) was determined by averaging the concentrations of the triplicate samples, subtracting the blank sample concentrations from that, multiplying the value with the solution volume, and dividing the value by the specimen surface area. The solution volume was 10 mL for the single solution measurements (Table 4-1), and 10 mL for 1 h, 7.5 mL for 4 h, 10 mL for 6 h, and 7.5 mL for 24 h time points in the sequential tests (Table 4-2).

For the tests in sliding conditions, a significant amount of Co, Cr, and Mo was detected in the blank sample solutions due to the stainless steel holders in the test-setup, further described and discussed in the result and discussion sections. Therefore, these solutions were treated as samples and are denoted control in the following. The released amount of Co, Cr and Mo was calculated by multiplying the concentration value with the solution volume, and dividing the value by the surface area. The surface area was estimated to 50.98 cm<sup>2</sup> for the control samples (based on the stainless steel sample holder surface area in contact with the solution) and equally to 50.98 cm<sup>2</sup> for the CoCrMo disk specimens in the wear test (considering the contribution from the sample holder). The solution volume in the wear tests was 45 mL, 35 mL, 45 mL, and 35 mL, for 1, 4, 6, and 24 h time points, respectively.

## 4.2.6 X-Ray Photoelectron Spectroscopy (XPS)

X-ray photoelectron spectroscopy (XPS, Ultra DLD spectrometer, Kratos Analytical, Manchester, UK) was used to analyze the surface composition of the CoCrMo disks after exposure in static conditions (selected specimens). All measurements were performed on two separate surface areas of each disk, sized approximately  $300 \times 700 \mu\text{m}$  by using a monochromatic Al  $K_{\alpha}$  X-ray source (150W). The information depth was equal to, or less than, 10 nm. The measurements were based on the CoCrMo disks, which were exposed in static conditions to the four sequential solutions (Table 4-2) and on one non-exposed (only grinded, cleaned, and air-exposed) CoCrMo disk for reference. The pass energy used for detailed spectra was 20 eV, generated for Co 2p, Cr 2p, O 1s, N 1s, C 1s and Mo 3d. The C 1s binding energy at 285.0 eV was used as binding energy reference.

## 4.2.7 Statistical Calculations

In order to identify the statistical significance of any differences among conditions, a student's t-test of unpaired data with unequal variance was used in the software KaleidaGraph 4.0 for independent samples. The student's t-test of paired data was used for dependent samples (same CoCrMo disk but different time points). A p-value below 0.05 was considered as a statistically significant difference.

# 4.3 Results and Discussion

## 4.3.1 Non-Sequential Release of Metals in Static Conditions

The total amount of Co, Cr and Mo in solution samples after contact with the CoCrMo disks for 4 h and 24 h in PBS, PBS+10 g/L Fbn, PBS+10 g/L BSA, PBS+10 g/L BSA+10 g/L Fbn and PBS+40 g/L BSA+2.67 g/L Fbn are presented in Fig. 4-3. The released and non-precipitated amounts of Co, Cr and Mo increased in all cases with time, except for PBS+40 g/L BSA+2.67 g/L Fbn (not significant  $p=0.37$ ). Although the reduction in concentration of Co between the 4 h and 24 h in the solution PBS+40 g/L BSA+2.67 g/L Fbn was not statistically significant, there was a descending tendency. This may be caused by metal-protein complexation and concomitant agglomeration [6; 29], which can result in precipitation of metals from solution. Compared with PBS, there was no

statistically significant change for the released amounts of Co in the presence of albumin or fibrinogen after 4 and 24 h. According to previous results [30; 31], BSA would accelerate the corrosion of CoCrMo alloy in PBS solution. However, there was no detected increase in metal release in static conditions in this study. On the contrary, there was a significant decrease of released amount of Mo in the presence of albumin after 4 h. This phenomenon may be caused by precipitation of metals from solution. Clark and Williams [32] investigated the effects of proteins on metal corrosion.

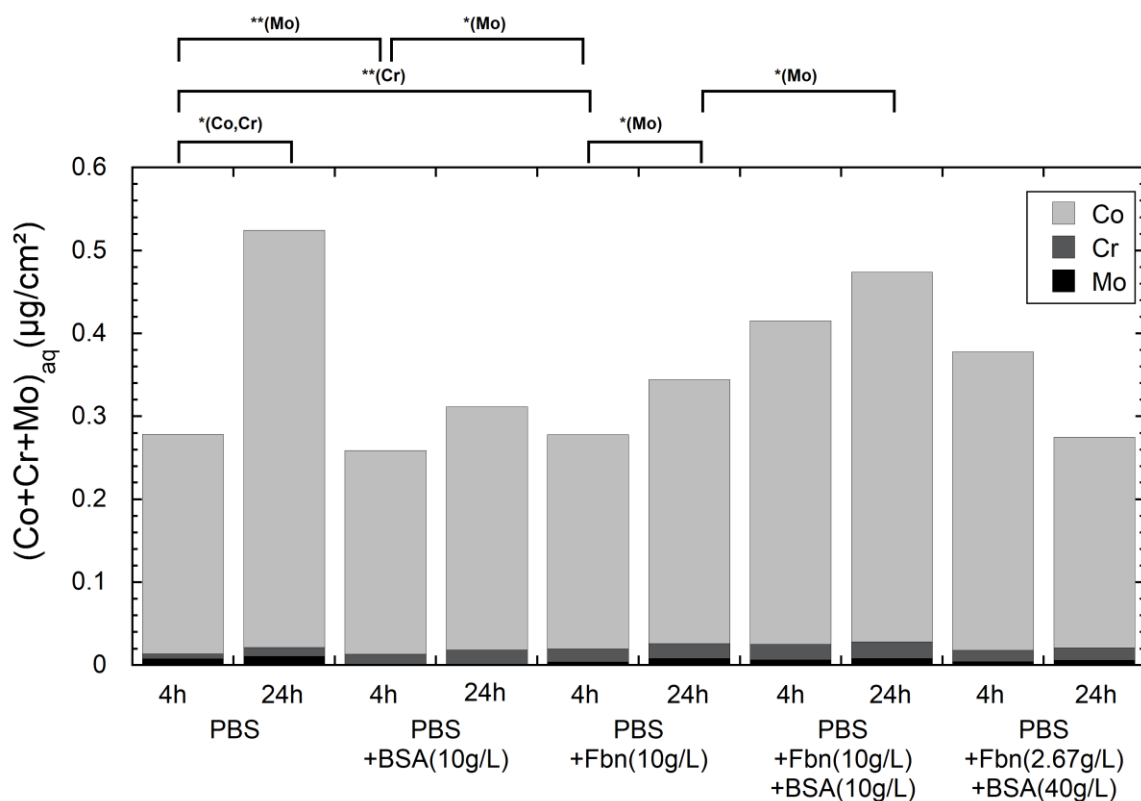


**Figure 4-3: Released and non-precipitated amounts ( $\mu\text{g}/\text{cm}^2$ ) of Co, Cr and Mo in solution from CoCrMo disks exposed to PBS, PBS+BSA (10g/L), PBS+Fbn (10g/L), PBS+Fbn (10g/L)+BSA(10g/L) or PBS+Fbn (2.67g/L)+BSA (40g/L) at pH 7.2-7.4 after 4 h and 24 h at 37 °C. Significant differences are indicated by asterisks: \*  $p < 0.05$ , \*\* $p < 0.01$ ;  $n = 3$ .**

They showed that both BSA and Fbn could accelerate the dissolution of Co and Cr from pure cobalt and chromium metal powders compared with saline alone, while the opposite

(inhibited dissolution) was the case for Mo powder, which dissolved at a significantly higher rate than the Co and Cr powder. As discussed further below, this different influence of proteins on Co, Cr, and Mo release (and precipitation) might be explained by the fact that Cr and Co are binding to proteins, while Mo (which is released as negatively charged molybdate ion) is most probably not binding to proteins. In static conditions, the measured amounts of metals in solution were relatively similar in all these different solutions. These findings are different compared with findings for the sequential solutions (next section), but similar to previous findings in similar exposure conditions [33].

#### 4.3.2 Sequential Release of Metals in Static Conditions

The released and non-precipitated amounts of Co, Cr and Mo in four sequential solutions are shown in Fig. 4-4. The released amount of Co (Fig. 4-4a), Cr (Fig. 4-4b) and Mo (Fig. 4-4c) in the first sequential solution, which was PBS followed by PBS (“PBS, PBS”), was slightly higher than the other three protein-containing solutions.



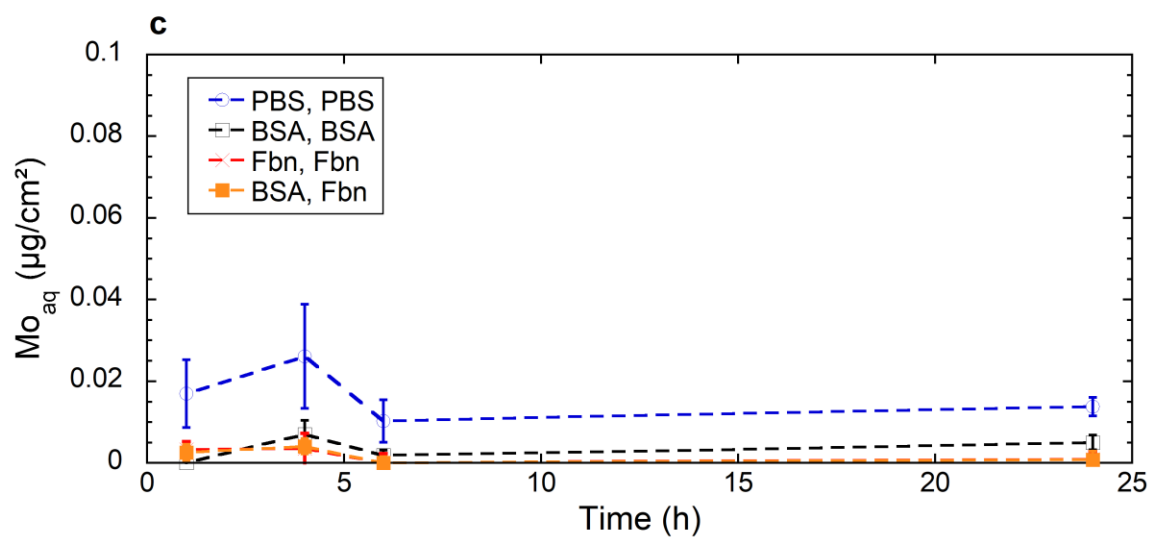
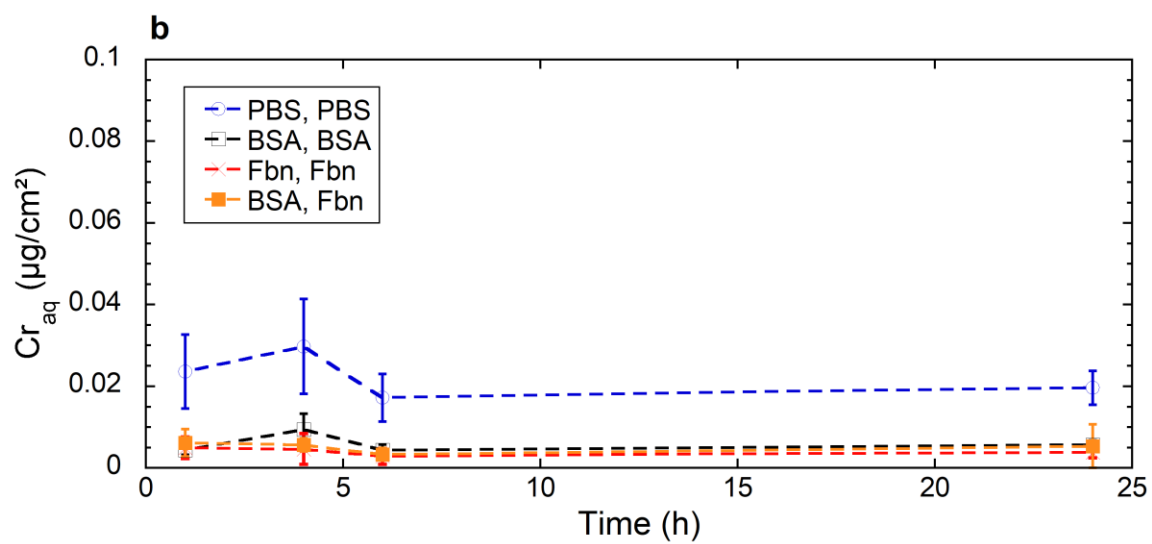
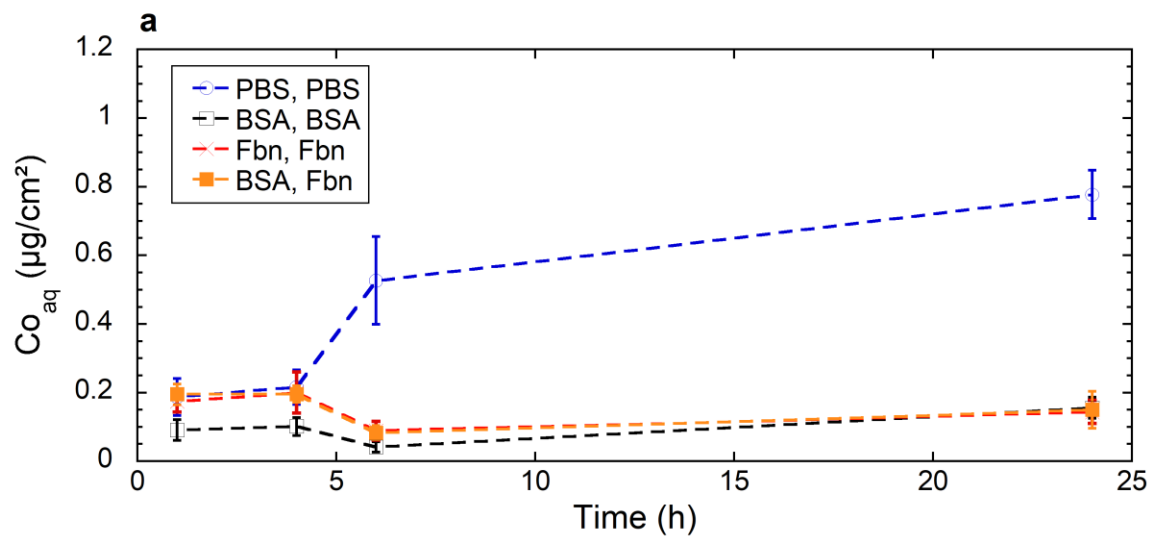


**Figure 4-4: Released and non-precipitated amounts of Co (a), Cr (b) and Mo (c) in solution from disks of a CoCrMo alloy exposed to four sequential solutions (pH 7.2-7.4); PBS followed by PBS (PBS, PBS), PBS+ 40 g/L BSA followed by PBS+40 g/L BSA (BSA, BSA), PBS+2.67 g/L Fbn followed by PBS+2.67 g/L Fbn (Fbn, Fbn), and PBS+ 40 g/L BSA followed by 2.67 g/L Fbn (BSA, Fbn); exposed at 37 °C and sampled after 1, 4, 6 and 24 h. The second solution was added after 5 h. The error bars show the standard deviation of independent triplicate disks.**

The released amount of Co, Cr and Mo was almost similar in the three protein-containing sequential solutions (“BSA, BSA”, “Fbn, Fbn” and “BSA, Fbn”). The concentration of Co in solution increased with time only in the “PBS, PBS” sequence, but not for the protein-containing solutions, Fig. 4-4a. This phenomenon could either indicate that there is a protective (hindering) effect of the proteins or that released metals are preferentially bound to proteins that precipitate from solution or cover the surface of the CoCrMo disk. This effect is also most probably influenced by the experimental set-up (Fig. 4-1), since all solution samples were pipetted from the top of the tubes, as in a previous study on stainless steel [22]. Protein aggregates were obviously visible on the CoCrMo surfaces, which have been immersed in the Fbn-containing solutions, Fig. 4-5.

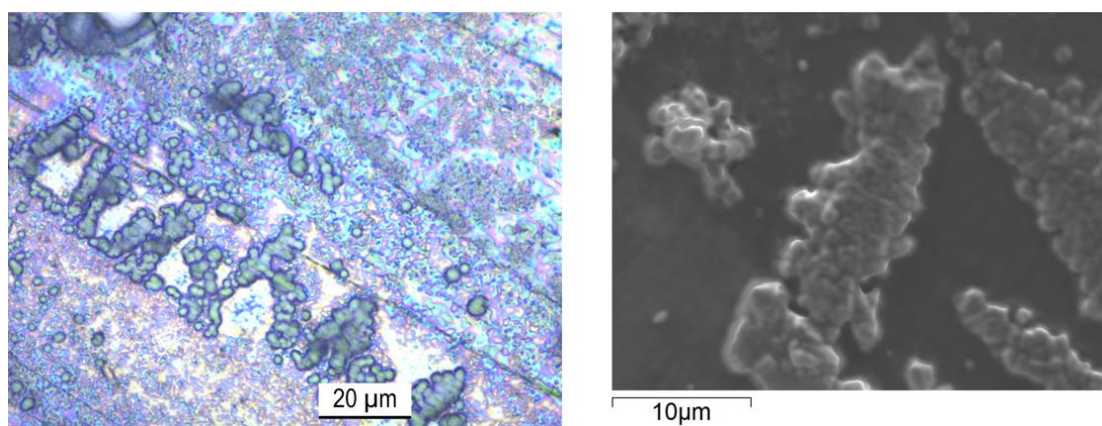


**Figure 4-5: Representative LOM (left) and SEM (right) micrographs of a CoCrMo disk, which was exposed to PBS with Fbn (10 g/L) for 24 h in static conditions.**

The composition of these aggregates was confirmed as protein-originating (nitrogen, carbon, oxygen, and solution components, no main alloying elements) by energy dispersive X-ray spectroscopy, Table 4-3.

**Table 4-3: EDS results of CoCrMo disks exposed to PBS with 10 g/L Fbn for 24 h, with a spot focus on the protein aggregates.**

	C (wt.%)	N (wt.%)	O (wt.%)	Na (wt.%)	P (wt.%)	Cl (wt.%)
CoCrMo	32	6.2	5.6	27	1.5	29

#### 4.3.3 Surface Characterization after Sequential Exposure in Static Conditions

The investigated outermost surface of CoCrMo revealed oxidized (deriving from oxides, hydroxides or oxyhydroxides) metal peaks in addition to common peaks deriving from adventitious carbon (contamination from the air). The relative metal composition (based on the mass of oxidized metals) of the outermost ( $\leq 10$  nm) surface (hydr)oxide of CoCrMo disks after grinding (1200 grit SiC paper) and after exposure to the four sequential solutions for 24 h in static conditions is shown in Fig. 4-6, with binding energies and assignments shown in Table 4-4.

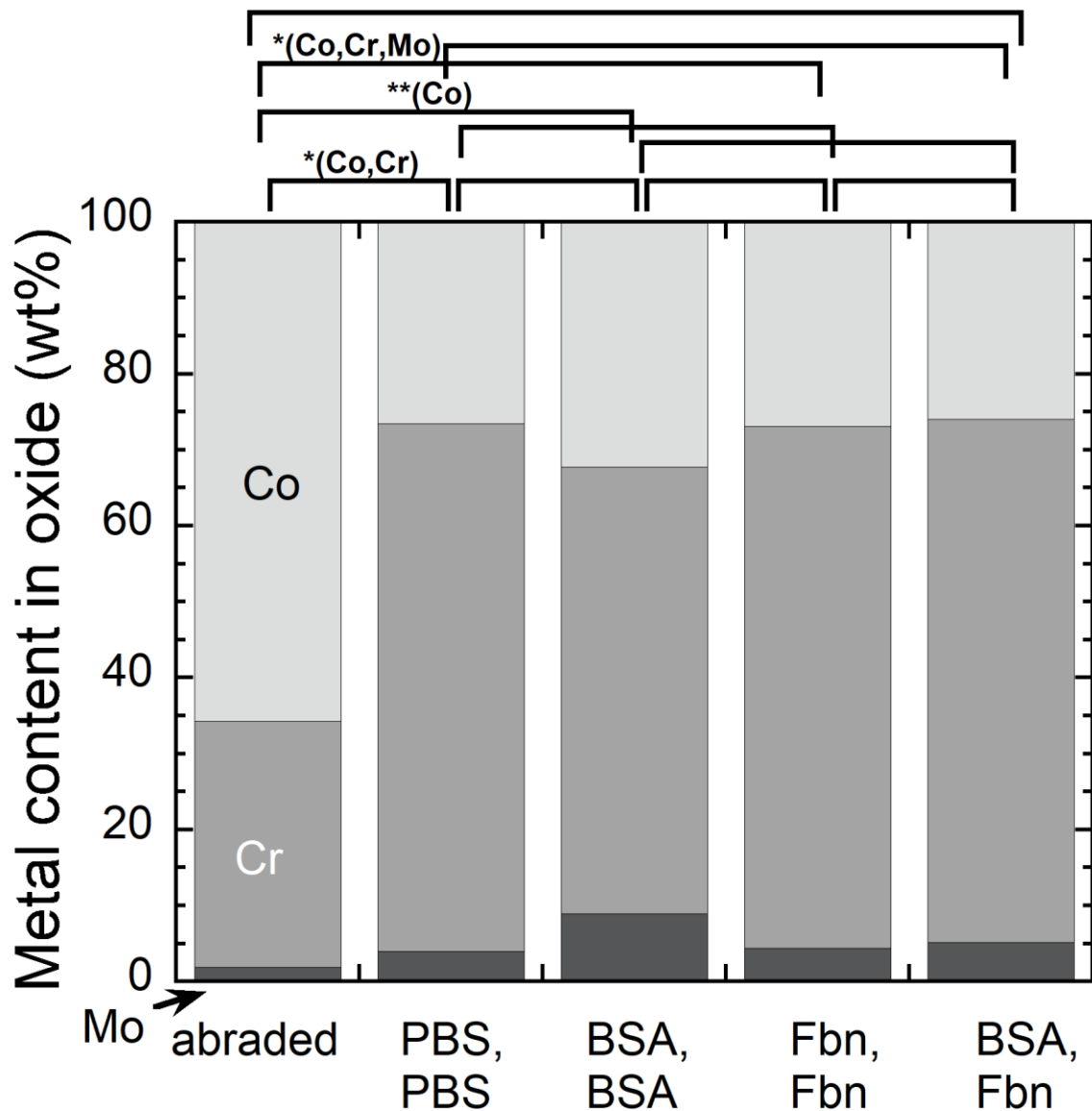


**Figure 4-6: Relative metal content in the outermost surface oxide of the CoCrMo alloy being abraded (as non-exposed reference) and exposed to four sequential solutions (pH 7.2-7.4); PBS followed by PBS (PBS, PBS), PBS+ 40 g/L BSA followed by PBS+40 g/L BSA (BSA, BSA), PBS+2.67 g/L Fbn followed by PBS+2.67 g/L Fbn (Fbn, Fbn), and PBS+ 40 g/L BSA followed by 2.67 g/L Fbn (BSA, Fbn); exposed at 37 °C for 24 h; studies by means of X-ray photoelectron spectroscopy; statistically significant differences are indicated by asterisks: \*  $p < 0.05$ , \*\*  $p < 0.01$ ;  $n = 2$ .**

**Table 4-4: Observed binding energies and assignments of Co, Cr, Mo, N, C and O of the outermost surface of CoCrMo disks based on X-ray photoelectron spectroscopy (XPS) measurements [34; 35].**

Sample	Binding energy <sup>a</sup> (eV)	Assignment
Co 2p <sub>3/2</sub>	778.8±0.16	Co metal
	782.3±2.3	Oxidized Co
Cr 2p <sub>3/2</sub>	574.6±0.16	Cr metal
	577.7±0.8	Cr(III)
Mo 3d	228.2±0.2, 231.3±0.2	Mo metal
	232.6±0.3, 235.8±0.1	MoO <sub>3</sub>
N 1s	394.4±0.07(only detected if no BSA present)	Metal nitride
	399.5±0.9	Amine/amide species
C 1s	285.0	C-C, C-H bonds
	286.7±0.2	C-N, C-O bonds
	288.5±0.3	C=C-O, O=C-N bonds
O 1s	530.7±0.3	Lattice oxide
	531.8±0.3	Hydroxide, hydrated, or defective oxide
	533.2±0.3	Water, organic oxide

<sup>a</sup>all binding energies normalized to C 1s at 285.0 eV

The surface (hydr)oxide was composed of oxidized cobalt (Co 2p<sub>3/2</sub> at 782.3 ± 2.3 eV), Cr (Cr 2p<sub>3/2</sub> at 577.7 ± 0.8 eV corresponding to CrIII) and Mo (Mo 3d at 232.6 ± 0.3 and 235.8 ± 0.1 eV corresponding to MoO<sub>3</sub>). All exposed CoCrMo surfaces showed an enrichment of Cr, a reduced amount of Co, and an increased amount of Mo in the surface (hydr)oxide. Compared with the non-exposed CoCrMo reference, there was an enrichment of Cr (p<0.05) in the surface (hydr)oxide exposed to “PBS, PBS”. It is in agreement with previous findings [33; 36] that the (hydr)oxide film is mainly composed of Cr<sub>2</sub>O<sub>3</sub> and that Mo and Co oxides contribute less. There was no significant difference among the specimens exposed in the four different sequential solutions. Note that phosphorus wasn't investigated in this study, but is likely to be incorporated as phosphate in the surface (hydr)oxide after exposure to PBS [37].

#### 4.3.4 Sequential Release of Metal under Sliding Conditions

Fig. 4-7 shows released and non-precipitated amounts of Co (Fig. 4-7a), Cr (Fig. 4-7b) and Mo (Fig. 4-7c) under sliding conditions compared with control samples, for which the released metals derive from the specimen holders and not the specimens. Fig. 4-7 further compares sliding conditions with static conditions (“non-slide”) after 24 h.

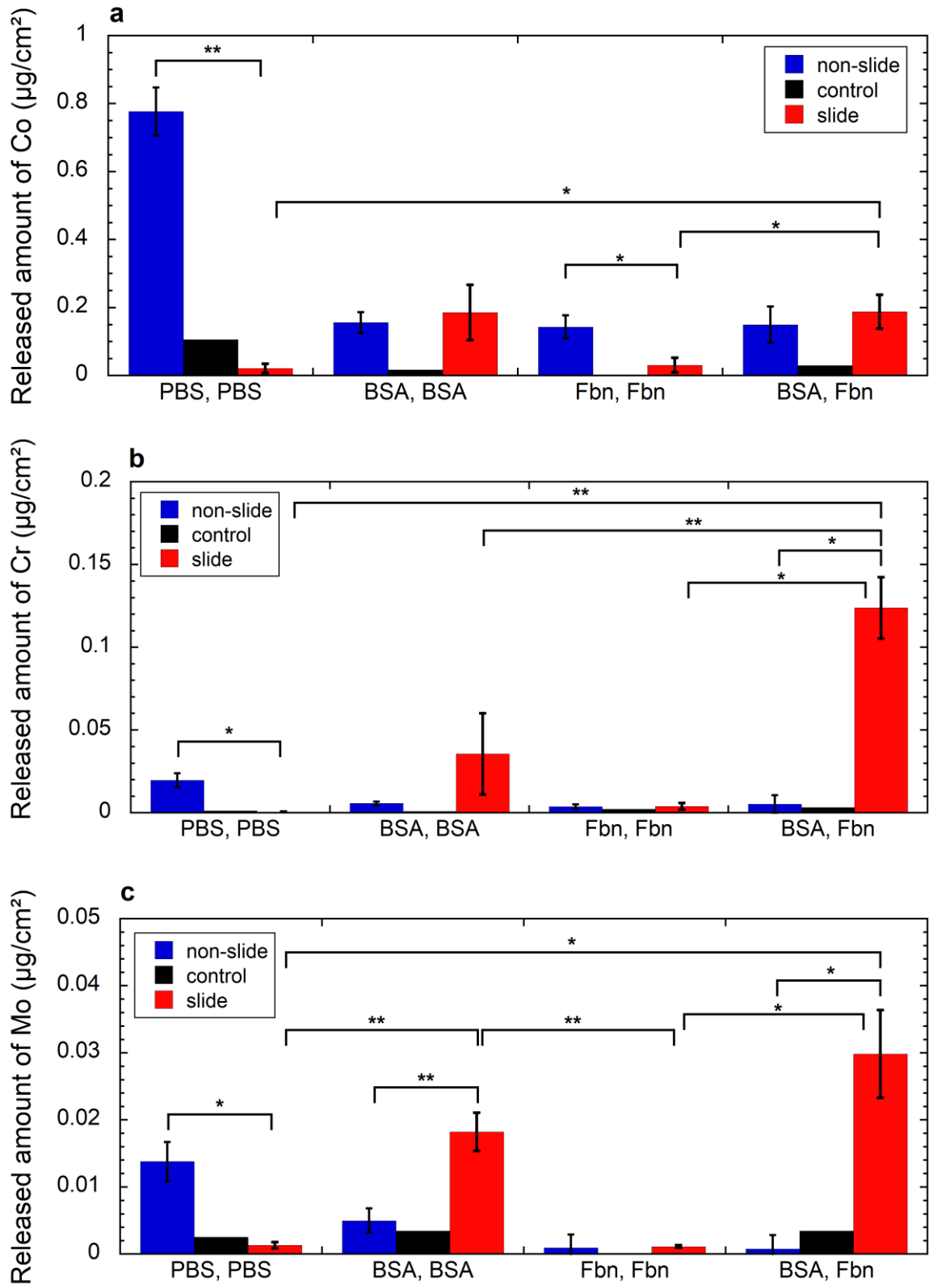


**Figure 4-7: Released and non-precipitated amounts of Co (a), Cr (b) and Mo (b) in solution from disks of CoCrMo alloy exposed to four solutions under sliding (slide) and non-sliding (non-slide) conditions (pH 7.2-7.4); PBS followed by PBS (PBS, PBS), PBS+40 g/L BSA followed by PBS+40 g/L BSA (BSA, BSA), PBS+2.67 g/L Fbn followed by PBS+2.67 g/L Fbn (Fbn, Fbn), and PBS+ 40 g/L BSA followed by 2.67 g/L Fbn (BSA, Fbn); exposed at 37 °C and sampled after 24 h. The control denotes the background control in the test-setup under sliding conditions (Fig. 4-2).**

**The error bars show the standard deviation of independent triplicate disks.**

**Significant differences are indicated by asterisks: \*  $p < 0.05$ , \*\* $p < 0.01$ ;  $n = 3$ .**

The specimen holders, which were made of stainless steel (confirmed by energy dispersive X-ray spectroscopy), released all three metals to some extent. This points towards contamination from previous runs (involving both CoCrMo materials and phosphate-containing solutions) and an insufficient cleaning procedure. The cleaning procedure was a detergent and organic solvent-based method using ultrasound and several rinsing steps. The cleaning procedure was designed to remove proteins but to keep the surface oxide, possibly including metal contaminants, of stainless steel intact.

The released and non-precipitated amounts of metals in PBS solutions under sliding conditions were significantly lower ( $p < 0.05$ ) than under static conditions, and even lower than the control sample (with the only contribution deriving from the specimen holder). This phenomenon may be caused by the locally increased surface pH outside the sliding surfaces, and consequently corrosion product deposition [38]. The reduced release of Co was also statistically significant in the “Fbn, Fbn” sequence under sliding as compared to static conditions, Fig.4-7a. These phenomena were probably caused by the formation and removal of metal-protein aggregates and wear particles from the contact area, as supported by an earlier found rapid decrease in friction coefficient due to removal of protein aggregates from the contact area in a similar test rig [28]. We speculate that the precipitation processes could have been accelerated under sliding conditions (either due to the increase of pH outside of the wear track or due to increased protein aggregation, or both). This is supported by the observation that the control included higher amounts of aqueous cobalt as compared to the solution in contact with the CoCrMo specimen under



sliding conditions in the “PBS, PBS” solution. In the BSA-containing solutions, the released amount of Cr was greater than control samples and samples exposed under static conditions, Fig.4-7b. This agrees with a previous study [39], which showed that tribocorrosion and fretting corrosion could induce the formation of particles, which contain more chromium. Also, these Cr and phosphate-enriched particles were mainly found in the synovial fluid [39]. The released amount of Cr in the mixed protein containing solutions, as compared to single protein solutions, was statistically significant higher, further discussed in the section ‘Vroman effect’. The released amount of Mo in the BSA-containing solutions was higher than in static conditions and for control samples, Fig.4-7c. This observation is likely explained by an increased metal release in the BSA-containing solutions and reduced binding of molybdate ions to precipitating proteins as compared to CrIII and CoII ions. It is clear that CrIII and CoII ions bind strongly (irreversibly) to albumin [6-9], however molybdate ions have also been found to bind to albumin under certain conditions, but only at certain potential values and in a reversible manner [25; 26]. A previous study investigating the release of Co, Cr, and Mo from CoCrMo in PBS and PBS+36 g/L BSA at no applied potential in static and sliding conditions, after shorter time periods than investigated in this study, revealed a significant increase for all three metals in both PBS and PBS+36g/L BSA under sliding as compared to static conditions, and in the presence of BSA as compared to PBS alone [31].

The coefficient of friction during the 24 h exposures under sliding conditions is shown in Fig. 4-8.

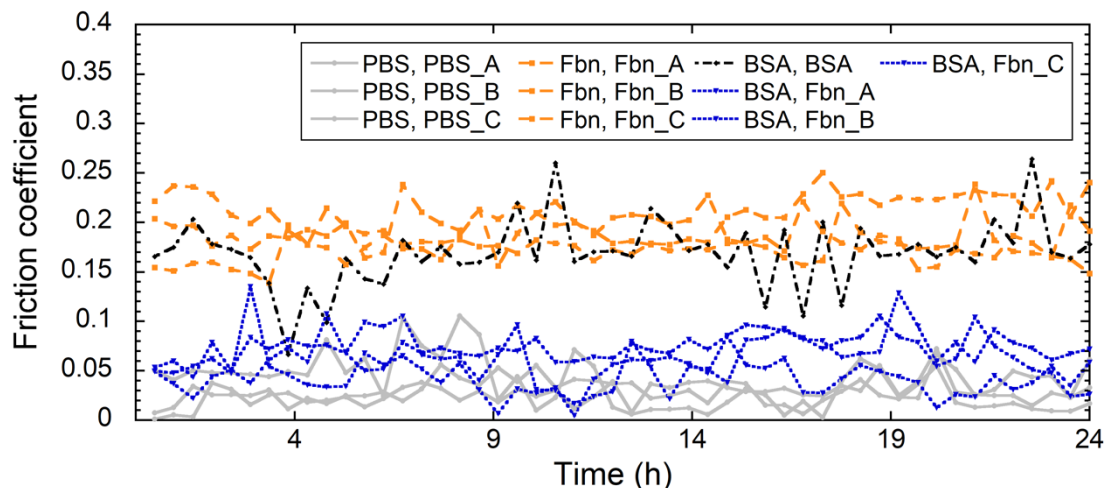


**Figure 4-8: Changes in coefficient of friction under sliding conditions. A, B, C denotes different replicate measurements. Only one data set available for “BSA, BSA”.**

The coefficient of friction of the “Fbn, Fbn” sequence was clearly larger than for the other sequential exposures. The coefficient of friction of “PBS, PBS” was the smallest among the solutions. According to previous findings [40], the surface roughness is expected to decrease with the adsorption of BSA and Fbn, and the roughness after adsorption of Fbn should be lower than after adsorption of BSA. Similarly, a rougher surface for stainless steel was observed in PBS as compared to a whey protein solution in a previous study under sliding conditions [41]. The surface roughness is not expected to be the most important factor for the true contact area, but the softness of the surface is important, as the hardness of the softer surface is indirectly proportional to the true surface area [42]. It is expected that the protein layers might be softer than the UHMWPE counter surface and that Fbn forms a thicker layer as compared to BSA (c.f. Fig. 4-5), which hence increases the contact area and the coefficient of friction. The effect of BSA remains unclear from the friction measurements, since only one data set of the friction coefficient was available for the sequence “BSA, BSA”. The sequence “BSA, Fbn” was resulting in significantly lower coefficients of friction as compared to “Fbn, Fbn” and it is unclear whether this is caused by a thinner adsorbed layer in the mixed solution [24] or another reason. Previous studies also highlighted the ability of protein layers to entrap wear particles [43; 44], which could increase the overall wear.

### 4.3.5 Influence of Metal Precipitation

In order to investigate the effect of metal precipitation for measurements under the sliding conditions, the mass ratios of Co, Cr, and Mo between the bottom and top part of collected solution samples after centrifugation was evaluated, Fig. 4-9. If this ratio is 1, no precipitation is expected, as the metals would be present as ions or soluble species. In most cases, however, the mass ratios were above one, which means that the metals were enriched in the bottom of the centrifuge tube. This was more pronounced for protein-containing solutions than for PBS alone in the case of Co and Cr. CrIII is expected to bind more efficiently to proteins as compared to CoII and molybdate [10; 45], and this is clearly indicated by the mass ratios, Fig. 4-9. Cr is initially more preferentially found in the heavier bottom part of the centrifuge tubes as compared to Co – especially for protein-containing solutions, Figs. 4-9a and 4-9b. In contrast, Mo is initially found more preferentially in the top part of the centrifuge tubes (ratio is lower than 1), which indicates repulsion from protein aggregates or wear particles, Fig 4-9c. This could be due to similar charge of molybdate ions, wear particles, and proteins. After longer exposure time, however, Mo is found more preferentially in the bottom part of the centrifuge tubes in the case of the protein-containing solutions.

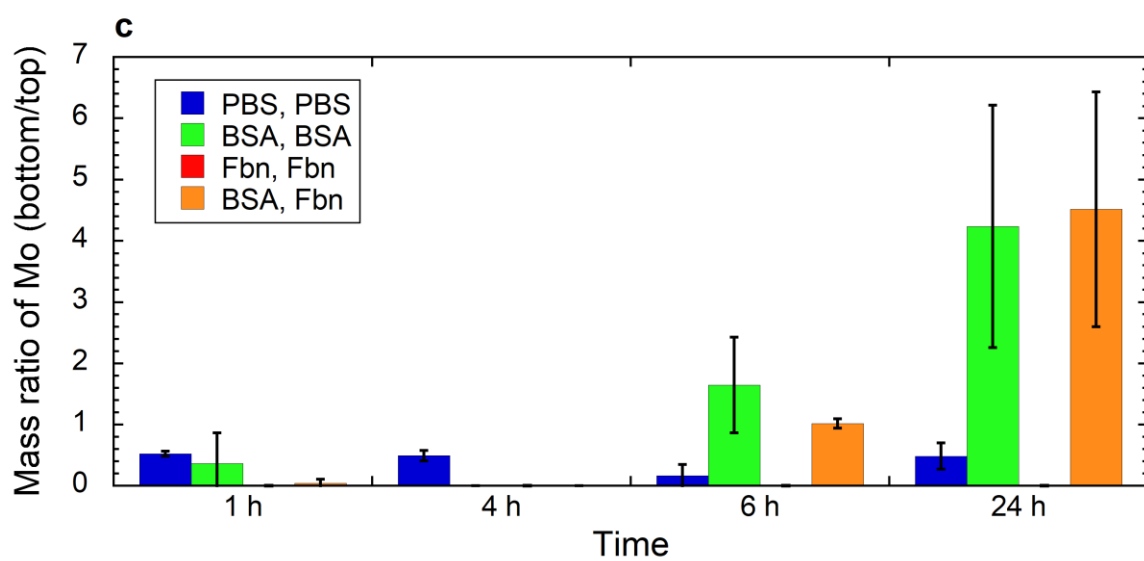
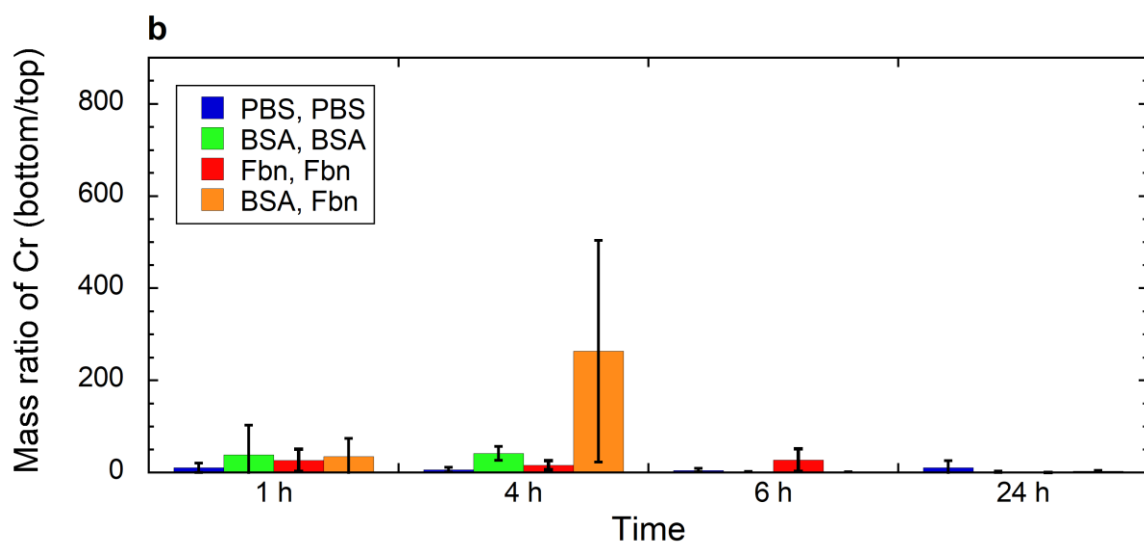
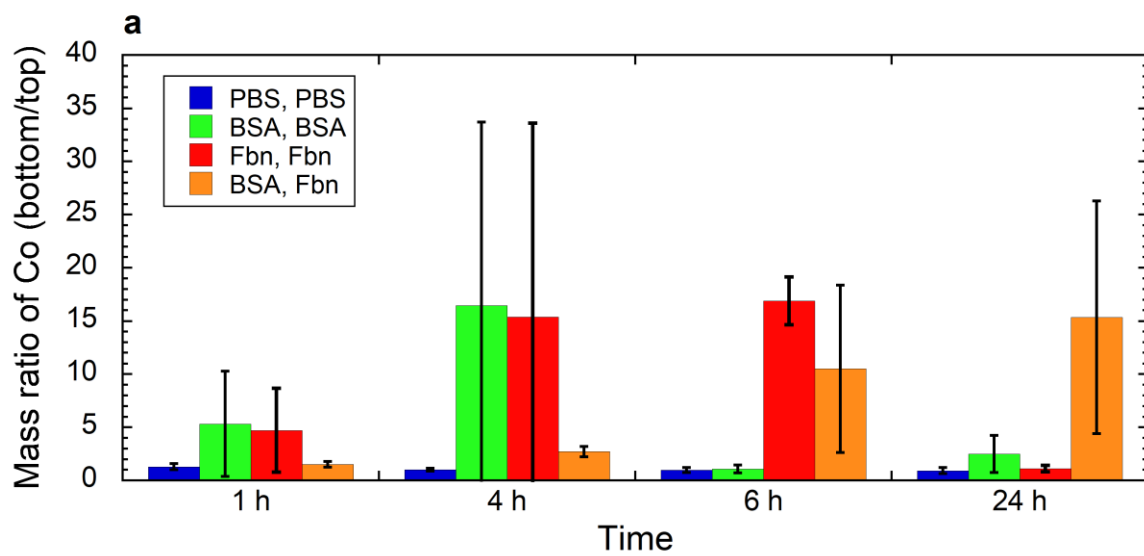


**Figure 4-9: The mass ratios of Co (a), Cr (b) and Mo (c) between the bottom and top part of collected solution samples (under sliding conditions) after centrifugation.**

**The Mo values that are equal to zero mean that the bottom fraction was non-detectable. The bottom part of the centrifuge tube contains heavier constituents (wear particles, protein aggregates), if present, compared to the top part of the centrifuge tube.**

It was clearly indicated that the experimental conditions induced metal precipitation, which explains why the released amounts of metals were lower under sliding conditions as compared to static conditions and control samples. It can hence be concluded from our experimental data that PBS and protein-containing solutions pose a risk to underestimating the release of especially Co and Cr from CoCrMo under sliding and static conditions.

#### 4.3.6 Vroman effect

A previous study on stainless steel 316L in a similar test setup in static conditions revealed significantly increased metal release in solutions containing first BSA and then Fbn, as compared to single protein solutions [22]. In this study on CoCrMo, we did not find an increase. Although this effect could have been overshadowed by the strong metal precipitation in this study, we did also not detect any difference in surface oxide composition by means of XPS. However, in sliding conditions, there was an increase of released Cr in the mixed protein solution as compared to single protein solutions. From this study alone, no conclusion can be drawn on the Vroman effect.

#### 4.3.7 Significance, Limitation, and Future directions

This work showed the influence of protein aggregation on accurate interpretations of metal release studies. The true released amount of metals can be underestimated due to protein aggregation and precipitation of protein aggregates and solidified metal species, especially when exploring the metal release in protein-containing solutions.

The main limitation of this study was the experimental setup for the tests under sliding condition. There was a significant released amount of metals in the control solution

samples, which was caused by contamination from the stainless steel holders. Future studies should focus on combining different surface analytical, electrochemical, and solution analytical methods to investigate and compare physical (wear), electrochemical and other chemical degradation processes simultaneously. Also, protein aggregation and precipitation processes should be quantified and accounted for.

## 4.4 Conclusions

This study aimed at investigating the effect of different proteins (albumin and fibrinogen) on metal release from CoCrMo in static and sliding conditions. The following main conclusions were drawn:

1. PBS and proteins could induce significant precipitation of metals and protein aggregates, which resulted in strong underestimation of released metals, especially under sliding conditions and for released Co and Cr. This effect was minor for released Mo.
2. The released amounts of metals increased with time under static conditions, except for solutions containing high protein concentrations (due to increased precipitation).
3. Cr was strongly enriched in the surface oxide of CoCrMo in all solutions, and this was accompanied by metal release dominated by Co.
4. Protein aggregates were found to precipitate on the surface of CoCrMo under static conditions.
5. Compared with static conditions, the amount of measurable (non-precipitated) released metals under sliding conditions was lower in PBS and Fbn, but higher in BSA-containing solutions.
6. The friction coefficient was clearly greater in the solution containing only fibrinogen as compared to PBS.

## 4.5 References

- [1] Ren, F., et al. "Fabrication, Tribological and Corrosion Behaviors of Ultra-Fine Grained Co–28cr–6mo Alloy for Biomedical Applications." *journal of the mechanical behavior of biomedical materials*, vol. 60, 2016, pp. 139-147.
- [2] Gilbert, J. "Corrosion in the Human Body: Metallic Implants in the Complex Body Environment." *Corrosion*, vol. 73, no. 12, 2017, pp. 1478-1495.
- [3] Landolt, D., et al. "Electrochemical Methods in Tribocorrosion: A Critical Appraisal." *Electrochimica Acta*, vol. 46, no. 24-25, 2001, pp. 3913-3929.
- [4] Hedberg, Y. S., et al. "Role of Proteins in the Degradation of Relatively Inert Alloys in the Human Body." *npj Materials Degradation*, vol. 2, 2018, p. 26.
- [5] Shenoy, A. A., et al. "Nontribological Corrosion Modes Dominate Wrought CoCrMo Acetabular Taper Corrosion: A Retrieval Study." *Journal of Biomedical Materials Research Part B: Applied Biomaterials*, vol. 109, no. 12, 2021, pp. 2000-2013.
- [6] Yang, J., et al. "Competitive Binding of Chromium, Cobalt and Nickel to Serum Proteins." *Biomaterials*, vol. 15, no. 4, 1994, pp. 262-268.
- [7] Friedberg, F. "Effects of Metal Binding on Protein Structure." *Quarterly Reviews of Biophysics*, vol. 7, no. 01, 1974, pp. 1-33.
- [8] Paustenbach, D. J., et al. "A Review of the Health Hazards Posed by Cobalt." *Critical reviews in toxicology*, vol. 43, no. 4, 2013, pp. 316-362.
- [9] Bal, W., et al. "Binding of Transition Metal Ions to Albumin: Sites, Affinities and Rates." *Biochimica et Biophysica Acta (BBA)-General Subjects*, vol. 1830, no. 12, 2013, pp. 5444-5455.
- [10] Hedberg, Y. S., et al. "Synergistic Effects of Metal-Induced Aggregation of Human Serum Albumin." *Colloids and Surfaces B: Biointerfaces*, vol. 173, 2019, pp. 751-758.

- [11] Österberg, R., et al. "Cr (III)-Induced Polymerization of Human Albumin." *Biological Trace Element Research*, vol. 3, no. 3, 1981, pp. 157-167.
- [12] Sargeant, A., et al. "Hip Implants—Paper VI—Ion Concentrations." *Materials & Design*, vol. 28, no. 1, 2007, pp. 155-171.
- [13] Münch, H. J., et al. "The Association between Metal Allergy, Total Knee Arthroplasty, and Revision." *Acta orthopaedica*, vol. 86, no. 3, 2015, pp. 378-383.
- [14] Noli, F., et al. "Neutron Activation Analysis for Determination of Metal Ions in Biological Fluids of Patients after CoCrMo Arthroplasty." *Journal of Radioanalytical and Nuclear Chemistry*, vol. 322, 2019, pp. 621-628.
- [15] Roos, P. M., et al. "Metals in Motor Neuron Diseases." *Experimental Biology and Medicine*, vol. 231, no. 9, 2006, pp. 1481-1487.
- [16] Roos, P. M., et al. "Metal Concentrations in Cerebrospinal Fluid and Blood Plasma from Patients with Amyotrophic Lateral Sclerosis." *Biological Trace Element Research*, vol. 151, no. 2, 2013, pp. 159-170.
- [17] Cortizo, M. C., et al. "Metallic Dental Material Biocompatibility in Osteoblastlike Cells." *Biological Trace Element Research*, vol. 100, no. 2, 2004, pp. 151-168.
- [18] Koronfel, M. A., et al. "Understanding the Reactivity of CoCrMo-Implant Wear Particles." *npj Materials Degradation*, vol. 2, no. 1, 2018, p. 8.
- [19] Hedberg, Y. S., et al. "Correlation between Surface Physicochemical Properties and the Release of Iron from Stainless Steel AISI 304 in Biological Media." *Colloids and Surfaces B: Biointerfaces*, vol. 122, 2014, pp. 216-222.
- [20] Hirsh, S. L., et al. "The Vroman Effect: Competitive Protein Exchange with Dynamic Multilayer Protein Aggregates." *Colloids and Surfaces B: Biointerfaces*, vol. 103, 2013, pp. 395-404.



- [21] Schricker, S. R., et al. "Modulating Protein Adhesion and Conformation with Block Copolymer Surfaces." *Handbook of Nanomaterials Properties*, Springer, 2014, pp. 1343-1376.
- [22] Hedberg, Y. S., et al. "Interaction of Albumin and Fibrinogen with Stainless Steel - Influence of Sequential Exposure and Protein Aggregation on Metal Release and Corrosion Resistance." *Corrosion*, vol. 73, no. 12, 2017, pp. 1423-1436.
- [23] Myant, C. W., et al. "The Effect of Transient Conditions on Synovial Fluid Protein Aggregation Lubrication." *Journal of the mechanical behavior of biomedical materials*, vol. 34, 2014, pp. 349-357.
- [24] Parkes, M., et al. "Synovial Fluid Lubrication: The Effect of Protein Interactions on Adsorbed and Lubricating Films." *Biotribology*, vol. 1, 2015, pp. 51-60.
- [25] Martin, E. J., et al. "Dominant Role of Molybdenum in the Electrochemical Deposition of Biological Macromolecules on Metallic Surfaces." *Langmuir*, vol. 29, no. 15, 2013, pp. 4813-4822.
- [26] Martin, E. J., et al. "Viscoelastic Properties of Electrochemically Deposited Protein/Metal Complexes." *Langmuir*, vol. 31, no. 13, 2015, pp. 4008-4017.
- [27] Fialho, J. C., et al. "Computational Hip Joint Simulator for Wear and Heat Generation." *Journal of Biomechanics*, vol. 40, no. 11, 2007, pp. 2358-2366.
- [28] Hedberg, Y. S., et al. "Can Cobalt(II) and Chromium(III) Ions Released from Joint Prostheses Influence the Friction Coefficient?" *ACS Biomaterials Science & Engineering*, vol. 1, no. 8, 2015, pp. 617-620.
- [29] Hedberg, Y. S., et al. "Metal Release and Speciation of Released Chromium from a Biomedical CoCrMo Alloy into Simulated Physiologically Relevant Solutions." *Journal of Biomedical Materials Research Part B: Applied Biomaterials*, vol. 102, no. 4, 2014, pp. 693-699.

- [30] Yan, Y., et al. "Study of the Tribocorrosion Behaviors of Albumin on a Cobalt-Based Alloy Using Scanning Kelvin Probe Force Microscopy and Atomic Force Microscopy." *Electrochemistry Communications*, vol. 64, 2016, pp. 61-64.
- [31] Espallargas, N., et al. "A Metal Ion Release Study of CoCrMo Exposed to Corrosion and Tribocorrosion Conditions in Simulated Body Fluids." *Wear*, vol. 332, 2015, pp. 669-678.
- [32] Clark, G. C. F., et al. "The Effects of Proteins on Metallic Corrosion." *Journal of biomedical materials research*, vol. 16, no. 2, 1982, pp. 125-134.
- [33] Wei, Z., et al. "Can Gamma Irradiation During Radiotherapy Influence the Metal Release Process for Biomedical CoCrMo and 316l Alloys?" *Journal of Biomedical Materials Part B*, vol. 106, no. 7, 2018, pp. 2673-2680.
- [34] Biesinger, M. C., et al. "Resolving Surface Chemical States in Xps Analysis of First Row Transition Metals, Oxides and Hydroxides: Cr, Mn, Fe, Co and Ni." *Applied Surface Science*, vol. 257, no. 7, 2011, pp. 2717-2730.
- [35] Naumkin, A. V., et al. *NIST X-Ray Photoelectron Spectroscopy Database, Version 4.1*, 2012. National Institute of Standards and Technology.
- [36] Contu, F., et al. "Electrochemical Behavior of CoCrMo Alloy in the Active State in Acidic and Alkaline Buffered Solutions." *Journal of the Electrochemical Society*, vol. 150, no. 9, 2003, p. B419.
- [37] Lewis, A. C., et al. "The Entrapment of Corrosion Products from CoCr Implant Alloys in the Deposits of Calcium Phosphate: A Comparison of Serum, Synovial Fluid, Albumin, EDTA, and Water." *Journal of orthopaedic research*, vol. 24, no. 8, 2006, pp. 1587-1596.
- [38] Gilbert, J. L., et al. "In Vivo Corrosion of Modular Hip Prosthesis Components in Mixed and Similar Metal Combinations. The Effect of Crevice, Stress, Motion, and Alloy Coupling." *Journal of biomedical materials research*, vol. 27, no. 12, 1993, pp. 1533-1544.

- [39] Wang, Q., et al. "CoCrMo Metal Release in Metal-on-Highly Crosslinked Polyethylene Hip Implants." *Journal of Biomedical Materials Research Part B: Applied Biomaterials*, vol. 108, no. 4, 2020, pp. 1213-1228.
- [40] Silva, B. P., et al. "Corrosion Resistant Coatings for Dental Implants." *Bio-Tribocorrosion in Biomaterials and Medical Implants*, Elsevier, 2013, pp. 250-308.
- [41] Atapour, M., et al. "Metal Release from Stainless Steel 316l in Whey Protein - and Simulated Milk Solutions under Static and Stirring Conditions." *Food Control*, vol. 101, 2019, pp. 163-172.
- [42] Knothe, K. "Contact Mechanics and Friction: Physical Principles and Applications." SAGE Publications Sage UK: London, England, 2011.
- [43] Sun, D., et al. "The Effects of Protein and Ph on the Tribo-Corrosion Performance of Cast CoCrMo — a Combined Electrochemical and Tribological Study." *Advanced Tribology*, 2010, pp. 825-826.
- [44] Arenas, M. A., et al. "Electrochemical Noise Measurements of AISI 316l During Wear in Simulated Physiological Media." *Corrosion Engineering, Science and Technology*, vol. 49, no. 7, 2014, pp. 656-660.
- [45] Tainer, J. A., et al. "Metal-Binding Sites in Proteins." *Current Opinion in Biotechnology*, vol. 2, no. 4, 1991, pp. 582-591.

## Chapter 5

### 5 In vitro corrosion and biocompatibility behavior of CoCrMo alloy manufactured by laser powder bed fusion parallel and perpendicular to the build direction

#### 5.1 Introduction

The demand for high-performance orthopedic biomaterials has grown dramatically in the last decades, driven by the rise in the geriatric population, rising bone diseases, and improving living standards [1]. Ceramic and metallic biomaterials exhibit strength, toughness, modulus, and fracture and fatigue resistance [2]. Still, some challenges of orthopedic and dental biomaterials are improving the bio-functionality and reducing the relatively high manufacturing costs [3]. Additive manufacturing (AM) has recently become a key technology to overcome these challenges. Also, due to its greater customizability, speed, and accuracy, additive manufacturing attracted increasing attention for industrial manufacturing of metallic implants [4; 5].

Among different metallic biomaterials, cobalt-chromium-molybdenum (CoCrMo) alloys offer unique mechanical properties and low wear and corrosion rates [6]. These implant materials are conventionally produced by casting and forging processes. In recent years, AM technologies, including Laser Powder Bed Fusion (LPBF), have made significant progress in manufacturing hip, knee, and spinal implant applications [7-9]. The fabrication of customized implants by AM technology can address some key challenges, such as the design of implants that are a mismatch between the joint prosthesis and bone, non-physiological load bearing, and unsatisfactory osteointegration [10]. However, components manufactured by LPBF are characterized by non-equilibrium physical, metallurgical and chemical properties. The formation of porosity, high residual stresses and defects are some of the main challenges associated with LPBF CoCrMo [11]. The corrosion behavior is another critical issue since the release of Co and Cr ions and the formation of corrosion products cause adverse health effects [12; 13]. Also, it has been reported that metal ion release associated with wear and corrosion [14; 15] plays a vital role in the biocompatibility of CoCrMo alloys [8].

Various investigations focused on the corrosion aspects of CoCrMo alloys fabricated by AM methods. Hedberg et al. [16] investigated the corrosion behavior of LPBF CoCrMo compared with its cast counterpart and reported superior behavior of the LPBF alloy. A study on laser metal-deposited CoCrMo indicated that the formation of fine grains and a low extent of Mo segregation could improve corrosion resistance [17]. Also, the content and distribution of precipitates have been reported to influence the corrosion resistance of LPBF CoCrMoW alloy [18]. In another study on the corrosion of LPBF CoCrMo, it was stated that the plane parallel to the build direction (XZ plane) released more metal ions than those in the XY plane [19].

In addition to the AM microstructure aspects, the surface roughness of the AM metallic specimens is a decisive factor influencing their corrosion properties and biocompatibility [20; 21]. This study aimed to investigate the corrosion resistance, bioactivity, biocompatibility, and microstructure of LPBF CoCrMo (low carbon content) in the XY and XZ plane of the building direction for as-printed and abraded surfaces. To simulate a physiological environment, citric acid was added to phosphate-buffered saline (PBS) at pH 7.4. It has previously been shown that citric acid species are strongly metal complexing agents at neutral pH [22; 23] and induce similar metal release and corrosion as protein environments [24; 25]. For reference, PBS without citric acid and citric acid without a buffer are also included in this study.

## 5.2 Materials and methods

### 5.2.1 Sample fabrication and characterization

The alloy in this study was fabricated from an inert gas-atomized powder (chemical composition in Table 5-1) and purchased from Renishaw, UK, with a mean particle size of approximately 15-45  $\mu\text{m}$ . Rectangular alloy specimens (15 mm  $\times$  15 mm  $\times$  2 mm) were fabricated by the LPBF method using optimized industrial parameters for fully dense specimens and a Renishaw AM400 Selective Laser Melting System (ADEISS, London, Canada). Two types of specimens were fabricated; one placed parallel and the other perpendicular to the building direction, denoted as XZ and XY, respectively. The processing parameters are listed in Table 5-2 and one layer was rotated 67° to the

previous layer. After fabrication, these specimens were heat treated with a particular route as follows: 1) the specimens were gradually heated to 450 °C for 60 min, 2) then kept at this temperature for 45 min, 3) then reheated to 750 °C for 45 min, 4), then kept at this temperature for 60 min, and 5) furnace cooled to room temperature. After the heat treatment, the surfaces were sandblasted using a dental sandblasting mixture (with 63-125  $\mu\text{m}$  zirconia with 28-33 wt.% silica and less than 10 wt.% alumina), ultrasonically cleaned in isopropyl alcohol and deionized water, and dried in a convection oven. This surface finish is denoted ‘as-received’. Half of the specimens were further abraded using P1200 SiC paper with deionized water as a lubricant, followed by ultrasonic cleaning in acetone and ethanol (5 min each) and drying using nitrogen gas, denoted ‘abraded’.

**Table 5-1: As per supplier information, chemical composition of CoCrMo (F75) alloy powder.**

Element	Cr	Mo	Mn	Si	N	Fe	Ni	C	W	Co
wt.%	28.0	6.10	0.77	0.57	0.22	0.20	0.05	0.02	0.02	Bal.

**Table 5-2: LPBF setup and parameters.**

Power	Spot size	Scan speed	Layer thickness	Scan spacing
200 W	70 $\mu\text{m}$	2 m/s	40 $\mu\text{m}$	70 $\mu\text{m}$

### 5.2.2 Microstructure and surface roughness characterization

Before microstructural analyses, all specimens were polished with 0.25  $\mu\text{m}$  diamond paste and then electropolished for 20 s at 4 V using a 1:9 (by volume) solution of HCl and H<sub>2</sub>O. Optical microscopy (OM, Nikon EpipHot 300) and scanning electron microscopy (SEM, Philips XL 30) techniques were utilized for characterization. Phase identification was also conducted using X-ray diffraction (XRD, Phillips, Netherlands) equipped with a CuK $\alpha$  radiation source ( $\lambda = 0.154 \text{ nm}$ , 40 kV, 40 mA) scanning from 20 to 80° (2 $\theta$ ). The roughness value ( $R_a$ ) of different specimens was determined using a Stylus profilometer (Mitutoyo SJ210). In addition, surface topography mapping and roughness measurements were performed using a ZEISS LSM 800 confocal microscope

manufactured by Carl Zeiss Microscopy GmbH. The surface roughness and surface area were calculated using version 7.4.8341 of Mountains ConfoMap software. The calculations were performed by the standard ISO 25178-2:2012.

### 5.2.3 X-ray photoelectron spectroscopy (XPS)

XPS can probe the outermost (7-10 nm) surface of the specimens and was used to characterize the surface composition of unexposed as-received XY, as-received XZ, abraded XY and abraded XZ specimens. The XPS analyses were carried out with a Kratos AXIS Supra X-ray photoelectron spectrometer using a monochromatic Al  $K_{\alpha}$  source (15 mA, 15 kV). XPS has detection limits ranging from 0.1 - 0.5 atomic percent depending on the element. The instrument work function was calibrated to give a binding energy (BE) of 83.96 eV for the Au 4f<sub>7/2</sub> line for metallic gold. The spectrometer dispersion was adjusted to give a BE of 932.62 eV for the Cu 2p<sub>3/2</sub> line of metallic copper. The Kratos charge neutralizer system was used on all specimens. All specimens were mounted electrically isolated from the instrument sample holder for these analyses. For all measurements, survey scan analyses were carried out with an analysis area of 300 × 700 μm and a pass energy of 160 eV, and high-resolution analyses were carried out with an analysis area of 300 × 700 μm and a pass energy of 20 eV. High-resolution C 1s, O 1s, Si 2p (selected samples), Co 2p, Cr 2p, and Mo 3d were run. All high-resolution spectra were charge-corrected using adventitious carbon (C 1s, 284.8 eV). Peak convolution was conducted according to previously published protocols [26-28].

### 5.2.4 Corrosion studies

The corrosion behavior of the printed specimens was assessed using electrochemical impedance spectroscopy (EIS) and potentiodynamic polarization in three solutions of phosphate-buffered saline (PBS, 8.77 g/L NaCl, 1.28 g/L Na<sub>2</sub>HPO<sub>4</sub>, 1.36 g/L KH<sub>2</sub>PO<sub>4</sub>, 350 μL/L 50% NaOH, pH 7.2–7.4), citric acid (CA, 5 g/L citric acid, pH=2.40), and CA + PBS (pH = 7.40) solutions. The choice of citrate-containing PBS was based on its similarity to many biological environments, including protein environments, due to its complexation capacity [22-25]. Citrate has been used as a simplified model molecule for

many physiological solutions [29-32]. PBS without CA and CA without a buffer served as reference solutions.

These evaluations were conducted in a three-electrode system, with a Ag/AgCl (saturated KCl) reference electrode, platinum counter electrode sheet and CoCrMo specimens as working electrodes, all coupled to an AMETEK potentiostat/galvanostat (PARSTAT 2273). Before each test, the specimens were immersed for 45 min, and the open circuit potential (OCP) was measured to reach a steady state condition. EIS tests were conducted at OCP with an alternating current (AC) amplitude of 10 mV<sub>rms</sub> and a frequency range of 100,000 to 0.01 Hz. The potentiodynamic polarization tests were conducted from -250 to 1500 mV vs. open circuit potential with a scanning rate of 1 mV/s. Selected corrosion parameters ( $i_{\text{corr}}$ ,  $\beta_a$ ,  $\beta_c$  and  $E_{\text{corr}}$ ) were obtained based on the Tafel extrapolation method.

### 5.2.5 Bioactivity studies

To investigate hydroxyapatite formation on the surface (in the following referred to as “bioactivity”) of the printed specimens and the effect of grinding (with P1200 SiC paper), the specimens were immersed in 20 mL simulated body fluid (SBF) and incubated at 37 °C for 7, 14 and 28 days (no shaking) in an incubator (Memmert GmbH, Germany) to prevent being exposed to the light. After immersion, the specimens were removed from the SBF, rinsed with distilled water, and dried in an oven. The surface morphology and composition (information depth of micrometers) were studied using scanning electron microscopy (SEM; SE detector; Philips XI30) and energy dispersive X-ray spectroscopy (EDX). The composition of SBF is depicted in Table 5-3.



**Table 5-3: Composition of the simulated body fluid (SBF), with pH 7.4, adjusted with 1 M HCl; adapted from [33].**

Reagent	Composition (g/L)
NaCl	8.035
NaHCO <sub>3</sub>	0.355
KCl	0.225
K <sub>2</sub> HPO <sub>4</sub> ·3H <sub>2</sub> O	0.231
MgCl <sub>2</sub> ·6H <sub>2</sub> O	0.311
CaCl <sub>2</sub>	0.292
Na <sub>2</sub> SO <sub>4</sub>	0.072

### 5.2.6 Cell culture

Osteoblast-like MG63 cells (Pasteur Institute of Iran, Iran) were aseptically cultured in DMEM (Dulbecco's Modified Eagle Medium) supplemented with 10% fetal bovine serum (FBS) and 1% penicillin/streptomycin (Sigma-Aldrich Co; USA) at 37 °C in a humidified 5% CO<sub>2</sub> incubator in the dark. The media was exchanged 2-3 times per week, and the cells were sub-cultured at 80% confluency. Rectangular 5×5 mm<sup>2</sup> scaffolds were sterilized in 70% ethanol for 1 h, followed by UV irradiation of both sides for 1 h. The sterilized scaffolds were submerged in the cell culture medium overnight, and then the media inside the wells were aspirated, and the cells were seeded on top of the scaffolds. The cells were used at passage 5–7 and seeded at a 5×10<sup>3</sup> cell/scaffold density before adding 500 μL of cell culture medium to each well. To enhance the seeding efficiency, the cells were added in a minimal volume of media (i.e., 10 μL). Then 500 μL of culturing media was added after 10 min to enable sufficient adherence of the cells to the scaffold. The scaffolds were kept at 37 °C in a humidified 5% CO<sub>2</sub> condition, and the media was changed every second day until the end of the experiment on day 7.

### 5.2.7 Cell adhesion and morphological characterization

The morphology of adhered cells on the specimens was visualized by SEM. After 7 days, the cells on the specimens were washed with PBS, then fixed with 4% (w/v) PFA (paraformaldehyde) in PBS for 30 min at 37 °C. After three times washing with PBS, the

cell-seeded surfaces were dehydrated before SEM imaging by successive immersions in 30%, 50%, 70%, 90%, and 100% ethanol solutions for 30 min at each concentration. They were then submerged in 100% hexamethyldisilazane (Sigma-Aldrich Co; USA) for another 30 min at room temperature and finally imaged by SEM after complete drying in air.

### 5.2.8 Cell viability

The relative (to negative control) viability of cells seeded on the specimens was studied by the MTT assay. MTT stands for 3-(4,5-dimethylthiazol-2-yl)-2,5-diphenyltetrazolium bromide (Sigma-Aldrich Co; USA). MTT solution (0.5 mg/ml in DMEM and penicillin/streptomycin without FBS) was prepared fresh and filtered (0.2  $\mu$ m cellulose membrane Syringe Filter) at each time point (i.e., day 1, 3 & 7). After these time points, the culture medium (DMEM) in the wells was completely replaced with 300  $\mu$ L MTT solution. The cells were incubated at 37 °C under a 5% CO<sub>2</sub> atmosphere for 4 h. Then, the MTT solutions were aspirated, and 300  $\mu$ L dimethyl sulfoxide (DMSO, Sigma-Aldrich Co; USA) was added to each well, and the plate was placed on a shaker for 10 min to dissolve formazan crystals completely. The solutions in the wells were transferred to a 96-well plate, and the absorbance was measured using a microplate reader at 630 nm. The viability assay was run with three replications for each specimen and the negative control. The viability is presented as a percentage of the negative control, where 100% or higher corresponds to no cytotoxicity (all cells at least as viable as in the negative control), and 0% corresponds to maximal cytotoxicity (all cells dead). The optical density corresponding to cell adsorption (OD) was read for wells containing the specimens and compared to the control wells without the specimens, as in Eq. (5-1), to reveal the cell viability in %.

$$\text{Cell Viability \%} = \frac{OD(\text{specimen}) - OD(\text{blank})}{OD(\text{control}) - OD(\text{blank})} \times (100) \quad \text{Eq. (5-1)}$$

In this equation, OD(specimen) corresponds to the cell adsorption of the metallic specimen, OD(blank) corresponds to the DMSO solution (background), and OD(control) corresponds to the cell adsorption rate of the cell-seeded and plasma-pre-treated well without metallic specimens.

### 5.2.9 Statistical analysis

When comparing two sets of data from independent specimens for different conditions, a student's t-test with unequal variance for unpaired data was used (KaleidaGraph v. 4.0). P values  $<0.05$  (less than 5% probability that the two data sets are equal) are counted as statistically significant differences.

## 5.3 Results and discussion

### 5.3.1 Microstructure and surface roughness

Fig. 5-1 (a-c) depicts the surface morphology of the fabricated specimens after the electro-etching treatment to obtain metallographic information. A heterogeneous microstructure with tracked and scaled segments is revealed for specimens prepared from transverse (XY-plane) and longitudinal (XZ-plane) directions, respectively [34]. A network of overlapping melt pools was observed in the XY plane. In contrast, half-cylinder melt pools were observed for the XZ plane, agreeing with literature findings for powder bed fusion processes and fusion welding procedures [35]. Because of loose/solid powder around the melt pool, competitive growth occurs for LPBF, yielding various growth directions. The observed ripple solidification could be due to the sequential solidification of teardrop melt pools during the LPBF process. Vertical columnar grains in the XZ plane could be caused by heterogeneous nucleation, as previous layers act as nucleation sites for subsequent layers [35].

As the formation of defects and porosity is detrimental to the functional performance of the LPBF materials, optical images were also recorded without etching and presented in Fig. 5-1 (d-f). ImageJ software recorded 2% and 3% porosity values for the XZ and XY planes. As-received XY and XZ specimens show distinctly different surface morphologies and roughness, as depicted in Fig. 5-1 (g-h), with a rougher appearance for XY. Fine columnar and cellular microstructures are visible on the surfaces of abraded/etched specimens (Fig. 5-1, i-j).

Different void types were observed for the abraded XY and XZ planes using optical microscopy, Figure S1 (supplementary information). For the XY plane, only gas

porosities (round) were observed; however, both gas porosities and lack of fusion defects were observed for the XZ plane. The morphology of the voids can be influenced by various factors, including energy density, heat flow and solidification of the melt pool during the LPBF process [36]. Lack of fusion defects are formed due to inadequate penetration of the molten pool of a layer into the previously printed layers. Hence, they are only seen for the XZ plane with a high density of melt pool boundaries (Fig. 5-1b).

XRD spectra of abraded XY and XZ specimens are presented in Fig. 5-1 (k), showing face-centered cubic (FCC)  $\gamma$  phase as the main phase in the printed specimens, while hexagonal close-packed (HCP)  $\epsilon$  phase peaks could also be found [17; 34; 35]. No other phase was identified (instrumental detection limit  $\sim 5$  vol.%). The  $\epsilon$  phase derives from martensitic transformation ( $\gamma \rightarrow \epsilon$ ) during subsequent heating processes (subsequent layers) [16; 37]. Furthermore, heat treatment can alter the phase composition of CoCrMo alloy. Specifically, the heat treatment of the specimens at 750 °C for 1 hour increased the transformation to martensite [38].

Figure 5-1 (l) depicts the surface roughness values of the abraded and as-received XY and XZ surfaces, with a higher surface roughness ( $R_a = 5.3 \pm 0.6 \mu\text{m}$ ) for the as-received XY compared to the as-received XZ ( $2.6 \pm 0.3 \mu\text{m}$ ). A similar trend was seen for the maximum profile peak height ( $R_z$ ), being 20% higher for XY compared to XZ ( $59 \pm 3.5$  compared with  $47 \pm 2.7 \mu\text{m}$ ). For abraded specimens, there was no significant difference. The higher surface roughness of the as-received XY than XZ was also confirmed by confocal microscopy, Fig. S2. For a geometrical area of 2.25 cm<sup>2</sup>, confocal microscopy found an actual surface area of 2.79 and 2.39 cm<sup>2</sup> for as-received XY and XZ, respectively. The higher roughness of as-received XY (top plane, a single layer of melted and solidified powders) could be attributed to defects of material filling or the localized lack of fusion. It has been claimed that the spatter ejection of molten material from the pool could facilitate the formation of cavities and a coarser surface [20].

In all, the microstructural investigation confirms a dense LPBF printing and distinct microstructures for XY and XZ planes. As-received XY was coarser than XZ.

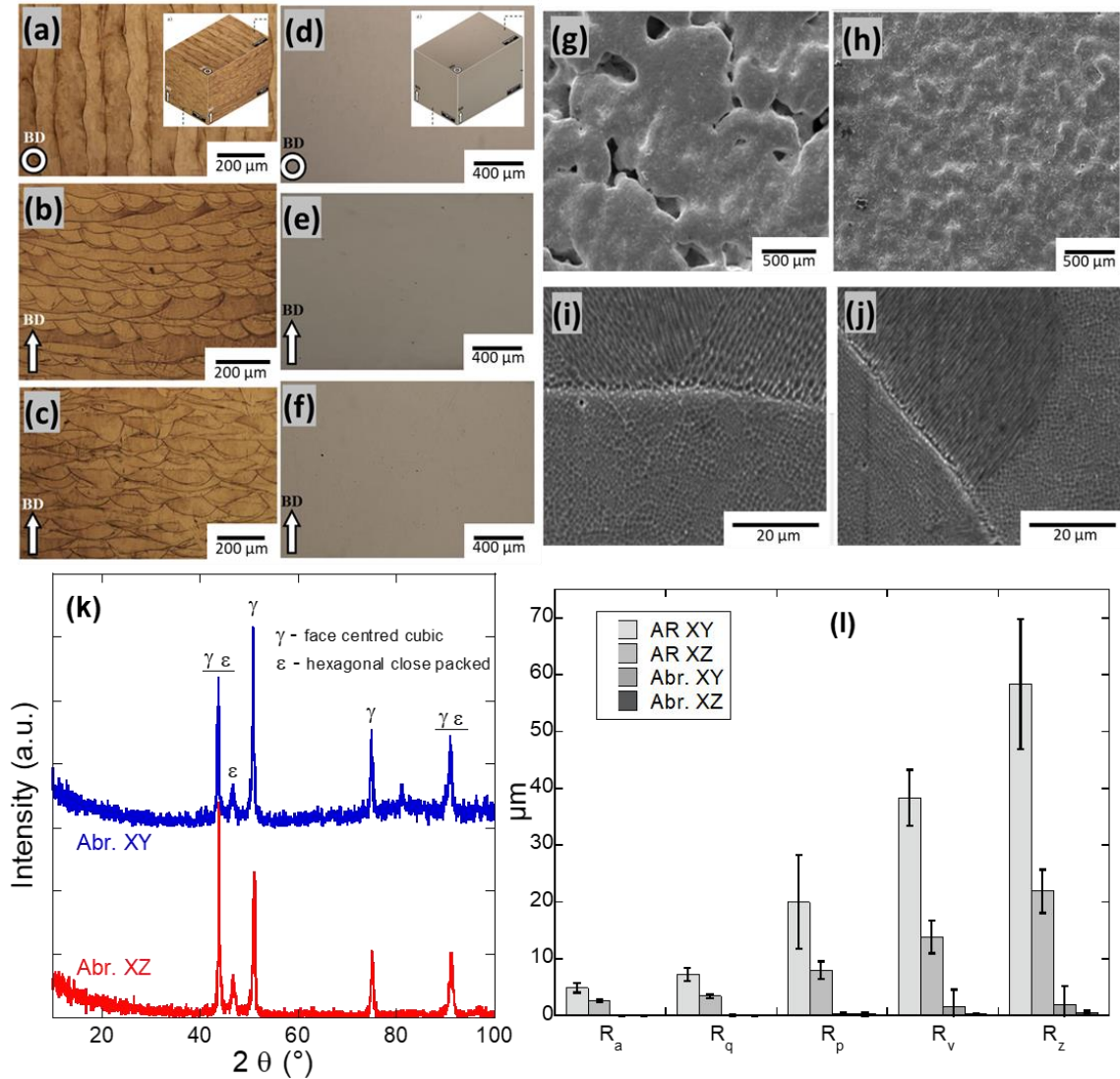


**Figure 5-1: Optical micrographs of different planes of the CoCrMo specimens: (a,d) top (XY plane), (b,e) mid (XZ plane), (c,f) bottom (XZ plane) areas (inset: merged sides in 3D). SEM micrographs of the printed CoCrMo specimens at (g) low magnification view of as-received XY, (h) low magnification view of as-received XZ, (i) high magnification view of the abraded and etched XY, (j) low magnification view of abraded and etched XZ. (k) XRD patterns of the abraded XY and XZ specimens. (l) Surface texture parameters of the printed CoCrMo in the as-received and abraded conditions. The error bars show the standard deviation of triplicate measurements.  $R_a$  (arithmetical mean deviation of the assessed profile),  $R_p$**

**(maximum peak height),  $R_q$  (root mean square average of the profile),  $R_v$  (maximum valley depth) and  $R_z$  (maximum height of the profile).**

### 5.3.2 Surface characterization

XPS was used to determine the surface (7-10 nm) composition and the speciation of Co, Cr, and Mo, Fig. 5-2. Carbon, oxygen, and silicon were the three most abundant elements on the surface. Carbon originates mainly from adventitious carbon, which is well-known [39]. The C 1s high-resolution spectrum further confirms the absence of carbides and the dominance of C-C and C-H bonds, Figs. S3-S6. The high-resolution peak of O 1s revealed the dominance of a peak at  $532.4 \pm 0.1$  eV, which can be assigned to oxygen originating from organic substances or SiO<sub>2</sub>. Because of the concomitant presence of silicon, we also analyzed the Si 2p high-resolution for two of the specimens (as-received and abraded XY). Based on the peak positions (Si 2p<sub>3/2</sub> 102.15-102.18 eV), Fig. S7, the most probable origin is silicone [28], a common contaminant. Within the detection depth (7-10 nm), metallic peaks of Co, Cr, and Mo were detected in all cases (Figs. 2b and S3-S6), suggesting a rather thin (a few nanometers) surface oxide. Co, Cr, and Mo oxide species were relatively similar for all specimens: Co(OH)<sub>2</sub>, Cr<sub>2</sub>O<sub>3</sub>, Cr(OH)<sub>3</sub>, and Mo oxide in the valence states of IV, V, and VI. There appears to have been a consistent growth of oxidized molybdenum after the polishing procedure, which is expected for neutral water exposure [40].

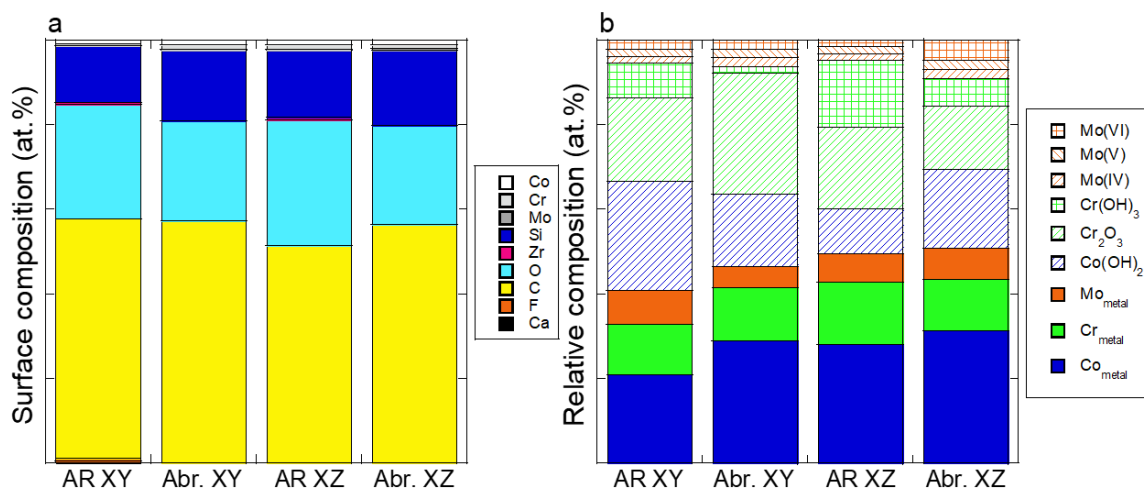


**Figure 5-2: Surface composition estimated from the XPS wide spectra (a) and relative surface composition and speciation of the elements Co, Cr, and Mo (b) of as-received (AR) and abraded (Abr.) CoCrMo surfaces in XY and XZ planes. Corresponding spectra are shown in Figs. S3-S7 (supplementary information).**

### 5.3.3 Corrosion

#### 5.3.3.1 Open circuit potential and cyclic polarization

The OCP shifted towards more positive potentials for all specimens and solutions during 2,800 seconds of immersion. There was no statistically significant difference between the different surface conditions (abraded, as-received, XY, XZ) within one solution. There were significant ( $P < 0.05$ ) differences between the three solutions in all cases, except for abraded XY in CA compared with PBS-CA. PBS solution (pH 7.4) resulted in the most negative OCP ( $-0.27 \pm 0.04$  VAg/AgCl) after 2,800 s of immersion, with PBS+CA (pH 7.4) showing a more positive OCP ( $-0.052 \pm 0.012$  V), and the most acidic solution having the most positive OCP ( $0.17 \pm 0.038$  V). This positive shift with time indicates a passivating behavior (gradual improvement of the passive film on the surface) [34] upon immersion in a physiologically relevant solution. This has been reported previously for biomedical CoCrMo alloys [41; 42].

Similar to the OCP, the  $E_{\text{corr}}$  value (the corrosion potential, which is the potential at which the net current is zero during the polarization) was not significantly different among the different specimens but showed a significant difference between CA (pH 2.4) and PBS (pH 7.4), as well as between CA and PBS+CA (pH 7.4), due to the pH difference (potentials in aqueous systems shift with pH), Table 5-4 and Fig. 5-3. In PBS (Fig. 5-3b, Table 5-4), however, the  $E_{\text{corr}}$  seemed to be different among the specimens (Abr. XY < Abr. XZ < AR XZ < AR XY), with a difference of at most 460 mV but this was not statistically significant ( $P > 0.05$ ). The corrosion current density ( $i_{\text{corr}}$ ), which is the current density determined from the intersection of the anodic and cathodic branch (linear extrapolation), was not different among the solutions and not different between the specimens in CA (pH 2.4) and PBS+CA (pH 7.4). However, in PBS (pH 7.4), there was a statistically significant ( $P < 0.05$ ) difference in corrosion current density between as-received XY ( $0.075 \pm 0.008 \mu\text{A}/\text{cm}^2$ ) and as-received XZ ( $0.015 \pm 0.003 \mu\text{A}/\text{cm}^2$ ), as well as between as-received XY and abraded XY ( $0.017 \pm 0.012 \mu\text{A}/\text{cm}^2$ ). This difference cannot be explained by the difference in actual surface area (at most 25% difference, section 3.1). Likewise, for the passive current density (here defined as the current density where the anodic branch becomes horizontal [43]), only the difference between as-received XY ( $0.74 \pm 0.37 \mu\text{A}/\text{cm}^2$ ) and as-received XZ ( $0.07 \pm 0.04 \mu\text{A}/\text{cm}^2$ ) in PBS (pH 7.4) was statistically significant. Hence, there seems to be a larger influence of the plane (XY vs. XZ) for as-received surfaces, and abrasion seems to result in lower corrosion currents and a larger passive region, Fig. 5-3 and Table 5-4. This finding agrees with previous work on the corrosion of LPBF 316L [4].

There were no indications of localized corrosion (lower potential during reverse scan than during forward scan, Fig. 5-3), which agrees with previous work [44]. The rapid increase in current density at high potentials can hence be attributed to water oxidation and maybe transpassive dissolution but not localized corrosion [45-47]. This conclusion was further confirmed by inspection by optical microscopy after the polarization.

While there was no significant difference among solutions for the corrosion and passive corrosion density, the transpassive region (current increase at high potentials) occurred clearly at lower potentials in PBS+CA compared to PBS (both at pH 7.4). This is



supported by the work conducted on LPBF 316L in PBS and PBS + citric acid [29] and may be attributed to the formation of metal-citrate species, which can increase dissolution in some cases [4, 40]. Also, there was a clear oxidation shoulder peak around 0.7 V in both solutions, which is assumed to be the formation of a phosphate-chromium complex [32].

For other alloys, porosity has been discussed as an important factor for the pitting corrosion susceptibility or repassivation ability [21]. In this study, the specimens were fabricated with the highest possible density (low porosity) and exhibited a very high pitting corrosion resistance under all conditions. As observed in this study and previous studies [48], small pores do not detrimentally affect the pitting resistance of CoCrMo alloys.

In all, the CoCrMo specimens were passive and not undergoing localized corrosion. There was an effect of the building direction for as-received specimens (highest corrosion for as-received XY) and an effect of the solution (highest currents in PBS+CA) at high potentials.

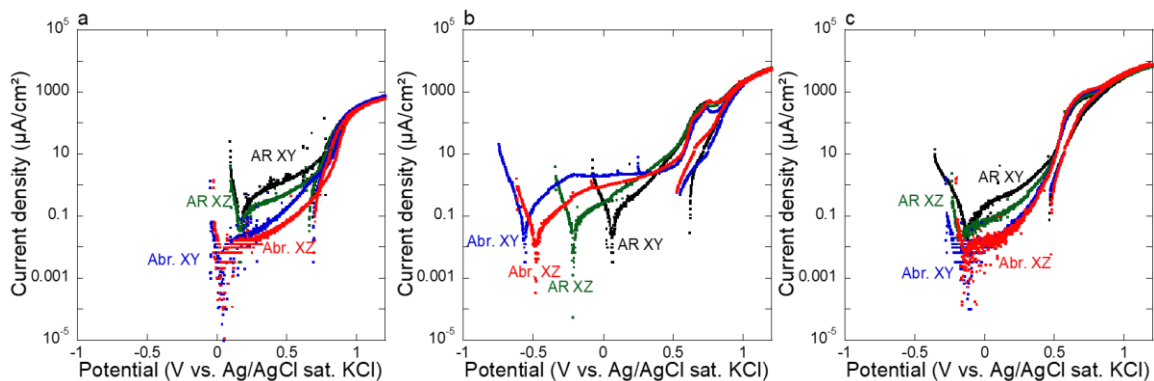


**Figure 5-3: Representative cyclic polarization curves (forward and reverse scans) for as-received (AR) and abraded (Abr.) CoCrMo specimens in XY and XZ plane in citric acid (pH=2.4) (a), PBS (pH 7.4) (b), and PBS + citric acid (pH = 7.4) (c) solutions at room temperature.**

**Table 5-4: Cathodic and anodic Tafel constants ( $\beta_a$  and  $\beta_c$ ), corrosion current densities ( $i_{corr}$ ), passive current densities ( $i_{pass}$ ) and corrosion potentials ( $E_{corr}$ ) based on potentiodynamic polarization of the LPBF CoCrMo specimens after 1 h immersion in citric acid (CA) (pH=2.4), PBS (pH 7.4), and CA + PBS (pH = 7.4) solutions at room temperature.**

Systems	Materials	Tafel parameters				
		$\beta_a$ (mV)	$\beta_c$ (mV)	$i_{corr}$ ( $\mu\text{A}/\text{cm}^2$ )	$i_{pass}$ ( $\mu\text{A}/\text{cm}^2$ )	$E_{corr}$ (mV <sub>Ag/AgCl</sub> )
CA	As-received XY	95±74	169±16	0.3±0.2	0.8±0.4	135±30
	Abraded XY	22±20	230±139	0.004±0.002	0.02±0.01	-19±40
	As-received XZ	290±201	190±96	0.1±0.02	0.2±0.04	140±31
	Abraded XZ	37±7	151±19	0.001±0.0004	0.02±0.01	59±37
PBS	As-received XY	96±4	137±38	0.07±0.01	0.7±0.4	23±49
	Abraded XY	71±9	171±17	0.02±0.01	0.3±0.4	-432±197
	As-received XZ	61±7	191±46	0.02±0.003	0.07±0.04	-219±17
	Abraded XZ	64±19	180±3	0.01±0.003	0.1±0.1	-411±117
CA+PBS	As-received XY	100±1	136±1	0.05±0.05	0.4±0.4	-84±33
	Abraded XY	71±32	57±22	0.002±0.002	0.01±0.01	-138±46

As-received XZ	61±40	91±21	0.04±0.05	0.2±0.2	-89±112
Abraded XZ	49±17	109±59	0.004±0.005	0.03±0.04	-216±114

### 5.3.3.2 Electrochemical impedance spectroscopy

Figure 5-4 shows Nyquist (a-c) and Bode plots (d-e) based on EIS after 1 h immersion at OCP. The Nyquist plots are all semicircular arcs indicating a typical passive state with high impedance values with capacitive behavior. The semicircle diameter in these curves equals the charge transfer resistance, which is related to corrosion resistance. The Bode plots show three distinctive regions. The absolute impedance is independent of frequency in the high frequencies (the phase angle is around 0°). In these frequencies, the impedance corresponds to the resistance of the electrolyte between working and reference electrodes. A purely capacitive response is obtained in the low to medium frequency levels. In these frequencies, the absolute impedance exhibits a linear relationship with the frequency (a slope approaching -1). In the low-frequency range, the absolute impedance is independent of the frequency.

The electrolyte resistance was higher in CA (pH 2.4) than in the PBS-containing electrolytes, Fig. 5-4 and Table 5-5. In the medium and low-frequency segments, the Bode plots represent the charge transport characteristics across the double layer and the passive oxide film, respectively. Here, the maximum phase angle values are between 70 and 90° within a wide range of frequencies (0.1 to 100 Hz). Higher values mean more stable passive oxide films and a higher corrosion resistance [49].

The simplified Randles equivalent electrical circuit (EEC) was used to fit the EIS results (Fig. 5-4), similar to other studies on the corrosion behavior of CoCrMo alloy in simulated physiological solutions [49-51]. The goodness of fitting ( $\chi^2$ ) values were below 10<sup>-3</sup>. Table 5-5 shows the resulting fitting parameters.  $R_s$  denotes the solution resistance,  $R_p$  is the native oxide film resistance, CPE is the constant phase element,  $C_{eff}$  is the

effective capacitance, and  $n$  is the phase constant exponent. A CPE was used due to the non-ideal capacitance of the capacitive elements because of different physical phenomena, such as surface heterogeneity originating from surface roughness, pores, impurities and grain boundaries [52; 53]. The impedance of the CPE is defined as  $Z_{CPE}=[Y_o(j\omega)^n]^{-1}$  where,  $Y_o$  is the frequency-independent constant,  $j$  is the imaginary unit ( $j^2=-1$ ),  $\omega$  is the angular frequency, and  $n$  ( $0 \leq n \leq 1$ ) is the phase constant exponent representing surface irregularities. Depending on  $n$ , CPE can be related to a pure resistor ( $n=0$ ,  $Y_o=R$ ), a pure capacitor ( $n=1$ ,  $Y_o=C$ ), or the Warburg impedance ( $n=0.5$ ,  $Y_o=W$ ). The  $C_{eff}$  values were determined as follows [54]:

$$C_{eff} = Q^{1/n} \times R_p^{(1-n)/n} \quad \text{Eq. (5-2)}$$

The effective capacitance can be linked to the film thickness as follows [55]:

$$C_{eff} = \varepsilon \times \varepsilon_0 \times A/d \quad \text{Eq. (5-3)}$$

where  $\varepsilon$  is the relative dielectric constant ( $\varepsilon_0$  is the permittivity in vacuum),  $A$  is the surface area, and  $d$  denotes the film thickness.

The EIS data revealed that the solution, the roughness (as-received versus abraded), and the build direction influenced the barrier characteristics of the passive layers formed on the surfaces. According to the fitted data presented in Table 5-5,  $R_p$  was significantly ( $P<0.05$ ) lower in PBS compared with CA and CA+PBS (only for XY) for the abraded specimens and lower in CA+PBS compared with CA for the abraded XZ specimen. This behavior can be attributed to the adsorption of citrate ions on the oxide layer and their complexation with metal ions in the oxide, which accelerates passivation (chromium enrichment due to preferential dissolution of cobalt) [32; 56]. The superior passivity characteristics of the samples in this work agree with the results reported for LPBF 316L stainless steel in a citrate buffer and PBS solutions [29].

The  $C_{eff}$  was higher for the as-received compared with the abraded specimens for both XY and XZ planes, statistically significant in both PBS (for both XY and XZ) and CA+PBS (for XZ). A similar trend was seen for CPE (statistically significant in CA and CA+PBS). Further, the  $C_{eff}$  was higher ( $P<0.05$ ) for as-received XZ samples in CA+PBS

than in PBS. Based on Eq. 5-3, an increase in the  $C_{eff}$  means a decrease in the thickness of the passive layer or the dielectric constant of the passive layer [57]. Hence, it seems that the passive film formation was accelerated for abraded CoCrMo surfaces and, in some cases (as-received XZ), in the presence of citrate species. A similar trend was found for  $R_p$  for as-received XZ in the solutions containing CA (higher  $R_p$  for abraded than as-received surfaces).

Hence, the barrier characteristics of the passive layer formed on the as-received surfaces (for both XY and XZ samples) were inferior to the abraded samples, and the difference in the actual surface area cannot explain this. An inferior barrier could be attributed to the higher porosity and surface defects, such as lack of fusion and non-melted metal powders, or other factors, such as the sandblasting procedure [21; 58].

In line with the cyclic polarization data, the corrosion resistance, estimated from EIS, was lowest for the as-received XY. It was also lower for as-received than for abraded specimens, Fig. 5-4 and Table 5-5.

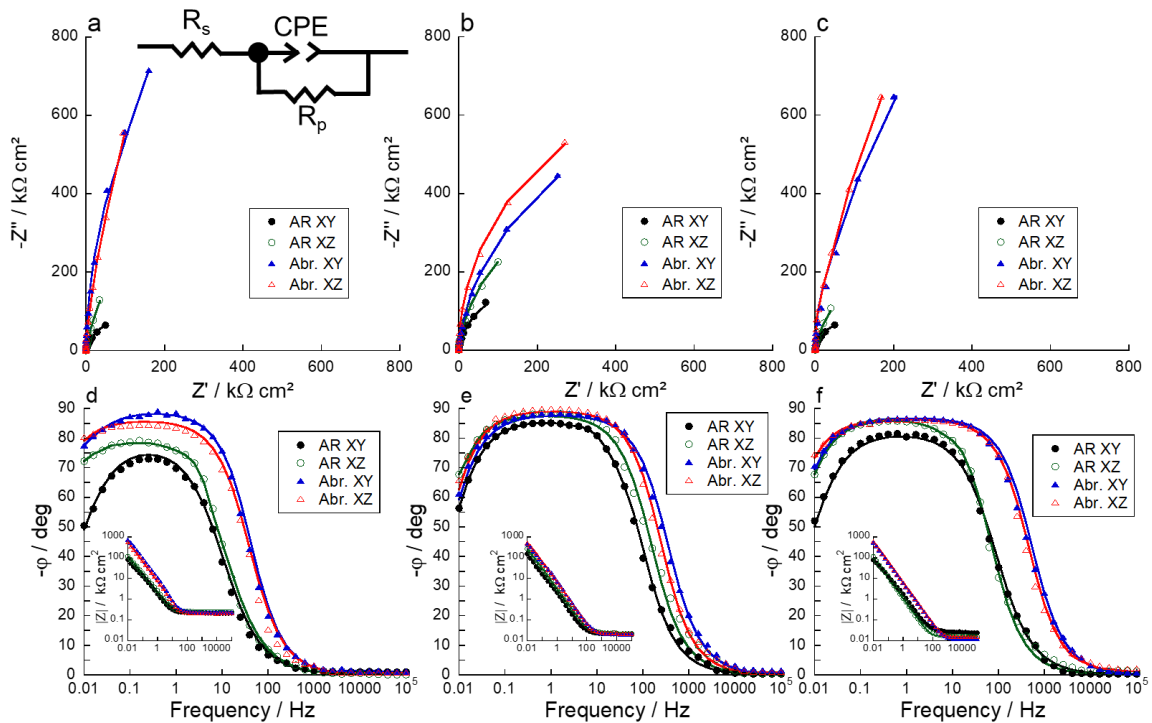


**Figure 5-4: Representative Nyquist (a-c), Bode phase angle (d-f), and Bode impedance (insets in d-f) plots of as-received and abraded CoCrMo in planes XY and XZ after 1 h immersion in citric acid (pH 2.4) (a, d), PBS (pH 7.4) (b, e), and PBS + citric acid (pH 7.4) (c, f) at room temperature. The inset in (a) shows the equivalent electrical circuit for the analysis of the impedance spectra (Table 5-5).**

**Lines – fit; symbols – data points.**

**Table 5-5: EIS fitting parameters (average and standard deviation of two independent specimens). A one-time constant (Randles equivalent electrical circuit) was applied.**

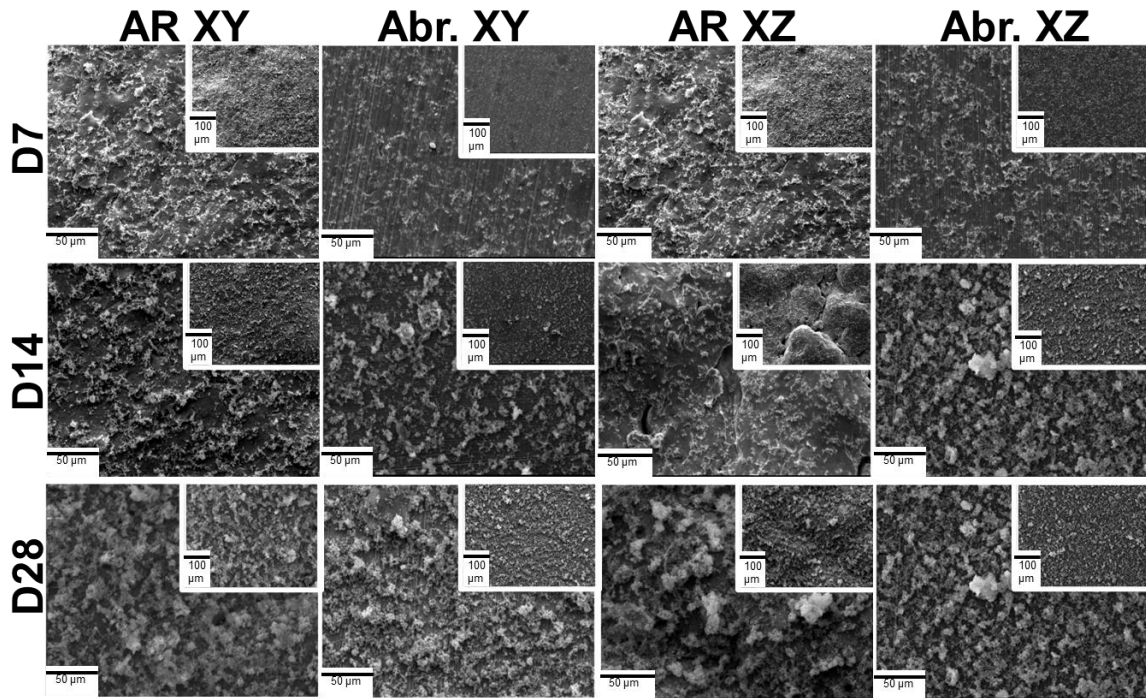
Systems	Material s	Parameter s					
		$R_s$ ( $\Omega \text{ cm}^2$ )	CPE ( $Y_0, \mu\text{Fcm}^{-2}\text{s}^{-n}$ )	$C_{\text{eff}}$ ( $\mu\text{Fcm}^{-2}$ )	n	$R_p$ ( $\text{M}\Omega \text{ cm}^2$ )	$\chi^2$ ( $10^{-3}$ )
CA	As- received XY	220±0.78	123±9. 3	87±28	0.91±0.0 6	1.7±2.2	0.52±0.0 4
	Abraded XY	230±13	19±3.2	12±0.5	0.93±0.0 3	37±4.6	0.36±0.0 7
CA	As- received XZ	255±8.8	92±9.2	58±11	0.89±0.0 1	18±3.0	0.58±0.1 0
	Abraded XZ	205±7.1	23±2.3	15±6.2	0.93±0.0 5	39±1.0	0.25±0.0 4

PBS	As- received XY	24±2.3	104±20	50±6.2	0.89±0.0	3.9±1.7	0.42±0.0
					1		4
	Abraded XY	23±3.3	23±3.9	15±7.6	0.94±0.0	13±3.4	0.28±0.0
					4		4
	As- received XZ	23±1.3	50±1.6	18±5.4	0.87±0.0	7.4±0.6	0.51±0.1
					3	5	3
	Abraded XZ	31±2.6	27±4.7	17±2.5	0.94±0.0	13±2.8	0.48±0.0
					4		4
CA+PB S	As- received XY	28±1.5	113±6.	74±9.7	0.93±0.0	1.7±0.2	0.64±0.0
			3		3	0	4
	Abraded XY	18±2.5	23±3.4	15±3.1	0.95±0.0	25±2.7	0.73±0.0
					4		4
	As- received XZ	17±1.0	161±15	97±8.8	0.92±0.0	3.2±0.4	0.19±0.0
					3	3	4
	Abraded XZ	19±0.56	20±0.6	15±3.2	0.97±0.0	20±0.61	0.21±0.0
					2		2

#### 5.3.4 Bioactivity and biocompatibility

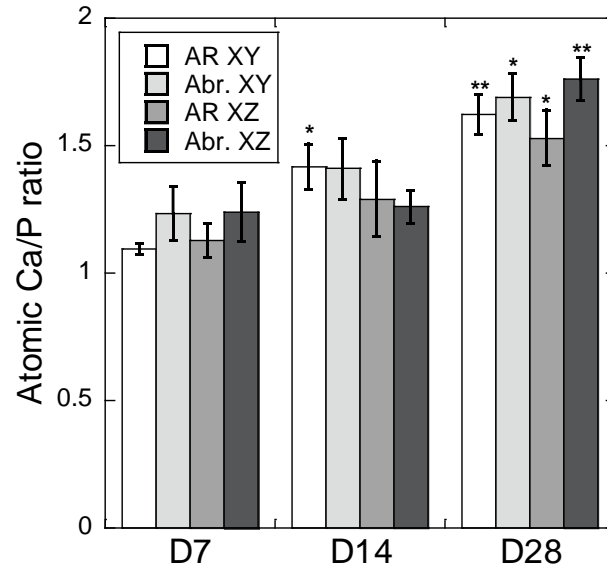
Any precipitation of hydroxyapatite layers on the surface of the specimens was investigated in a bioactivity assay after incubation at 37 °C (static conditions) in SBF for 7, 14, and 28 days. The specimens were evaluated using SEM (Fig. 5-5), and the atomic Ca/P ratio was investigated using EDS (Fig. 5-6). EDS further confirmed that Ca and P

were the only elements of that surface layer. Fig. 5-5 reveals gradually increasing/covering layers of precipitates on all specimens ( $P < 0.05$ ). After 28 days, almost the entire surface was covered with a thick layer of aggregates. The atomic Ca/P gradually increased with exposure time for all specimens, and there was no significant difference found among the specimens. After 28 days, the Ca/P ratio was  $1.65 \pm 0.1$ , which is close to the ratio of natural hydroxyapatite of 1.67 [59].



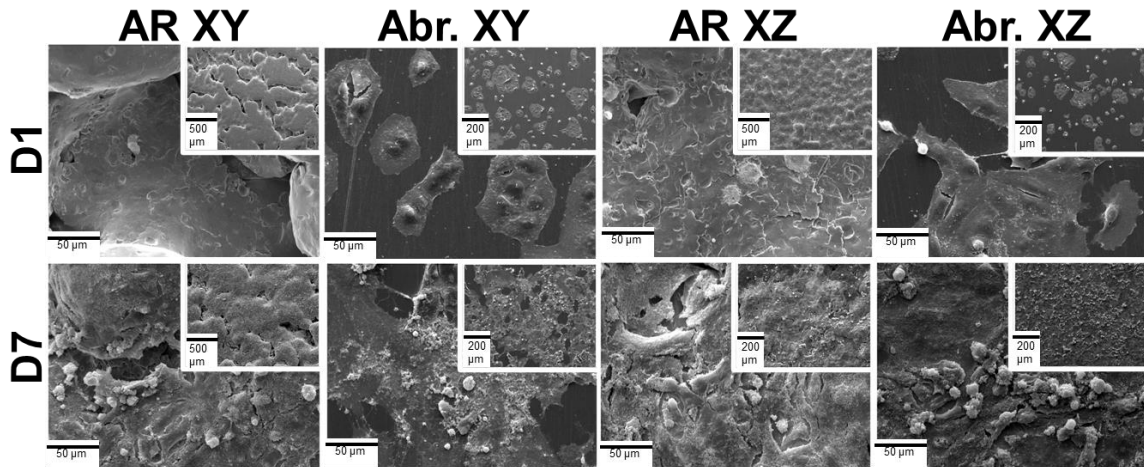
**Figure 5-5: SEM images of different specimens after immersion for 7 (D7), 14 (D14), and 28 (D28) days at 37 °C in simulated body fluid. Insets show overview images at lower magnification.**





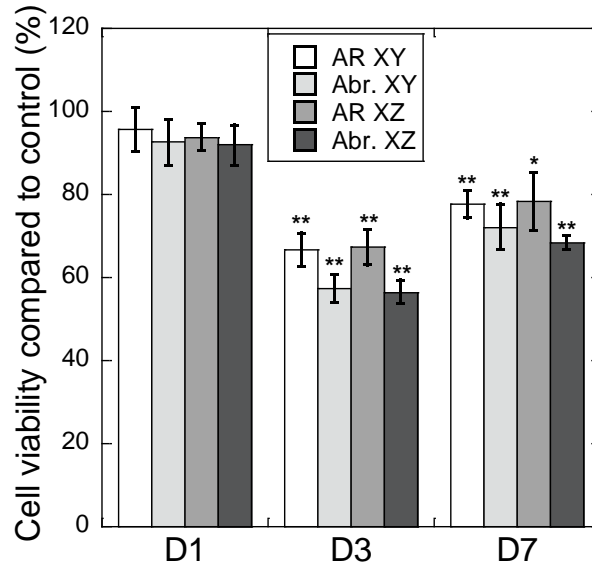
**Figure 5-6: Atomic Ca/P ratio (using EDS) of different specimens after immersion for 7 (D7), 14 (D14), and 28 (D28) days at 37 °C in simulated body fluid. The error bars show the standard deviation among triplicate measurements. The asterisks indicate statistically significant increases compared to the specimens after 7 days (D7): \* -  $p < 0.05$ ; \*\* -  $p < 0.01$ . Examples of corresponding SEM images are shown in Figure S8.**

Fig. 5-7 shows SEM images of the adhesion and expansion capability of MG63 cells cultured on the surface of as-received and abraded XY and XZ CoCrMo surfaces. Fewer cells were adhered on as-received than on polished surfaces after one day, independent of building direction. Over time, on Day 7, the rate of adhesion and cell proliferation increased sharply for all specimens. However, slightly more cells adhered to the as-received specimens after 7 days, possibly related to higher surface roughness [60]. The morphology of all cells on the surface of the specimens is relatively stretched, and the cells completely cover the surface after 7 days. Lamellipodia and filopodia can be seen at higher magnification, indicating the tendency of the cells to attach to the surface of the specimens.



**Figure 5-7: SEM images of the cell-seeded as-received (AR) or abraded (Abr.) XY and XZ CoCrMo surfaces after days 1 and 7. The inset images show images at lower magnification.**

The cell viability was determined using the MTT assay after one, three, and seven days, Fig. 5-8. There was no significant difference among the specimens. All specimens showed fully viable cells (compared to control) after one day but significantly decreased viability of cells after three and seven days. Some decrease of viability from Day 1 to 3 for the CoCrMo specimens was expected due to the control sample having better cell adhesion conditions due to the plasma treatment of the cell culture plates, which makes the well surfaces charged and hydrophilic. Thus, cells on the control surface started their proliferation phase faster than on the metallic surfaces, leading to higher viability for Day 1. The cell viability increased slightly for all specimens from Day 3 to Day 7 because, during this period, cells on the metallic specimens had enough time to secrete extracellular matrix proteins on the surface, aiding in adherence, migration, and proliferation of cells on the surface. After three and seven days, there was a slightly higher viability, however not statistically significant ( $P > 0.05$ ), for the as-received CoCrMo surfaces compared to their abraded counterparts. Based on the rate of cell viability in the MTT test, all specimens would be considered biocompatible materials by ISO-10993 [61].



**Figure 5-8: Cell viability as compared to control, determined using the MTT assay after 1 (D1), 3 (D3), and 7 (D7) days at 37 °C for triplicate specimens. The asterisks indicate a statistically significant decrease (\* -  $P < 0.05$ ; \*\* -  $P < 0.01$ ) in cell viability.**

### 5.3.5 Further discussion

As-received, rougher surfaces showed inferior corrosion barrier properties compared with abraded surfaces in this study. The difference in actual surface area cannot explain the difference. Like in this study, a negative influence of surface roughness on corrosion was reported for various LPBF materials [62-64]. It is well known that the LPBF specimens are associated with higher roughness (range from 10  $\mu\text{m}$  to 30  $\mu\text{m}$ ) than parts fabricated with conventional methods, such as milling ( $\sim 1 \mu\text{m}$ ) [11]. The surface roughness of the LPBF products can be affected by factors such as the fabrication strategy, laser power, powder geometry, and heat input [65]. However, the roughness is not the only factor changing between as-received and abraded surfaces. The crystal structure, microstructure, residual stresses, unfused particles, and impacts from surface treatments (sandblasting, grinding) are also changing [16; 66], so it is not straightforward to determine which physicochemical factor influenced corrosion and biocompatibility most.

While the rougher, as-received surfaces had detrimental corrosion behavior in this study, they showed higher bioactivity (adsorption of hydroxyapatite) and slightly higher cell

viability. It has been reported that hydroxyapatite acts as a barrier layer and is beneficial for the corrosion resistance of CoCrMo [67]. Various factors such as porosity, surface properties, mechanical properties and ion release rate can affect the biological activities of cells [9]. Increasing surface roughness at the micro and nano scales has been shown to increase cell interaction and adhesion to the surface [2]. Therefore, the slightly increased cell viability of the rougher, as-received, CoCrMo surfaces in this study was expected.

Using potentiodynamic polarization, only the combination of citrate species and oxidative potentials resulted in higher corrosion/dissolution for CoCrMo in this study. This observation agrees with the reported corrosion current densities of CoCrMo as a function of citrate concentration [56], only slightly changing at the concentration of citrate used in this study (26 mM). The increased current of CoCrMo specimens at high oxidation potential and in the presence of citrate species is interesting from several perspectives. First, complexation caused by citrate is very similar to what is expected in physiological environments, where many biomolecules have complexing properties to metals. Citrate species are only able to complex metals at pH values, for which they are not fully protonated, so the control solution of citric acid at pH 2.4 is not a complexing solution [23]. It has previously been reported that there can be synergistic effects of oxidizing and complexing agents for the dissolution of metals from passive surface oxides, as reported for proteins and hydrogen peroxide for titanium-aluminum alloys [68]. While applied potentials are not directly relevant to the human body, they simulate inflammatory and infectious conditions under which strong oxidative redox potentials can occur [8; 69]. Without any applied potential, the presence of citrate instead resulted in an increased corrosion resistance, as evident from this study's EIS measurements at open circuit potential. This agrees with findings in a combined electrochemical and XPS study on CoCrMo, suggesting that Co preferentially dissolves in the presence of citrate and that passivity is only affected at elevated potential ranges (under oxidation) in similar testing conditions as in this study [32].

This study found a higher corrosion susceptibility for as-received surfaces built in the XY plane compared with the XZ plane for highly dense LPBF CoCrMo specimens. This difference disappeared after surface abrasion – removing the influence of surface

roughness and surface treatments. XPS further revealed minor differences in oxide thickness and composition. Hence, we suspect that the as-built surface, but not underlying layers or anisotropy of the microstructure, cause the differences in corrosion behavior. The XZ plane had more defects and more melt pool boundaries. Our specimens were prepared after a biomedical manufacturing protocol, using heat treatment and low-carbon CoCrMo feed powder, resulting in negligible carbide precipitates at grain boundaries. This means that any detrimental microstructure anisotropy was minimized in this study. The beneficial effects of heat treatment and low carbon have been reported previously [56]. An electrochemical study [8] on abraded LPBF CoCrMo (low carbon, but not heat treated) in NaCl with H<sub>2</sub>O<sub>2</sub> revealed a higher corrosion susceptibility (lower corrosion resistance) for the XY than the XZ plane, explained by more grain boundaries and secondary precipitates. Discussions in these and other [29, 49] studies have suggested that the number of grain boundaries can have both positive and negative effects on the corrosion resistance and that secondary phases and grain boundary precipitates are to be avoided. This work highlights that a suitable heat treatment strategy can eliminate any anisotropic effects of microstructure in LPBF CoCrMo.

This study is limited by its experimental conditions and design. Lower corrosion resistance under static corrosion testing conditions for the as-received XY plane was found but also higher cell viability and bioactivity for the as-received surfaces. It remains to be investigated which effects would dominate the corrosion process under long-term in-vivo conditions. Future studies should also examine the tribocorrosion behavior, which would be most relevant for CoCrMo alloys.

## 5.4 Conclusions

This study aimed to investigate the corrosion resistance, bioactivity, biocompatibility, and microstructure of LPBF CoCrMo (low carbon content, heat treated) in the XY and XZ plane of the building direction for as-printed (as-received) and abraded surfaces. The following main conclusions were drawn:

1. LPBF printing resulted in distinct microstructures for XY and XZ planes. As-received XY was coarser than XZ.
2. As-received XY showed the lowest corrosion resistance among the specimens. As-received surface conditions resulted in lower corrosion resistance than abraded surfaces, even when considering the actual surface area. There was no influence of building direction on corrosion resistance, bioactivity, or cell viability for abraded surfaces. Hence, the lower corrosion resistance for as-received surfaces was caused by surface factors and not microstructural features.
3. Hydroxyapatite precipitated and formed on all surfaces but slightly more on as-received (rough) surfaces. Likewise, in terms of cell viability, all surfaces counted as biocompatible. However, the as-received surfaces had slightly higher cell viability.
4. All CoCrMo surfaces exhibited passive conditions and were not showing signs of localized corrosion in citric acid (pH 2.4), PBS (pH 7.4), and PBS and citric acid (pH 7.4).
5. PBS containing the complexing citrate species from citric acid at pH 7.4 resulted in lower corrosion resistance as compared to both PBS (pH 7.4) and citric acid (pH 2.4) alone, but only at elevated (oxidative) potentials. The lowest corrosion resistance was found in PBS by electrochemical impedance spectroscopy at open circuit potential, probably due to an acceleration of passive film formation by the citrate species.

## 5.5 References

- [1] Nouri, A., et al. "Additive Manufacturing of Metallic and Polymeric Load-Bearing Biomaterials Using Laser Powder Bed Fusion: A Review." *Journal of Materials Science & Technology*, vol. 94, 2021, pp. 196-215.
- [2] Shekhawat, D., et al. "A Short Review on Polymer, Metal and Ceramic Based Implant Materials." *IOP Conference Series: Materials Science and Engineering*, vol. 1017, IOP Publishing, 2021, p. 012038.
- [3] Zhou, J., et al. "Biomaterials and Nanomedicine for Bone Regeneration: Progress and Future Prospects." *Exploration*, vol. 1, Wiley Online Library, 2021, p. 20210011.
- [4] Atapour, M., et al. "Corrosion and Metal Release Investigations of Selective Laser Melted 316L Stainless Steel in a Synthetic Physiological Fluid Containing Proteins and in Diluted Hydrochloric Acid." *Electrochimica Acta*, vol. 354, 2020, p. 136748.
- [5] Ghomi, E. R., et al. "Future of Additive Manufacturing in Healthcare." *Current Opinion in Biomedical Engineering*, vol. 17, 2021, p. 100255.
- [6] Zhou, K., et al. "Effect of Surface Energy on Protein Adsorption Behaviors of Treated CoCrMo Alloy Surfaces." *Applied Surface Science*, vol. 520, 2020, p. 146354.
- [7] De Castro Girão, D., et al. "An Assessment of Biomedical CoCrMo Alloy Fabricated by Direct Metal Laser Sintering Technique for Implant Applications." *Materials Science and Engineering: C*, vol. 107, 2020, p. 110305.
- [8] Hu, Y., et al. "Degradation Behavior of Selective Laser Melted CoCrMo Alloys in H<sub>2</sub>O<sub>2</sub>-Containing Chloride Solutions." *Corrosion Science*, vol. 195, 2022, p. 109981.
- [9] Bandyopadhyay, A., et al. "Additively Manufactured Calcium Phosphate Reinforced CoCrMo Alloy: Bio-Tribological and Biocompatibility Evaluation for Load-Bearing Implants." *Additive manufacturing*, vol. 28, 2019, pp. 312-324.

- [10] Cortis, G., et al. "Additive Manufacturing Structural Redesign of Hip Prostheses for Stress-Shielding Reduction and Improved Functionality and Safety." *Mechanics of Materials*, vol. 165, 2022, p. 104173.
- [11] Kong, D., et al. "Corrosion of Metallic Materials Fabricated by Selective Laser Melting." *npj Materials Degradation*, vol. 3, no. 1, 2019, p. 24.
- [12] Mirea, R., et al. "In Vitro Physical-Chemical Behavior Assessment of 3d-Printed CoCrMo Alloy for Orthopaedic Implants." *Metals*, vol. 11, no. 6, 2021, p. 857.
- [13] Hedberg, Y. S., et al. "Metal Release and Speciation of Released Chromium from a Biomedical CoCrMo Alloy into Simulated Physiologically Relevant Solutions." *Journal of Biomedical Materials Research Part B: Applied Biomaterials*, vol. 102, no. 4, 2014, pp. 693-699.
- [14] Cornacchia, G., et al. "Microstructural, Mechanical, and Tribological Characterization of Selective Laser Melted CoCrMo Alloy under Different Heat Treatment Conditions and Hot Isostatic Pressing." *Advanced Engineering Materials*, vol. 24, no. 4, 2022, p. 2100928.
- [15] Li, H. Q., et al. "Tribological and Corrosion Performance of the Plasma-Sprayed Conformal Ceramic Coating on Selective Laser Melted CoCrMo Alloy." *Journal of the Mechanical Behavior of Biomedical Materials*, vol. 119, 2021, p. 104520.
- [16] Hedberg, Y. S., et al. "In-Vitro Biocompatibility of CoCrMo Dental Alloys Fabricated by Selective Laser Melting." *Dental materials*, vol. 30, no. 5, 2014, pp. 525-534.
- [17] Li, J., et al. "The Effect of Specific Energy Density on Microstructure and Corrosion Resistance of CoCrMo Alloy Fabricated by Laser Metal Deposition." *Materials*, vol. 12, no. 8, 2019, p. 1321.
- [18] Dong, X., et al. "Influence of Microstructure on Corrosion Behavior of Biomedical Co-Cr-Mo-W Alloy Fabricated by Selective Laser Melting." *Corrosion Science*, vol. 170, 2020, p. 108688.



- [19] Kajima, Y., et al. "Reduction in Anisotropic Response of Corrosion Properties of Selective Laser Melted Co–Cr–Mo Alloys by Post-Heat Treatment." *Dental materials*, vol. 37, no. 3, 2021, pp. 98-108.
- [20] Tonelli, L., et al. "CoCr Alloy Processed by Selective Laser Melting (Slm): Effect of Laser Energy Density on Microstructure, Surface Morphology, and Hardness." *Journal of Manufacturing Processes*, vol. 52, 2020, pp. 106-119.
- [21] Atapour, M., et al. "Corrosion of Binder Jetting Additively Manufactured 316L Stainless Steel of Different Surface Finish." *Journal of the Electrochemical Society*, vol. 167, no. 13, 2020, p. 131503.
- [22] Mazinianian, N., et al. "Influence of Citric Acid on the Metal Release of Stainless Steels." *Corrosion Science and Technology*, vol. 14, no. 4, 2015, pp. 166-171.
- [23] Mazinianian, N., et al. "Metal Release Mechanisms for Passive Stainless Steel in Citric Acid at Weakly Acidic Ph." *Journal of the Electrochemical Society*, vol. 163, no. 10, 2016, pp. C686-C693.
- [24] Hedberg, Y. S., et al. "Metal Release from Stainless Steel Powders and Massive Sheet – Comparison and Implication for Risk Assessment of Alloys." *Environmental Science: Processes & Impacts*, vol. 15, no. 2, 2013, pp. 381-392.
- [25] Kocijan, A., et al. "The Influence of Complexing Agent and Proteins on the Corrosion of Stainless Steels and Their Metal Components." *Journal of Materials Science: Materials in Medicine*, vol. 14, no. 1, 2003, pp. 69-77.
- [26] Biesinger, M. C., et al. "Resolving Surface Chemical States in XPS Analysis of First Row Transition Metals, Oxides and Hydroxides: Cr, Mn, Fe, Co and Ni." *Applied Surface Science*, vol. 257, no. 7, 2011, pp. 2717-2730.
- [27] Baltrusaitis, J., et al. "Generalized Molybdenum Oxide Surface Chemical State XPS Determination Via Informed Amorphous Sample Model." *Applied Surface Science*, vol. 326, 2015, pp. 151-161.

- [28] Biesinger, M. C. "X-Ray Photoelectron Spectroscopy (XPS) Reference Pages. 2020." 2018.
- [29] Al-Mamun, N. S., et al. "Corrosion Behavior and Biocompatibility of Additively Manufactured 316l Stainless Steel in a Physiological Environment: The Effect of Citrate Ions." *Additive manufacturing*, vol. 34, 2020, p. 101237.
- [30] Duffo, G. S., et al. "Development of an Artificial Saliva Solution for Studying the Corrosion Behavior of Dental Alloys." *Corrosion*, vol. 60, no. 6, 2004, pp. 594-602.
- [31] Milosev, I., et al. "The Behavior of Stainless Steels in Physiological Solution Containing Complexing Agent Studied by X-Ray Photoelectron Spectroscopy." *Journal of biomedical materials research*, vol. 52, no. 2, 2000, pp. 404-412.
- [32] Milošev, I., et al. "The Composition of the Surface Passive Film Formed on CoCrMo Alloy in Simulated Physiological Solution." *Electrochimica Acta*, vol. 48, no. 19, 2003, pp. 2767-2774.
- [33] Kokubo, T., et al. "How Useful Is SBF in Predicting in Vivo Bone Bioactivity?" *Biomaterials*, vol. 27, no. 15, 2006, pp. 2907-2915.
- [34] Li, H., et al. "Microstructural Features of Biomedical Cobalt–Chromium–Molybdenum (CoCrMo) Alloy from Powder Bed Fusion to Aging Heat Treatment." *Journal of Materials Science & Technology*, vol. 45, 2020, pp. 146-156.
- [35] Sing, S. L., et al. "Effect of Solution Heat Treatment on Microstructure and Mechanical Properties of Laser Powder Bed Fusion Produced Cobalt-28chromium-6molybdenum." *Materials Science and Engineering: A*, vol. 769, 2020, p. 138511.
- [36] Aripin, M. A., et al. "Effects of Build Orientations on Microstructure Evolution, Porosity Formation, and Mechanical Performance of Selective Laser Melted 17-4 Ph Stainless Steel." *Metals*, vol. 12, no. 11, 2022, p. 1968.

- [37] Yamanaka, K., et al. "Local Strain Evolution Due to Athermal  $\Gamma \rightarrow E$  Martensitic Transformation in Biomedical CoCrMo Alloys." *Journal of the Mechanical Behavior of Biomedical Materials*, vol. 32, 2014, pp. 52-61.
- [38] Zhang, Y., et al. "Enhancing the Mechanical Property of Laser Powder Bed Fusion CoCrMo Alloy by Tailoring the Microstructure and Phase Constituent." *Materials Science and Engineering: A*, vol. 862, 2023, p. 144449.
- [39] Biesinger, M. C. "Assessing the Robustness of Adventitious Carbon for Charge Referencing (Correction) Purposes in XPS Analysis: Insights from a Multi-User Facility Data Review." *Applied Surface Science*, vol. 597, 2022, p. 153681.
- [40] Wei, Z., et al. "Metal Release from a Biomedical CoCrMo Alloy in Mixed Protein Solutions under Static and Sliding Conditions: Effects of Protein Aggregation and Metal Precipitation." *Journal of Bio-and Tribo-Corrosion*, vol. 8, no. 1, 2022, pp. 1-11.
- [41] Sovar, M. M., et al. "Stability of Bioactivated Co-Cr Alloys in Biological Environment." *Key Engineering Materials*, vol. 361, Trans Tech Publ, 2008, pp. 737-740.
- [42] Hodgson, A. W. E., et al. "Passive and Transpassive Behavior of CoCrMo in Simulated Biological Solutions." *Electrochimica Acta*, vol. 49, no. 13, 2004, pp. 2167-2178.
- [43] Mahlooji, E., et al. "Electrophoretic Deposition of Bioactive Glass–Chitosan Nanocomposite Coatings on Ti-6Al-4V for Orthopedic Applications." *Carbohydrate Polymers*, vol. 226, 2019, p. 115299.
- [44] Bettini, E., et al. "Influence of Metal Carbides on Dissolution Behavior of Biomedical CoCrMo Alloy: SEM, TEM and AFM Studies." *Electrochimica Acta*, vol. 56, no. 25, 2011, pp. 9413-9419.
- [45] Hsu, R. W. W., et al. "Electrochemical Corrosion Studies on Co–Cr–Mo Implant Alloy in Biological Solutions." *Materials Chemistry and Physics*, vol. 93, no. 2, 2005, pp. 531-538.

- [46] Liverani, E., et al. "Corrosion Resistance and Mechanical Characterization of Ankle Prostheses Fabricated Via Selective Laser Melting." *Procedia CIRP*, vol. 65, 2017, pp. 25-31.
- [47] Valero, V. C., et al. "Electrochemical Characterisation of Biomedical Alloys for Surgical Implants in Simulated Body Fluids." *Corrosion Science*, vol. 50, no. 7, 2008, pp. 1954-1961.
- [48] Sander, G., et al. "On the Corrosion and Metastable Pitting Characteristics of 316L Stainless Steel Produced by Selective Laser Melting." *Journal of the Electrochemical Society*, vol. 164, no. 6, 2017, p. C250.
- [49] Gong, X., et al. "Corrosion Behavior of CoCrMo Alloy Fabricated by Electron Beam Melting." *Corrosion Science*, vol. 139, 2018, pp. 68-75.
- [50] Ribeiro, A. M., et al. "Synergism between Corrosion and Wear on CoCrMo–Al<sub>2</sub>O<sub>3</sub> Biocomposites in a Physiological Solution." *Tribology International*, vol. 91, 2015, pp. 198-205.
- [51] Xiang, D. D., et al. "Improving Biotribological Properties and Corrosion Resistance of CoCrMo Alloy Via a Cr-Glc Nanocomposite Film in Simulated Body Fluids." *Surface and Coatings Technology*, vol. 378, 2019, p. 124840.
- [52] Vidal, C. V., et al. "Adsorption of Bovine Serum Albumin on CoCrMo Surface: Effect of Temperature and Protein Concentration." *Colloids and Surfaces B: Biointerfaces*, vol. 80, no. 1, 2010, pp. 1-11.
- [53] Kötz, R., et al. "Principles and Applications of Electrochemical Capacitors." *Electrochimica Acta*, vol. 45, no. 15-16, 2000, pp. 2483-2498.
- [54] Hirschorn, B., et al. "Determination of Effective Capacitance and Film Thickness from Constant-Phase-Element Parameters." *Electrochimica Acta*, vol. 55, no. 21, 2010, pp. 6218-6227.

- [55] Namus, R., et al. "The Influence of Cathodic Potentials on the Surface Oxide Layer Status and Tribocorrosion Behavior of Ti6Al4V and CoCrMo Alloys in Simulated Body Fluid." *Biotribology*, vol. 30, 2022, p. 100212.
- [56] Kocijan, A., et al. "Electrochemical Study of Co-Based Alloys in Simulated Physiological Solution." *Journal of Applied Electrochemistry*, vol. 34, no. 5, 2004, pp. 517-524.
- [57] Muñoz, A. I., et al. "Interactive Effects of Albumin and Phosphate Ions on the Corrosion of CoCrMo Implant Alloy." *Journal of the Electrochemical Society*, vol. 154, no. 10, 2007, pp. C562-C570.
- [58] Zhang, B., et al. "Defect Formation Mechanisms in Selective Laser Melting: A Review." *Chinese Journal of Mechanical Engineering*, vol. 30, 2017, pp. 515-527.
- [59] Chaharmahali, R., et al. "Surface Characterization and Corrosion Behavior of Calcium Phosphate (Ca-P) Base Composite Layer on Mg and Its Alloys Using Plasma Electrolytic Oxidation (PEO): A Review." *Journal of Magnesium and Alloys*, vol. 9, no. 1, 2021, pp. 21-40.
- [60] Rosales, L. J. I., et al. "Effect of Roughness, Wettability and Morphology of Engineered Titanium Surfaces on Osteoblast-Like Cell Adhesion." *Colloids and Surfaces A: Physicochemical and Engineering Aspects*, vol. 365, no. 1-3, 2010, pp. 222-229.
- [61] Cambiaghi, A. "Biological Evaluation of Medical Devices as an Essential Part of the Risk Management Process: Updates and Challenges of ISO 10993-1: 2018." *Eurofins Medical Device Testing*: Lancaster, PA, USA, 2018.
- [62] Leon, A., et al. "Effect of Surface Roughness on Corrosion Fatigue Performance of AlSi10Mg Alloy Produced by Selective Laser Melting (SLM)." *Materials Characterization*, vol. 131, 2017, pp. 188-194.
- [63] Hilbert, L. R., et al. "Influence of Surface Roughness of Stainless Steel on Microbial Adhesion and Corrosion Resistance." *International Biodeterioration & Biodegradation*, vol. 52, no. 3, 2003, pp. 175-185.

- [64] Deligianni, D. D., et al. "Effect of Surface Roughness of the Titanium Alloy Ti-6Al-4V on Human Bone Marrow Cell Response and on Protein Adsorption." *Biomaterials*, vol. 22, no. 11, 2001, pp. 1241-1251.
- [65] Calignano, F., et al. "Influence of Process Parameters on Surface Roughness of Aluminum Parts Produced by DMLS." *The International Journal of Advanced Manufacturing Technology*, vol. 67, 2013, pp. 2743-2751.
- [66] Panigrahi, P., et al. "Intergranular Pitting Corrosion of CoCrMo Biomedical Implant Alloy." *Journal of Biomedical Materials Research Part B: Applied Biomaterials*, vol. 102, no. 4, 2014, pp. 850-859.
- [67] Khobragade, N. N., et al. "Effect of Concentration and Surface Roughness on Corrosion Behavior of Co-Cr-Mo Alloy in Hyaluronic Acid." *Materials Research Express*, vol. 5, no. 1, 2018, p. 015403.
- [68] Hedberg, Y. S., et al. "Mechanistic Insight on the Combined Effect of Albumin and Hydrogen Peroxide on Surface Oxide Composition and Extent of Metal Release from Ti6Al4V." *Journal of Biomedical Materials Research Part B: Applied Biomaterials*, vol. 107, no. 3, 2019, pp. 858-867.
- [69] Larsen, A., et al. "In Vitro Liberation of Charged Gold Atoms: Autometallographic Tracing of Gold Ions Released by Macrophages Grown on Metallic Gold Surfaces." *Histochemistry and cell biology*, vol. 128, no. 1, 2007, pp. 1-6.

## Chapter 6

# 6 The Influence of the Manufacturing Process on the Corrosion of CoCrMo Alloy in Simulated Physiological Environments

## 6.1 Introduction

CoCrMo alloys are high-performance materials that are widely used in the biomedical field due to their excellent strength, wear resistance and corrosion resistance [1-3]. Additionally, they have been shown to be biocompatible, which makes them suitable for use as medical implants and in other applications within the human body [4]. CoCrMo alloys are cobalt-based alloys that are known for their ability to withstand high loads and extreme environments. Their unique combination of properties makes them ideal for use in a variety of biomedical applications, such as orthopedic implants, dental implants, and surgical instruments [5-7].

The principles and concepts of additive manufacturing have been established since the introduction of the layer-by-layer fabrication of metals by selectively melting powders using electrons, lasers, or plasma beams by Ciraud in a 1972 patent [8]. In recent years, additive manufacturing has seen numerous applications in the biomedical field, including the production of medical implants, prosthetics, and other devices, allowing for the creation of highly customized and intricate products [9].

The benefits of using additive manufacturing to produce biomedical CoCrMo components are many, as compared to traditional manufacturing methods. One of the key advantages is the capability to design and produce sophisticated and complex geometries, which might be challenging or impossible to achieve through traditional methods [10]. By using additive manufacturing, it is feasible to produce components that have intricate internal structures, complicated shapes, and multiple material layers in a single manufacturing cycle [11]. This enables the production of highly customized products that are tailored to meet specific functional requirements. And not only that, but also the

additive manufactured low carbon CoCrMo alloy, have higher corrosion resistance and lower metal release susceptibility than cast alloy [12].

The building orientation in an additive manufacturing process refers to the orientation of the part relative to the building direction. The orientation of the part may have an influence on its mechanical properties and the microstructure distribution [13-17], which can have a significant impact on the quality and performance of the CoCrMo alloy component produced. The building orientation can have an impact on the microstructure and surface finish of the CoCrMo alloy, which can ultimately affect its corrosion resistance [18; 19]. Then, it can lead to an increased risk of metal release. As the corrosion process proceeds, new surfaces may be created on the metal, which are then exposed to the biological environment and may release metal ions. Therefore, the building orientation may have an influence on the metal release of the CoCrMo alloy produced by additive manufacturing.

The aim of this study is to study the metal release process of CoCrMo alloy produced by laser powder bed fusion (LPBF - a common additive manufacturing method to produce fully dense parts for biomedical implants) as a function of the building orientation. This is studied by solution analytical, surface analytical, and electrochemical methods in a simulated physiological environment containing bovine serum albumin or hydrochloric acid (simulating confined spaces).

## 6.2 Materials and Methods

### 6.2.1 Materials and sample preparation

Materials used in this study were provided by Additive Design in Surgical Solutions Centre (Renishaw AM 400 Selective Laser Melting System) in form of additively manufactured coupons. All test alloy substrates were produced using an inert gas-atomized powder with a mean particle size of approximately 15-45  $\mu\text{m}$  (Renishaw, UK). The chemical composition of the powder is listed in Table 6-1. Specimens were printed to 15 mm width  $\times$  15 mm length  $\times$  2 mm thickness by the LPBF method and built in two different orientations as shown in Figure 6-1; one with the long side parallel to the



building direction (XOZ) and the other with the long side perpendicular to the building direction (XOY).

**Table 6-1: Chemical composition of the CoCrMo alloy powder. Bal. – balance (remainder to 100 wt.%).**

Element	Co	Cr	Mo	Mn	Si	N	Fe	Ni	C	W
wt. %	Bal.	28.0	6.10	0.77	0.57	0.22	0.20	0.05	0.02	0.02

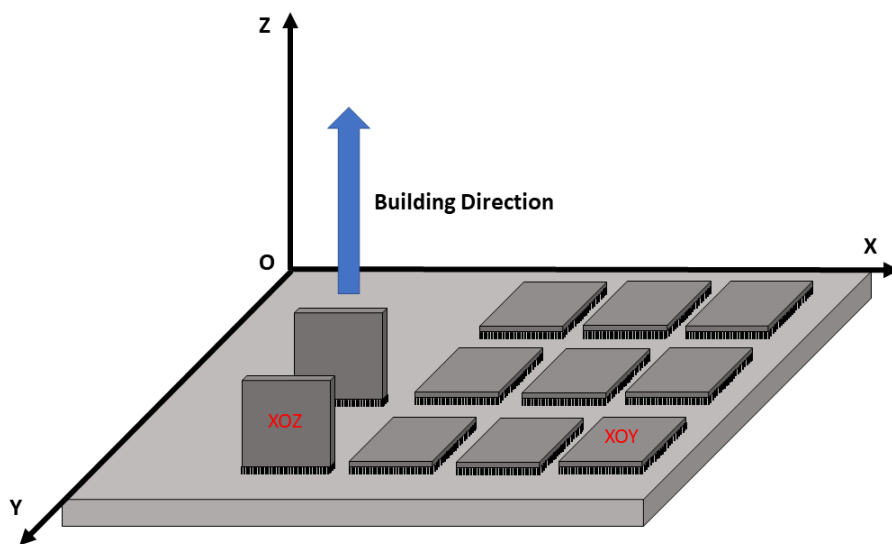


**Figure 6-1: Building direction and orientation of LPBF printed CoCrMo alloy coupons.**

A layer thickness of 40  $\mu\text{m}$ , a beam size of 70  $\mu\text{m}$ , and a laser power of 200 W were applied. The laser was discontinuous, the exposure time varied between 40 and 50  $\mu\text{s}$  depending on the location, and the point distance varied between 60 and 70  $\mu\text{m}$ . One layer was rotated 67° to the previous layer. The scan speed was approximately 2 m/s. After being fabricated, the additively manufactured coupons underwent a heat treatment process to improve their microstructure, enhance mechanical properties, improve dimensional stability, and relieve residual stress. The heat treatment process involved gradually heating the coupons to 450 °C over a period of 60 minutes, holding them at this

temperature for 45 minutes, reheating to 750 °C over 45 minutes, holding them at this temperature for 60 minutes, and then cooling them to room temperature in a furnace (Figure 6-2).

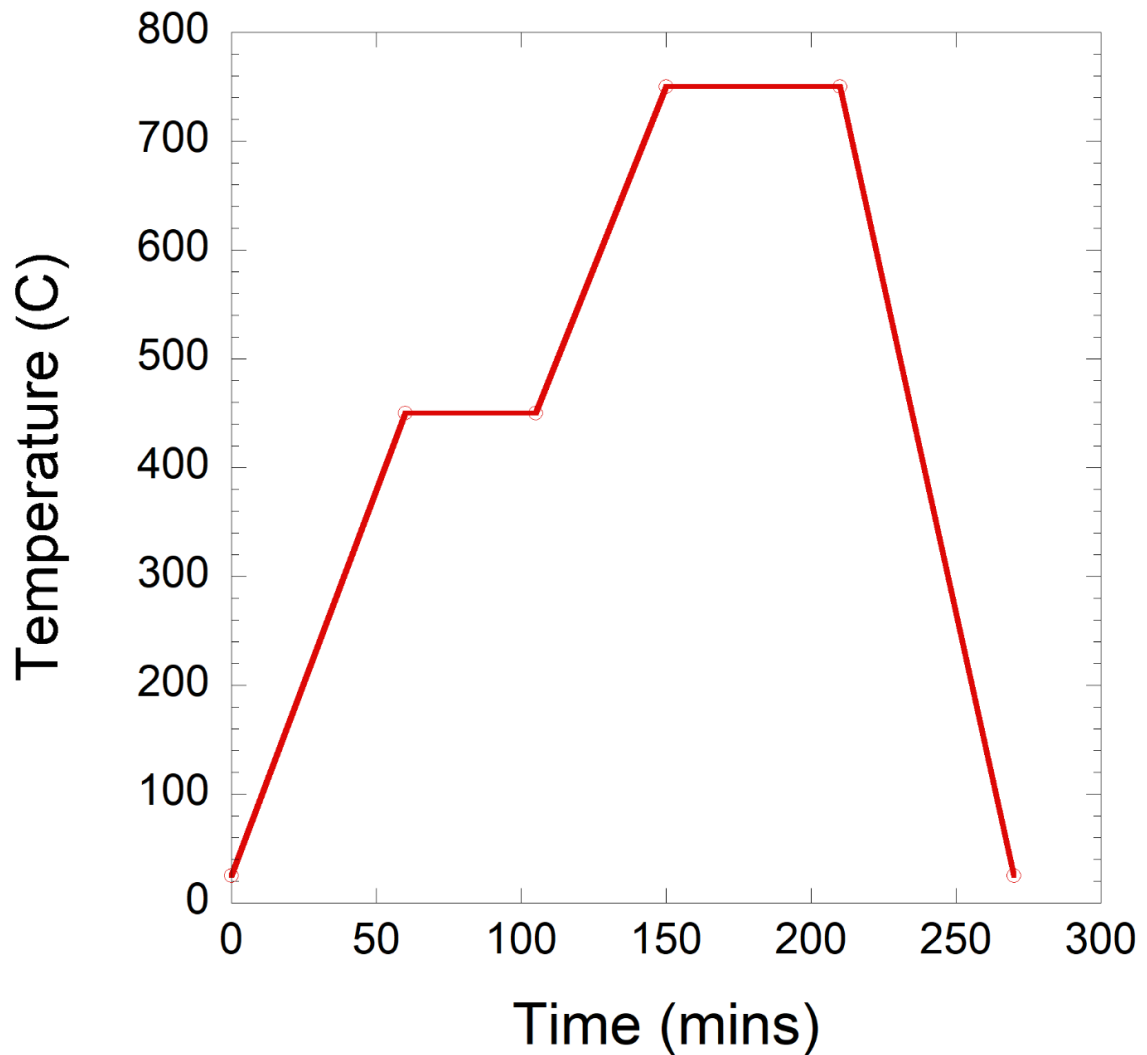


**Figure 6-2: The heat treatment process after the additive manufacturing process.**

The coupons were then sandblasted with ceramic beads (ZirPro Microblast®) in the size of 63-125  $\mu\text{m}$  with a composition of zirconia, silica (28-33 wt.%) and alumina (<10 wt.%). The sand blasting improves the surface finish of the coupons.

Half of the coupons were ultrasonically cleaned in acetone and isopropyl alcohol for 5 minutes subsequently and dried by nitrogen gas at room temperature. Those were referred

to as “as-received”. The second half of the coupons were ground to P1200 using SiC paper, and mirror-polished to 1  $\mu\text{m}$  using water-based diamond particles and deionized water. Thereafter, they were ultrasonically cleaned in acetone and isopropyl alcohol and dried by nitrogen gas which was referred to as “polished”.

### 6.2.2 Metal release test procedure and electrochemistry measurements

After the polishing or cleaning, the prepared coupons were placed for 24 hours in a desiccator (<10% relative humidity) to grow the surface oxide reproducibly prior to the electrochemical measurements. The relatively rough surface conditions of the as-received coupons and the need to study as-received conditions disabled the use of embedding procedures and flat-cell-designed electrochemical cells. Therefore, the coupon was clamped in a platinum plated electrode holder and completely immersed in the 50 mL solution (see below). One blank sample (solution without any coupons) and triplicate samples were exposed in parallel for each material and solution. The exposure was conducted in an acid-cleaned water-jacked electrochemical cell for 24 hours. The temperature of exposure was controlled at 37 °C (VWR Refrigerated Circulating Bath). Two different solutions were used in this study, simulating normal physiological conditions and crevice conditions (a confined space in the implant design, in which the pH can drop significantly), respectively. The normal physiological conditions were simulated by 5 mM 2-(N-morpholino)ethanesulfonic acid (MES), 5 g/L NaCl, and 10 g/L bovine serum albumin (A7906, Sigma Aldrich), adjusted with 50% NaOH to pH 7.2-7.4, and ultrapure water (18.2 M $\Omega$ cm resistivity, Millipore, Canada). The crevice conditions were simulated by a 0.027 mM HCl solution (pH 1.5-1.7). The MES buffer was chosen as buffer instead of a phosphate buffer because phosphate ions can bind to cobalt ions, which has previously been shown to cause precipitation [20-22]. The precipitation may cause an underestimation of the metal release from the CoCrMo alloy. A concentration of 10 g/L bovine serum albumin (BSA) was selected as a high protein concentration (simulating the protein concentration found in human body fluids) that still would minimize the effect of protein aggregation and precipitation [23]. Also, it is very close to the expected concentration of 12 g/L of albumin in synovial fluid [24]. The

electrochemistry measurements were performed concurrently with the exposure. After 24 hours exposure time, the coupons were rinsed with 1 mL ultrapure water to add any surface-adhered released metals to the solution for analysis. The solution was sampled and adjusted to a pH below 2 for initial solution preservation prior to the analysis with inductively coupled plasma mass spectrometry (ICP-MS) on cobalt (Co), chromium (Cr) and molybdenum (Mo) (see next sections). The coupons were placed back into 50 mL of fresh solution prior to potentiodynamic polarization.

The electrochemical measurements were performed using a Solartron Modulab PSTAT 1MS/s connected to a unified power system (APC smart-UPS C SMC1500C) with a three-electrode setup. An Ag/AgCl (saturated KCl) electrode was used as reference electrode and a platinum wire as the counter electrode, while the working electrode was the coupon being tested, which was clamped by a platinum plated electrode holder (Figure 6-3). The open circuit potential (OCP), electrochemical impedance spectroscopy (EIS) and potentiodynamic polarization (PDP) were performed in both solutions. The experimental procedure of the exposure and electrochemical measurement is shown in Figure 6-4. EIS was performed after 10 min and 21 hours OCP by applying an alternating current voltage with an amplitude of 10 mV<sub>rms</sub> and sweeping the frequency from 100,000 Hz to 0.001 Hz. The aim of the non-destructive EIS measurements was to investigate the corrosion resistance and any protein adsorption on the CoCrMo alloy as a function of time, while also allowing metal release measurements. The corrosion resistance of the material was further assessed by performing PDP. This was done by scanning from OCP to a positive voltage of 1.25 V versus OCP at a scan speed of 0.167 mV/s. The PDP measurements were performed after 24 hours exposure and 10 mins OCP stabilization. After the electrochemical measurements, the coupons were rinsed with ultrapure water, dried with nitrogen gas, and stored in a desiccator prior to the surface analysis.

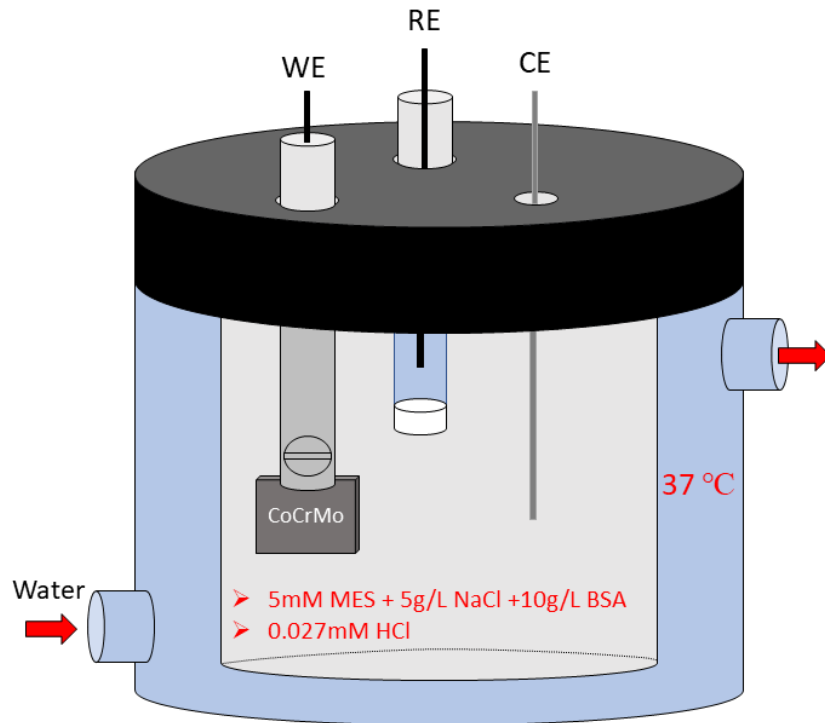


**Figure 6-3: Schematic drawing of exposure and electrochemical measurement.**

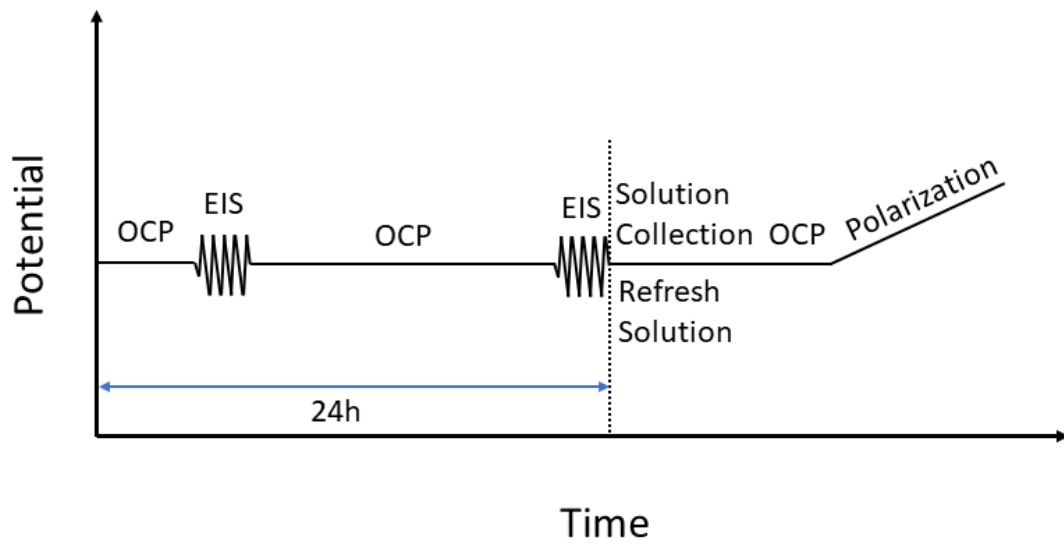


**Figure 6-4: Experimental procedure of exposure and electrochemical measurement.**

### 6.2.3 Microwave digestion

In preparation of ICP-MS analysis, all protein-rich solution samples were digested to prevent the formation of hydrogels in the samples and the potential loss of analyte. 3 mL of each protein-rich solution samples (MES, NaCl, BSA) were diluted four times with diluted nitric acid (1.89 vol.% HNO<sub>3</sub>) and digested using a Milestone ETHOD microwave digester (EPA method 3025). The temperature ramp settings were 170 °C over 10 min and 10 min hold time at 170 °C. The final dilution factor was calculated by the ratio between the final volume of the diluted solution samples to the initial sample volume.

### 6.2.4 Trace metal analysis in solution

The concentration of Co, Cr and Mo ions in the solution samples were quantified using ICP-MS (iCAP Q; Thermo Scientific, Canada). The limits of detection (LOD) and the limits of quantification (LOQ) are provided in Table 6-2. These were calculated by 3 and 10 times the standards deviation of the noise level, respectively. For the calibration, standard solutions of 0, 10, 30, 60 and 100 µg/L Co, Cr and Mo were prepared in the digested 5 mM MES+ 10 g/L NaCl + 10 g/L BSA blank solution diluted with 2 % HNO<sub>3</sub>, and used to analyze the amount of released, non-precipitated metals from CoCrMo immersed in the protein-rich solution. In addition, the standard solutions of 0, 10, 30, 60 and 100 µg/L Co, Cr and Mo were prepared in the 2% HNO<sub>3</sub> for analyzing the amount of released, non-precipitated metals from CoCrMo immersed in the 0.027 M HCl. When the concentration of the samples exceeded the range of the calibration, they were diluted and re-analyzed.

**Table 6-2: The limits of detection and quantification of Co, Cr and Mo.**

	LOD (µg/L)	LOQ (µg/L)
Co	0.001	0.002
Cr	0.002	0.006
Mo	<0	<0

### 6.2.5 X-ray diffraction (XRD) analysis

The as-received and polished specimens with different building orientations were measured by X-ray diffraction (Rigaku SmartLab X-R-D) to obtain crystallographic phase information. XRD was performed with a Cu  $K_{\alpha}$  ( $\lambda=1.5405981 \text{ \AA}$ ) X-ray radiation source, 40 KV, 45 mA, a scanning speed of 3 deg/min between  $20^{\circ}$  and  $80^{\circ}$  ( $2\theta$ ), and data was analyzed by HighScore Plus software (Version 3.0e).

### 6.2.6 Scanning electron microscopy (SEM) and confocal microscopy

Scanning electron microscopy (SEM) was conducted using a Hitachi SU3500 and Hitachi SU3900 instrument, with backscattered electrons as the imaging mode. Energy dispersive X-ray spectroscopy was conducted using a beam energy of 10 keV. The surface topography mapping and roughness measurements were performed using a ZEISS LSM 800 confocal microscope, which was manufactured by Carl Zeiss Microscopy GmbH. The roughness measurements were calculated using version 7.4.8341 of Mountains ConfoMap software. The calculations were performed in accordance with the ISO 25178-2:2012 standard.

### 6.2.7 X-ray photoelectron spectroscopy (XPS)

XPS can probe the outermost (7-10 nm) surface of the specimens and was used to characterize the surface composition of unexposed as-received XOY, as-received XOZ, polished XOY and polished XOZ specimens. The XPS analyses were carried out with a Kratos AXIS Supra X-ray photoelectron spectrometer using a monochromatic Al  $K_{\alpha}$  source (15 mA, 15 kV). XPS has detection limits ranging from 0.1 - 0.5 atomic percent depending on the element. The instrument work function was calibrated to give a binding energy (BE) of 83.96 eV for the Au 4f<sub>7/2</sub> line for metallic gold. The spectrometer dispersion was adjusted to give a BE of 932.62 eV for the Cu 2p<sub>3/2</sub> line of metallic copper. The Kratos charge neutralizer system was used on all specimens. All specimens were mounted electrically isolated from the instrument sample holder for these analyses. For all measurements, survey scan analyses were carried out with an analysis area of  $300 \times 700 \mu\text{m}$  and a pass energy of 160 eV, and high-resolution analyses were carried out

with an analysis area of  $300 \times 700 \mu\text{m}$  and a pass energy of 20 eV. High-resolution C 1s, O 1s, Co 2p, Cr 2p, and Mo 3d were run. All high-resolution spectra were charge-corrected using adventitious carbon (C 1s, 284.8 eV). Peak convolution was conducted according to previously published protocols [25-27].

### 6.2.8 Contact angle analysis

The deionised water was used to carry out the contact angle measurement with the KRUSS Drop Shape Analyzer Contact Angle (DSA30E). The result is the average of a minimum of three measurements per determination. All tests were conducted at room temperature. The contact angle measurements were calculated using the ADVANCE software.

### 6.2.9 Statistical analysis

A Student's t-test for unpaired data with unequal variance was used to compare two sets of data and determine if the observed differences were statistically significant. The test determined that any differences were considered significant when the p-value was less than 0.05, with a smaller p-value indicating a higher level of significance.

## 6.3 Results and Discussion

### 6.3.1 Surface characterization

The morphology and topography of the fabricated CoCrMo coupons are shown in Figure 6-5 and Figure 6-6. The as-received CoCrMo coupon presents a more complex topographical landscape when printed in a horizontal (XOY) orientation than vertical (XOZ) orientation. On average, the results indicate that the coupons printed in a vertical orientation had a smoother surface than those printed in a horizontal orientation. Powder can be clearly seen in the valley area of the as-received horizontal sample. In addition, the porosity of the horizontal samples was larger than the porosity of vertical samples after polishing. This is in agreement with our previous findings (Chapter 5).

Figure 6-7 shows the X-ray diffraction pattern of a polished CoCrMo coupon that was printed in both horizontal and vertical orientations, with peaks at  $43.9^\circ$  ( $2\theta$ ),  $47.0^\circ$ ,  $51.0^\circ$ ,



and  $75.1^\circ$ . All XRD peaks of the CoCrMo alloy show not only the presence of the  $\gamma$  (FCC, face centred cubic) phase, but also a significant portion of a second phase,  $\epsilon$  (HCP, hexagonal close-packed) phase. Table 6-3 shows the percentage of  $\gamma$  (FCC) and  $\epsilon$  (HCP) phases in the polished LPBF fabricated CoCrMo alloy built in different orientations. The  $\gamma$ -phase in the horizontal sample makes up 79% of the sample, while the  $\epsilon$ -phase makes up the remaining 21%. In the vertical sample, the  $\gamma$ -phase dominates at 83% and the  $\epsilon$ -phase comprises 17%.

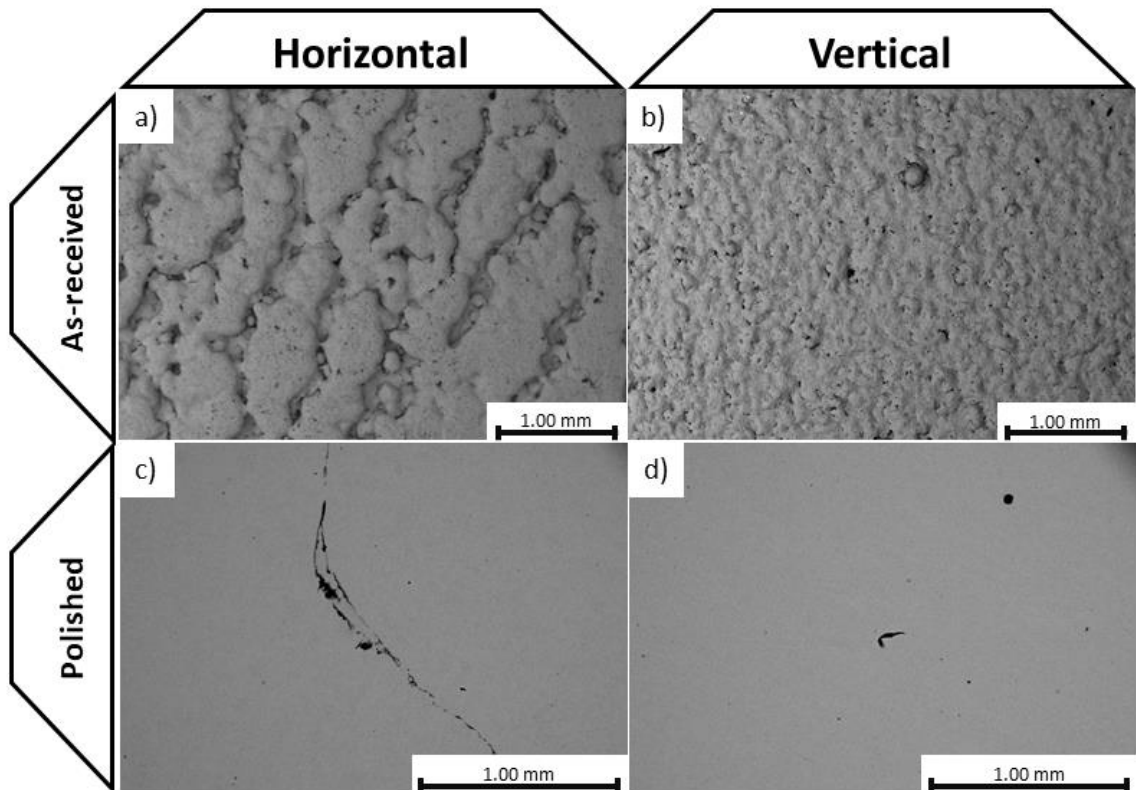


**Figure 6-5: SEM images of the LPBF fabricated CoCrMo alloy of different surface treatments in different print orientations: a) as-received horizontal (XOY), b) as-received vertical (XOZ), c) polished horizontal, and d) polished vertical.**

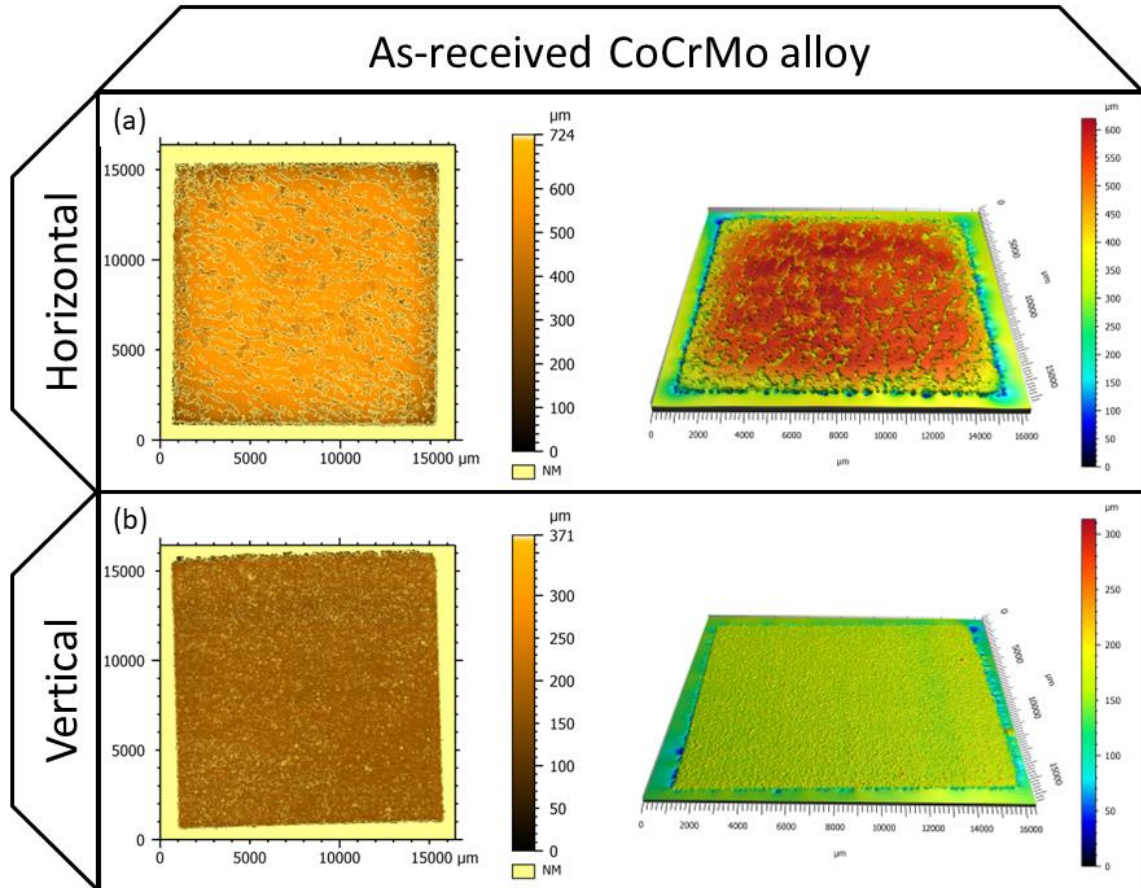


**Figure 6-6: Confocal microscopy images of as-received CoCrMo alloy fabricated in horizontal (a) and vertical (b) orientations.**

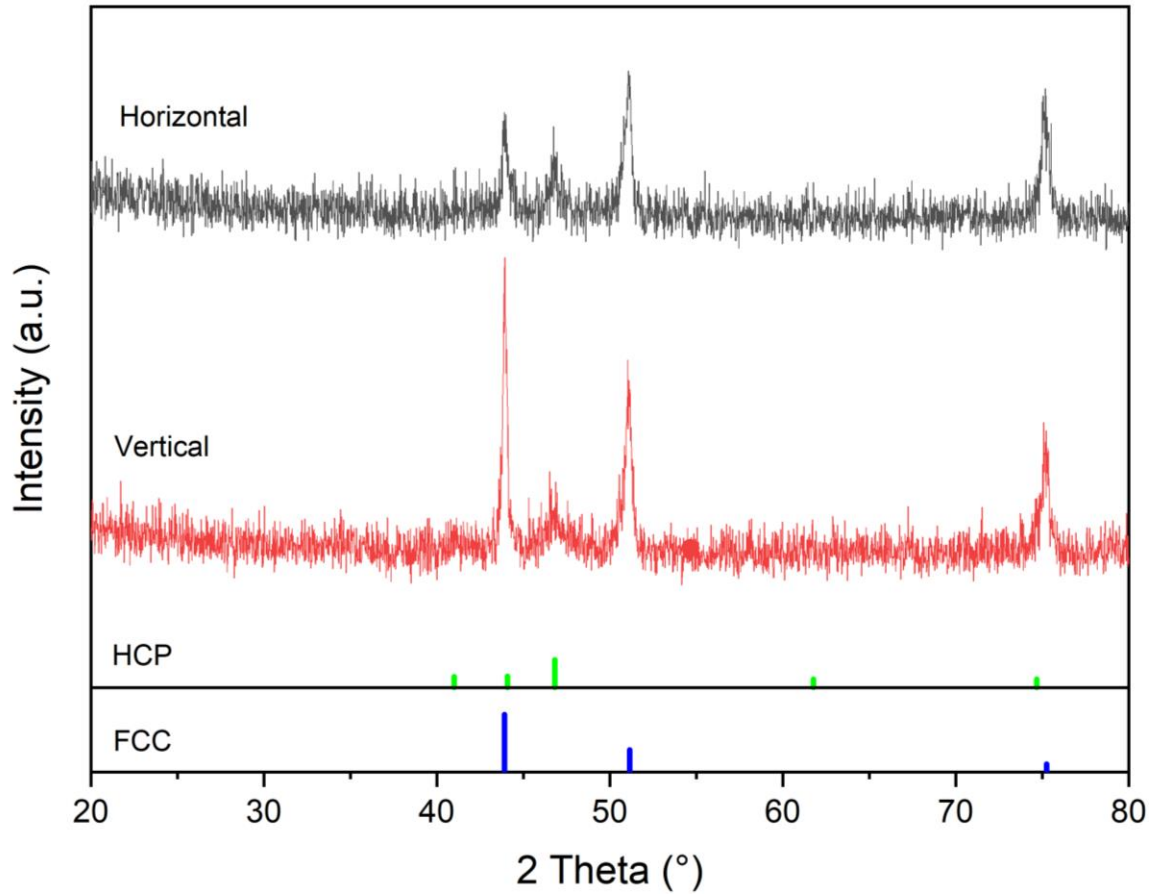


**Figure 6-7: XRD spectra for the horizontal (XOY) and vertical (XOZ) fabricated CoCrMo alloy after polishing.**

**Table 6-3: The percentage of  $\gamma$  (FCC) and  $\varepsilon$  (HCP) phases in the polished LPBF fabricated CoCrMo alloy built in different orientations.**

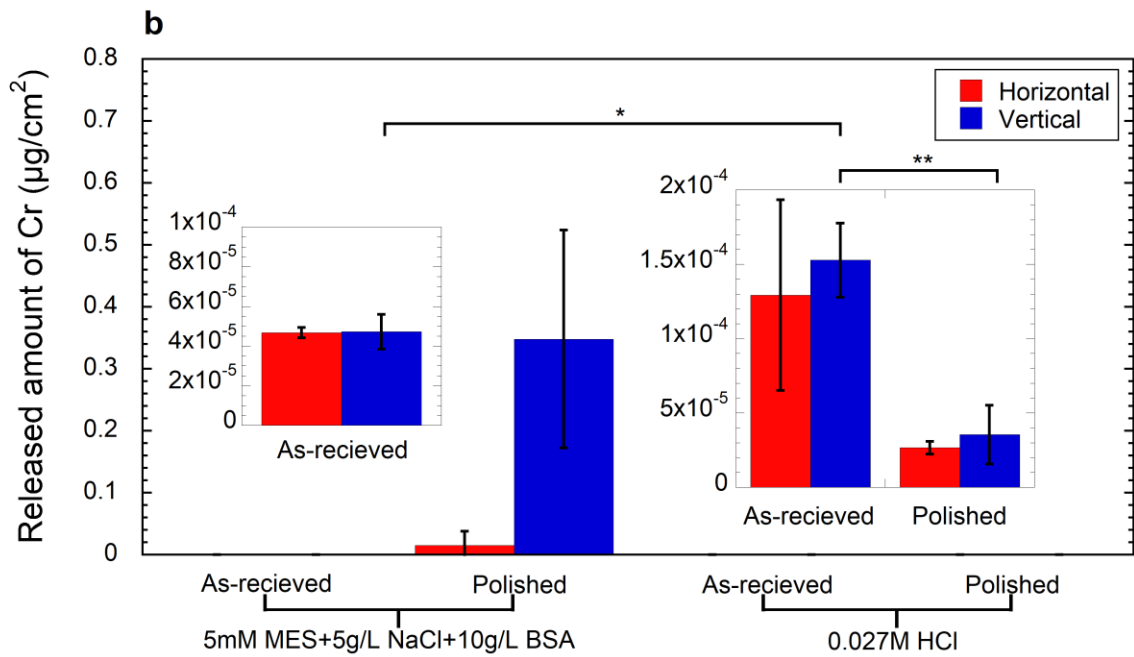
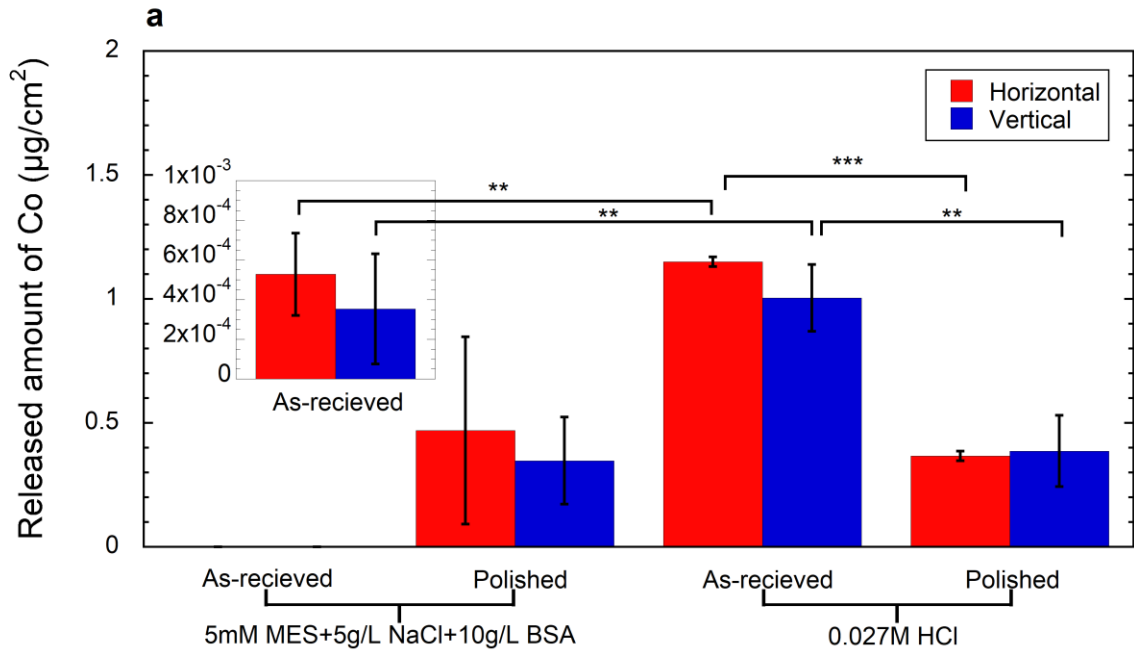
Sample	$\gamma$ (%)	$\varepsilon$ (%)
Horizontal	79	21
Vertical	83	17

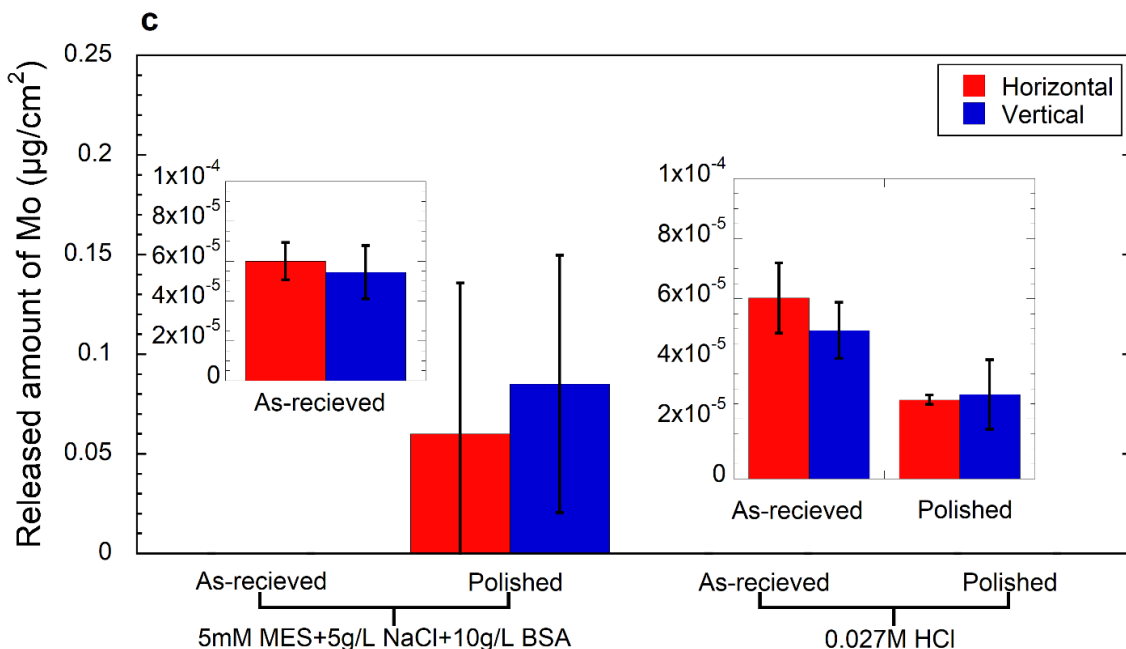
### 6.3.2 Metal release

Figure 6-8 shows the released amount of individual metals (Co, Cr, and Mo) from the LPBF fabricated CoCrMo alloy upon exposure to the MES+BSA and HCl solutions after 24 h at 37 °C. The proportion of the main alloy constituents released did not match the overall composition of the material in the HCl solution, which agrees with previous studies [12; 28]. The amount of cobalt released from the CoCrMo alloy was nearly 99% in the HCl solution, indicating that it had dissolved from a passive state. The release of Co, Cr, and Mo in the MES+BSA was close to their bulk composition, indicating a higher degree of active corrosion and aligning with the electrochemical results presented in section 6.3.3. The released amount of Co was significantly higher than the released amounts of Cr and Mo both in the MES+BSA and HCl solutions. This was mainly attributed to the fact that Co is the major component in the CoCrMo alloy.

The released amounts of metals from horizontal and vertical samples did not display a significant difference in both solutions. Still, the released amount of Co from the polished CoCrMo coupons exposed in the MES+BSA solutions was slightly higher for the vertical sample than horizontal one ( $p=0.079$ , 22.5-fold). For the MES+BSA system, there were more metals released from the polished samples than as-received samples. However, in the HCl solution, the released amount of Co and Cr from the polished samples was significantly lower than the as-received ones ( $p<0.01$ ;  $p<0.001$  for Co).

To summarize, as-received CoCrMo alloys released more Co and Cr when they were exposed to the HCl solution than to the MES+BSA solution, which was statistically significant. In contrast, the released amount of Cr from polished CoCrMo alloy immersed in the MES+BSA solution was higher than in the HCl solution.





**Figure 6-8: Released and non-precipitated amount of Co (a), Cr (b) and Mo (c) per geometric surface area in solution from the LPBF CoCrMo alloy fabricated in horizontal (XOY) and vertical (XOZ) orientations, with and without polishing, after 24 h exposure in MES (5mM) +NaCl (5g/L) +BSA (10g/L) at pH 7.2-7.4 and HCl (0.027M) at 37 °C.**

### 6.3.3 Electrochemistry

#### 6.3.3.1 Open circuit potential investigations

At the start of each test, the OCP was measured for 10 minutes, and then again 21 hours after the first EIS measurement. Figure 6-9 shows the OCP of the CoCrMo alloy fabricated in different orientations with and without polishing, upon immersion in the MES+BSA and HCl. The OCP was generally found to be very positive, further discussed below. The OCP of the as-received horizontal (XOY) sample in the MES+BSA solution was greater than that of the as-received vertical (XOZ) sample. However, the OCP decreased over time and showed evidence of corrosion during exposure. The OCP of the polished samples was similar to that of the as-received vertical sample. Additionally, the OCP of the polished vertical sample started to decrease after 5 hours of exposure. In

addition, the OCP of the as-received sample showed more fluctuations during exposure in the MES+BSA solution than the polished samples.

The OCP of all samples immersed in the HCl solution increased over time. Particularly, the OCP of polished samples (0.525 V) was higher than that of the as-received samples (0.456 V) and was shifting towards more positive potentials. During the 24 h exposure, there were more fluctuations for the as-received samples than that of polished samples. There was no significant difference between the horizontal and vertical samples. The OCP measurements were obtained through three repeated trials, with at least two of these trials being the same in the study.

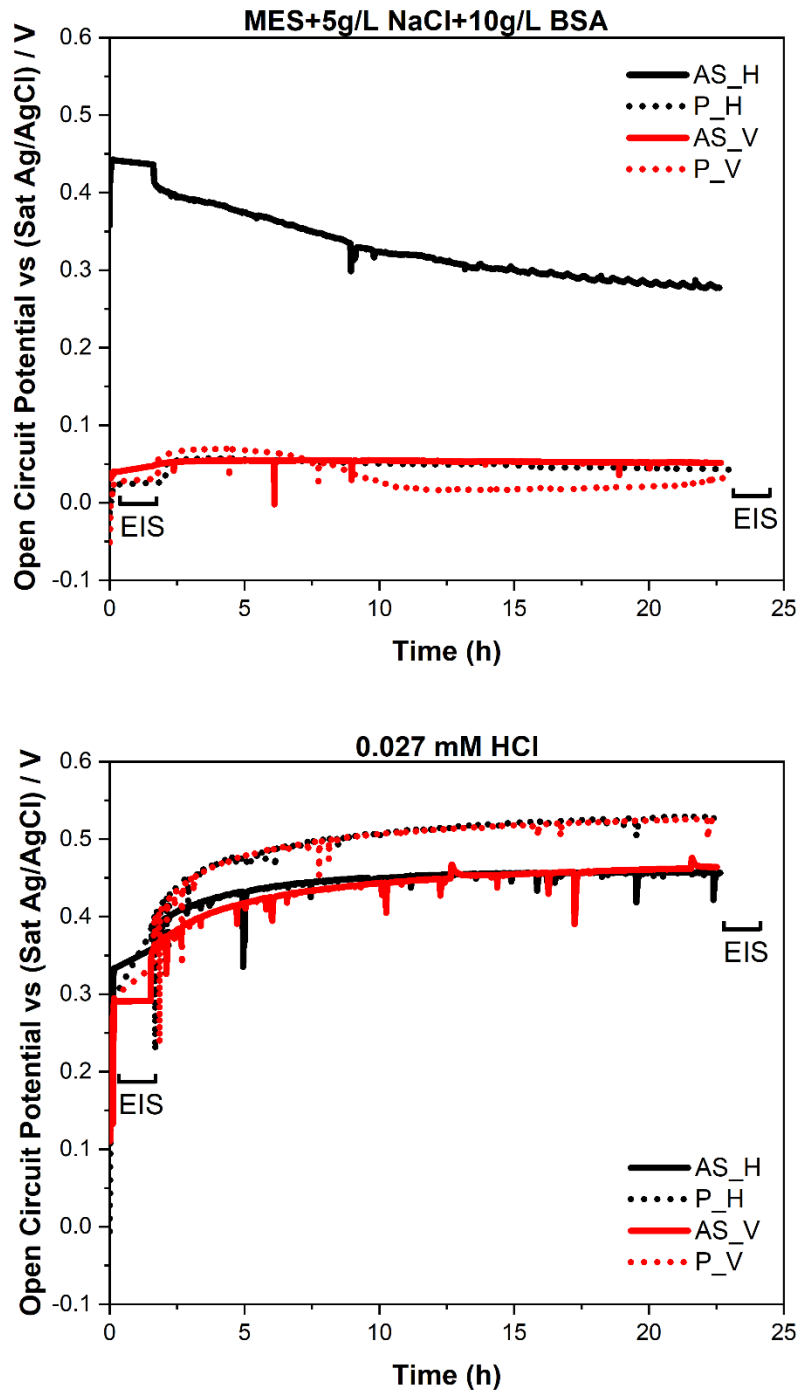


**Figure 6-9: Open circuit potential (representative curves) of CoCrMo alloy fabricated in horizontal (XOY) and vertical (XOZ) orientations, with and without**



**polishing, in MES (5mM) +NaCl (5g/L) +BSA (10g/L) (top) at pH 7.2-7.4 and HCl (0.027M) (bottom) at 37 °C.**

### 6.3.3.2 Potentiodynamic polarization

The corrosion potential ( $E_{\text{corr}}$ ), corrosion current density ( $i_{\text{corr}}$ ) and passive current density ( $i_{\text{pass}}$ ) of various specimens were extracted from the potentiodynamic polarization measurements (Figure 6-10 and Table 6.4). The passive current density value was extracted from the curves at the potential 120 mV more positive to the corrosion potential. According to the results of the student-t test, there was no significant difference in the values of  $E_{\text{corr}}$ ,  $i_{\text{corr}}$ , and  $i_{\text{pass}}$  between the different orientations, but there was a significant difference in different solutions and surfaces. This difference was particularly pronounced for the polished samples. The LPBF CoCrMo alloy had lower corrosion potential and higher  $i_{\text{corr}}$  in the MES+BSA system compared to the HCl. The value of  $E_{\text{corr}}$  in the MES+BSA solution was higher to that in NaCl or PBS solution with BSA in previous studies [29], however, it is unclear whether that is caused by the general shift in potential due to the setup (further discussed below). In the HCl solution, as-received samples had a higher corrosion current density than polished samples, especially for the horizontal sample (XOY orientation) ( $p=0.013$ ), which is in agreement with higher Cr release (Figure 6-8).

In the anodic region, the current increased as a function of potential which agreed with another study [30]. The  $i_{\text{pass}}$  of the MES+BSA system did not show significant differences between the samples. However, it was observed to be higher compared to the HCl, particularly in the polished samples. In the HCl solution, the  $i_{\text{pass}}$  was found to be higher in the as-received sample compared to the polished ones, and this difference was statistically significant ( $p<0.05$ ).

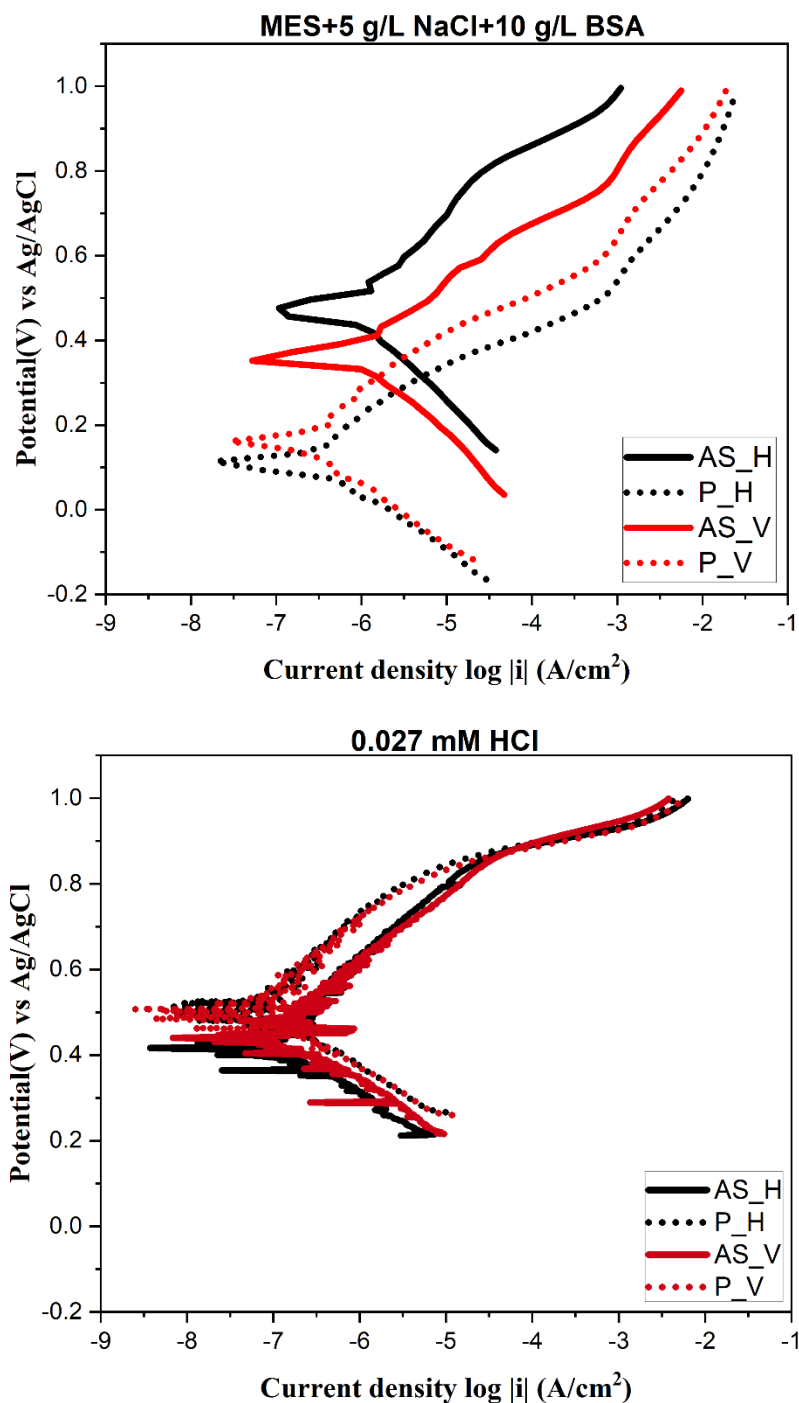


**Figure 6-10: Potentiodynamic polarization curves (starting at the lowest potential and ending at 1.0 V Ag/AgCl) of the as-received (AS) and polished (P) horizontal (H, XOY) and vertical (V, XOZ) CoCrMo samples in 5 mM MES+5 g/L NaCl+10 g/L BSA (top) or 0.027 mM HCl (bottom). Scan rate: 0.167 mV/s.**

**Table 6-4: The corrosion current densities ( $i_{\text{corr}}$ ), passive current densities ( $i_{\text{pass}}$ , here defined as the current density +120 mV versus  $E_{\text{corr}}$ ) and corrosion potentials ( $E_{\text{corr}}$ ) based on potentiodynamic polarization of the CoCrMo specimens immersed in MES+BSA (pH=7.2), and HCl solutions at 37 °C. Mean values and standard deviations of triplicate samples. H – horizontal (XOY); V – vertical (XOZ).**

Systems	Samples	$i_{\text{corr}}$ ( $\mu\text{A}/\text{cm}^2$ )	$E_{\text{corr}}$ (mV <sub>Ag/AgCl</sub> )	$i_{\text{pass}}$ ( $\mu\text{A}/\text{cm}^2$ )
MES+BSA	As-received H	1.73 ± 0.71	350 ± 160	10.92 ± 4.99
	Polished H	0.98 ± 0.16	130 ± 10	10.74 ± 3.72
	As-received V	1.62 ± 1.17	250 ± 170	16.17 ± 10.27
	Polished V	3.62 ± 2.84	110 ± 40	19.18 ± 13.39
HCl	As-received H	0.15 ± 0.05	440 ± 0	1.66 ± 0.16
	Polished H	0.08 ± 0.07	520 ± 20	0.93 ± 0.27
	As-received V	0.19 ± 0.10	440 ± 50	2.19 ± 0.47
	Polished V	0.13 ± 0.00	510 ± 20	0.61 ± 0.32

### 6.3.3.3 EIS

As the OCP was not sufficiently stable after 10 minutes, the initial EIS data could not be analyzed further. However, it was evident that the resistance was significantly lower than after 22 hours. The Nyquist and Bode plots from the EIS after 22 hours of exposure in MES+BSA and HCl at the open circuit potential are shown in Figure 6-11 and Figure 6-12, respectively. EIS is a non-destructive and sensitive technique that provides insights into the features of the surface layer (such as surface oxide and adsorbed substances) and the dominant corrosion processes in a specific environment [31]. The phase angle in EIS represents the phase shift between the voltage and current signals in a material. The magnitude of the phase angle provides information about the nature of the impedance in

the material. A negative phase angle between  $60^\circ$  and  $80^\circ$  suggests that the impedance in the material is predominantly capacitive in nature, Figure 6-12. This implies that the material has a capacitive surface layer, which may consist of surface oxides and adsorbed species [2]. The size of the capacitive loop in the Nyquist plots reflects the corrosion performance, with larger loops indicating better corrosion resistance [32]. The results of the polarization measurements were consistent with the corrosion resistance measurements, with all specimens showing better resistance to corrosion in the HCl solution compared to the MES+BSA solution after 22 or 24 h, Figure 6-11.

In HCl, the corrosion resistance of both horizontal and vertical samples was comparable. The corrosion resistance only depended on the surface treatment. The polished CoCrMo alloy exhibited improved corrosion resistance compared to the as-received sample. However, the corrosion resistance of various samples in the MES+BSA solution was more complex; the as-received vertical sample showed the greatest corrosion resistance, while the as-received horizontal sample displayed the lowest resistance.

The electrical equivalent circuit (EEC) with two time-constants was chosen to fit the EIS data in the two different solutions (Figure 6-13 and Table 6.5), justified as follows. The EEC of CoCrMo samples immersed in MES+BSA solution can be represented as a combination of solution resistance in series with a parallel combination of a capacitance modeled as a constant phase element ( $CPE_{ads}$ ) and an adsorption resistance (Figure 6-13 (b)). The adsorption resistance is in series with a parallel combination of a capacitance modeled as a  $CPE_{ox}$  and an oxide resistance (to represent the oxide layer). This is justified by the interfaces between the solution, the protein adsorbed layer, the oxide layer, and the metal. This EEC had been applied in a previous study of CoCrMo alloy in protein-containing solutions [33-35]. In the HCl solution, the EEC is represented by a series combination of a solution resistance,  $CPE_{ox}$ , and an oxide resistance. The oxide resistance is further connected in series with another combination of a  $CPE_{pore}$  and a pore resistance (representing the resistance caused by the pores in the oxide layer), shown in Figure 6-13 (a). The presence of pores in the oxide layer of CoCrMo metal samples, as indicated by SEM image in Figure 6-5, can affect the ion transport and charge transfer process at the metal-electrolyte interface. In HCl solution, the EEC considers the

presence of pores by including a pore resistance in the circuit representation, which is similar to other studies with porous surfaces [36-39].

The EEC was employed to analyze the EIS data. The resulting parameters in both MES+BSA and HCl solutions are presented in Table 6-5. The close match between the experimental and theoretical values of the model is indicated by chi-squared values ( $\chi^2$ ) that are less than 0.005, demonstrating the robustness of the applied EEC approach.

The results clearly show higher corrosion resistance of the polished than the as-received samples for both print orientations in the HCl solution. There was no difference between the different print orientations. In the MES+BSA solution, the as-received vertical sample had a higher corrosion resistance than the as-received horizontal sample. However, the polished horizontal sample had a higher corrosion resistance than the polished vertical sample.

These findings agree with the findings from the potentiodynamic polarization after 24 h exposure; that the corrosion resistance of CoCrMo in the HCl solution is higher than in the MES+BSA solution.

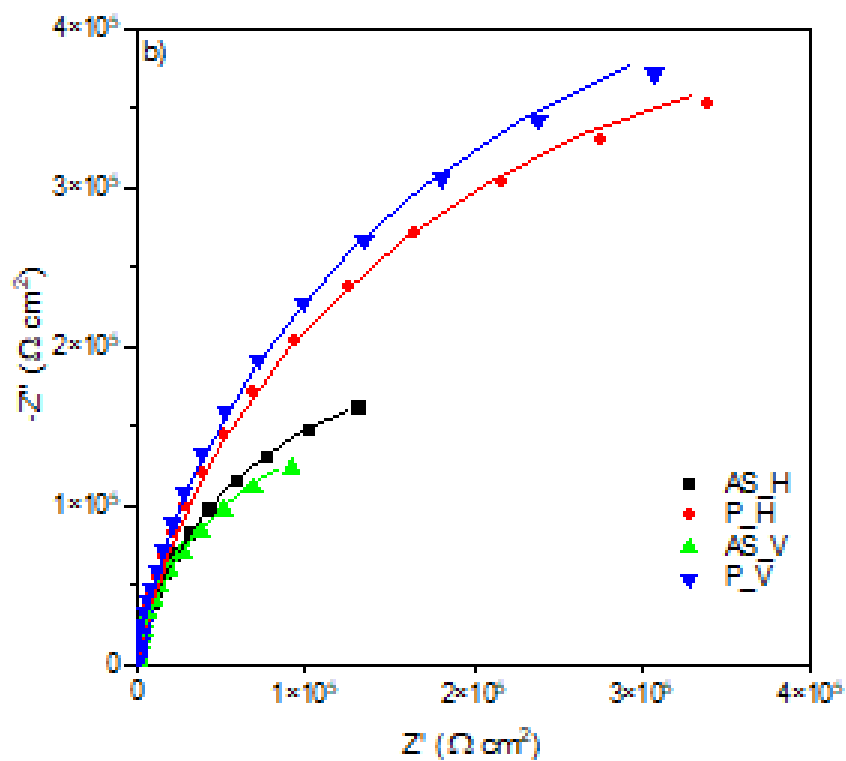
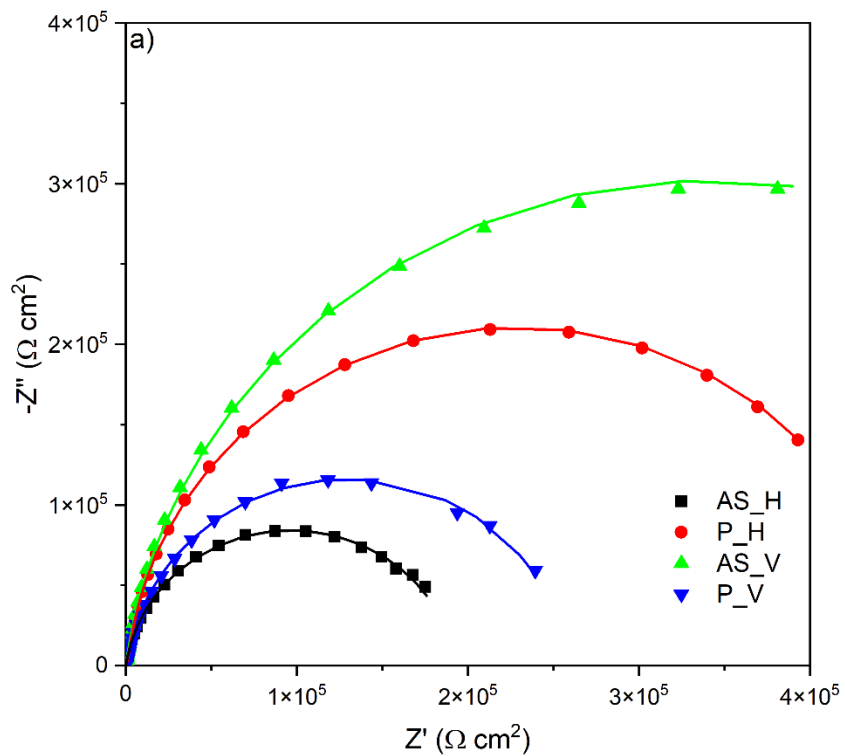


**Figure 6-11: Experimental impedance plots (Nyquist format) for the as-received and polished CoCrMo alloy fabricated in horizontal (XOY) and vertical (XOZ) orientation after 22 h immersion at 37 °C in the a) MES+BSA, and b) HCl solutions.**

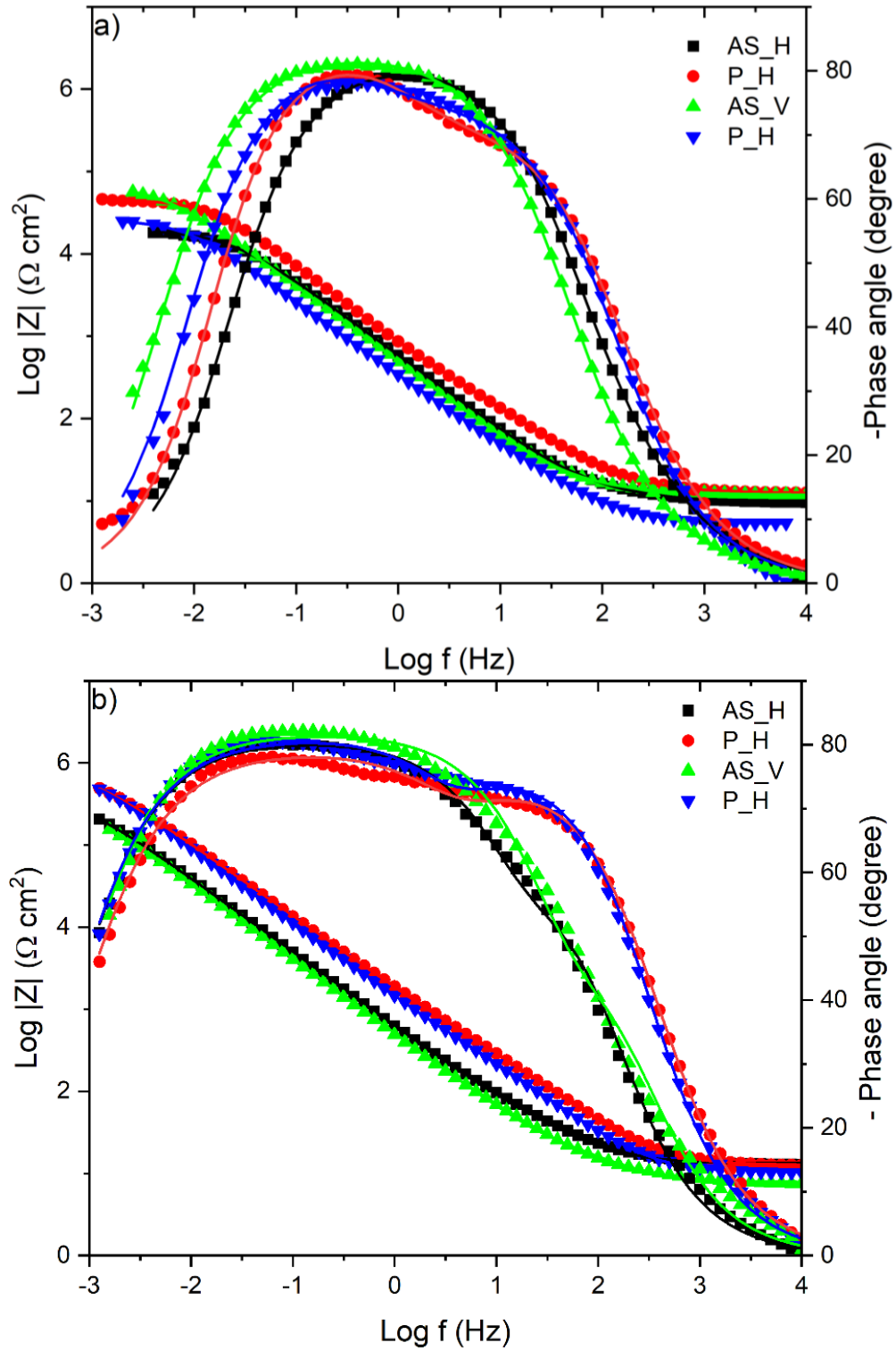


**Figure 6-12: Experimental impedance plots (Bode format) for the as-received and polished CoCrMo alloy fabricated in horizontal and vertical orientation after 22 h immersion at 37 °C in the a) MES+BSA, and b) HCl solutions.**

**Table 6-5: EIS parameters and fitting data (average and standard deviation of at least three independent specimens) based on the equivalent circuit models used for MES+BSA and HCl solutions.**

MES+BSA								
Sample	$R_s$ ( $\Omega$ $\text{cm}^2$ )	$CPE_{ads}$ ( $\mu\text{Fcm}^{-2}\text{s}^{-n}$ )	$n_1$	$R_{ads}$ ( $\Omega$ $\text{cm}^2$ )	$CPE_{ox}$ ( $\mu\text{Fcm}^{-2}\text{s}^{-n}$ )	$n_2$	$R_{ox}$ ( $\Omega$ $\text{cm}^2$ )	$X^2$ ( $10^{-3}$ )
As-received Horizontal	$10 \pm 0.3$	$341 \pm 35$	0.92	$43134 \pm 33709$	$2004 \pm 1948$	0.64	$5 \pm 0$	3.86
Polished Horizontal	$8 \pm 7$	$430 \pm 305$	0.95	$36822 \pm 12232$	$1968 \pm 1440$	0.72	$95 \pm 80$	2.24
As-received Vertical	$11 \pm 1$	$361 \pm 22$	0.92	$43826 \pm 34392$	$8918 \pm 1723$	0.53	$149 \pm 200$	9.46
Polished Vertical	$5 \pm 1$	$613 \pm 55$	0.93	$24450 \pm 1986$	$3153 \pm 713$	0.70	$64 \pm 5$	2.97
HCl								
Sample	$R_s$ ( $\Omega$ $\text{cm}^2$ )	$CPE_{ox}$ ( $\mu\text{Fcm}^{-2}\text{s}^{-n}$ )	$n_1$	$R_{ox}$ ( $\Omega$ $\text{cm}^2$ )	$CPE_{pore}$ ( $\mu\text{Fcm}^{-2}\text{s}^{-n}$ )	$n_2$	$R_{pore}$ ( $\Omega$ $\text{cm}^2$ )	$X^2$ ( $10^{-3}$ )
As-received Horizontal	$11 \pm 3$	$171 \pm 29$	0.89	$162 \pm 49$	$97 \pm 18$	0.91	$489475 \pm 104064$	0.07



Polished Horizontal	$13 \pm 0.04$	$97 \pm 12$	0.87	$1288 \pm 1754$	$18 \pm 4$	0.92	$991300 \pm 122612$	3.12
As-received Vertical	$10 \pm 3$	$191 \pm 3$	0.91	$45 \pm 21$	$148 \pm 40$	0.91	$342450 \pm 15598$	0.05
Polished Vertical	$10 \pm 1$	$115 \pm 7$	0.89	$1585 \pm 1108$	$20 \pm 2$	0.97	$969690 \pm 3280$	2.33

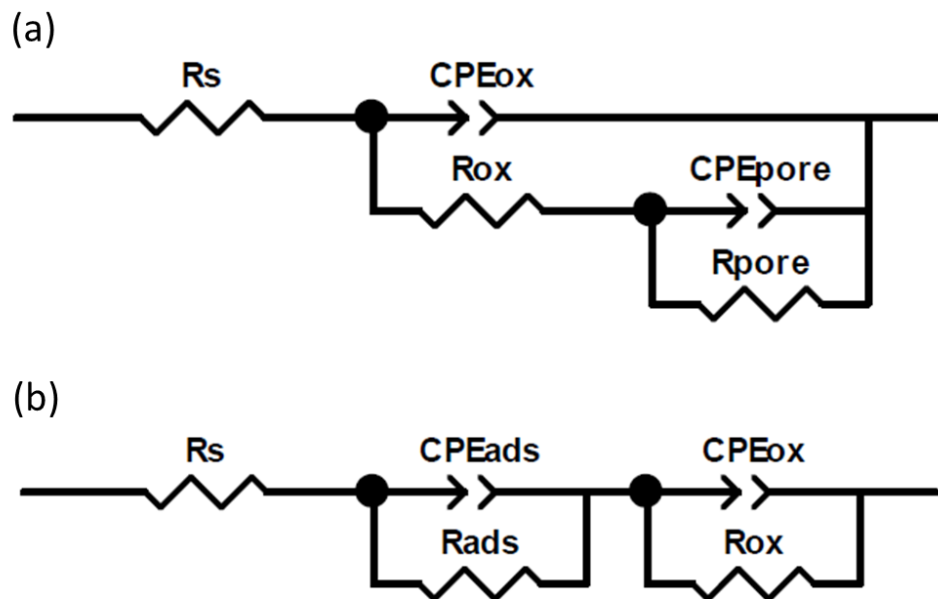


**Figure 6-13: The equivalent electric circuits of as-received and polished CoCrMo alloy fabricated in horizontal and vertical orientation immersed at 37 °C in (a) HCl, and (b) MES+BSA, used for the numerical fitting of the impedance data.**

#### 6.3.4 Contact angle and surface roughness

Contact angle measurements were performed using ultrapure water. The values of the contact angle of CoCrMo alloy fabricated in different orientations with and without polishing are shown in the Table 6.6. The data was analyzed through t-tests and was considered statistically significant when  $p < 0.05$ . Compared to the vertical sample, the

horizontal samples have lower values in both the as-received and polished states. However, the difference is not statistically significant. Only one difference, between the as-received vertical and polished horizontal samples, was found to be significant ( $p < 0.001$ ).

**Table 6-6: Mean contact angle values.**

Sample	Contact angle (°)
As-received Horizontal	44.83 ± 10.69
As-received Vertical	63.24 ± 2.57
Polished Horizontal	43.24 ± 2.23
Polished Vertical	52.78 ± 8.75

The surface roughness and surface area of as-received samples are shown in the Table 6.7.  $S_q$  and  $S_a$  are root mean square and arithmetic mean value of the ordinate values (ISO 25178-2:2012 standard). The horizontal sample has a larger root mean square ( $S_q$ ) value, surface roughness average ( $S_a$ ), and surface area when compared to the vertical sample. Additionally, the actual surface area is greater (up to 24%) than the geometrical surface area of 2.25 cm<sup>2</sup>. This means that the metal release and current densities, which are normalized to the geometrical surface area, are expected to be up to 24% larger for as-received than for polished samples due to this difference in actual surface area only.

**Table 6-7: The surface roughness and surface area of CoCrMo alloy fabricated in horizontal and vertical orientations for the 1.5 × 1.5 cm (2.25 cm<sup>2</sup>) coupon.**

	$S_q$ (μm)	$S_a$ (μm)	Area (cm <sup>2</sup> )
Horizontal	56	43	2.79
Vertical	12	8.7	2.39

### 6.3.5 XPS

XPS was employed to determine the composition of the surface (7-10 nm), as shown in Figure 6-14 and already presented and discussed in Chapter 5. Carbon, oxygen, and silicon were the three most abundant elements found on the surface. As discussed in chapter 5, there was evidence of silicone on the surface of all samples. Further, there was also evidence of some incorporation of the ceramic beads mixture in the surface, especially for the as-received surfaces. The metallic peaks of Co, Cr, and Mo were detected within the XPS detection depth (7-10 nm) in all cases, indicating a surface oxide layer that is only a few nanometers thick.

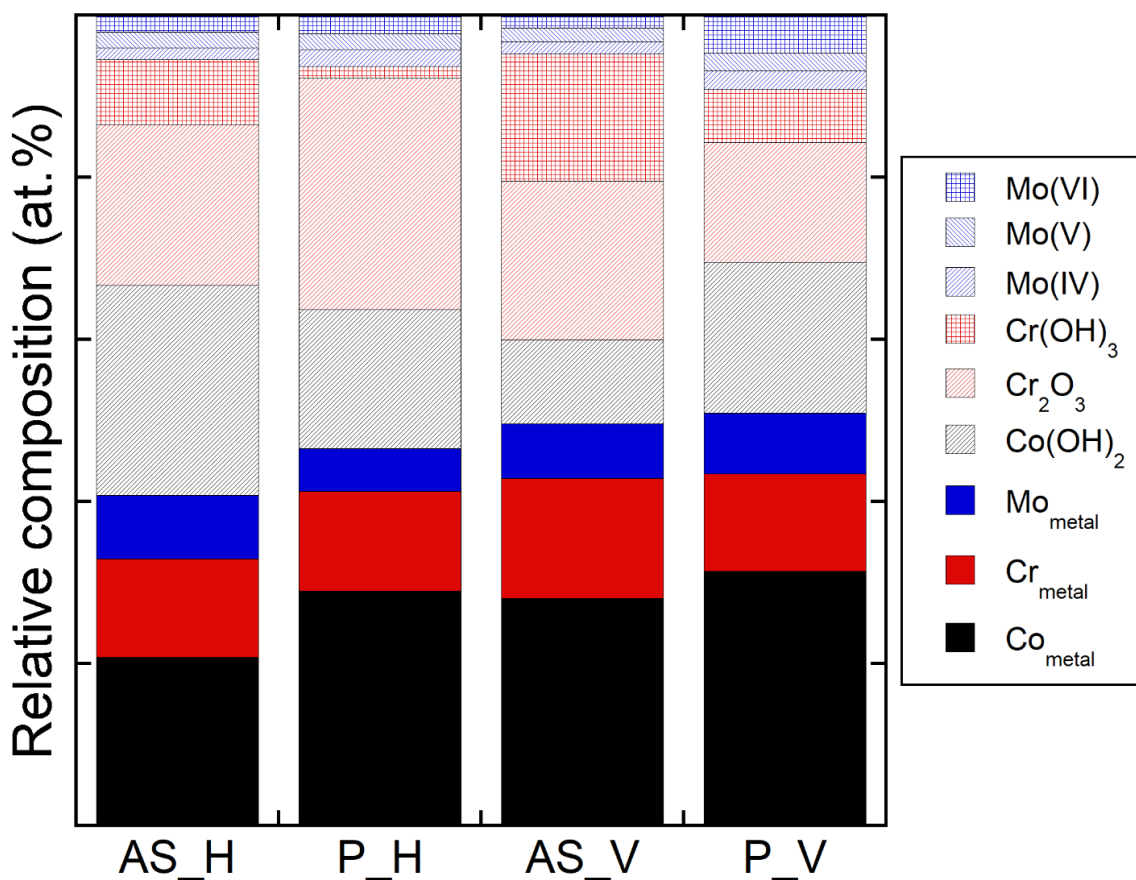


**Figure 6-14: Relative surface composition and speciation of the elements Co, Cr, and Mo estimated from the XPS wide spectra of as-received (AS) and polished (P) CoCrMo surfaces fabricated in horizontal (H) and vertical (V) orientation.**

## 6.4 Further Discussion

This study focused on HCl solution (pH 1.5) and MES+BSA solution (pH 7.2-7.4), while our previous study (Chapter 5) focused on phosphate buffered saline (PBS, pH 7.4), PBS with 5 g/L citric acid (CA) at pH 7.4, and CA at pH 2.4. In most of these solutions, the as-received, rougher samples exhibited a lower corrosion resistance than the polished CoCrMo coupons. The higher surface area and roughness of the as-received CoCrMo alloy can contribute to its lower resistance to corrosion in HCl solution, compared to the polished samples. The increased surface roughness of the as-received surface can provide more sites for the initiation of corrosion, which can lead to a higher overall corrosion rate and an increased risk of pitting corrosion or lack of repassivation ability (the ability to form a stable oxide film after initial pitting). Pitting corrosion is a type of localized corrosion that occurs in small, confined areas of a metal surface, leading to the formation of deep, narrow holes or pits [40; 41]. This study, as well as others, have found that surface roughness has a negative effect on the corrosion resistance of various materials produced through the LPBF process [42-47]. In contrast, a polished or abraded surface can have a more uniform and homogeneous surface, which can reduce the number of sites for corrosion initiation and improve the overall corrosion resistance of the alloy [48-50]. As discussed in Chapter 5, the surface roughness is not the only parameter that is different between the as-received and polished surfaces. Especially the sandblasting procedure is expected to also influence the corrosion resistance [12; 51], but also the extent of unfused particles, residual stresses, and the microstructure. In this study, XRD was applied, however, it was not possible to obtain sufficient signals (due to surface roughness) for the as-received samples, so it is unclear whether the microstructure is different between as-received and polished samples. A previous study suggests that this is the case [12]. XPS revealed no significant difference in oxide composition between the as-received and polished specimens.

However, the difference between as-received and polished samples was not following the same trend in the MES+BSA solution. The adsorption of albumin can affect the exposed surface area and corrosion resistance [34; 52]. Generally, BSA has a net negative charge in the MES buffer at pH 7.2-7.4 [53; 54]. In this study, the OCP of the as-received

horizontal sample was 300 mV more positive than for the other samples in MES+BSA. Since the concentration of the net negatively charged BSA was higher than 2 g/L, the coverage of protein would be increased [35]. As a result, the adsorption of BSA on the surface led to a decreased corrosion resistance, in the case of as-received horizontal sample. Therefore, the corrosion resistance of samples immersed in the MES+BSA followed the trend; as-received vertical > polished horizontal > polished vertical > as-received horizontal.

The results of this study showed that the surface area and roughness can impact metal release as well as corrosion behavior. Specifically, the release of Co and Cr from the as-received samples was found to be higher compared to the polished samples when they were immersed in HCl solutions. However, the opposite was observed in MES+BSA, where the released amount of metals from the as-received samples was found to be lower compared to the polished samples. According to the electrochemical findings, the corrosion resistance of CoCrMo in the MES+BSA system was weaker compared to that in the HCl system. As a result, it can be expected that CoCrMo will release more metals in the MES+BSA compared to HCl. The metal release results also indicated that active corrosion was present in the MES+BSA, but the overall metal release and Co release was lower in MES+BSA than in HCl. This disparity was attributed to protein aggregation and metal precipitation, especially in the case of Co, which forms oxides at neutral pH. Instead, the release of Cr and Mo were higher or comparable in MES+BSA than in HCl. Mo forms solid oxides at low pH and is responsible for a higher pitting resistance and a passivation ability in acidic solutions [55-57]. We speculate that the relatively high content of Mo (6 wt.%) in the alloy was responsible for the superior corrosion resistance in HCl.

The metal release can be affected by various factors such as microstructure, solution, presence of organic substances, pH, temperature, protein aggregation and metal precipitation [23; 58-61]. The released amount of metals from the CoCrMo alloy can also be influenced by protein aggregation and metal precipitation in the protein containing solutions, which may lead to an underestimation of the metal release [62; 63]. The buildup of metals and metal-protein conjugates in the pores of the as-received samples

due to protein aggregation and metal precipitation can also result in an underestimation of metal release.

The CoCrMo alloy fabricated in vertical orientation had slightly higher contact angles than the horizontal ones, which means that the vertical samples had a more hydrophobic surface (and lower porosity). Hydrophobic surfaces with non-polarity can enhance BSA adsorption [64-68]. One possible explanation for the higher Cr release from the polished vertical sample could hence be a better BSA adsorption. Cr release is stronger affected by proteins than Co and Mo release, as shown in other studies (Chapter 4), and there was not more Cr available in the surface oxide for the polished vertical than the polished horizontal surface based on the XPS results.

This study discovered slight variations between the horizontal and vertical printed CoCrMo alloys. X-ray diffraction results revealed that the polished vertical sample had a slightly higher FCC phase [69] and a lower HCP phase [70] compared to the polished horizontal sample. During the LPBF process, the final microstructure can be greatly influenced by the cooling rate during the build procedure [71]. The sample built with the long side parallel to the building direction (vertical orientation) may have experienced a slower cooling rate compared to the sample built with the long side perpendicular to the building direction (horizontal), which could result in a higher proportion of FCC phases in the vertical sample [72]. In addition, there is reheating between the layers during the LPBF build process. The vertical sample, being in contact with the build platform for a longer time, would indeed experience more reheating compared to the horizontal sample [12]. This could result in more HCP phase being transformed to FCC phase, leading to a higher proportion of FCC phase in the vertical sample.

This study is limited by its experimental conditions and design. The OCP value of CoCrMo was found more positive than in past studies [73-75], which may be attributed to the galvanic potential created by the platinum plated electrode holder, to which all samples were attached. This plate was also immersed in the solution, which could have resulted in the increased potential. In addition, this study did not examine tribocorrosion or the influence of friction, which is important for the biomedical applications of

CoCrMo alloys. Future studies should examine the tribocorrosion on the CoCrMo alloy with different print orientations.

## 6.5 Conclusions

The purpose of this study was to assess the release of metals, corrosion resistance and microstructure of CoCrMo manufacturing by the LPBF in horizontal (XOY) and vertical (XOZ) orientations for as-received and polished surfaces in two relevant simulated physiological environments: normal and crevice conditions. The following main conclusions were drawn:

1. The as-received horizontal LPBF CoCrMo exhibited a coarser microstructure than the vertical plane, with more of the HCP phase present, possibly due to a more rapid cooling rate.
2. The corrosion resistance was greater in HCl (pH 1.5) than in MES+BSA (pH 7.4) after 22 h of pre-exposure. This might possibly be explained by a passivation process supported by the Mo content of the alloy.
3. The amount of Co released from the specimens after 24 hours of exposure in the MES+BSA was lesser than in the HCl, which was probably due to the occurrence of protein aggregation and metal precipitation. In contrast, the amount of Cr and Mo were equal or more released in MES+BSA than in HCl.
4. CoCrMo alloys that have undergone polishing exhibit increased resistance to corrosion in HCl and MES+BSA (for one orientation) solutions than their as-received counterparts.
5. The corrosion resistance of the CoCrMo alloy showed only a slight variation between samples produced in different orientations.
6. The polished vertical sample showed a tendency to release more Cr than the polished horizontal sample in the MES+BSA (pH 7.2-7.4) solution.

## 6.6 References

- [1] Igual, M. A., et al. "Effect of the Environment on Wear Ranking and Corrosion of Biomedical CoCrMo Alloys." *Journal of Materials Science: Materials in Medicine*, vol. 22, 2011, pp. 437-450.
- [2] De Castro Girão, D., et al. "An Assessment of Biomedical CoCrMo Alloy Fabricated by Direct Metal Laser Sintering Technique for Implant Applications." *Materials Science and Engineering: C*, vol. 107, 2020, p. 110305.
- [3] Milošev, I. "CoCrMo Alloy for Biomedical Applications." *Biomedical Applications*, Springer, 2012, pp. 1-72.
- [4] Bandyopadhyay, A., et al. "Additively Manufactured Calcium Phosphate Reinforced CoCrMo Alloy: Bio-Tribological and Biocompatibility Evaluation for Load-Bearing Implants." *Additive manufacturing*, vol. 28, 2019, pp. 312-324.
- [5] Mantripragada, V. P., et al. "An Overview of Recent Advances in Designing Orthopedic and Craniofacial Implants." *Journal of biomedical materials research Part A*, vol. 101, no. 11, 2013, pp. 3349-3364.
- [6] Minciuna, M. G., et al. "Structural Characterization of Some CoCrMo Alloys with Medical Applications." *Revista de Chimie (Bucharest)*, vol. 65, no. 3, 2014, p. 335.
- [7] Gurel, S., et al. "From Corrosion Behavior to Radiation Response: A Comprehensive Biocompatibility Assessment of a CoCrMo Medium Entropy Alloy for Utility in Orthopedic and Dental Implants." *Intermetallics*, vol. 149, 2022, p. 107680.
- [8] Ciraud, P. "Verfahren Und Vorrichtung Zur Herstellung Beliebiger Gegenstände Aus Beliebigen Schmelzbarem Material." German patent application DE, vol. 2263777, 1973.
- [9] Kumar, R., et al. "The Role of Additive Manufacturing for Biomedical Applications: A Critical Review." *Journal of Manufacturing Processes*, vol. 64, 2021, pp. 828-850.



- [10] Nirish, M., et al. "Suitability of Metal Additive Manufacturing Processes for Part Topology Optimization—a Comparative Study." *Materials Today: Proceedings*, vol. 27, 2020, pp. 1601-1607.
- [11] Wong, K. V., et al. "A Review of Additive Manufacturing." *International scholarly research notices*, vol. 2012, 2012.
- [12] Hedberg, Y. S., et al. "In-Vitro Biocompatibility of CoCrMo Dental Alloys Fabricated by Selective Laser Melting." *Dental materials*, vol. 30, no. 5, 2014, pp. 525-534.
- [13] Lewandowski, J. J., et al. "Metal Additive Manufacturing: A Review of Mechanical Properties." *Annual review of materials research*, vol. 46, 2016, pp. 151-186.
- [14] Shamsaei, N., et al. "An Overview of Direct Laser Deposition for Additive Manufacturing; Part II: Mechanical Behavior, Process Parameter Optimization and Control." *Additive manufacturing*, vol. 8, 2015, pp. 12-35.
- [15] Dowling, L., et al. "A Review of Critical Repeatability and Reproducibility Issues in Powder Bed Fusion." *Materials & Design*, vol. 186, 2020, p. 108346.
- [16] Watring, D. S., et al. "Effects of Laser-Energy Density and Build Orientation on the Structure–Property Relationships in as-Built Inconel 718 Manufactured by Laser Powder Bed Fusion." *Additive manufacturing*, vol. 36, 2020, p. 101425.
- [17] Gorsse, S., et al. "Additive Manufacturing of Metals: A Brief Review of the Characteristic Microstructures and Properties of Steels, Ti-6al-4v and High-Entropy Alloys." *Science and Technology of advanced MaTerialS*, vol. 18, no. 1, 2017, pp. 584-610.
- [18] Bourell, D., et al. "Additive Manufacturing of Cobalt Alloys." 2020.
- [19] Tan, C., et al. "Microstructural Characterization and Properties of Selective Laser Melted Maraging Steel with Different Build Directions." *Science and Technology of advanced MaTerialS*, vol. 19, no. 1, 2018, pp. 746-758.

- [20] Mei, N., et al. "Influence of Biocorona Formation on the Transformation and Dissolution of Cobalt Nanoparticles under Physiological Conditions." *ACS omega*, vol. 4, no. 26, 2019, pp. 21778-21791.
- [21] Atapour, M., et al. "Corrosion and Metal Release Investigations of Selective Laser Melted 316l Stainless Steel in a Synthetic Physiological Fluid Containing Proteins and in Diluted Hydrochloric Acid." *Electrochimica Acta*, vol. 354, 2020, p. 136748.
- [22] Wang, X., et al. "Location of Cobalt Impurities in the Surface Oxide of Stainless Steel 316l and Metal Release in Synthetic Biological Fluids." *Materials & Design*, vol. 215, 2022, p. 110524.
- [23] Wei, Z., et al. "Metal Release from a Biomedical CoCrMo Alloy in Mixed Protein Solutions under Static and Sliding Conditions: Effects of Protein Aggregation and Metal Precipitation." *Journal of Bio-and Tribo-Corrosion*, vol. 8, no. 1, 2022, pp. 1-11.
- [24] Bennike, T., et al. "A Normative Study of the Synovial Fluid Proteome from Healthy Porcine Knee Joints." *Journal of proteome research*, vol. 13, no. 10, 2014, pp. 4377-4387.
- [25] Biesinger, M. C., et al. "Resolving Surface Chemical States in XPS Analysis of First Row Transition Metals, Oxides and Hydroxides: Cr, Mn, Fe, Co and Ni." *Applied Surface Science*, vol. 257, no. 7, 2011, pp. 2717-2730.
- [26] Baltrusaitis, J., et al. "Generalized Molybdenum Oxide Surface Chemical State XPS Determination Via Informed Amorphous Sample Model." *Applied Surface Science*, vol. 326, 2015, pp. 151-161.
- [27] Biesinger, M. C. "X-Ray Photoelectron Spectroscopy (XPS) Reference Pages. 2020." 2018.
- [28] Hodgson, A. W. E., et al. "Passive and Transpassive Behavior of CoCrMo in Simulated Biological Solutions." *Electrochimica Acta*, vol. 49, no. 13, 2004, pp. 2167-2178.

- [29] Vidal, C. V., et al. "Electrochemical Characterisation of Biomedical Alloys for Surgical Implants in Simulated Body Fluids." *Corrosion Science*, vol. 50, no. 7, 2008, pp. 1954-1961.
- [30] Soares, F., et al. "Galvanic Corrosion of Ti Dental Implants Coupled to CoCrMo Prosthetic Component." *International Journal of Biomaterials*, vol. 2021, 2021.
- [31] Yusuf, S., et al. "Microstructure and Corrosion Performance of 316l Stainless Steel Fabricated by Selective Laser Melting and Processed through High-Pressure Torsion." *Journal of Alloys and Compounds*, vol. 763, 2018, pp. 360-375.
- [32] Jin, Z. H., et al. "Corrosion Behavior of 316l Stainless Steel and Anti-Corrosion Materials in a High Acidified Chloride Solution." *Applied Surface Science*, vol. 322, 2014, pp. 47-56.
- [33] Vidal, C. V., et al. "Adsorption of Bovine Serum Albumin on CoCrMo Surface: Effect of Temperature and Protein Concentration." *Colloids and Surfaces B: Biointerfaces*, vol. 80, no. 1, 2010, pp. 1-11.
- [34] Valero, V. C., et al. "Study of the Adsorption Process of Bovine Serum Albumin on Passivated Surfaces of CoCrMo Biomedical Alloy." *Electrochimica Acta*, vol. 55, no. 28, 2010, pp. 8445-8452.
- [35] Rahimi, E., et al. "Albumin Protein Adsorption on CoCrMo Implant Alloy: Impact on the Corrosion Behavior at Localized Scale." *Journal of the Electrochemical Society*, vol. 169, no. 3, 2022, p. 031507.
- [36] Ribeiro, A. M., et al. "Electrochemical Characterization of Hot Pressed CoCrMo–Hap Biocomposite in a Physiological Solution." *Materials and Corrosion*, vol. 66, no. 8, 2015, pp. 790-795.
- [37] Furko, M., et al. "Complex Electrochemical Studies on Silver-Coated Metallic Implants for Orthopaedic Application." *Journal of Solid State Electrochemistry*, vol. 20, no. 1, 2016, pp. 263-271.

- [38] Pontes, J. R., et al. "Influence of Processing Method of CoCrMo Dental Alloy on the Corrosion Behavior in Artificial Saliva." *Materials and Corrosion*, 2022.
- [39] Williamson, R. S., et al. "Effect of Duty Cycle on the Crystallinity, Pore Size, Surface Roughness and Corrosion Resistance of the Anodized Surface on Titanium." *Surface and Coatings Technology*, vol. 277, 2015, pp. 278-288.
- [40] Frankel, G. S. "Pitting Corrosion of Metals: A Review of the Critical Factors." *Journal of the Electrochemical Society*, vol. 145, no. 6, 1998, pp. 2186-2198.
- [41] Sharland, S. M. "A Review of the Theoretical Modelling of Crevice and Pitting Corrosion." *Corrosion Science*, vol. 27, no. 3, 1987, pp. 289-323.
- [42] Leon, A., et al. "Effect of Surface Roughness on Corrosion Fatigue Performance of AlSi10Mg Alloy Produced by Selective Laser Melting (SLM)." *Materials Characterization*, vol. 131, 2017, pp. 188-194.
- [43] Melia, M. A., et al. "How Build Angle and Post-Processing Impact Roughness and Corrosion of Additively Manufactured 316l Stainless Steel." *npj Materials Degradation*, vol. 4, no. 1, 2020, p. 21.
- [44] Ryu, J. J., et al. "Influence of Roughness on Surface Instability of Medical Grade Cobalt–Chromium Alloy (CoCrMo) During Contact Corrosion–Fatigue." *Applied Surface Science*, vol. 273, 2013, pp. 536-541.
- [45] Arslan, E., et al. "Influence of Surface Roughness on Corrosion and Tribological Behavior of Cp-Ti after Thermal Oxidation Treatment." *Journal of Materials Engineering and Performance*, vol. 19, 2010, pp. 428-433.
- [46] Sajjad, U., et al. "Enhancing Corrosion Resistance of Al 5050 Alloy Based on Surface Roughness and Its Fabrication Methods; an Experimental Investigation." *Journal of Materials Research and Technology*, vol. 11, 2021, pp. 1859-1867.
- [47] Mitchell, J., et al. "Effect of Surface Roughness on Pitting Corrosion of Az31 Mg Alloy." *Metals*, vol. 10, no. 5, 2020, p. 651.

- [48] Liu, J., et al. "Effect of Surface Abrasion on Pitting Corrosion of Al-Li Alloy." *Corrosion Science*, vol. 138, 2018, pp. 75-84.
- [49] De Oliveira, A. C., et al. "The Effect of Mechanical Polishing and Finishing on the Corrosion Resistance of AISI 304 Stainless Steel." *Corrosion Engineering, Science and Technology*, vol. 51, no. 6, 2016, pp. 416-428.
- [50] Szewczenko, J., et al. "Corrosion Resistance of Ti-6al-4v Alloy after Diverse Surface Treatments." *Materialwissenschaft und Werkstofftechnik*, vol. 41, no. 5, 2010, pp. 360-371.
- [51] Panigrahi, P., et al. "Intergranular Pitting Corrosion of CoCrMo Biomedical Implant Alloy." *Journal of Biomedical Materials Research Part B: Applied Biomaterials*, vol. 102, no. 4, 2014, pp. 850-859.
- [52] Muñoz, A. I., et al. "Interactive Effects of Albumin and Phosphate Ions on the Corrosion of CoCrMo Implant Alloy." *Journal of the Electrochemical Society*, vol. 154, no. 10, 2007, pp. C562-C570.
- [53] Meechai, N., et al. "Translational Diffusion Coefficients of Bovine Serum Albumin in Aqueous Solution at High Ionic Strength." *Journal of colloid and interface science*, vol. 218, no. 1, 1999, pp. 167-175.
- [54] Motoki, E., et al. "Effect of Dodecyltrimethylammonium Chloride on the Adsorption of Bovine Serum Albumin to the Surface of Hydroxyapatite." *Phosphorus Research Bulletin*, vol. 20, 2006, pp. 135-140.
- [55] Mörsdorf, A., et al. "Bioaccessibility of Micron-Sized Powder Particles of Molybdenum Metal, Iron Metal, Molybdenum Oxides and Ferromolybdenum - Importance of Surface Oxides." *Regulatory toxicology and pharmacology*, vol. 72, no. 3, 2015, pp. 447-457.
- [56] Lu, Y. C., et al. "An Xps Study of the Passive and Transpassive Behavior of Molybdenum in Deaerated 0.1 M HCl." *Corrosion Science*, vol. 29, no. 8, 1989, pp. 927-937.

- [57] Pardo, A., et al. "Pitting Corrosion Behavior of Austenitic Stainless Steels – Combining Effects of Mn and Mo Additions." *Corrosion Science*, vol. 50, no. 6, 2008, pp. 1796-1806.
- [58] Lu, Y., et al. "Microstructure, Mechanical Property and Metal Release of as-SLM CoCrW Alloy under Different Solution Treatment Conditions." *Journal of the mechanical behavior of biomedical materials*, vol. 55, 2016, pp. 179-190.
- [59] Lewis, A. C., et al. "Effect of Synovial Fluid, Phosphate-Buffered Saline Solution, and Water on the Dissolution and Corrosion Properties of CoCrMo Alloys as Used in Orthopedic Implants." *Journal of Biomedical Materials Research Part A: An Official Journal of The Society for Biomaterials, The Japanese Society for Biomaterials, and The Australian Society for Biomaterials and the Korean Society for Biomaterials*, vol. 73, no. 4, 2005, pp. 456-467.
- [60] Dufils, J., et al. "Influence of Molybdate Ion and Ph on the Fretting Corrosion of a CoCrMo–Titanium Alloy Couple." *Biotribology*, vol. 11, 2017, pp. 20-28.
- [61] Kerwell, S., et al. "Electrochemically Induced Film Formation on CoCrMo Alloy for Hip Implant Application." *Journal of Bio-and Tribo-Corrosion*, vol. 3, 2017, pp. 1-18.
- [62] Hedberg, Y. S., et al. "Interaction of Albumin and Fibrinogen with Stainless Steel: Influence of Sequential Exposure and Protein Aggregation on Metal Release and Corrosion Resistance." *Corrosion*, vol. 73, no. 12, 2017, pp. 1423-1436.
- [63] Hedberg, Y. S., et al. "Synergistic Effects of Metal-Induced Aggregation of Human Serum Albumin." *Colloids and Surfaces B: Biointerfaces*, vol. 173, 2019, pp. 751-758.
- [64] Roach, P., et al. "Interpretation of Protein Adsorption: Surface-Induced Conformational Changes." *Journal of the American Chemical Society*, vol. 127, no. 22, 2005, pp. 8168-8173.
- [65] Michiardi, A., et al. "The Influence of Surface Energy on Competitive Protein Adsorption on Oxidized NiTi Surfaces." *Biomaterials*, vol. 28, no. 4, 2007, pp. 586-594.

- [66] Baszkin, A., et al. "The Interaction of Plasma Proteins with Polymers. I. Relationship between Polymer Surface Energy and Protein Adsorption/Desorption." *Journal of biomedical materials research*, vol. 14, no. 4, 1980, pp. 393-403.
- [67] Anand, G., et al. "Conformational Transitions of Adsorbed Proteins on Surfaces of Varying Polarity." *Langmuir*, vol. 26, no. 13, 2010, pp. 10803-10811.
- [68] Zhou, K., et al. "Effect of Surface Energy on Protein Adsorption Behaviors of Treated CoCrMo Alloy Surfaces." *Applied Surface Science*, vol. 520, 2020, p. 146354.
- [69] Yamanaka, K., et al. "Mechanical Properties of as-Forged Ni-Free Co–29cr–6mo Alloys with Ultrafine-Grained Microstructure." *Materials Science and Engineering: A*, vol. 528, no. 18, 2011, pp. 5961-5966.
- [70] Lee, S. H., et al. "Effect of Carbon Addition on Microstructure and Mechanical Properties of a Wrought Co–Cr–Mo Implant Alloy." *Materials transactions*, vol. 47, no. 2, 2006, pp. 287-290.
- [71] Safaei, K., et al. "Additive Manufacturing of Niti Shape Memory Alloy for Biomedical Applications: Review of the LPBF Process Ecosystem." *Jom*, 2021, pp. 1-16.
- [72] Mutua, J., et al. "Optimization of Selective Laser Melting Parameters and Influence of Post Heat Treatment on Microstructure and Mechanical Properties of Maraging Steel." *Materials & Design*, vol. 139, 2018, pp. 486-497.
- [73] Vidal, C. V., et al. "Effect of Thermal Treatment and Applied Potential on the Electrochemical Behavior of CoCrMo Biomedical Alloy." *Electrochimica Acta*, vol. 54, no. 6, 2009, pp. 1798-1809.
- [74] Munoz, A. I., et al. "In Vivo Electrochemical Corrosion Study of a CoCrMo Biomedical Alloy in Human Synovial Fluids." *Acta biomaterialia*, vol. 21, 2015, pp. 228-236.
- [75] Ionita, D., et al. "Effect of Human Albumin on Corrosion and Biological Behavior of CoCrMo." *Materials and Corrosion*, vol. 68, no. 8, 2017, pp. 876-882.

## Chapter 7

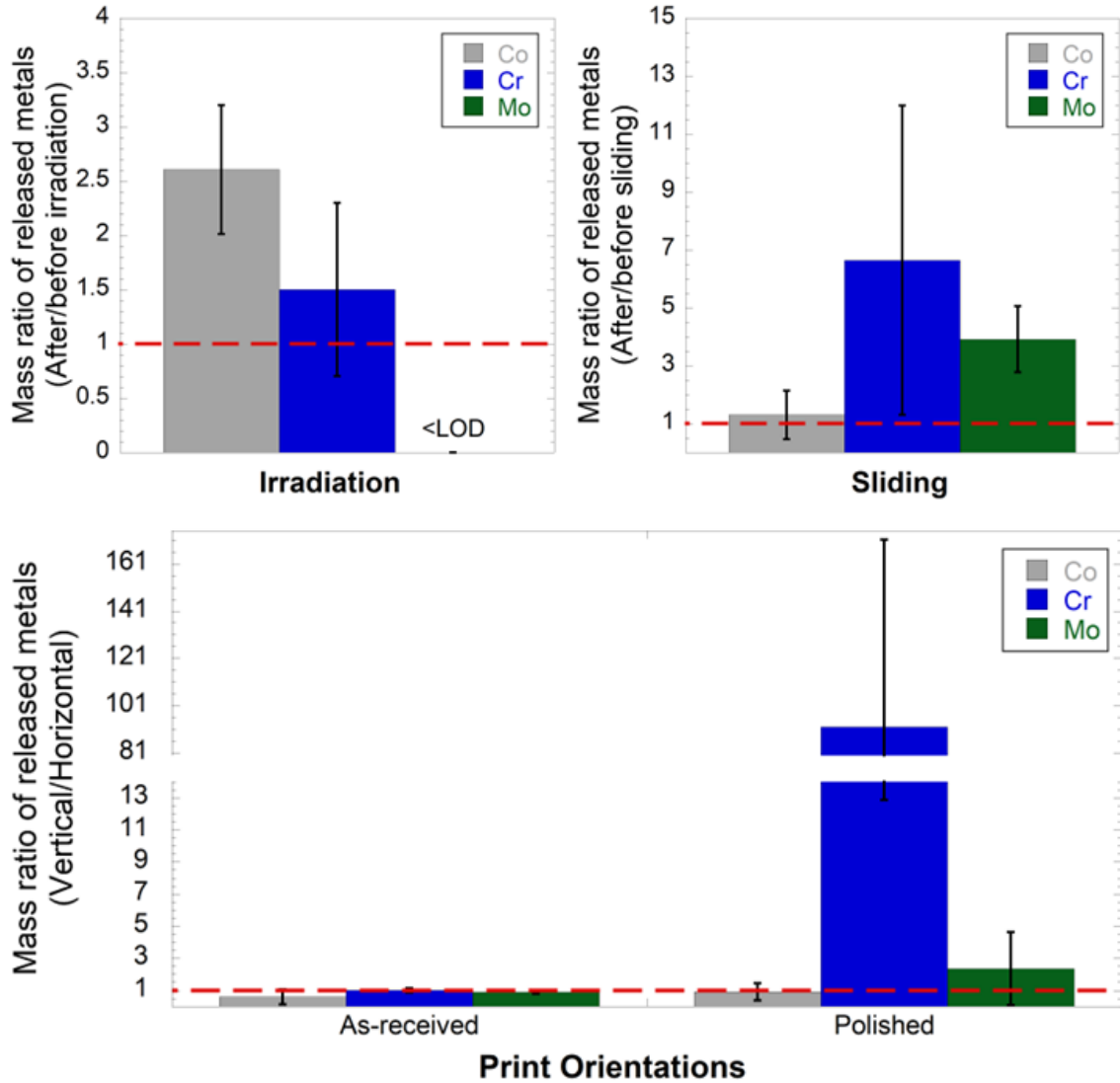
### 7 Conclusions and outlook

#### 7.1 Conclusions

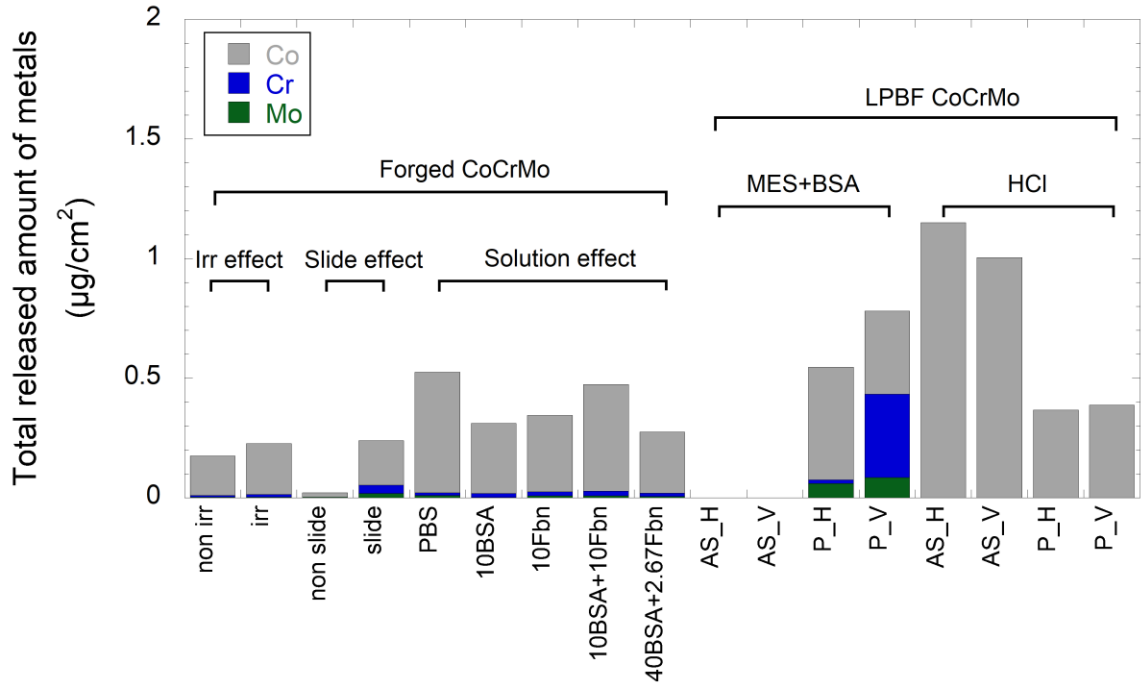
The objectives of this Ph.D. thesis focused on examining the impact of various factors, such as irradiation, sliding conditions, and manufacturing process, on the oxide characteristics, metal release process, electrochemical stability, and the bioavailability of CoCrMo in various simulated synthetic physiological fluids.

Figure 7-1 was created to demonstrate the effects of irradiation, sliding, and printing orientation on metal release in CoCrMo alloy. The figure shows the mass ratios between the amounts of metals released before and after irradiation and sliding, as well as the mass ratio between CoCrMo alloys printed vertically and horizontally using LPBF technology with different surface treatments. Ratios greater than 1 indicate a positive effect of the respective condition, while ratios lower than 1 indicate a negative impact. Figure 7-2 shows the total released amounts of metals from the forged and LPBF CoCrMo before and after irradiation and sliding, and in different solutions. It proves that irradiation and sliding can induce the release of metals from the CoCrMo alloys exposed in the various protein-containing solutions. The LPBF CoCrMo alloys fabricated in vertical orientation released higher amounts of Cr compared to the horizontal orientation, suggesting that print orientation may have an impact on metal release.





**Figure 7-1: Impact of irradiation (Chapter 3), sliding (Chapter 4) and manufacturing process (vertical/horizontal print orientation, Chapter 6) on metal release ratios from CoCrMo alloy exposed to the protein-containing solutions.**



**Figure 7-2: The total released amount of metals from forged and LPBF CoCrMo in different solutions, under different conditions (summary of Chapters 3, 4, and 6).**

The effect of the irradiation, at a dose of relevance for cancer radiation treatment, on the metal release and surface passivation was small but detectable. The results indicate that irradiated CoCrMo alloys release higher amounts of metals directly after irradiation as compared to non-irradiated CoCrMo alloys (Chapter 3).

Sliding resulted in a lower measurable (non-precipitated) amount of released metals in PBS and Fbn solutions, but a higher measurable amount in BSA-containing solutions. Also, the coefficient of friction was greater in the solution containing only Fbn than in the PBS solution (Chapter 4).

Furthermore, the studies on building direction and surface treatments (Chapters 5-6) suggest that the as-received horizontal LPBF CoCrMo exhibits a coarser microstructure than the vertical plane, possibly due to a less rapid cooling rate. The amount of Co released from the specimens after exposure in MES+BSA was lower than in HCl, which was probably due to the occurrence of protein aggregation and metal precipitation. In contrast, the amount of Cr and Mo were equal or more released in MES+BSA than in

HCl. The polished vertical sample showed a tendency to release more Cr than the polished horizontal sample in the MES+BSA (pH 7.2-7.4) solution (Chapter 6).

In terms of corrosion resistance, the studies found that as-received LPBF CoCrMo surfaces exhibit lower corrosion resistance than abraded surfaces. This is in contrast to the metal release, which is mainly determined (in this case, at pH 7.4) by solution chemistry. The orientation of LPBF CoCrMo surfaces showed slight variations in microstructure and corrosion resistance but did not have a significant impact on cell viability or bioactivity (Chapter 5 and Chapter 6). Comparing the solution compositions in Chapters 5 and 6, it appears that the phosphate-containing solutions (PBS, in Chapters 3-5) had a corrosion-inhibiting effect and resulted in precipitation of cobalt and chromium phosphates, which was not the case in Chapter 6 (MES+BSA solution).

The studies on the effect of the concentration and types of proteins on the metal release of CoCrMo surfaces suggest that proteins can induce significant precipitation of metals and protein aggregates, especially at high protein concentrations, leading to a strong underestimation of released metals, especially under sliding conditions and for released Co and Cr. This effect was minor for released Mo. Additionally, protein aggregates were found to precipitate on the surface of CoCrMo, potentially leading to changes in surface chemistry and metal release (Chapter 3, 4 and 6).

These findings have important implications for the design and development of implant materials intended for use in high-protein environments, such as those found in the human body. It is important to consider the potential impact of protein aggregation and metal precipitation on the performance of CoCrMo materials and to optimize their composition and surface properties to minimize metal release and maintain optimal corrosion resistance.

## 7.2 Outlook

In this work, metal release, surface characterizations, corrosion behavior and bioactivity have been investigated for the CoCrMo alloy under different exposure conditions. In the field of CoCrMo as implant materials, there is a continued need for ongoing research and development to improve the safety and minimize potential health hazards. Future work in the field of implant materials should focus on the following aspects:

1. To gain a better understanding of the impact of metal release on patient health, it is necessary to conduct further biocompatibility studies and develop more effective strategies for monitoring and mitigating this effect. This can be achieved by using in-vivo models to study the biocompatibility of implant materials under various conditions.
2. To advance our understanding of the impact of tribocorrosion on metal release in CoCrMo alloys, as well as the interplay between mechanical wear and corrosion, further research is essential. This can be accomplished using experimental and computational methods, which can provide a deeper understanding of the fundamental mechanisms governing tribocorrosion.
3. It is necessary to investigate the fundamental mechanisms underlying protein aggregation in CoCrMo alloys, using advanced analytical techniques and computational methods, to identify the key factors that contribute to protein adsorption, protein-protein interactions, and the formation of protein aggregates.
4. Developing a comprehensive database of metal release from CoCrMo alloys can provide a valuable resource for researchers and engineers in the field of biomedical engineering. The database could include information on the chemical and physical properties of CoCrMo alloys, the specific conditions under which the alloys were exposed to, the time frame of exposure, the type and concentration of protein solutions used, and the corresponding amounts of metal released or corrosion parameters measured under those conditions.
5. To mitigate underestimation of released metals, phosphate-containing buffers should be avoided, and it is recommended to investigate any corrosion-inhibiting effects

and the formation of solids from metal ions by solution components. It is also recommended to standardize in-vitro metal release tests. The standard needs to be specific to the metal or alloy, since the formation of solid precipitates is specific to the metal and solution.

## Appendices

## Appendix A: Chapter 5 Supplementary

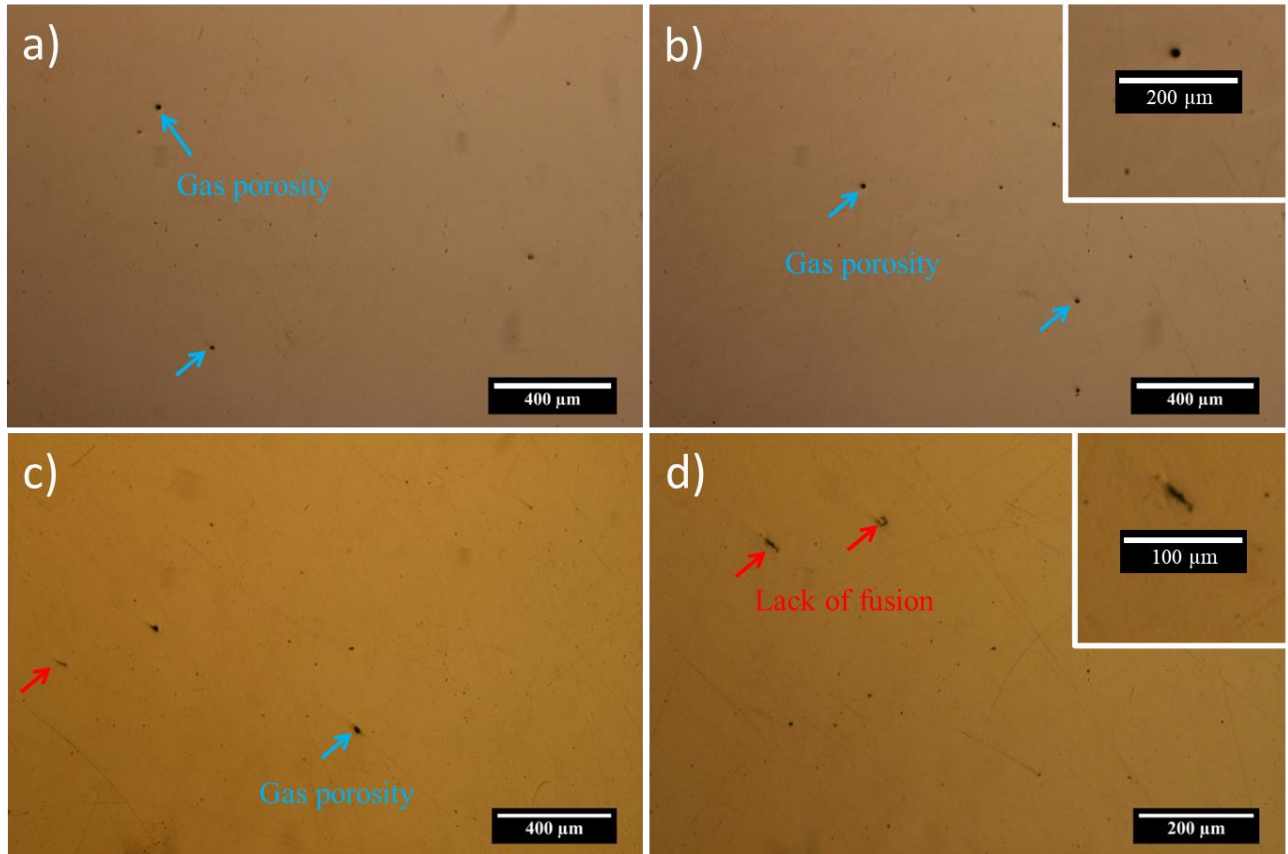


**Figure S1: Voids in printing in (a, b) XY direction including gas porosities and (c, d) XZ directions including gas porosities and lack of fusion. Images by means of optical microscopy.**

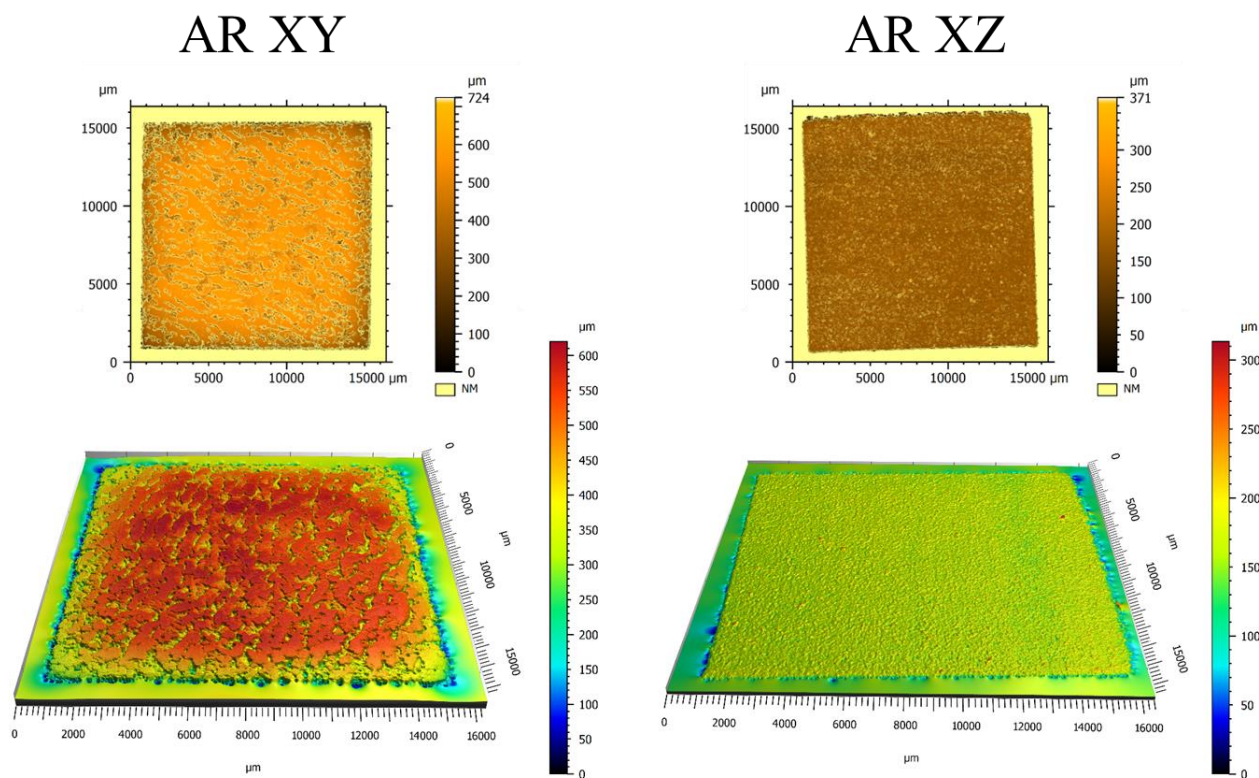


**Figure S2: Confocal microscopy images of as-received XY (left) and as-received XZ (right) CoCrMo surfaces. The estimated surface areas for this 2.25 cm<sup>2</sup> geometrical area were 2.79 cm<sup>2</sup> (left: AR XY) and 2.39 cm<sup>2</sup> (right: AR XZ), respectively.**

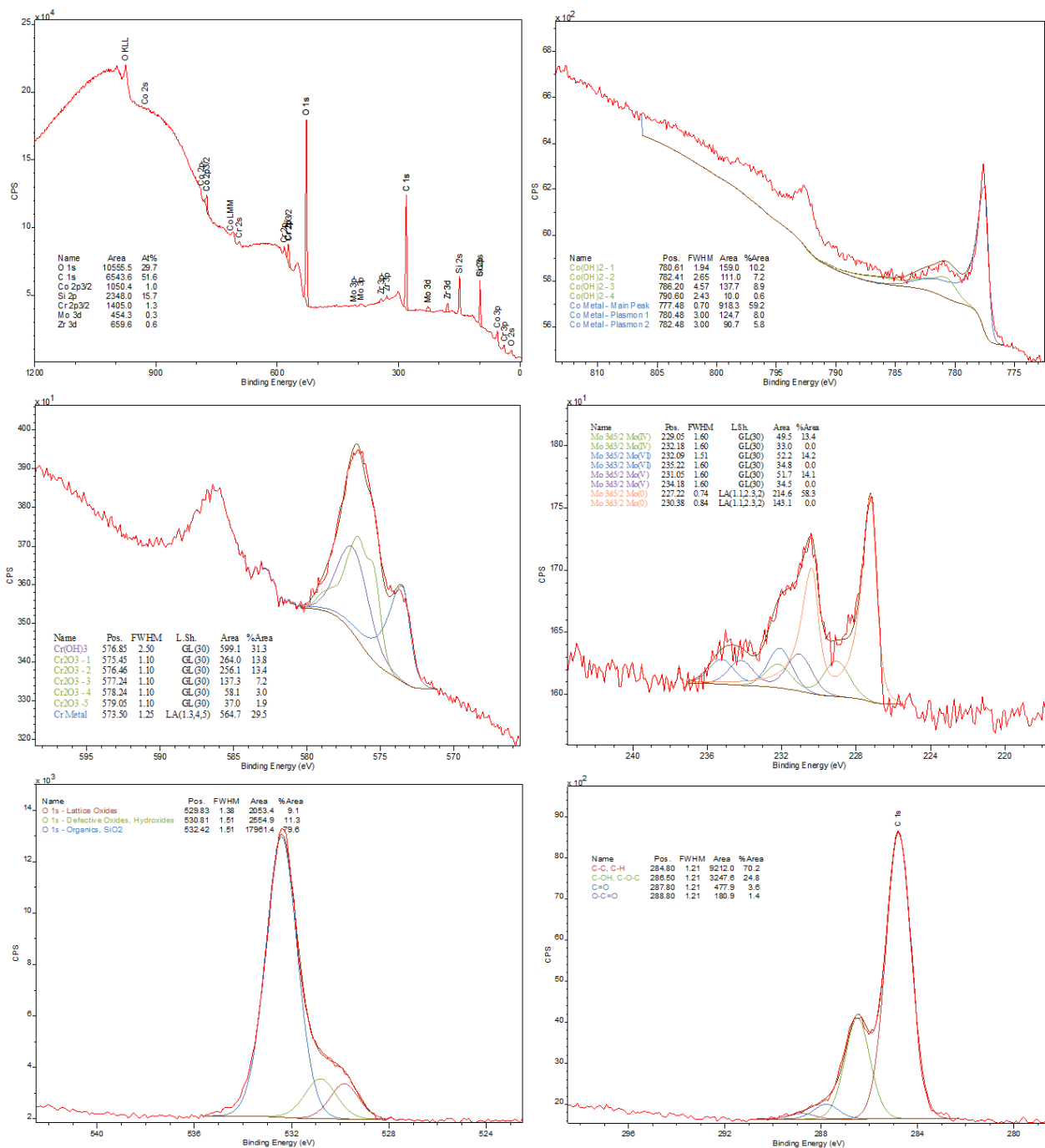


**Figure S3: As-received XZ: XPS wide spectrum and Co 2p, Cr 2p, Mo 3d, O 1s, and C 1s high-resolution spectra. The red points/lines are the raw data, the brown line is the background, the black line is the envelope fit, and the individually fitted species are colored as indicated.**



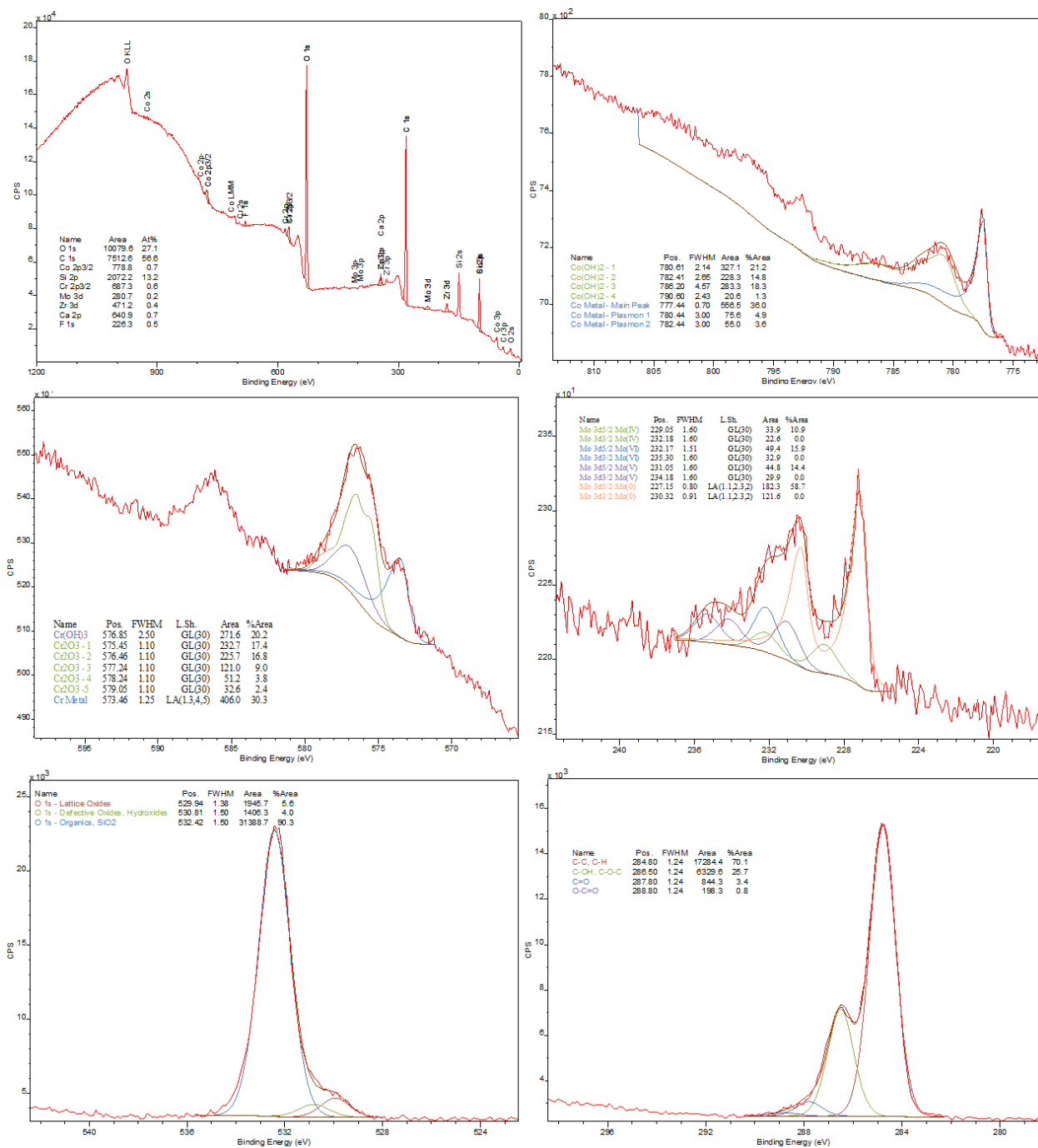


**Figure S4: As-received XY: XPS wide spectrum and Co 2p, Cr 2p, Mo 3d, O 1s, and C 1s high-resolution spectra. The red points/lines are the raw data, the brown line is the background, the black line is the envelope fit, and the individually fitted species are colored as indicated.**

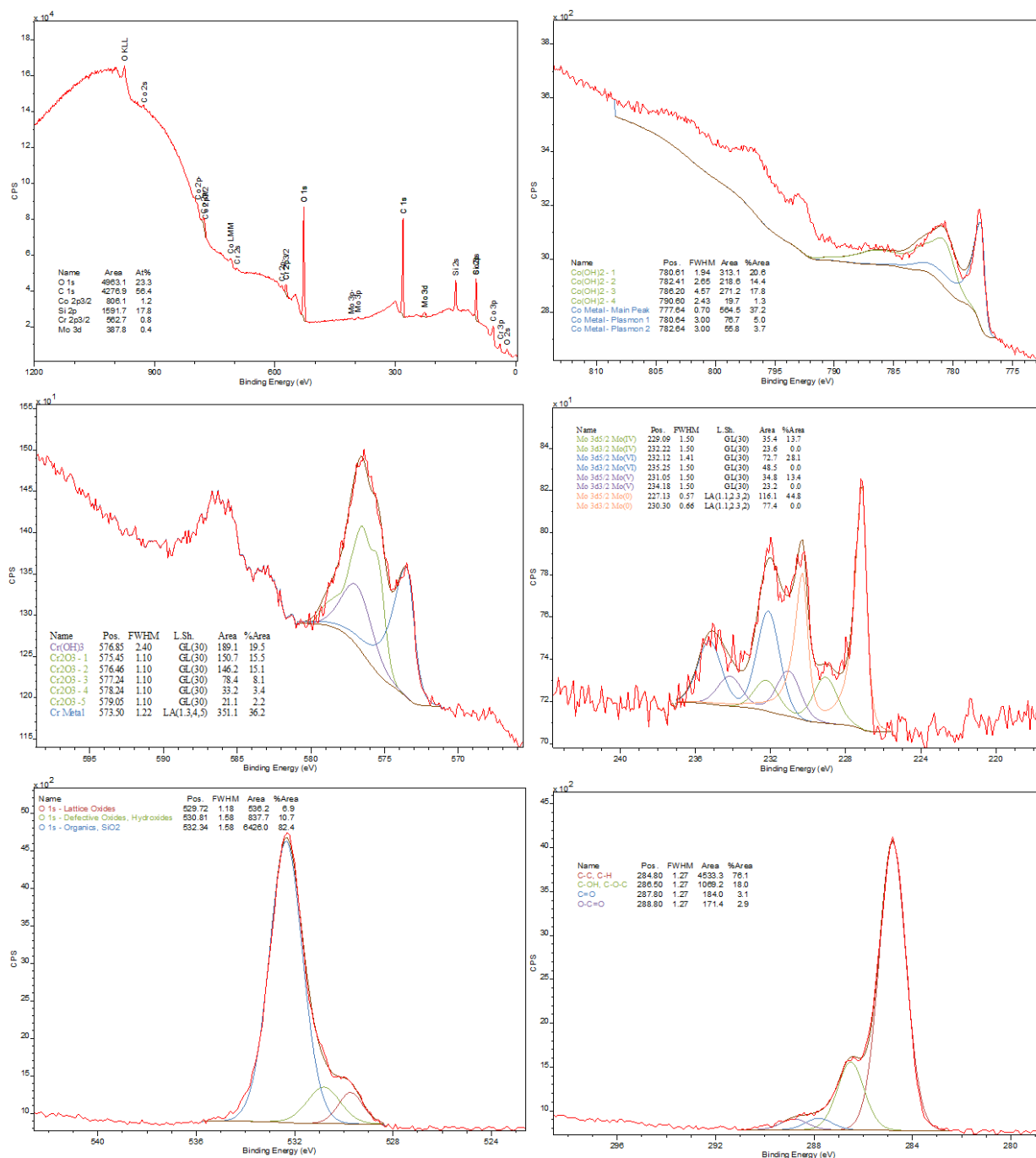


**Figure S5: Abraded XZ: XPS wide spectrum and Co 2p, Cr 2p, Mo 3d, O 1s, and C 1s high-resolution spectra. The red points/lines are the raw data, the brown line is the background, the black line is the envelope fit, and the individually fitted species are colored as indicated.**

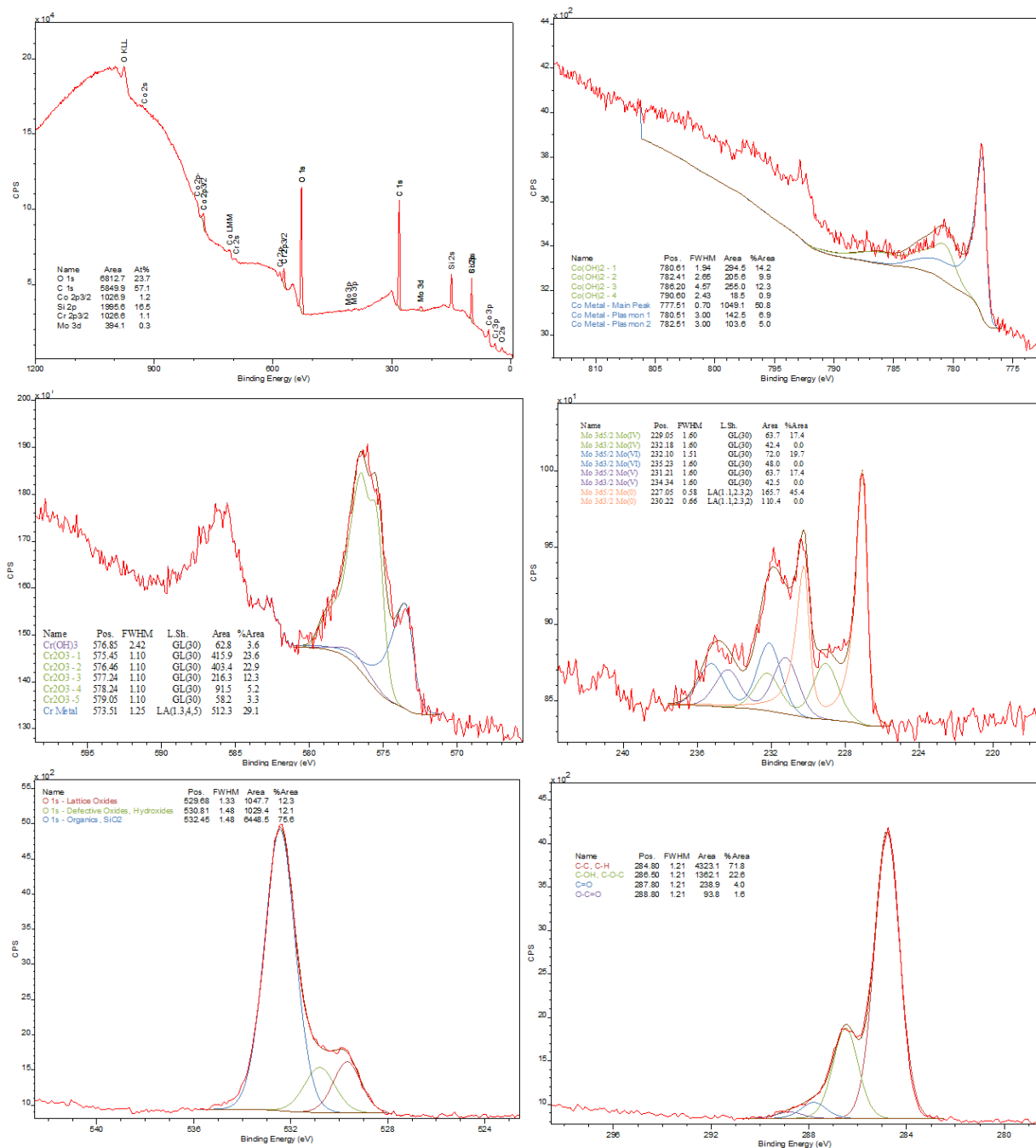


**Figure S6: Abraded XY: XPS wide spectrum and Co 2p, Cr 2p, Mo 3d, O 1s, and C 1s high-resolution spectra. The red points/lines are the raw data, the brown line is the background, the black line is the envelope fit, and the individually fitted species are colored as indicated.**

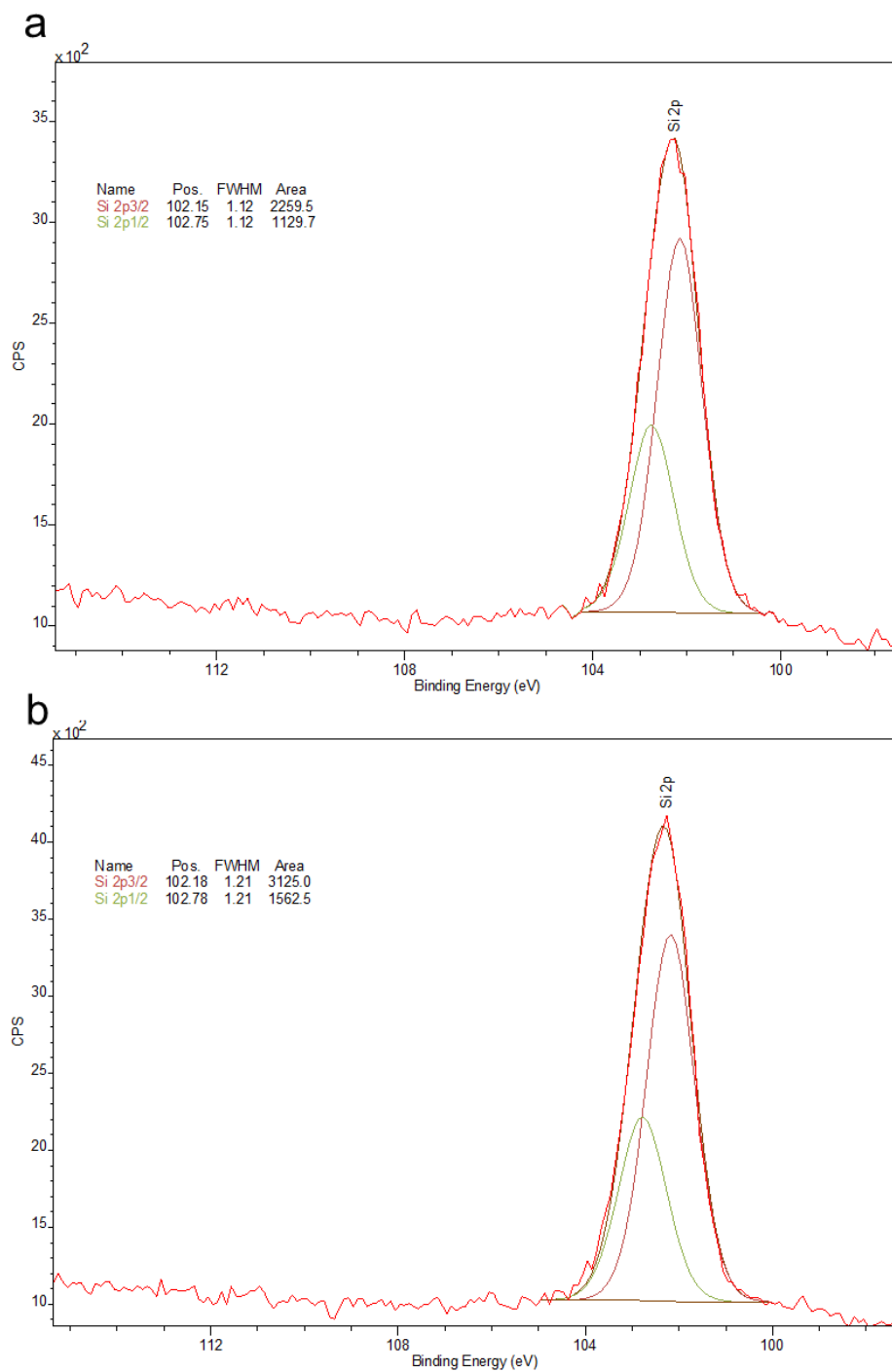


**Figure S7: Abraded (a) and as-received (b) XY: XPS Si 2p high-resolution spectra. The red points/lines are the raw data, the brown line is the background, the black line is the envelope fit, and the individually fitted species are colored as indicated.**

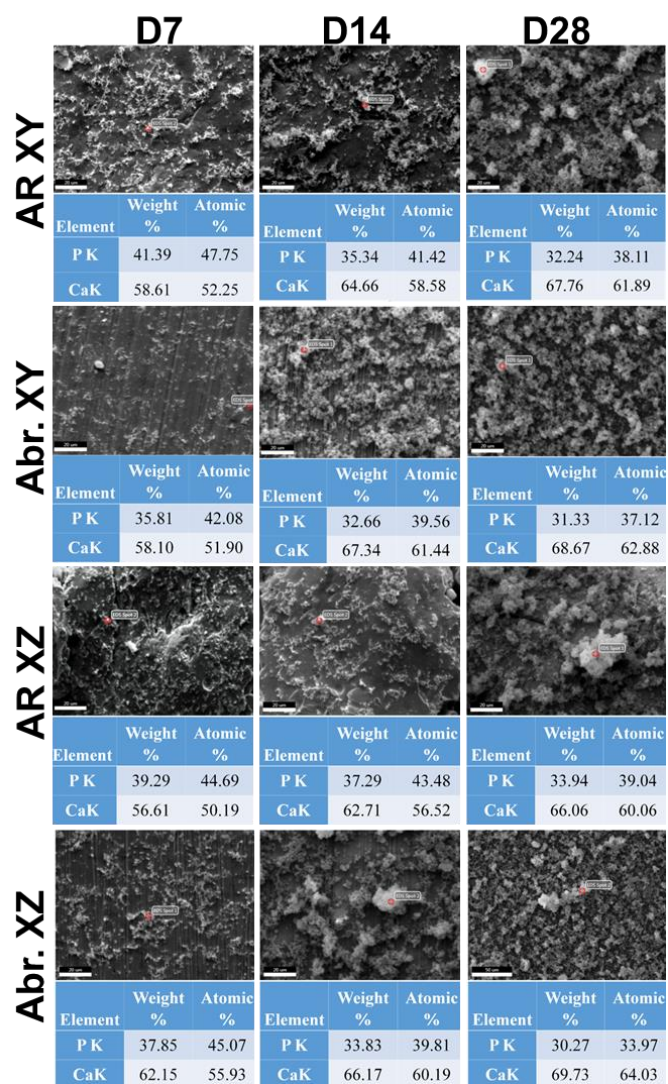
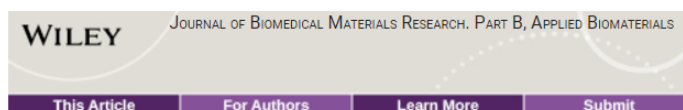


**Figure S8: Representative SEM images indicating the EDS spot analysis of one replicate measurement in Figure 5 in the main manuscript.**

## Appendix B: Copyright and Permission

### Chapter 3:



[J Biomed Mater Res B Appl Biomater](#). 2018 Oct; 106(7): 2673–2680.

PMCID: PMC6175212

Published online 2018 Feb 9. doi: [10.1002/jbm.b.34084](https://doi.org/10.1002/jbm.b.34084)

PMID: [29424962](https://pubmed.ncbi.nlm.nih.gov/29424962/)

### Can gamma irradiation during radiotherapy influence the metal release process for biomedical CoCrMo and 316L alloys?

[Zheng Wei](#), <sup>1, 2</sup> [Jonathan Edin](#), <sup>1, 2</sup> [Anna Emelie Karlsson](#), <sup>1, 2</sup> [Katarina Petrovic](#), <sup>1, 2</sup> [Inna L. Soroka](#), <sup>2</sup> [Inger Odnevall Wallinder](#), <sup>1</sup> and [Yolanda Hedberg](#)<sup>1</sup>

▶ [Author information](#) ▶ [Article notes](#) ▶ [Copyright and License information](#) [Disclaimer](#)

[Copyright](#) © 2018 The Authors Journal of Biomedical Materials Research Part B: Applied Biomaterials Published by Wiley Periodicals, Inc.

This is an open access article under the terms of the <http://creativecommons.org/licenses/by-nc-nd/4.0/> License, which permits use and distribution in any medium, provided the original work is properly cited, the use is non-commercial and no modifications or adaptations are made.

### Chapter 4:

**SPRINGER NATURE** Metal Release from a Biomedical CoCrMo Alloy in Mixed Protein Solutions Under Static and Sliding Conditions: Effects of Protein Aggregation and Metal Precipitation

Author: Zheng Wei et al


Publication: Journal of Bio- and Tribo-Corrosion

Publisher: Springer Nature

Date: Dec 6, 2021

Copyright © 2021, The Author(s), under exclusive licence to Springer Nature Switzerland AG

### Chapter 5:



In vitro corrosion and biocompatibility behavior of CoCrMo alloy manufactured by laser powder bed fusion parallel and perpendicular to the build direction

Author: Masoud Atapour, Saber Sanaei, Zheng Wei, Mohammadali Sheikholeslam, Jeffrey D. Henderson, Ubong Eduok, Yara K. Hosein, David W. Holdsworth, Yolanda S. Hedberg, Hamid Reza Ghorbani

Publication: Electrochimica Acta

Publisher: Elsevier

Date: 20 March 2023

© 2023 Elsevier Ltd. All rights reserved.

## Curriculum Vitae

**Name:** Zheng Wei

### Education:

**The University of Western Ontario, London, Ontario, Canada** 01/2021-present  
 Department of Chemistry  
 Candidate of Ph.D.  
 Supervisor: Dr. Yolanda Hedberg

**KTH Royal Institute of Technology, Stockholm, Sweden** 10/2018-10/2020  
 Candidate of Ph.D. (Licentiate)  
 Supervisor: Dr. Yolanda Hedberg

**KTH Royal Institute of Technology, Stockholm, Sweden** 09/2015-12/2017  
 Major: Materials Science  
 Degree: Master of Science

**The University of Sheffield, Sheffield, United Kingdom** 09/2011-01/2013  
 Major: Advanced Metallurgy  
 Degree: Master of Metallurgy

**Kunming University of Technology and Science, Kunming, China** 09/2007-06/2011  
 Major: Metallurgical Engineering  
 Degree: Bachelor of Engineering

### Work Experience:

**Manager** 04/2012-06-2014  
 Xi'An Bo Zhou Mechanical and Electrical Trading Co., Ltd., Xi'An, China

**Quality Engineer** 08/2014-08/2015  
 Shougang Jingtang United Iron & Steel Co., Ltd., Tang Shan, China

**Research Engineer** 01/2018-06/2018  
 Division of Surface and Corrosion Science, KTH Royal Institute of Technology,  
 Stockholm Sweden

## Publications:

1. Y. Hedberg, M.-E. Karlsson, **Z. Wei**, M. Žnidaršič, I. Odnevall Wallinder, J. Hedberg. Interaction of albumin and fibrinogen with stainless steel - influence of sequential exposure and protein aggregation on metal release and corrosion resistance. *Corrosion* 73: 1423-1436, 2017.
2. **Z. Wei**, J. Edin, A. E. Karlsson, K. Petrovic, I. L. Soroka, I. Odnevall Wallinder, Y. Hedberg, Can gamma irradiation during radiotherapy influence the metal release process for biomedical CoCrMo and 316L alloys?. *Journal of Biomedical Materials Part B: Applied Biomaterials*, 106(7): 1673-2680, 2018.
3. S. Mc Carrick, **Z. Wei**, N. Moelijker, R. Derr, K.-A. Persson, G. Hendriks, I. Odnevall Wallinder, Y. S. Hedberg, H. L. Karlsson, High variability in toxicity of welding fume nanoparticles from stainless steel in lung cells and reporter cell lines: the role of particle reactivity and solubility, *Nanotoxicology*, 13:1293-1309, 2019.
4. Y. S. Hedberg, I. Dobryden, H. Chaudhary, **Z. Wei**, P. M. Claesson, C. Lendel. Synergistic effect of metal-induced aggregation of human serum albumin, *Journal of Colloids and Surface B: Biointerfaces*, 173:751-58, 2019.
5. X. Wang, G. Herting, **Z. Wei**, I. Odnevall Wallinder, Y. Hedberg, Bioaccessibility of nickel and cobalt in powders and massive forms of stainless steel, nickel- or cobalt-based alloys, and nickel and cobalt metals in artificial sweat, *Regulatory Toxicology and Pharmacology*, 106: 15-26, 2019.
6. M. Atapour, **Z. Wei**, H. Chaudhary, C. Lendel, I. Odnevall Wallinder, Y. Hedberg, Metal release from stainless steel 316L in whey protein - and simulated milk solutions under static and stirring conditions, *Food Control*, 101: 163-172, 2019.
7. Y. S. Hedberg, **Z. Wei**, F. Moncada. Chromium(III), chromium(VI), and cobalt release from leathers produced in Nicaragua, *Contact Dermatitis*, 80(3):149-155, 2019.
8. Y. S. Hedberg, **Z. Wei**, M. Matura, Quantification of aluminium release from Finn chambers under different in-vitro test conditions of relevance for patch testing, *Contact Dermatitis*, 83(5): 380-386, 2020.
9. Y. Hedberg, **Z. Wei**, F. Moncada, Release of hexavalent chromium from cement collected in Honduras and Sweden, *Contact Dermatitis*, 83(2):122-124, 2020.
10. Y. Hedberg, **Z. Wei**, M. Matura, High release of hexavalent chromium into artificial sweat in a case of leather shoe induced contact dermatitis, *Contact Dermatitis*, 82(3):179-181, 2020.
11. Y. S. Hedberg, **Z. Wei**, S. McCarrick, V. Romanovski, J. Theodore, E. M. Westin, R. Wagner, K.-A. Persson, H. L. Karlsson, I. Odnevall Wallinder, Welding fume nanoparticles from solid and flux-cored wires: solubility, toxicity, and role of fluorides, *Journal of Hazardous Materials*, 413: 125273, 2021.
12. S. Mc Carrick, V. Romanovski, **Z. Wei**, E. M. Westin, K.-A Persson, K. Trydell, R. Wagner, I. Odnevall Wallinder, Y. S. Hedberg, H. L. Karlsson, Genotoxicity and inflammatory potential of stainless steel welding fume particles - an in vitro study on standard vs Cr(VI)-reduced flux-cored wires and the role of released metals, *Archives of Toxicology*, 95(9): 2961-2975, 2021.
13. E. M. Westin, S. Mc Carrick, L. Laundry-Mottiar, **Z. Wei**, M. C. Biesinger, I. Barker, R. Wagner, K.-A Persson, K. Trydell, I. Odnevall Wallinder, H. L. Karlsson, Y. S. Hedberg, New weldable 316L stainless flux-cored wires with reduced Cr (VI)



- fume emissions: part 1 - health aspects of particle composition and release of metals. *Welding in the World*, 65(12): 2319-2337, 2021.
14. E. M. Westin, S. Mc Carrick, L. Laundry-Mottiar, **Z. Wei**, M. C. Biesinger, I. Barker, R. Wagner, K. Persson, K. Trydell, I. Odnevall Wallinder, H. L. Karlsson, Y. S. Hedberg, New weldable 316L stainless flux-cored wires with reduced Cr (VI) fume emissions: part 2 - round robin creating fume emission data sheets. *Welding in the World*, 65(12): 2339-2348, 2021.
  15. **Z. Wei**, V. Romanovski, L. Filho, C. Persson, Y. Hedberg, Metal release from a biomedical CoCrMo alloy in mixed protein solutions under static and sliding conditions – effects of protein aggregation and metal precipitation. *Journal of Bio-and Tribocorrosion* 8, 19, 2022.
  16. M. Atapour, S. Sanaei, **Z. Wei**, M. Sheikholeslam, J. D. Henderson, U. Eduok, Y. K. Hosein, D. W. Holdsworth, Y. S. Hedberg, and H. R. Ghorbani, 2023. *In vitro* corrosion and biocompatibility behavior of CoCrMo alloy manufactured by laser powder bed fusion parallel and perpendicular to the build direction. *Electrochimica Acta*, p.142059.

### Technical reports:

1. **Z. Wei**, N. Mei, X. Wang, J. Hedberg, I. Odnevall Wallinder, Y. Hedberg, *'Bioaccessibility testing and characterization of five molybdenum compounds'*, commissioned by the international molybdenum development association, December 2019.
2. **Z. Wei**, Y. Hedberg, Å. Laurell Lyne, *'Analysresultat av avrinningsvatten från betong'*, [analytical results of runoff water from concrete], commissioned by Trafikverket, Stockholm, Sweden, June 2019.
3. **Z. Wei**, L. Racchio, I. Odnevall Wallinder, Y. Hedberg, *'Cobalt release testing from an iron ore powder in four synthetic body fluids (bio-elution testing)'*, commissioned by Höganäs Sweden AB, December 2018.
4. **Z. Wei**, L. Racchio, I. Odnevall Wallinder, Y. Hedberg, *'Cobalt release testing from three powders in four synthetic body fluids (bio-elution testing)'*, commissioned by Höganäs Sweden AB, December 2018.
5. X. Wang, **Z. Wei**, I. Odnevall Wallinder, Y. Hedberg, *'Nickel and cobalt release testing from three alloy grades in four synthetic body fluids (bioelution testing)'*, commissioned by Aperam, France, August 2018.
6. **Z. Wei**, I. Odnevall Wallinder, Y. Hedberg, *'Solution metal concentrations after corrosion tests of superaustenitic stainless steels'*, commissioned by Sandvik AB, Sweden, January 2018.
7. **Z. Wei**, I. Odnevall Wallinder, Y. Hedberg, *'Understanding of corrosion mechanisms of hyper-duplex stainless steel 2707 in HCl solutions at elevated temperature'*, technical report, commissioned by Sandvik AB, Sweden, January 2018.
8. Y. Hedberg, **Z. Wei**, I. Odnevall Wallinder, *'Cobalt release testing from several stainless steel grades according to the European test guideline for metals and alloys used in food contact materials and articles'*, technical report,

commissioned by the International Stainless Steel Forum, Belgium, February 2017.

### Conference contributions:

1. S. McCarrick, V. Romanovski, **Z. Wei**, E. M. Westin, K.-A. Persson, K. Trydell, R. Wagner, I. Odnevall, Y. S. Hedberg, H. L. Karlsson, '*Genotoxicity and inflammatory potential of stainless steel welding fume particles – an in vitro study on standard vs Cr(VI)-reduced flux-cored wires and the role of released metals*', oral presentation by K. Trydell, Joint Commission II and VIII meeting, **International Institute of Welding**, virtual conference, July 7-21, 2021.
2. E. M. Westin, S. McCarrick, **Z. Wei**, V. Romanovski, R. Wagner, K.-A. Persson, K. Trydell, I. Odnevall, H. L. Karlsson, Y. S. Hedberg, '*New weldable 316L stainless flux-cored wire with reduced Cr(VI) fume emissions*', oral presentation by Y. S. Hedberg, Joint Commission II and VIII meeting, **International Institute of Welding**, virtual conference, July 7-21, 2021.
3. S. McCarrick, V. Romanovski, **Z. Wei**, E. M. Westin, K.-A. Persson, K. Trydell, R. A. Wagner, I. Odnevall, Y. S. Hedberg, H. L. Karlsson, '*A comparison of in vitro toxicity and inflammation from stainless steel welding fume particles generated with standard versus Cr(VI)-reduced flux cored wires – the impact of released metals*', **Eurotox 2021** (26-29th September), online, 2021.
4. **Z. Wei**, V. Romanovski, L. Filho, C. Persson, Y. Hedberg, '*Metal release from a biomedical CoCrMo alloy in mixed protein solutions under static and sliding conditions – effects of protein aggregation and metal precipitation*', **MS&T21**, Columbus, Ohio, 17-21 October, 2021.
5. **Z. Wei**, S. McCarrick, V. Romanovski, J. Theodore, N. Mei, K.-A. Persson, O. Runnerstam, H.L. Karlsson, I. Odnevall Wallinder, Y. Hedberg, '*Minimized risk for exposure and release of harmful substances when welding stainless steels*', 23-25 October 2019, poster presentation, Materials and Formulations at Biointerfaces, **a symposium on surface chemistry and materials science**, Malmö, Sweden.
6. S. McCarrick, Y. Hedberg, **Z. Wei**, I. Odnevall Wallinder, H. Karlsson, '*High variation in the cytotoxic and genotoxic potential of welding fume particles*', **Swetox Academy Workshop**, August 2018, Stockholm, Sweden.

### Supervision of bachelor thesis:

1. N. Alexis, R. Kalifa, A. Lund, '*Release of potentially hazardous substances from welding fumes*', supervisors: **Z. Wei** and Y. Hedberg, 2019.

### Course Work (grad courses):

FKD 3420 Molecules and materials at interfaces, KTH, Sweden, 2018-10-18

FSG 3133 Engineering for a sustainable society, KTH, Sweden, 2018-12-07

FKD 3230 Surface, colloids and soft matter, KTH, Sweden, 2018-12-15

FKD 3090 Research frontiers in surface and corrosion science, KTH, Sweden, 2019-12-17

FKD 3320 Trace metal analysis and speciation, KTH, Sweden, 2019-12-18

FKA 3030 Research ethics, KTH, Sweden, 2020-06-05

C6F 3125 Health risk assessment: principle and applications, Karolinska Institute, Sweden, 2019-03-22

KZ 8014 Powder diffraction with X-ray and neutrons in materials chemistry, Stockholm University, Sweden, 2020-03-20

ECS short course, Fundamentals of electrochemistry: basic theory and thermodynamic methods, UWO, Canada

9608T Polymers in cell and drug delivery (Grade: 86), UWO, Canada

9547T Surface chemistry of nanoparticles (Grade: 92), UWO, Canada

9658 Graduate Seminar Course, Topic: New Contact Lenses for Drug Delivery (Presentation date: April 14<sup>th</sup> 2022), UWO, Canada